



**university of
groningen**



Insights from spectral stacking on the H I content of cluster galaxies in various environments

A tale of two clusters

PhD thesis

to obtain the degree of PhD of the
University of Groningen
on the authority of the Rector Magnificus
Prof. C. Wijmenga
and in accordance with
the decision by the College of Deans.

and

to obtain the degree of PhD of the
University of Cape Town
on the authority of the
Vice-Chancellor Prof. M. Phakeng
and in accordance with
the decision by the Doctoral Degrees Board.

Double PhD Degree

This thesis will be defended in public on

Monday 23 August 2021 at 16:15 hours

by

Julia Lynn Healy

born on 1 November 1991
in Cape Town, South Africa

The copyright of this thesis vests in the author. No quotation from it or information derived from it is to be published without full acknowledgement of the source. The thesis is to be used for private study or non-commercial research purposes only.

Published by the University of Cape Town (UCT) in terms of the non-exclusive license granted to UCT by the author.

Supervisors

Prof.Dr. M.A.W. Verheijen

Prof.Dr. S.-L. Blyth

Prof.Dr. J.M. van der Hulst

Prof.Dr. R.C. Kraan-Korteweg

Plagiarism Declaration

I, Julia Lynn Healy, know the meaning of plagiarism and declare that all of the work in the document, save for that which is properly acknowledged, is my own.

I confirm that I have been granted permission by the University of Cape Town's Doctoral Degrees Board to include the following publications in my thesis, and where co-authorships are involved, my co-authors have agreed that I may include the publications:

- H I content in Coma cluster substructure (Chapter 2, accepted for publication in *Astronomy & Astrophysics*)
The calibration and data reduction of the H I data cubes was performed by P. Serra, K. Yim, J.M van der Hulst, and G. Józsa. The list of H I detections was supplied to me by K. Hess, and T. Jarrett provided the stellar mass and star formation rates for the cluster galaxies.
- Abell 2626 and friends: large and small scale structure (Chapter 4, submitted to the *American Astronomical Society's journals*)
The observations and data reduction of the MMT redshifts were carried out by S. Willner.

Signature:

Signed by candidate

Abstract

The environment in which a galaxy resides has long been known to have an impact on how the galaxy evolves. The denser the environment, the stronger the influence. Clusters of galaxies, which are some of the densest known cosmic environments, provide a unique opportunity to study the ongoing environmental processes influencing galaxy evolution. Optical studies have shown that galaxy clusters are typically home to a higher fraction of older elliptical, bulge-dominated galaxies than the field which has a higher fraction of younger, disk-dominated galaxies. Which environmental processes are the cause of this morphology-density relation is still unknown. The dominant processes at play in the cluster environment tend to strongly impact the neutral hydrogen (H I) gas disks of galaxies. The H I disk often extends far out beyond the stellar disk making it susceptible to environmental processes before the stellar component of the galaxy is affected, and thus a useful tracer of the environment-driven galaxy evolution.

In this thesis I study how the ongoing environmental processes in two galaxy clusters, the Coma cluster and Abell 2626, affect the average H I content of galaxies of different morphologies in different local environments or substructure. In the analysis of both clusters, I primarily use the H I stacking technique which uses the optical position and redshift information to extract global H I profiles of galaxies that are not necessarily directly detected in H I. The global profiles are aligned using the redshifts, and co-added to create an average H I spectrum with improved signal-to-noise statistics.

Using yet-to-be published H I observations of the Coma cluster from the Westerbork Synthesis Radio Telescope, in combination with a new compilation of redshifts across the cluster, I explore the average H I content of galaxies located in different substructures within the cluster compared to cluster galaxies not associated with any substructure. While no conclusions can be made about which environment in Coma has a more dominant effect on the H I content, the analysis showed that there was a clear bimodality in the H I content of the cluster galaxies: either the galaxies were detected in H I, or the H I masses were well below the detection threshold. Where galaxies were not directly detected, they were found to be at least 10–50 times more H I deficient than field galaxies of the same type.

Unlike the Coma cluster, Abell 2626 has not been as well studied, and so little is known about this cluster and its environs. In the second part of the thesis, I present new radio and optical observations of the cluster. Abell 2626 was observed by MeerKAT as part of the first open call for proposals. These observations have yielded H I data for Abell 2626 at the same H I mass sensitivity as the Westerbork observations of the Coma cluster, which is 2.5 times more nearby. Using the multi-object spectrograph, Hectospec, on the MMT telescope, we have created a spectroscopic catalogue of the Abell 2626 field that matches the MeerKAT observations and is 70% complete at $r = 19.1$ mag. The new spectroscopic catalogue around Abell 2626 enabled the characterisation of both the large scale structure in front of and behind the cluster, as well as the identification of substructure associated with the cluster. I am also able to determine that Abell 2626 is a rich cluster, comparable to the similarly sized Virgo cluster. I explore how the average H I content of galaxies of different luminosity,

colour, and morphology change across the different local environments and substructure within the cluster. I find that late-type cluster galaxies located in substructures contain on average more HI than the late-type cluster galaxies not in substructures. I postulate that this suggests that the group environment protects the late-type galaxies from gas stripping mechanisms dominant in the global cluster environment. The HI stacking analysis shows that while Abell 2626 is not as HI deficient as the more massive Coma cluster, the Abell 2626 cluster galaxies do show a radial trend in the HI deficiencies as is observed in other clusters.

Contents

1	Introduction	1
1.1	Galaxies in the Universe	1
1.2	Tracing the evolution of galaxies	2
1.3	Galaxy clusters	6
1.3.1	H I in clusters	7
1.4	H I Stacking	10
1.5	This thesis	12
2	H I content in Coma cluster substructure	19
2.1	Introduction	20
2.2	Multiwavelength data	22
2.2.1	Optical spectroscopy	22
2.2.2	Photometric data	25
2.2.3	H I data	28
2.3	H I stacking method	29
2.4	H I in Coma	30
2.4.1	H I – M_* scaling relation	30
2.4.2	H I deficiencies	32
2.4.3	H I stacking in and around the cluster	34
2.5	Finding substructure in Coma	36
2.6	Identified substructures	37
2.6.1	Core substructures	37
2.6.2	Groups coincident with excess X-ray emission	38
2.6.3	Groups near the outskirts	41
2.6.4	H I in substructure versus the cluster	41
2.7	Summary	43
A	Miscellaneous figures and tables	45
B	Stacked spectra	48
C	Data tables of measurements from stacking	55
D	Coma catalogue	56
E	Coma atlas	57
3	A radio view of Abell 2626: the H I story	65
3.1	Introduction	66
3.2	MeerKAT Observations	67
3.3	Data processing	67
3.3.1	L-band continuum imaging	69
3.3.2	H I line data reduction	71
3.4	Galaxies with H I	72

3.4.1	H I Source finding	72
3.4.2	H I global properties	75
3.4.3	H I data quality checks	77
3.5	Summary	79
4	Abell 2626 and friends: large and small scale structure	83
4.1	Introduction	84
4.2	Spectroscopy	85
4.2.1	Literature redshifts	85
4.2.2	MMT Spectroscopy	86
4.2.3	Spectroscopic Completeness	89
4.3	Large-scale structure	90
4.3.1	Large scale structure in the MMT volume	90
4.3.2	Identifying A2625	90
4.3.3	Large scale structure beyond the MMT Volume	93
4.3.4	Large scale structure around A2626	94
4.3.5	Background clusters	96
4.4	A2626 and friends	97
4.5	Substructure in A2626	99
4.5.1	Identifying substructures	99
4.5.2	Substructure in A2626	100
4.5.3	Substructure in HW1	102
4.5.4	Substructure in A2637	103
4.6	Summary	103
5	H I beyond the detection threshold in Abell 2626	109
5.1	Introduction	110
5.2	Multi-wavelength data	111
5.2.1	Spectroscopy	111
5.2.2	Optical photometry	114
5.2.3	H I data	116
5.3	H I stacking	119
5.4	Characterising the cluster	120
5.4.1	The galaxy population	120
5.4.2	H I deficiency in the cluster	122
5.4.3	Optical luminosity and H I	125
5.4.4	H I in cluster substructures	128
5.5	Cluster and group impact on galaxy evolution	130
5.6	Summary and Conclusions	133
A	Stacked spectra	135
B	Data tables of measurements from stacking	149
6	Summary and Future Work	157
6.1	Thesis highlights	157
6.1.1	Identifying cluster substructure	157
6.1.2	Quantifying the cluster H I content	158
6.1.3	Local vs global environment	159
6.2	Future Work	160
6.2.1	Ongoing work with Abell 2626	160
6.2.2	H I surveys of galaxy clusters	160

6.2.3	H I deficiency scaling relation	161
6.2.4	Towards the future with the SKA	161
	Samenvatting voor niet-deskundigen	165
	Summary for non-experts	169
	Acknowledgements	173

List of Figures

1.1	Diagram of the Hubble Tuning Fork	2
1.2	Optical Colour-Magnitude Diagram	3
1.3	UV-optical colour-colour diagram from Schawinski et al. (2007; Fig. 7)	4
1.4	H I deficiency as a function radius from the cluster centre, from Solanes et al. (2001; Fig. 4)	8
2.1	Colour magnitude diagram for the Coma cluster	24
2.2	WIYN/Hydra targets, and observed sources.	25
2.3	Three examples of the cross-correlation results of Hydra spectra	26
2.4	Redshift histogram for the Coma cluster	27
2.5	Example of galaxy modelling with GALFITM	27
2.6	Stellar mass and star formation rate distribution	28
2.7	Stacked noise as a function of input spectra	30
2.8	Coma M_{HI} to M_{\star} scaling relation	31
2.9	hi deficiency of the Coma galaxies vs projected radius	33
2.10	Phase-space diagram for Coma	33
2.11	Stacked spectra for all, blue and red H I non-detections in different regions of the cluster	35
2.12	Coma substructure	37
2.13	Coma groups with x-ray excess	39
2.14	Stacked profiles for galaxies in different environments in increasing annuli from the cluster centre	42
2.15	Stacked profiles for galaxies in different environments in the virialised, non-virialised, and infal regions	43
A.1	Spectrum extraction method	46
A.2	Dressler-Shectman Test bubble plot	47
B.1	Stacked spectra for Figure 2.8 – full sample	48
B.2	Stacked spectra for Figure 2.8 – non-detections	49
B.3	Stacked profiles for Coma non-detections in bins of radius from cluster centre	50
B.4	Same as Figure B.3 for the sample of galaxies with $\log M_{\star} < 9.5$	51
B.5	Same as Figure B.3 for the sample of galaxies with $\log M_{\star} > 9.5$	52
B.6	Stacked spectra for each of the substructures S1–S10	53
B.7	Same as Figure B.6, but for substructures S11–S15.	54
E.1	Example atlas page for one galaxy in the WCS	57
3.1	MeerKAT L-band continuum image of the A2626 field	69
3.2	NVSS-MeerKAT flux comparison	70
3.3	Iterative ‘de-rippling’ of the H I cube	71
3.4	Spectral noise map	72
3.5	Noise per channel as a function of frequency	72

3.6	Sky distribution and histogram of the H I detections	73
3.7	H I global profile of a detection	75
3.8	Illustration of the calculation of the profile line width	75
3.9	H I mass as function of redshift	76
3.10	Global profiles for the 14 galaxies observed by MeerKAT in the ALFALFA survey	77
3.11	Fractional difference between ALFALFA and MeerKAT integrated fluxes . .	78
3.12	Comparison between ALFALFA and MeerKAT line widths	78
4.1	Literature redshift histogram and colour magnitude diagram used for the MMT target selection	87
4.2	MMT success rate	88
4.3	Spectroscopic completeness as a function of magnitude and radius from cluster centre	90
4.4	Spatial distribution of the spectroscopic completeness	91
4.5	Redshift histogram of all galaxies ($z \lesssim 0.46$) in the A2626 field, and spatial distribution of the spectral over-densities	92
4.6	Sky distribution of the galaxies identifying location of A2625	93
4.7	3-D distribution of the galaxy clusters in and around the Perseus–Pegasus filament	94
4.8	Sky distribution of the Perseus–Pegasus filament based on Batsuki & Burns (1985, Fig. 3)	95
4.9	Schematic of how A2626, HW1, and A2637 fit together	96
4.10	Sky distribution and redshift histogram for A2626, HW1, and A2637	98
4.11	Phase space diagrams for A2626, HW1, and A2637	99
4.12	Sky distribution of identified substructures, and the bubble plots used to identify substructure in A2626, HW1, and A2637	100
4.13	Sky distribution and velocity histograms of identified groups in A2626, HW1, and A2637.	101
5.1	Comparison between optical and H I redshifts for 161 H I detections	111
5.2	Spectroscopically confirmed members of Abell 2626	112
5.3	Examples of fits to the DECaLS data resulting in different χ_r^2 values	113
5.4	Examples of the visual morphological classifications for five galaxies in the cluster.	115
5.5	Comparison between visually identified galaxy morphologies and model-based morphologies	115
5.6	Example of the ellipse fitting method used to determine R_{25}	116
5.7	Distribution of the optical diameters of the A2626 galaxies	117
5.8	Example of a flattened SoFiA mask	118
5.9	Difference between the integrated flux density of detections using 2D and 3D spectrum extraction methods	118
5.10	Example of target and reference spectra extraction apertures	119
5.11	Two examples of H I detections missed by SoFiA	120
5.12	Stacked noise as a function of input spectra	121
5.13	Morphology-radius relation for A2626	121
5.14	H I deficiency as a function of projected radius	123
5.15	Spatial distribution of the cluster galaxies in increasingly fainter magnitude bins	125

5.16	M_{HI}/L_r as a function of absolute r magnitude (a) and projected distance from the cluster centre (b)	126
5.17	M_{HI}/L_r as a function of projected radius from the cluster centre comparing blue/red galaxy populations and bright/faint galaxy populations.	127
5.18	Spatial distribution and colour magnitude diagrams of the six substructures in A2626	128
5.19	M_{HI}/L_r as a function of projected radius from the cluster centre comparing cluster galaxies in groups and cluster galaxies not in groups	130
5.20	Magnitude distribution of galaxies in groups and not in groups in radial bins	131
5.21	Magnitude distribution of late-type galaxies in substructure and not in substructure	132
A.1	Stacked spectra for Figure 5.14	135
A.2	Stacked spectra for Figure 5.16a	136
A.3	Stacked spectra for Figure 5.16b	137
A.4	Stacked spectra for the blue galaxies in Figure 5.17a	138
A.5	Stacked spectra for the red galaxies in Figure 5.17a	139
A.6	Stacked spectra for the bright galaxies in Figure 5.17b	140
A.7	Stacked spectra for the faint galaxies in Figure 5.17b	141
A.8	Stacked spectra for the six substructures in A2626 determining the average M_{HI}	142
A.9	Stacked spectra for the six substructures in A2626 determining the average DEF_{HI}	143
A.10	Stacked spectra for the group galaxies in Figure 5.19a	144
A.11	Stacked spectra for the non-group galaxies in Figure 5.19a	145
A.12	Stacked spectra for all late-type galaxies in Figure 5.19b	146
A.13	Stacked spectra for the late-type galaxies in groups in Figure 5.19b	147
A.14	Stacked spectra for the non-group late-type galaxies in Figure 5.19b	148
1	Schema van de Hubble Stenvork	165
2	Meerdere golflengten van het Whirlpoolstelsel	166
3	HI stacking diagram	167
1	Diagram of the Hubble Tuning Fork	169
2	Multi-wavelength view of the Whirlpool galaxy	170
3	HI stacking diagram	171

List of Tables

2.1	Coefficients used to calculate M_{exp}	32
2.2	Details of the Coma substructure	38
A.1	Number of redshifts obtained from the different literature sources discussed in Section 2.2.1.1.	45
C.1	Average M_* and $f_{H\text{I}}$ measurements for Figure 2.8. Where there is no detection in the stacked spectrum, the the 3σ upper limit is used.	55
C.2	Average H I deficiency measurements in each radius bin for Figure 2.9. Where there is no detection in the stacked spectrum, the 3σ lower limit is used. The high stellar mass samples have $M_* > 10^{9.5} M_\odot$, and the low stellar mass sample, $M_* < 10^{9.5} M_\odot$	55
D.1	Catalogue of Coma galaxies within the Westerbork Coma Survey	56
3.1	MeerKAT observations and imaging parameters	68
4.1	Hectospec Configurations	88
4.2	Template Uncertainties	88
4.3	MMT Redshifts	89
4.4	Clusters and over-densities in the MMT footprint.	96
4.5	Groups identified in A2626 using the DS test	102
4.6	Groups identified in HW1 using the DS test	102
4.7	Groups identified in A2637 using the DS test	103
5.1	Number of galaxies for each morphological classification in annuli increasing from the cluster centre.	122
5.2	Details of the six substructures associated with A2626.	129
5.3	Results of the KS test for Figure 5.20	131
5.4	Results of the KS test for Figure 5.21	132
B.1	Average $DEF_{H\text{I}}$ measurements measured from the stacked spectra in Figure A.1149	
B.2	Average $M_{H\text{I}}/L_r$ measurements measured from the stacked spectra in Figure A.2149	
B.3	Average $M_{H\text{I}}/L_r$ measurements measured from the stacked spectra in Figure A.3150	
B.4	Average $M_{H\text{I}}/L_r$ measurements measured from the stacked spectra in Figure A.4150	
B.5	Average $M_{H\text{I}}/L_r$ measurements measured from the stacked spectra in Figure A.5150	
B.6	Average $M_{H\text{I}}/L_r$ measurements measured from the stacked spectra in Figure A.6 and Figure A.7	151
B.7	Average $M_{H\text{I}}/L_r$ measurements measured from the stacked spectra in Figure A.10 and Figure A.11	151
B.8	Average $M_{H\text{I}}/L_r$ measurements measured from the stacked spectra in Figure A.12, Figure A.13 and Figure A.14	151



“We’ve done the impossible, and that makes us mighty.”
– **Captain Malcolm Reynolds**
(Firefly episode 1: “Serenity”)

Chapter 1

Introduction

1.1 Galaxies in the Universe

Galaxies, like people, come in all shapes, sizes and colours. Efforts to classify and categorise galaxies date back to before the first classification scheme put forth by Hubble (1926) (e.g. Earl of Rosse, 1850; Herschel, 1786). This scheme was simple, with galaxies separated into three main groups: elliptical, spiral, or irregular (Hubble, 1926, 1936). De Vaucouleurs (1956) expanded the classification scheme, adding more descriptive details to the galaxy types. Spirals were also classified by tightness of the spiral arms and the presence (or lack) of a bar. The classification scheme became known as the Hubble Tuning Fork or Hubble Sequence which is presented in Figure 1.1. In the early years of the Hubble Sequence (circa 1936), it was thought that galaxies evolved from left to right along the sequence which is why elliptical galaxies are referred to as ‘early type’ galaxies, and spirals as ‘late type’ galaxies; this is now known in fact to be the reverse. Identifying galaxies has become an important element of extragalactic astronomy, because knowing what types of galaxies exist, and how they are similar or dissimilar to each other, enables astronomers to study the formation and evolution of galaxies.

The broad morphological types have been shown to correlate with galaxies’ physical properties such as gas content, star formation rate, colour (see Roberts, 1963, for review). While detections have been made of the cold gas, in particular the neutral atomic hydrogen (H I) gas, in galaxies of all morphological classes, the relative amounts of the detected H I vary. The relative fraction of the H I mass to stellar mass in early-type galaxies is low compared to the fraction of H I gas to stellar mass measured in late-type galaxies (e.g. Haynes & Giovanelli, 1984). And even within spiral class of galaxies, the H I gas fraction increases with decreasing tightness of the spiral arms. This is seen in the average trend of H I mass-to-light ratios for late-type galaxies (e.g. Verheijen, 1997). In order to understand the formation and evolution of galaxies, it is important to understand what drives the correlations, but also why some galaxies do not adhere to the expected relations. Almost as long as galaxies have been classified according to morphology, it has been noted that the morphological distribution of galaxies differs across different environments (Hubble & Humason, 1931). Dressler (1980) studied a sample of ~ 6000 galaxies across 55 low-redshift galaxy clusters, finding a radial dependence between galaxy morphology and the local surface density of galaxies. This finding became known as the *morphology-density* relation: early-type galaxies (elliptical and S0 galaxies) are the larger fraction of galaxies in dense cosmic environments such as galaxy clusters, while late-type galaxies (spiral and irregular) dominate in low-density cosmic environments (Dressler, 1980). Why exactly this relation arises is one of the big open questions

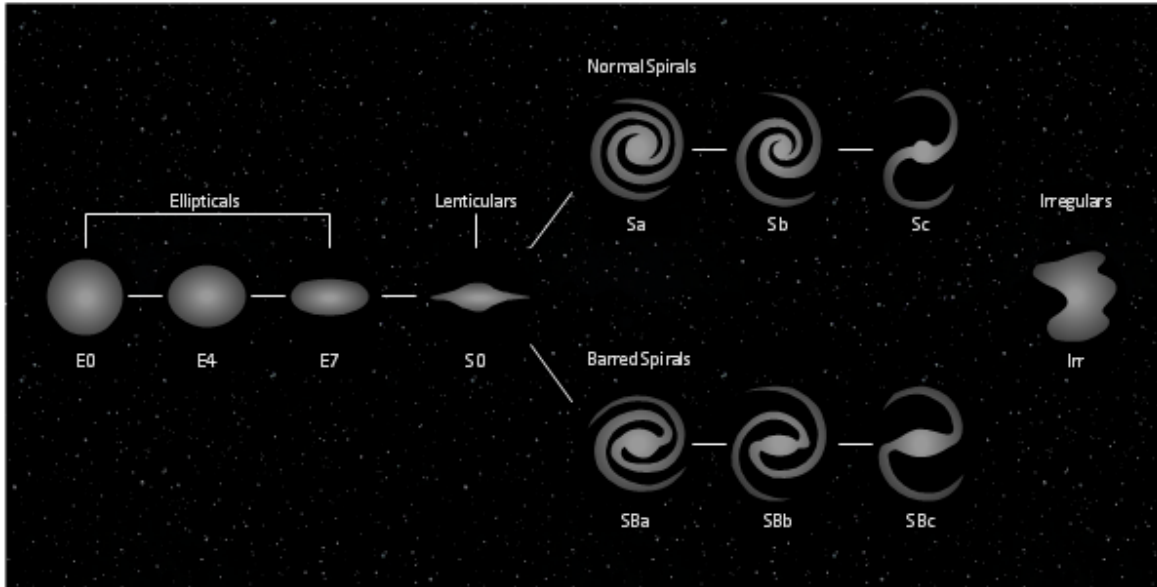


Figure 1.1: The Hubble Tuning Fork showing the characteristic shapes of elliptical, spiral, and irregular galaxies. The galaxies in this diagram also include the more specific classifications added by Gérard de Vaucouleurs. Image credit: <https://conceptdraw.com/a2353c3/preview>

of galaxy evolution studies.

Large optical photometric surveys, such as the Sloan Digital Sky Survey (SDSS, Strauss et al., 2002), have shown the galaxy population to be bimodal in the optical colour distribution (e.g. Strateva et al., 2001; Baldry et al., 2004). The colour bimodality has been explained by the existence of two distinct galaxy populations which are governed by different evolutionary processes (e.g. Baldry et al., 2004; Bell et al., 2004; Taylor et al., 2014). Figure 1.2 shows the colour-magnitude (CM) diagram for a selection of SDSS galaxies. Disk-dominated spiral galaxies tend to be blue in colour while bulge-dominated ellipsoidal galaxies tend to be redder. Colour has thus often been used as a proxy for morphological type (e.g. Strateva et al., 2001). However this is not always a safe assumption. While colour is not the optimal morphological divider, it can be effectively used as a proxy for determining the ages of galaxies (Tinsley, 1968; Tinsley & Larson, 1979), where galaxies with predominantly young stellar populations are blue and galaxies with predominantly older stellar populations are red. The recent large-scale citizen science project: Galaxy Zoo (Lintott et al., 2008, 2011), has provided visually identified morphologies for galaxies observed as part of SDSS. A key result using the Galaxy Zoo data has been the identification of blue early-type galaxies (Schawinski et al., 2009) and red spiral galaxies (Masters et al., 2010).

1.2 Tracing the evolution of galaxies

The star formation history, which is linked to the evolution history, of a galaxy can be traced through changes to the observed star formation rate (SFR) of the the galaxy. It has long been known that star formation depletes the galaxy’s gas reservoir (Schmidt, 1959). The Kennicutt-Schmidt law (Schmidt, 1959; Kennicutt, 1989, 1998) relates the SFR surface density to the gas surface density of galaxies. This has been shown to hold on both global and kilo-parsec scales (Bigiel et al., 2008; Leroy et al., 2012; Bacchini et al., 2019). Thus, in trying to understand what transforms galaxies from gas-rich star-forming spiral galaxies to

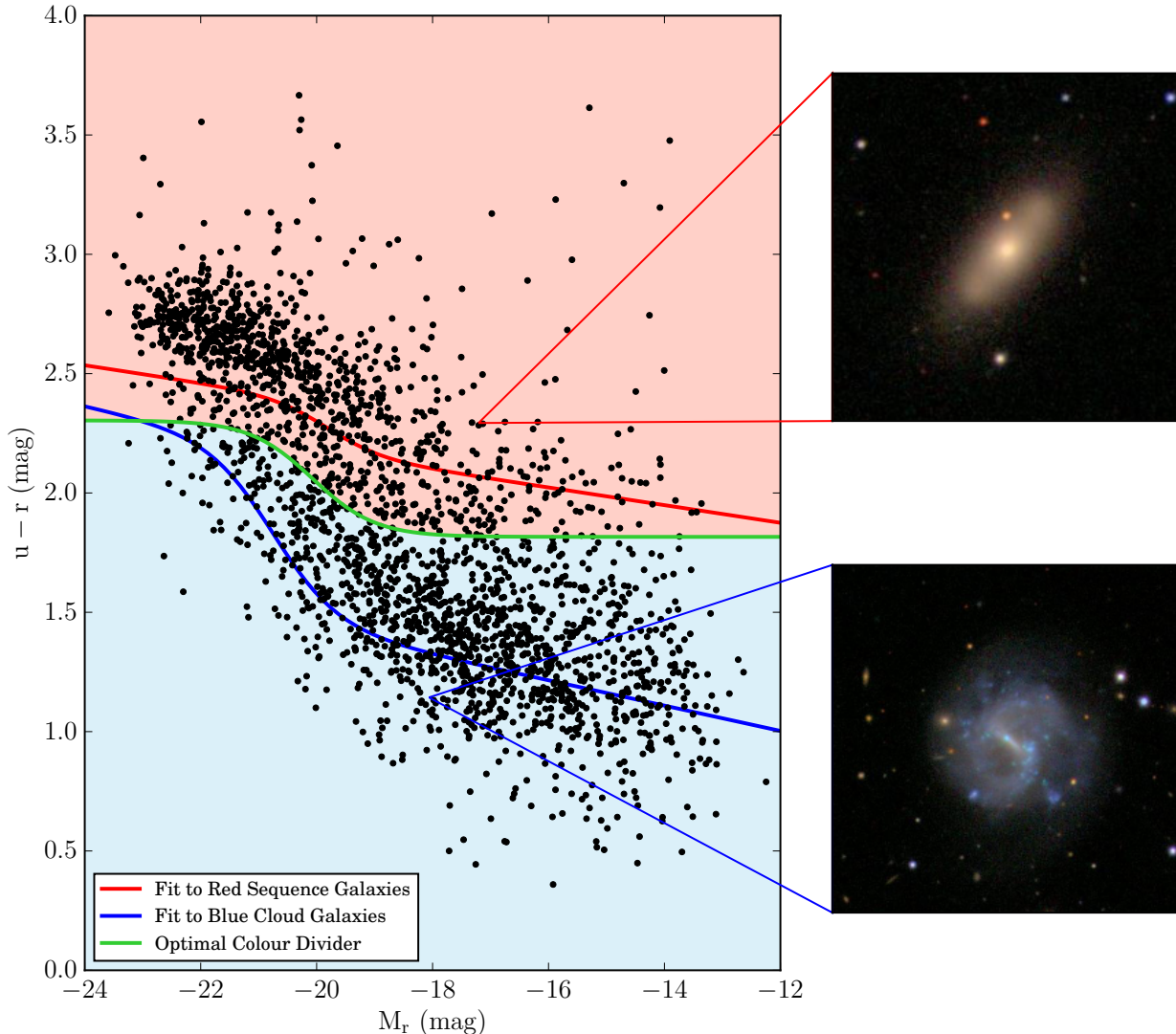


Figure 1.2: Optical Colour-Magnitude Diagram, the data points are taken from a sample of SDSS galaxies and the fitted lines are taken from the work of Baldry et al. (2004). The u - and r -band magnitudes have been corrected for Galactic extinction.

gas-poor quiescent elliptical galaxies, it is important to understand how the different mechanisms affect the gas supply and quench star formation.

For star-forming galaxies, one of the triggers of the next step in the evolutionary path towards quiescence is a change of the SFR, or more specifically, a decrease in the specific star formation rate (sSFR) (e.g. Bell et al., 2004; Salim et al., 2007; Schiminovich et al., 2007; Wyder et al., 2007). The SFR and stellar mass (M_*) of star-forming galaxies form a tight correlation, a relationship that is known as the star formation rate–stellar mass (SFR– M_*) relation (e.g. Brinchmann et al., 2004; Salim et al., 2007; Peng et al., 2010) and which has been shown to hold for local Universe galaxies as well as out to $z \sim 2 - 4$ (e.g. Brinchmann et al., 2004; Popesso et al., 2019). The tight correlation between stellar mass and star formation rate suggests a balance between the inflow and outflow of gas (Bouché et al., 2010; Lilly et al., 2013).

Most star-forming galaxies, regardless of star formation history, are located on the main sequence – galaxy colour only reflects the current status (the last Gyr or so) of star formation.

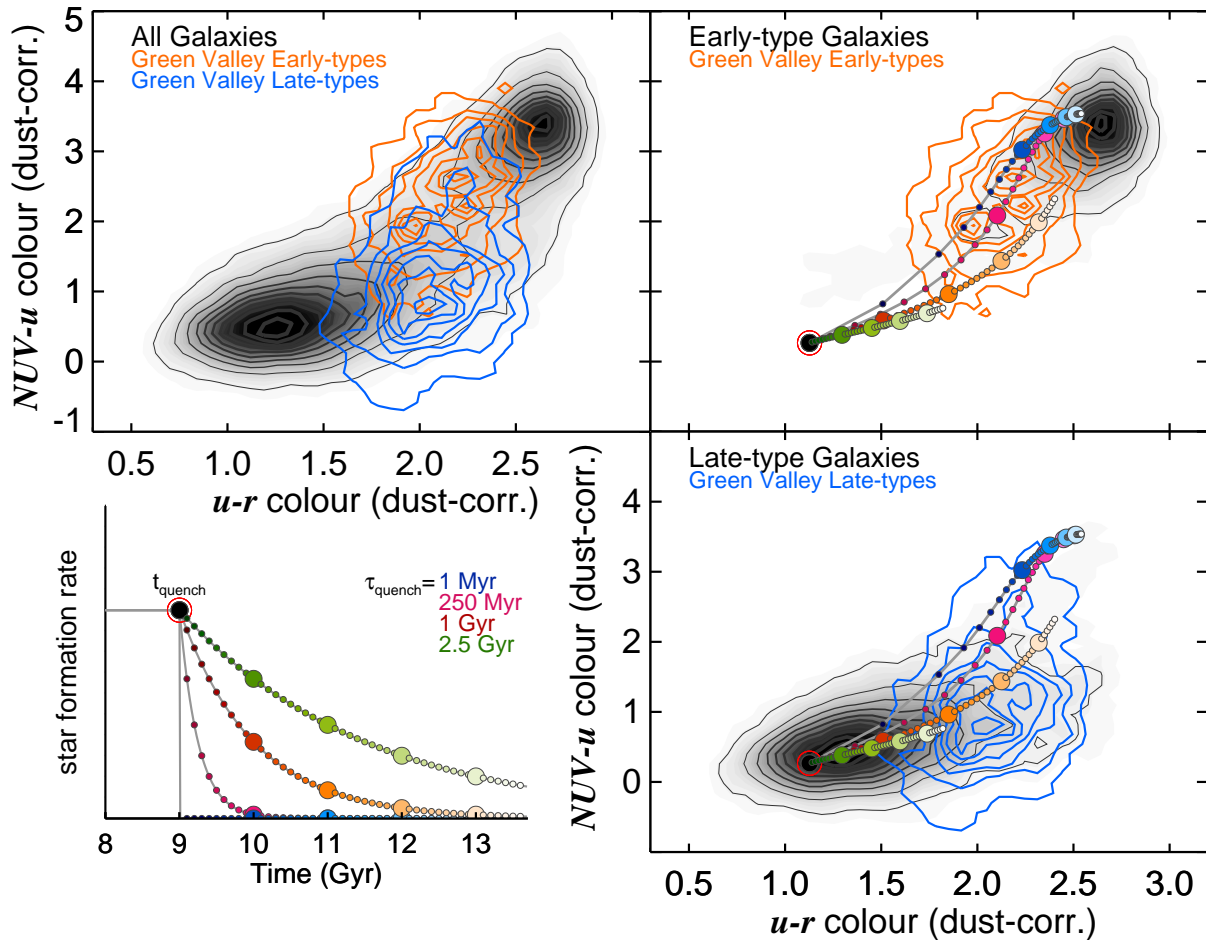


Figure 1.3: UV-optical colour-colour diagrams, corrected for dust extinction, taken from Schawinski et al. (2014, Fig. 7). The colour-colour diagrams constrain the rate at which the sSFR changes, allowing the timescales over which the galaxies are quenched to be determined. The grey contours in the three panels represent the underlying galaxy population of early and late type galaxies. Top left: the green valley early types are presented by the orange contours, and the green valley late types are represented by the blue contours. The right hand panels show only the early types (top) and late types (bottom). A series of evolutionary tracks are also plotted in the right panels, and correspond to the star formation histories shown in the bottom left panel.

When star formation is quenched, the specific star formation rate of the galaxy decreases and it leaves the SFR– M_* relation. The quenching of star formation will also be reflected as a reddening in the galaxy’s colour. Thus in order to study quenching mechanisms, one needs to probe the population of galaxies with specific star formation rates below the SFR– M_* relation. These galaxies tend to have intermediate colours that place them in the valley of the bimodal colour distribution, the so-called “green valley” galaxies (e.g. Brinchmann et al., 2004; Elbaz et al., 2007; Salim et al., 2007; Lee et al., 2012). The relatively small population of green valley galaxies is thought to be a kind of transition population between the so-called blue cloud and red sequence in colour-magnitude diagram. (e.g. Bell et al., 2004; Schiminovich et al., 2007; Wyder et al., 2007). These galaxies would have optical colours that place them around the green line shown in the colour-magnitude diagram in Figure 1.2. Given the connection between the galaxy colour and the ages of the stellar population, the colours of these galaxies have been interpreted as having been recently quenched (Salim et al., 2007).

Peng et al. (2010) showed that there were at least two quenching mechanisms, “mass

quenching” and “environmental quenching”, that occur over different timescales. Peng et al. (2010) describe “mass quenching” to be a continuous process, with “environmental quenching” only occurring when the environment around the galaxy changed. Using a sample of morphologically identified early-type and late-type green valley galaxies, Schawinski et al. (2014) showed that the two galaxy populations are quenched over very different timescales which is indicative of different quenching mechanisms. Figure 1.3 shows the dust-corrected ultraviolet- (UV) optical colour-colour diagram which they use to identify the star formation histories of the galaxies in their sample and constrain the rate of change of sSFR. From their analysis, Schawinski et al. (2014) determined that early-type galaxies (represented by the orange contours) which appear redder due to the older stellar populations, are quenched much more rapidly than late-type galaxies on timescales of $\tau_q < 250$ Myr. While for late-type galaxies (represented by the blue contours), which contain more younger stars thus making the galaxies bluer, $\tau_q > 1$ Gyr.

The difference in quenching timescales for the two galaxy populations is suggestive of two very different mechanisms. For the early-type galaxies, Schawinski et al. (2014) conclude that the quenching of star formation is triggered by a rapid destruction of the galaxy gas reservoir. This results in a rapid drop in the SFR, causing the galaxies to move off the SFR– M_\star relation. With almost no ongoing star formation, the galaxies do not increase in mass. Schawinski et al. (2014) suggest that the quenching event must be simultaneous with a morphological transformation as there are very few blue early-type galaxies observed, but the colour transformation occurs on longer timescales – dictated by stellar evolution. They also suggest the quenching event is likely to be major mergers. The quenching of late-types occurs more slowly. The galaxies are cut off from the cosmic web refuelling the galaxy gas reservoir (e.g. Kereš et al., 2005; Sancisi et al., 2008; de Blok et al., 2015). The balance between the inflow and outflow of gas that underpins the SFR– M_\star relation, is disrupted. The late-types continue to form stars at a declining rate, increasing in stellar mass until the gas reservoir is depleted; during this period, the galaxy colour changes as the SFR decreases. The rate at which the galaxy gas reservoir is depleted can be increased by environmental processes. The morphological transformation occurs on much longer timescales which is why red spiral galaxies are observed.

The fate of the gas reservoir of a galaxy clearly plays an important role in the transformation of the galaxy. This reservoir, or interstellar medium (ISM) is composed primarily of neutral atomic (H I), molecular (H_2), and ionised (H II) hydrogen gas. H II primarily traces the gaseous regions around hot stars such as those that have recently been formed. However, studies have shown that star formation correlates most strongly with the cold gas, in particular, the H_2 (Bigiel et al., 2008; Leroy et al., 2008, 2013). In a sample of spiral galaxies, Bigiel et al. (2008) found that the H I saturates at a surface density of $\Sigma = 9 M_\odot \text{pc}^{-2}$. Only H_2 was detected at higher surface densities, suggesting a phase transition from H I into H_2 . This highlights the importance of H I in the star formation process as it is the raw fuel from which the H_2 gas clouds that later give rise to new stars.

H I is not only important for ongoing star formation, but can also be an important tracer of how the gas supply to a galaxy is shutoff, thus quenching star formation. The H I galaxy disk is known to extend beyond the stellar disk, sometimes as much as twice the stellar disk radius (e.g. Broeils & Rhee, 1997). The H I disk, particularly the outer disk, is sensitive to interactions with intra-cluster medium (ICM) in galaxy clusters or intra-group medium (IGM) in galaxy groups, as well as gravitational interactions. This makes H I a very good

tracer of the physical processes prevalent in different cosmological environments.

1.3 Galaxy clusters

Galaxy clusters are some of the largest structures in the Universe. These large complexes are located at nodes in the filaments of the cosmic web. Due to the dense nature of the environment, galaxy clusters play an important role in enabling the study of environment-driven galaxy evolution. The identification and study of galaxy clusters date back to the 1950s when, using photographic plates, Abell (1958) created what has become one of the main cluster catalogues for the local Universe. The early catalogues (Abell, 1958; Zwicky et al., 1961; Abell et al., 1989) have been updated and memberships revised as large (and small, centred only on the cluster of interest) spectroscopic surveys (e.g. Colless et al., 2001; Strauss et al., 2002; Smee et al., 2012) provide accurate redshift distances to the galaxies.

Clusters are dynamic environments as they continue to grow through the accretion of individual galaxies and galaxy groups along filaments and from the field (e.g. Bravo-Alfaro et al., 2000). Observations show that a significant fraction of galaxy clusters (roughly 30 per cent) contain substructure, and it is suggested that substructure is an imprint of the accreted groups (Dressler & Shectman, 1988; Bird, 1994; Hou et al., 2012). While substructures are important to understand the formation history of clusters, they are also important identifiers of the local environment around a cluster galaxy.

While clusters have been shown to be very effective at quenching star formation and transforming galaxies from star-forming and gas-rich to quiescent and gas-poor (e.g. Giovanelli et al., 1981, 1982; Balogh et al., 1997; Oman et al., 2021), evidence is mounting that galaxies are “pre-processed” by the local group environment prior to cluster infall (e.g. Fujita, 2004; Hess et al., 2015; Kleiner et al., 2021). Many of the processes responsible for removing the gas disk from galaxies, and thus quenching star formation have also been observed in group environments (e.g. Vulcani et al., 2018; Džudžar et al., 2019). In order to fully understand what drives the observed morphology-density relation, it is important to identify in which environment, the global cluster environment or the local group/substructure environment, begins the process of transforming galaxies. This will contain important information on mechanisms and timescales of galaxy evolution. Examples of environmental processes include starvation (Larson et al., 1980), galaxy harassment (Moore et al., 1996), mergers, and ram-pressure stripping (Gunn & Gott, 1972).

Starvation: This process was proposed by Larson et al. (1980) as an explanation for the formation of S0 galaxies from spiral galaxies. The warm outlying gas halo is removed from the galaxy either through ram-pressure stripping or thermal evaporation which halts the supply of cold gas (e.g. Balogh et al., 2000; Kawata & Rauch, 2007; Peng et al., 2015; Bekki et al., 2002), star formation starts to decrease as the HI is used up. The process is sometimes referred to as “strangulation”.

Galaxy harassment: Galaxies in dense environments can experience fast encounters with other galaxies. During the encounter, the galaxies interact gravitationally which can affect their stellar and gas disks. When a galaxy experiences multiple encounters, this is called harassment (Moore et al., 1996). In cases where the harassment is strong enough, it can trigger a burst in star formation during which the galaxy uses up the remaining fuel (e.g. Moore et al., 1996). In cases where the interactions are not as strong, the gas disk can

be destabilised which facilitates the stripping of H I from the galaxy (e.g. Duc & Bournaud, 2008; Jaffé et al., 2016).

Mergers: Merger events occur when two (or more) galaxies collide with each other. This is particularly common in low-speed encounters between galaxies (e.g. Toomre & Toomre, 1972). Mergers can result in a rapid removal of the gas causing a rapid morphological transformation (e.g. Schawinski et al., 2014).

Ram-pressure stripping: First predicted by Gunn & Gott (1972), ram-pressure stripping occurs due to the interaction between the ICM, comprised of hot X-ray emitting gas, and the galaxy ISM. As the galaxy falls into the cluster, the ICM exerts a hydro-dynamical pressure on the galaxy. If the pressure is higher than the gravitational force the galaxy is exerting on the gas disk, then the gas is stripped which removes the raw fuel for star formation (e.g. Jaffé et al., 2015; Poggianti et al., 2016, 2019).

Ram-pressure stripping has been shown to be very effective at removing the gas from galaxies in clusters. Some models have predicted that the H I can be fully depleted by pericentric passage (e.g. Roediger & Brüggen, 2007; Oman & Hudson, 2016). It has also been shown to occur in less dense group environments (Vulcani et al., 2018). In all cases the galaxy undergoes a colour transformation becoming redder as the stellar population ages, this occurs roughly a Gyr after the sSFR decreases (e.g. Oman et al., 2021).

It is still unclear when the morphological change occurs (see Peterken et al., 2020, and references therein); this may depend largely on what triggered the quenching of star formation – mergers can result in rapid morphological changes (Schawinski et al., 2014), whereas starvation may result in much longer timescales over which the morphology is changed (e.g. Larson et al., 1980; Balogh et al., 2000; Peng et al., 2015).

1.3.1 H I in clusters

Galaxies located in galaxy clusters have long known to be H I deficient (Haynes et al., 1984; Solanes et al., 2001), this is usually attributed to ram-pressure stripping (Gunn & Gott, 1972) which is highly effective at removing the H I gas from disks of galaxies falling into clusters (e.g. Jaffé et al., 2016; Oman & Hudson, 2016). H I deficiency is defined as the difference between the logarithm of the expected H I mass, calculated from a scaling relation calibrated on field galaxies, and the logarithm of the measured H I mass (Haynes et al., 1984). Using a sample of ~ 1900 spiral galaxies in 18 clusters, Solanes et al. (2001) showed that the fraction of H I deficient spiral galaxies (H I deficient galaxies have less than half the expected mass based on their optical morphology and diameter) increases with decreasing radius to the cluster centre. The top panel of Figure 1.4, taken from Solanes et al. (2001), shows that the fraction of H I deficient spirals starts increasing inwards from 2 Abell radii (R_A) from a cluster. The Abell radius is defined as $R_A = 1.5 h^{-1}$ Mpc, which for a Coma-sized galaxy cluster is $\sim 2.2 R_{200}$ and for a Virgo-sized galaxy cluster is $\sim 3.8 R_{200}$. The R_{200} is the radius at which the average contained density is 200 times the critical density, this is assumed to contain the bulk of the virialised mass of the cluster. Assuming that the dominant mechanisms depleting the H I disks are related to the cluster environment, this means that the gas removal process begins while the galaxy is still in the outskirts of the clusters (Zinger et al., 2018). The lower panel of Figure 1.4 shows the measured H I deficiencies as a function of cluster-centric radius for all the galaxies in the sample. While the top panel shows a clear

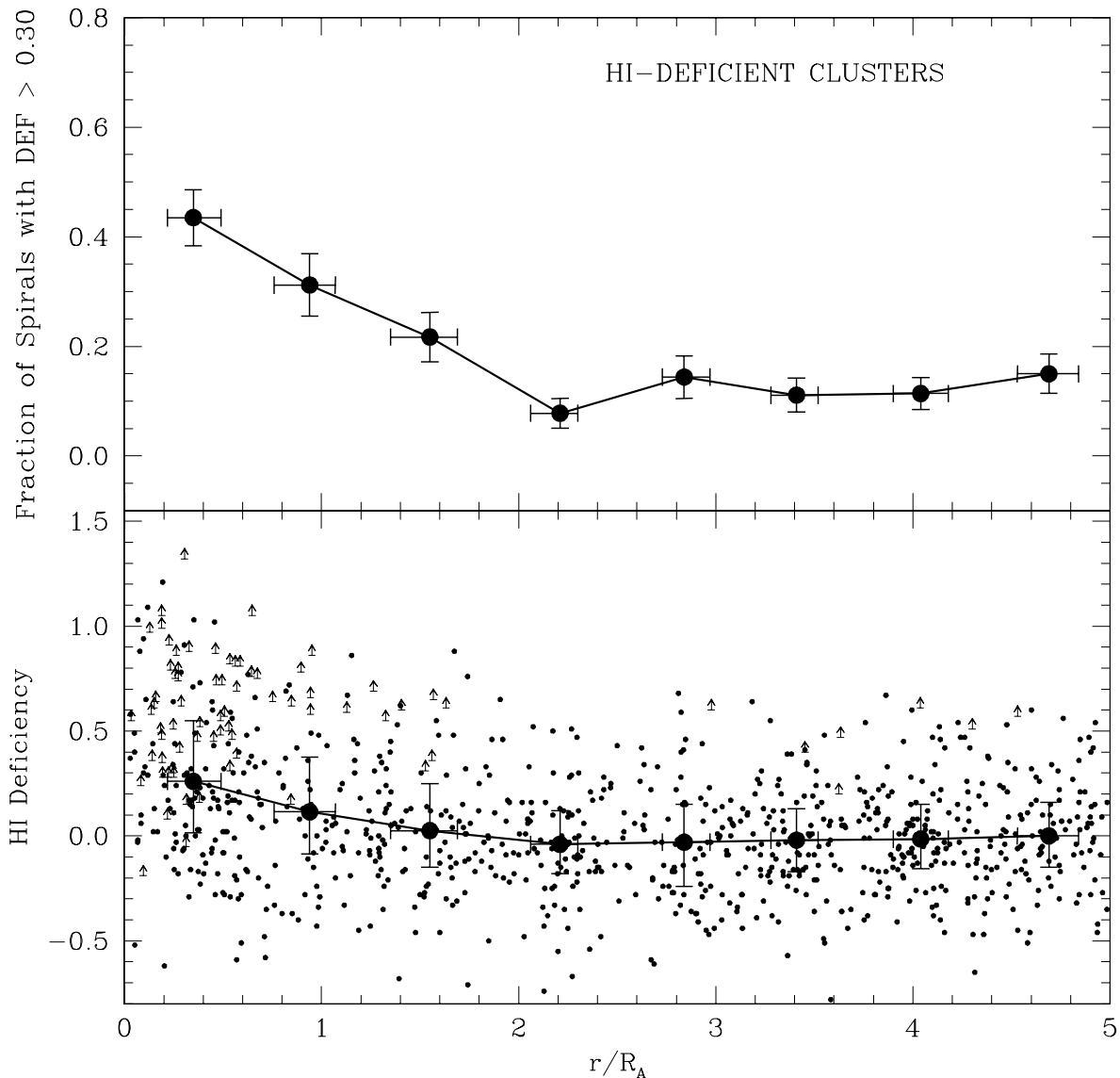


Figure 1.4: Taken from Solanes et al. (2001, ; Fig. 4), this figure shows the fraction of H I deficient spirals in H I deficient clusters (top panel) and in the bottom panel, the same set of galaxies as the top panel, but showing the individual H I deficiency measurements. The vertical error bars show the 1σ Poisson intervals, while the horizontal error bars and the large solid black circle indicate the quartile values and median of each radial bin. The small black dots indicated H I deficiency measurements of detected galaxies, while the arrows indicate the lower limits for the H I non-detected galaxies. R_A is the Abell radius, defined as $R_A = 1.5 h^{-1} \text{ Mpc}$.

trend towards more H I deficient galaxies in the cluster centre, a trend also present in the lower panel, the lower panel also indicates the wide spread in H I deficiencies. Some of the scatter may be due to projection effects in the radius, while the rest of the scatter is likely due to inherent differences in how individual galaxies are affected by the host cluster. It is also worth noting that the Abell radius does not scale with cluster size, which means that for different clusters $1R_A$ may be within the virial radius (R_{200}) or outside of it.

Observing H I can be time consuming, especially over large areas of the sky where galaxies are known to be H I deficient. As a result, up until recently many H I surveys of cluster galaxies have been targeted, undertaken using the optical properties of the galaxies to identify candidates (e.g. Haynes & Giovanelli, 1986; Gavazzi et al., 2006; Chung et al., 2009).

High resolution targeted H I surveys of spiral galaxies in clusters, such as the VLA¹ Imaging of Virgo spirals in Atomic gas (VIVA; Chung et al., 2009) showed that Virgo spirals at intermediate distances from the cluster core showed signs of H I deficiency with stripped tails pointing away from the cluster core. Other galaxies in the cluster outskirts also showed signs of H I deficiency. Some of these galaxies were already known to be H I deficient (Sanichis et al., 2002) and did not show indications of recent stripping which led to the theory that they may have already passed through the cluster core. While the VIVA survey has provided textbook examples of the effects environmental processes have on the H I disks of galaxies with a range in star formation properties, it is only a select view of galaxies that were expected to contain H I. Thus in order to fully understand the extent to which the H I in galaxies is processed by the cluster environment and how that affects the evolution of the galaxies, blind H I surveys are needed.

Deep blind H I surveys of higher redshift ($z > 0.1$) galaxies have shown that beyond the local Universe clusters show the same pattern of H I deficiency in their cores as seen in clusters in the nearby universe (e.g. Lah et al., 2009; Jaffé et al., 2016). At higher redshift, the area on the sky subtended by a cluster is much smaller than for similar sized clusters at low redshift. This makes it possible to observe the core and outskirts of higher redshift clusters in fewer pointings (depending on the telescope field of view). However, the observing time required to detect H I beyond $z > 0.1$ is high. The Blind Ultra Deep H I Environmental Survey (BUDHIES; Verheijen et al., 2007; Gogate et al., 2020) of Abell 963 (A963) and Abell 2192 (A2192) using the Westerbork Synthesis Radio Telescope (WSRT) consists of two deep pointings, 117×12 hours on clusters Abell 963, and 72×12 hours on Abell 2192 which resulted in 166 galaxies detected in H I over the redshift range $0.164 < z < 0.224$. Targeting a higher redshift cluster, Abell 370 (A370) at $z = 0.37$, Lah et al. (2009) used 63 hours of telescope time with the Giant Metrewave Radio Telescope (GMRT) but did not detect any galaxies in H I. Both studies found similar patterns of H I deficiency in the the cluster cores as what is seen in clusters at low redshift.

For all three clusters, there was complementary optical spectroscopy which provided redshifts and star formation rate indicators for the cluster galaxies. This enabled the use of the statistical technique, H I stacking (e.g. Chengalur et al., 2001; Zwaan et al., 2001; Fabbello et al., 2011, 2012; Brown et al., 2015; Healy et al., 2019). Using the optical redshifts to identify where in the H I spectrum the galaxy emission is expected, the H I spectra of galaxy samples are aligned and co-added to create an average H I spectrum that has an rms \sqrt{N} lower than the input spectra, where N is the number of input galaxies. Lah et al. (2009) separated the A370 galaxies based on optical colour (blue and red), and detectable O II emission as a star formation indicator. They found a result that would not have been possible without the unbiased H I coverage provided by the blind survey: red galaxies contain detectable amounts of H I that appeared to be contained within the central regions of the galaxies, and blue galaxies with no detectable O II emission contained detectable amounts of H I gas. However, it should be noted that the significance of the red detection is 1.8σ . Lah et al. (2009) conclude by saying that these results merit further investigation with more sensitive observations as many of the detections in the stacked spectra have a low statistical significance. In contrast, H I stacking analyses of the galaxies in A963 showed that only blue galaxies contained detectable H I emission (Jaffé et al., 2016).

In Jaffé et al. (2013), the authors showed that both A2192 and A963 showed the presence

¹Very Large Array

of substructure, however in the case of A963, it was marginal. Using a larger spectroscopic catalogue for A963, Jaffé et al. (2016) identified seven substructures associated with the cluster. The identified groups showed an increasing fraction of passive galaxies with group mass. Separating the groups into low, intermediate, and high mass samples, they showed that only passive galaxies in the lowest mass groups contained any H I. While blue galaxies in all groups contained H I, the average H I content decreased with increasing group mass (Jaffé et al., 2016). Jaffé et al. (2016) suggest “pre-processing” by the group environment as a possible quenching mechanism of galaxies prior to infall into the cluster.

In the local Universe, many clusters have had substructure identified (e.g. Adami et al., 2006; Ramella et al., 2007; Hess et al., 2015); however very few have accompanying H I surveys (e.g. Hess et al., 2015). Clusters within the Arecibo Legacy Fast ALFA² survey (ALFALFA; Haynes et al., 2011, 2018) footprint benefit from the survey’s H I coverage, but the large full width half maximum of the Arecibo beam ($\sim 3'$) means that only the largest galaxies are likely to be resolved, and confusion becomes an issue in the denser environments where galaxies are closer together. This is especially an issue for H I stacking analyses (e.g. Elson et al., 2016; Jones et al., 2016) which are crucial to be able to measure H I in the cluster galaxies which are not individually detected.

1.4 H I Stacking

The technique used in this thesis to study the H I content of the galaxies in clusters is known as H I stacking. H I stacking uses the redshifts of the galaxies in a sample to align the H I spectra in the rest-frame of each input galaxy; the spectra are then co-added to create a higher signal-to-noise (S/N) that is representative of the average of the sample. From this average spectrum, the average H I mass can be measured. Given how challenging it can be to directly detect the H I content of distant galaxies, or nearby H I deficient galaxies, stacking has become a popular technique to extract the average information of a sample of galaxy spectra that would otherwise not have been useful. Stacking is not only used for measuring the average H I content of samples where there are no direct H I detections, but it is also useful for determining population averages where there is a mix of direct and H I non-detections. Fabello et al. (2011) showed by stacking a mix of direct and non-detections compared to just stacking the non-detections that the addition of the direct detections does not necessarily dominate the stacked detection. In studies where the average H I of a population is the quantity of interest, it is important to stack both detections and non-detections.

In this thesis, I make use of a publicly accessible Python-based H I stacking software package called HISS³ (Healy et al., 2019). HISS takes as input, a catalogue of optical redshifts and the H I spectra, and outputs the stacked spectrum along with a number of diagnostic plots. One of the most important diagnostic tools for stacking is a plot of the noise in the stacked spectrum, and how that changes with the number of input spectra. If the noise in the input spectra are Gaussian, then the noise in the stacked spectrum should decrease by a factor of \sqrt{N} , where N is the number of input spectra.

HISS offers the users a certain amount of flexibility in terms of what type of weighting to use for the spectra, and in which units to stack the spectra. However, all spectra are stacked

²Arecibo L-band Feed Array

³<https://github.com/healytwin1/HISS>

regardless of the weighting and unit choices according to,

$$S_{\text{stack}} = \sum_{i=1}^N \frac{w_i S_i}{\sum_{i=1}^N w_i}, \quad (1.1)$$

where i is the number of the spectrum to be included in the stack, w_i is the weighting factor (this is usually 1 or $1/\sigma^2$, where σ is the rms noise of the spectrum in Jy), and S_i is the spectrum in the units chosen by the user (e.g. M_{HI} , M_{HI}/M_{\star} , $M_{\text{HI}}/M_{\text{exp}}$).

Optical redshifts play a crucial role in the success of HI stacking experiments, they are used to align the input spectra in the rest-frame before the spectra are co-added. However, depending on how the redshift of a galaxy is measured, there could be an offset between the optical redshift and the spectral location of the HI emission. There are a number of factors that could cause an offset: measuring the optical redshift in the outskirts of the galaxy rather than the galaxy centre; redshift measurements based on absorption rather than emission lines; the HI is in the process of being stripped, so may be lagging behind the galaxy; accuracy of the redshift. In most cases, the effect of this misalignment only results in a broader stacked profile (Maddox et al., 2013), which, if the only goal is to measure the average emission, the broader profile may not be an issue. However, it is worth noting that a stacked profile that has been broadened due to a misalignment between the HI emission and the optical redshift, may have a lower S/N ratio than the same sample with accurate redshifts. Maddox et al. (2013) also noted in their study on the quality of optical redshifts for HI stacking that redshifts measured using multiple emission line features had less of an offset relative to the HI redshift than redshifts measured using a single emission line or absorption lines.

The different features in the galaxy optical spectra used to determine the redshifts are also indicative of the morphology of the galaxy. In spiral and irregular galaxies, the redshift is typically measured using emission lines which arise due to the interstellar gas being heated by ionising radiation which is common around regions of star formation and OB type stars, or active galactic nuclei. Common emission lines include single and doubly ionised Oxygen, [O II] (3727.092, 3729.875 Å) and [O III] (4932.603, 4960.295, 5008.240 Å), and the Hydrogen Balmer lines: H α (6564.61 Å), H β (4862.68 Å), H δ (4102.89 Å), H γ (4341.68 Å). Absorption lines are the common method used to determine the redshifts of elliptical galaxies. The absorption lines arise due to absorption by atoms and molecules in older stellar atmospheres and by cold interstellar gas and dust. The most commonly used absorption lines include the Calcium H (3969.588 Å) and K (3934.777 Å) lines, G-band (4305.61 Å), and the Magnesium (5176.7 Å) and Sodium (5895.6 Å) lines.

Since the sensitivity of the stacked spectrum is dependent on the number of input spectra, the sensitivity limit is guided by the number of available redshifts. With blind HI surveys, such as the two presented in this work, one ideally needs as many redshifts as there are galaxies covered by the HI data. The largest single redshift database used in this thesis is the Sloan Digital Sky Survey (SDSS, Stoughton et al., 2002; Smee et al., 2012; Aguado et al., 2019), however this is known to be incomplete in regions where the targets are clustered in a compact region of the sky, such as galaxy clusters. Large spectroscopic surveys are only economical with telescopes that are host to multi-object spectrographs with wide-field cameras, such as Hydra on the 3.5m WIYN Telescope, or Hectospec on the 6m MMT Telescope. Even with these instruments, the time required to observe the emission or absorption features needed to measure redshifts is high. As a result, many of the existing redshift catalogues

contain only the targets of interest to the catalogue authors. This means that collating all the available redshifts on a particular region on the sky comes with a plethora of different selection biases and spectroscopic completeness limits. In cases where homogenising the selection effects and completeness limits is not possible, one should at least be aware of them when interpreting the results measured from the stacked profiles.

1.5 This thesis

In this thesis, I investigate how the H I content of galaxies in clusters relates to the optically observed morphology-density relation. This work is focused on the galaxy populations in two galaxy clusters: the Coma cluster (Chapter 2) and Abell 2626 (A2626, Chapters 3, 4, & 5). The Coma cluster is located at a distance of 100 Mpc making it the most nearby massive cluster. Coma has been well studied across the electromagnetic spectrum (see Biviano et al., 1996, for a historical review), and despite often being referred to as the prototypical virialised cluster, is known to have significant substructure (e.g. Colless & Dunn, 1996; Adami et al., 2005). On the other hand, A2626 is less well known and is twice as distant as Coma, at a distance of 250 Mpc. Although not as well studied, A2626 is known to contain galaxies exhibiting extreme signs of environmentally driven evolution (e.g. Moretti et al., 2019; Poggianti et al., 2019).

Galaxy clusters, as discussed in the earlier sections, are known to deplete the H I reservoirs of cluster galaxies very efficiently. By peri-centric passage all galaxies are expected to be quenched (Oman & Hudson, 2016). As the H I reservoir is depleted, the star formation is quenched which triggers a colour transformation as the stellar population ages. The timescales for morphological transformations vary depending on the process triggering the transformation. Tidal interactions and merger events may induce a morphological transformation more quickly than processes quenching star formation through gas depletion. The effectiveness of the processes known to remove the H I gas, and quench star formation (e.g. ram-pressure stripping, starvation, galaxy harassment), vary across different local density environments within clusters. Thus identifying substructure within the clusters, and comparing the H I content of the galaxies within substructure to cluster galaxies at similar locations as the substructure can shed light on which environment has a stronger influence on removing the H I from the galaxies (Chapter 2 and Chapter 5). Comparisons between the H I content of cluster galaxies and galaxies in substructure, particularly in the outskirts of the cluster may shed light on how much or if galaxies are processed in group environments prior to cluster infall.

This thesis is laid out as follows: in Chapter 2, I present the identification and confirmation of new and previously identified substructures in the Coma cluster using a large collation of literature redshifts supplemented by new redshift measurements obtained using Hydra on the WIYN Telescope. This redshift catalogue, in combination with multi-wavelength data providing measurements on the physical properties of the galaxies such as stellar mass, colour and visual morphology enable me to quantify the H I environment of the cluster, and probe the relationship between H I in substructure galaxies in different regions of the cluster.

The next three chapters are dedicated to A2626. In Chapter 3, I present newly obtained MeerKAT observations of A2626. I discuss the calibration of the raw data, and the imaging of the H I data cube. I also present the results of the H I source finding which shows the observed volume to be rich with H I detections. Chapter 4 focuses on the large scale environment in

which A2626 is embedded. I present new redshift measurements extending out to $z \sim 0.46$ for the area covered by the MeerKAT pointing, which were obtained using Hectospec on MMT. The MMT observing campaign more than doubled the known redshifts in the surveyed region, and enabled the identification of substructure within A2626, as well as the nearby A2637 which is also in the survey volume. We also spectroscopically confirmed a number of more distant clusters. Chapter 5 presents a detailed analysis of the H I content of galaxies in the different substructures identified in A2626. I use the H I stacking technique to probe the average H I content of the A2626 galaxies below the H I detection threshold. Unlike Coma, A2626 is able to provide more than just limits on the H I content of the galaxies in different regions of the cluster, enabling a richer analysis of the group vs cluster environment. Using visually classified morphologies for the galaxies, I investigate late-type galaxies in substructures inside the cluster and how the average H I content of this population changes with distance to the cluster centre compared to the late-type cluster galaxies not in substructure.

References

- Abell G. O., 1958, *The Astrophysical Journal Supplement Series*, 3, 211
- Abell G. O., Corwin Harold G. J., Olowin R. P., 1989, *The Astrophysical Journal Supplement Series*, 70, 1
- Adami C., Biviano A., Durret F., Mazure A., 2005, *Astronomy and Astrophysics*, 443, 17
- Adami C., et al., 2006, *Astronomy and Astrophysics*, 451, 1159
- Aguado D. S., et al., 2019, *The Astrophysical Journal Supplement Series*, 240, 23
- Bacchini C., Fraternali F., Iorio G., Pezzulli G., 2019, *Astronomy and Astrophysics*, 622
- Baldry I. K., Glazebrook K., Brinkmann J., Ivezić Z., Lupton R. H., Nichol R. C., Szalay A. S., 2004, *The Astrophysical Journal*, 600, 681
- Balogh M. L., Morris S. L., Yee H. K. C., Carlberg R. G., Ellingson E., 1997, *The Astrophysical Journal*, 488, L75
- Balogh M. L., Navarro J. F., Morris S. L., 2000, *The Astrophysical Journal*, 540, 113
- Bekki K., Couch W. J., Shioya Y., 2002, *The Astrophysical Journal*, 577, 651
- Bell E. F., et al., 2004, *Astrophysical Journal*, 608, 752
- Bigiel F., Leroy A., Walter F., Brinks E., de Blok W. J. G., Madore B., Thornley M. D., 2008, *The Astronomical Journal*, 136, 2846
- Bird C. M., 1994, *The Astronomical Journal*, 107, 1637
- Biviano A., Durret F., Gerbal D., Le Fèvre O., Lobo C., Mazure A., Slezak E., 1996, *Astronomy and Astrophysics*, 311, 95
- Bouché N., et al., 2010, *Astrophysical Journal*, 718, 1001
- Bravo-Alfaro H., Cayatte V., van Gorkom J. H., Balkowski C., 2000, *The Astronomical Journal*, 119, 580

- Brinchmann J., Charlot S., Heckman T. M., Kauffmann G., Tremonti C., White S. D. M., 2004, ArXiv eprints, astro-ph/0
- Broeils A. H., Rhee M. H., 1997, *Astronomy and Astrophysics*, 324, 877
- Brown T., Catinella B., Cortese L., Kilborn V., Haynes M. P., Giovanelli R., 2015, *Monthly Notices of the Royal Astronomical Society*, 452, 2479
- Chengalur J. N., Braun R., Wieringa M., 2001, *Astronomy and Astrophysics*, 372, 768
- Chung A., van Gorkom J. H., Kenney J. D. P., Crowl H., Vollmer B., 2009, *The Astronomical Journal*, 138, 1741
- Colless M., Dunn A. M., 1996, *The Astrophysical Journal*, 458, 435
- Colless M., et al., 2001, *Monthly Notices of the Royal Astronomical Society*, 328, 1039
- Dressler A., 1980, *The Astrophysical Journal*, 236, 351
- Dressler A., Shectman S. A., 1988, *The Astronomical Journal*, 95, 985
- Duc P.-A., Bournaud F., 2008, *The Astrophysical Journal*, 673, 787
- Džudžar R., et al., 2019, *Monthly Notices of the Royal Astronomical Society*, 483, 5409
- Earl of Rosse 1850, *Philosophical Transactions of the Royal Society of London*, 140, 499
- Elbaz D., et al., 2007, *Astronomy and Astrophysics*, 468, 33
- Elson E. C., Blyth S. L., Baker A. J., 2016, *Monthly Notices of the Royal Astronomical Society*, 460, 4366
- Fabello S., Catinella B., Giovanelli R., Kauffmann G., Haynes M. P., Heckman T. M., Schiminovich D., 2011, *Monthly Notices of the Royal Astronomical Society*, 411, 993
- Fabello S., Kauffmann G., Catinella B., Li C., Giovanelli R., Haynes M. P., 2012, *Monthly Notices of the Royal Astronomical Society*, 427, 2841
- Fujita Y., 2004, *Publications of the Astronomical Society of Japan*, 56, 29
- Gavazzi G., O’Neil K., Boselli A., van Driel W., 2006, *Astronomy and Astrophysics*, 449, 929
- Giovanelli R., Haynes M. P., Chincarini G. L., 1981, *The Astrophysical Journal*, 247, 383
- Giovanelli R., Haynes M. P., Chincarini G. L., 1982, *The Astrophysical Journal*, 262, 442
- Gogate A. R., Verheijen M. A. W., Deshev B. Z., van Gorkom J. H., Montero-Castaño M., Hulst J. M. v. d., Jaffé Y. L., Poggianti B. M., 2020, *Monthly Notices of the Royal Astronomical Society*, 496, 3531
- Gunn J. E., Gott J. Richard I., 1972, *The Astrophysical Journal*, 176, 1
- Haynes M. P., Giovanelli R., 1984, *The Astronomical Journal*, 89, 758
- Haynes M. P., Giovanelli R., 1986, *The Astrophysical Journal*, 306, 466

- Haynes M. P., Giovanelli R., Chincarini G. L., 1984, *Annual Review of Astronomy and Astrophysics*, 22, 445
- Haynes M. P., et al., 2011, *The Astronomical Journal*, 142, 170
- Haynes M. P., et al., 2018, *The Astrophysical Journal*, 861, 49
- Healy J., Blyth S.-L., Elson E., van Driel W., Butcher Z., Schneider S., Lehnert M. D., Minchin R., 2019, *Monthly Notices of the Royal Astronomical Society*, 487, 4901
- Herschel W., 1786, *Philosophical Transactions of the Royal Society of London*, 76, 457
- Hess K. M., Jarrett T. H., Carignan C., Passmoor S. S., Goedhart S., 2015, *Monthly Notices of the Royal Astronomical Society*, 452, 1617
- Hou A., et al., 2012, *Monthly Notices of the Royal Astronomical Society*, 421, 3594
- Hubble E. P., 1926, *The Astrophysical Journal*, 64, 321
- Hubble E., 1936, *Realm of the Nebulae*. Yale University Press, New Haven, <https://ui.adsabs.harvard.edu/abs/1936rene.book.....H/abstract>
- Hubble E., Humason M. L., 1931, *The Astrophysical Journal*, 74, 43
- Jaffé Y. L., Poggianti B. M., Verheijen M. A. W., Deshev B. Z., van Gorkom J. H., 2013, *Monthly Notices of the Royal Astronomical Society*, 431, 2111
- Jaffé Y. L., Smith R., Candlish G. N., Poggianti B. M., Sheen Y.-K., Verheijen M. A. W., 2015, *Monthly Notices of the Royal Astronomical Society*, 448, 1715
- Jaffé Y. L., et al., 2016, *Monthly Notices of the Royal Astronomical Society*, 461, 1202
- Jones M. G., Papastergis E., Haynes M. P., Giovanelli R., 2016, *Monthly Notices of the Royal Astronomical Society*, 457, 4393
- Kawata D., Rauch M., 2007, *The Astrophysical Journal*, 663, 38
- Kennicutt R. C. J., 1989, *The Astrophysical Journal*, 344, 685
- Kennicutt Jr. R. C., 1998, *The Astrophysical Journal*, 498, 541
- Kereš D., Katz N., Weinberg D. H., Davé R., 2005, *Monthly Notices of the Royal Astronomical Society*, 363, 2
- Kleiner D., et al., 2021
- Lah P., et al., 2009, *Monthly Notices of the Royal Astronomical Society*, 399, 1447
- Larson R. B., Tinsley B. M., Caldwell C. N., 1980, *The Astrophysical Journal*, 237, 692
- Lee K. S., et al., 2012, *Astrophysical Journal*, 752, 66
- Leroy A. K., Walter F., Brinks E., Bigiel F., de Blok W. J. G., Madore B., Thornley M. D., 2008, *The Astronomical Journal*, 136, 2782
- Leroy A. K., et al., 2012, *The Astronomical Journal*, 144, 3

- Leroy A. K., et al., 2013, *The Astronomical Journal*, 146, 19
- Lilly S. J., Carollo C. M., Pipino A., Renzini A., Peng Y., 2013, *Astrophysical Journal*, 772, 119
- Lintott C. J., et al., 2008, *Monthly Notices of the Royal Astronomical Society*, 389, 1179
- Lintott C., et al., 2011, *Monthly Notices of the Royal Astronomical Society*, 410, 166
- Maddox N., Hess K. M., Blyth S.-L., Jarvis M. J., 2013, *Monthly Notices of the Royal Astronomical Society*, 433, 2613
- Masters K. L., et al., 2010, *Monthly Notices of the Royal Astronomical Society*, 405, 783
- Moore B., Katz N., Lake G., Dressler A., Oemler A., 1996, *Nature*, 379, 613
- Moretti A., et al., 2019, *The Astrophysical Journal*, 889, 9
- Oman K. A., Hudson M. J., 2016, *Monthly Notices of the Royal Astronomical Society*, 463, 3083
- Oman K. A., Bahé Y. M., Healy J., Hess K. M., Hudson M. J., Verheijen M. A., 2021, *Monthly Notices of the Royal Astronomical Society*, 501, 5073
- Peng Y. J., et al., 2010, *Astrophysical Journal*, 721, 193
- Peng Y., Maiolino R., Cochrane R., 2015, *Nature*, 521, 192
- Peterken T., Merrifield M., Aragón-Salamanca A., Avila-Reese V., Boardman N. F., Drory N., Lane R. R., 2020, *Monthly Notices of the Royal Astronomical Society: Letters*, 500, L42
- Poggianti B. M., et al., 2016, *The Astronomical Journal*, 151, 78
- Poggianti B. M., et al., 2019, *The Astrophysical Journal*, 889
- Popesso P., et al., 2019, *Monthly Notices of the Royal Astronomical Society*, 483, 3213
- Ramella M., et al., 2007, *Astronomy and Astrophysics*, 470, 39
- Roberts M. S., 1963, *Annual Review of Astronomy and Astrophysics*, 1, 149
- Roediger E., Brüggén M., 2007, *Monthly Notices of the Royal Astronomical Society*, 380, 1399
- Salim S., et al., 2007, *The Astrophysical Journal Supplement Series*, 173, 267
- Sanchis T., Solanes J. M., Salvador-Sole E., Fouque P., Manrique A., 2002, *The Astrophysical Journal*, 580, 164
- Sancisi R., Fraternali F., Oosterloo T., Van Der Hulst T., 2008, *Astronomy and Astrophysics Review*, 15, 189
- Schawinski K., et al., 2009, *Monthly Notices of the Royal Astronomical Society*, 396, 818
- Schawinski K., et al., 2014, *Monthly Notices of the Royal Astronomical Society*, 440, 889

- Schiminovich D., et al., 2007, *The Astrophysical Journal Supplement Series*, 173, 315
- Schmidt M., 1959, *The Astrophysical Journal*, 129, 243
- Smee S., et al., 2012, *Astronomical Journal*, 146, 2013
- Solanes J. M., Manrique A., García-Gómez C., González-Casado G., Giovanelli R., Haynes M. P., 2001, *The Astrophysical Journal*, 548, 97
- Stoughton C., et al., 2002, *The Astronomical Journal*, 123, 485
- Strateva I., et al., 2001, *The Astronomical Journal*, 122, 1861
- Strauss M. A., et al., 2002, *The Astronomical Journal*, 124, 1810
- Taylor R., Minchin R. F., Herbst H., Davies J. I., Rodriguez R., Vazquez C., 2014, *Monthly Notices of the Royal Astronomical Society*, 443, 2634
- Tinsley B. M., 1968, *The Astrophysical Journal*, 151, 547
- Tinsley B. M., Larson R. B., 1979, *Monthly Notices of the Royal Astronomical Society*, 186, 503
- Toomre A., Toomre J., 1972, *The Astrophysical Journal*, 178, 623
- Verheijen M. A. W., 1997, PhD thesis, University of Groningen, <https://ui.adsabs.harvard.edu/abs/1997PhDT.....13V/abstract>
- Verheijen M., van Gorkom J. H., Szomoru A., Dwarakanath K. S., Poggianti B. M., Schiminovich D., 2007, *The Astrophysical Journal*, 668, L9
- Vulcani B., et al., 2018, *Monthly Notices of the Royal Astronomical Society*, 480, 3152
- Wyder T. K., et al., 2007, *The Astrophysical Journal Supplement Series*, 173, 293
- Zinger E., Dekel A., Kravtsov A. V., Nagai D., 2018, *Monthly Notices of the Royal Astronomical Society*, 475, 3654
- Zwaan M. A., Van Dokkum P. G., Verheijen M. A., 2001, *Science*, 293, 1800
- Zwicky F., et al., 1961, *Catalogue of galaxies and of clusters of galaxies, Vol. I*. California Institute of Technology (CIT), Pasadena, <https://ui.adsabs.harvard.edu/abs/1961cgcg.book.....Z/abstract>
- de Blok W. J. G., Fraternali F., Heald G., Adams E. A. K., Bosma A., Koribalski B. S., 2015, *Advancing Astrophysics with the Square Kilometre Array (AASKA14)*, pp 1 – 22
- de Vaucouleurs G., 1956, *Occ. Notes RAS*, 3, 18



“You’ve never heard of the Millennium Falcon? It’s the ship that made the Kessel run in less than 12 parsecs.” – Han Solo
(Star Wars IV: A New Hope)

Chapter 2

H I content in Coma cluster substructure

J. Healy,^{1,2} S-L. Blyth,² M.A.W. Verheijen,¹ K.M. Hess,^{1,3} P. Serra,⁴ J.M. van der Hulst,^{1,3}
T.H. Jarrett,² K. Yim⁵ and G. I. G. Józsa^{6,7,8}

Based on the paper accepted for publication on 3 November 2020, *Astronomy & Astrophysics*, Volume 650, A76

¹ Kapteyn Astronomical Institute, University of Groningen, Landleven 12, 9747 AV Groningen, the Netherlands

² Department of Astronomy, University of Cape Town, Private Bag X3, Rondebosch 7701, South Africa

³ Netherlands Institute for Radio Astronomy (ASTRON), Oude Hoogeveensedijk 4, 7991 PD Dwingeloo, the Netherlands

⁴ INAF - Osservatorio Astronomico di Cagliari, Via della Scienza 5, I-09047 Selargius (CA), Italy

⁵ Korea Astronomy and Space Science, Institute, 776 Daedeok-daero, Yuseong-gu, Daejeon 34055, Korea

⁶ South African Radio Astronomy Observatory, 2 Fir Street, Black River Park, Observatory, Cape Town, 7925, South Africa

⁷ Department of Physics and Electronics, Rhodes University, PO Box 94, Makhanda, 6140, South Africa

⁸ Argelander-Institut für Astronomie, Auf dem Hügel 71, D-53121 Bonn, Germany

Abstract

Galaxy clusters are some of the largest structures in the universe. These very dense environments tend to be home to higher numbers of evolved galaxies than found in lower-density environments. It is well known that dense environments can influence the evolution of galaxies through the removal of the neutral gas (H I) reservoirs that fuel star formation. It is unclear which environment has a stronger effect: the local environment (i.e. the substructure within the cluster), or the cluster itself. Using the new H I data from the Westerbork Coma Survey, we explore the average H I content of galaxies across the cluster comparing galaxies that reside in substructure to those that do not. We applied the Dressler-Shectman test to our newly compiled redshift catalogue of the Coma cluster to search for substructure. With so few of the Coma galaxies directly detected in H I, we used the H I stacking technique to probe the average H I content below what can be directly detected. Using the Dressler-Shectman test, we find 15 substructures within the footprint of the Westerbork Coma Survey. We compare the average H I content for galaxies within substructure to those not in substructure. Using the H I stacking technique, we find that those Coma galaxies not detected in H I are more than 10–50 times more H I deficient than expected, which supports the scenario of an extremely efficient and rapid quenching mechanism. By studying the galaxies that are not directly detected in H I, we also find Coma to be more H I deficient than previously thought.

2.1 Introduction

In our current picture of cosmology, Λ cold dark matter (Λ CDM), larger structures (e.g. galaxy clusters) are built up through the hierarchical merging of smaller structures (e.g. galaxy groups or individual galaxies) (Springel et al., 2005). Using dark matter simulations, McGee et al. (2009) showed that 45 per cent of galaxies accreted onto a Coma-sized cluster would have done so in groups. Their results suggest that the group environments play an important role in the evolution of galaxies prior to accretion onto the cluster. Traces of the accretion history of a cluster can be observed through substructure in the kinematics of the galaxies in the cluster (e.g. Dressler & Shectman, 1988b; Hou et al., 2012). Observations have shown that roughly 30 per cent of clusters contain kinematic substructure (Dressler & Shectman, 1988b; Bird, 1994; Hou et al., 2012). The observational evidence of substructure is further supported by dark matter simulations, which estimate that a similar fraction of clusters contain significant substructure (Knebe & Mueller, 1999).

Given the prevalence of substructure within clusters, there have been many efforts to identify substructure. Groups of galaxies identified through substructure within the X-ray emission of the cluster (e.g. Neumann et al. 2001, 2003; Zhang et al. 2009; Parekh et al. 2015) may be older, more evolved groups that have had their own intra-cluster medium (ICM) prior to accretion onto the cluster. An alternative possibility is that the X-ray emission associated with such groups might not belong to them, but rather to the cluster ICM that was disturbed by the fast peri-centre passage of such recently accreted groups. Another identification method is a hierarchical clustering technique, a mathematical algorithm which sorts data into “clusters” based on an affinity parameter. This particular method, introduced by Serna & Gerbal (1996), assigns galaxies to groups by minimising the binding energy. However, one of the more common methods of identifying substructure is to look for kinematic deviations (δ values) between groups of galaxies and the cluster as a whole. This method is known as the Dressler-Shectman (DS) test (Dressler & Shectman, 1988b). Aside from the original study in which Dressler & Shectman (1988b) looked for kinematic substructures in the Abell cluster catalogue, the DS test has been used to study the substructure in Abell 2192 and Abell 963 (Jaffé et al., 2013), the Antlia cluster (Hess et al., 2015), and the Coma cluster (Colless & Dunn, 1996). All of the above methods are effective at finding substructure, however each method is sensitive to different density environments within a cluster. Knebe & Mueller (1999) studied the effectiveness of the DS test using numerical simulations of clusters and also compared the DS test to other methods such as the friends-of-friends (FoF) algorithm. These authors found that the DS test and FoF algorithm find similar structures, but there is a large scatter. Knebe & Mueller (1999) attributed the scatter (and also the differences in subgroups for the same cluster in the literature) to velocity projection effects that can artificially increase the δ values in the DS test.

Neumann et al. (2003) identified substructure in the Coma cluster by finding over-densities in the X-ray emission in the cluster. At the core of the cluster, these authors found an X-ray over-density associated with the two cD galaxies (NGC 4889 and NGC 4874). This X-ray over-density is offset from the X-ray centre of the cluster and has been attributed to the haloes of the individual galaxies (Vikhlinin et al., 2001; Andrade-Santos et al., 2013). Previous kinematic substructure analyses (e.g. Colless & Dunn, 1996) have identified separate groups associated with NGC 4889 and NGC 4874. Colless & Dunn (1996) and White et al. (1993) suggested that the NGC4889 group is merging with the NGC 4874 group, which was dislodged from the centre of the cluster potential as a result of the interaction. This would account for the velocity differences between the two galaxies themselves and also with respect to the cluster velocity.

Studies using the DS test and hierarchical clustering technique have found groups throughout the cluster, but both methods are sensitive to the availability of optical redshifts for a cluster (Adami et al., 2005). This is particularly evident when comparing the first DS test results from Dressler & Shectman (1988b), who found no significant substructure within the Coma cluster (their catalogue contained 100–200 galaxies over a 2 deg^2 area), with later work on the Coma cluster by Colless &

Dunn (1996), who found that there is significant substructure with a larger redshift catalogue over a similar area of the sky.

Identifying substructure within galaxy clusters is not only important to understand the build-up of the cluster, the local environments identified by substructure also provide insight into the evolution of galaxies (Dressler & Shectman, 1988b; Neumann et al., 2001, 2003; Adami et al., 2005; Hess et al., 2015). Dressler (1980) found that galaxies residing in dense environments tend to be passive with more evolved morphologies, while low-density environments have higher fractions of less evolved, actively star-forming galaxies. This observed phenomenon is now referred to as the morphology-density relation. Uncovering the cause of the morphology-density relation is related to understanding the evolutionary pathway from late-type spiral (Sa/Sb/Sc/Sd) galaxies to early-type elliptical (dE/E) galaxies. On the traditional Hubble galaxy morphology ladder, lenticular (S0) galaxies bridge the gap between the ellipticals and the spirals. While S0s are thought to be quenched spirals (see Coccato et al., 2020, and references therein), it is not known how or even if S0s transition to elliptical galaxies. In cluster environments in which the fraction of S0 galaxies tends to be high, gas removal processes dominate the evolutionary mechanisms (see Aguerri, 2012, for a review). It is still unclear which environment has a stronger effect in driving morphological evolution: Does the cluster drive these mechanisms, or are galaxies in groups pre-processed (e.g. Zabludoff & Mulchaey, 1998; Porter et al., 2008; Wilman et al., 2009) prior to infall onto the cluster?

Studying the neutral atomic gas (HI) in galaxies can provide an early picture of which environment (group or cluster) plays the strongest role in triggering the morphological evolution of galaxies as they migrate into clusters. The HI disc extends beyond the stellar disc of the galaxy (particularly in the field), making it the most susceptible to environmental interactions (e.g. Haynes & Giovanelli, 1984; Serra et al., 2013; Jaffé et al., 2015). Strangulation, the process that removes gas from the halo thus halting the fresh supply of HI to the galaxy, is thought to be one of the main drivers behind the morphology-density relation (Balogh et al., 2000; Balogh & Morris, 2000; Van Den Bosch et al., 2008). However, strangulation alone cannot fully explain the transition of galaxies from blue star-forming spiral galaxies to the red, passive lenticular and elliptical galaxies that dominate the galaxy clusters. The effects of galaxy harassment can completely destroy the discs of Sc/Sd galaxies such that the orbits of the constituent stars are affected. It is thought that this could explain the formation of dwarf elliptical (dE) galaxies that are prevalent in the centre of clusters (Mo et al., 2010). Ram-pressure stripping (Gunn & Gott, 1972; Chung et al., 2009; Kapferer et al., 2009; Abramson et al., 2011; Jaffé et al., 2015; Yoon et al., 2017) is the process by which the gas is stripped from the disc of a galaxy owing to its interaction with the intra-cluster or intra-group medium. Ram-pressure stripping is highly effective at rapidly removing the gas from the discs of galaxies, and could be a driving factor in affecting the transition of Sa/Sb to S0s (Mo et al., 2010). Signatures of these different processes affecting the evolution of galaxies are particularly evident in the HI. Strangulation results in a truncated or anaemic HI disc, while galaxies that have undergone ram-pressure stripping or harassment tend to have asymmetric HI discs or tails. The effectiveness of these processes in dense environments means that galaxies in clusters are more HI deficient than their field counterparts (e.g. Solanes et al., 1996; Chung et al., 2009).

The Coma cluster (Abell 1656), a nearby rich cluster, is one of the most well-studied galaxy clusters in the Universe (see Biviano et al., 1996, for historical review). One of the most comprehensive projects targeting Coma and spanning the entire electromagnetic spectrum, is the Coma Cluster Treasury Survey¹ (CCTS). At the heart of the survey was an observing programme using the Advanced Camera for Surveys (ACS) on the Hubble Space Telescope (HST). The goal of the Coma ACS survey was to image the core and the infall region (Carter et al., 2008), however the observing programme was never completed owing to the failure of the ACS. While the HST imaging was never completed, contributions to the CCTS from observing programmes on other telescopes

¹<http://astronomy.swin.edu.au/coma/project-overview.htm>

have provided rich insight into our understanding of the cluster and its population (e.g. Yagi et al., 2007; Smith et al., 2008; Yagi et al., 2010).

At a distance of ~ 100 Mpc and velocity dispersion of ~ 1000 km s $^{-1}$, Coma is the nearest large cluster to us. While Coma is often held up as a large, relaxed cluster, studies of its X-ray emission show a complex dynamical state (see Neumann et al., 2001, 2003, and references therein). There are many theories as to the formation of Coma, however the presence and difference in velocities of the two large cD galaxies (NGC 4874 and NGC 4889) at the centre of the cluster suggest that Coma is the result of a merger (Fitchett & Webster, 1987). Coma has been the target of many redshift surveys in an effort to understand the distribution and kinematics of the galaxies within the cluster and identify any substructure (e.g. Colless & Dunn, 1996; Chiboucas et al., 2010; Albareti et al., 2017). The presence of substructure in the cluster is now well established (e.g. Fitchett & Webster, 1987; Mellier et al., 1988; Neumann et al., 2001, 2003; Adami et al., 2005). Many of the galaxy groups making up the substructure are thought to have been accreted onto the cluster, and in some cases could still be on first infall (e.g. Neumann et al., 2001, 2003; Adami et al., 2005).

There have also been a number of surveys of the HI content of galaxies in Coma, both targeted (e.g. Bravo-Alfaro et al., 2001; Gavazzi et al., 2006) and blind (e.g. Beijersbergen, 2003; Haynes et al., 2018). These works have provided insight into the ongoing gas removal processes affecting the galaxies in the cluster, as well as an understanding of the HI deficiency of the cluster. The previous Coma HI surveys have lacked coverage, sensitivity, resolution, or some combination thereof. In this work, we use HI observations from the blind, high-sensitivity and high-resolution survey with the Westerbork Synthesis Radio Telescope (WSRT): the Westerbork Coma Survey (WCS; Molnar et al. in prep). With the wealth of information already available, in combination with new HI observations of the cluster, we can explore the morphologies of the Coma galaxies in conjunction with their gas properties and local environment. Coma is known to be home to a large number of S0 galaxies: the relative fraction of S0s, ellipticals, spirals and mergers is 42 per cent, 22 per cent, 32 per cent, and 4 per cent, respectively (Beijersbergen, 2003). This makes Coma an ideal laboratory to study HI properties of galaxies of different morphologies in the different local environments.

In this chapter, we make use of data from a blind HI survey of the Coma cluster (Section 2.2.3) from Molnar et al. (in prep) to study the HI gas properties of the different galaxy types in different environments within the cluster. Most of the galaxies in Coma are not individually detected in HI, thus we make use of the HI stacking technique (Section 2.3) to improve the signal-to-noise ratios (S/N) of groups of HI spectra. The optical spectroscopy and photometry used in this work are presented in Section 2.2. We explore the global HI properties of the galaxies in Coma by deriving optical–HI scaling relations and by determining the HI deficiency at different locations within the cluster (Section 2.4). We use the substructure within the cluster as a measure of the local environment (Section 2.5), and use HI stacking to probe the HI content of samples of galaxies within local environments relative to the global HI properties of the cluster (Section 2.6.4). Throughout this chapter we use $H_0 = 70$ km s $^{-1}$ Mpc $^{-1}$ ($h = 0.7$), $\Omega_m = 0.7$, and $\Omega_\Lambda = 0.3$.

2.2 Multiwavelength data

2.2.1 Optical spectroscopy

A full, wide-area redshift census of Coma is essential to this work for two reasons: First, HI stacking requires spectroscopic redshifts to align the HI non-detected spectra; second, we require redshifts in order to more accurately characterise the environment (substructure) within the cluster, as well any infalling groups. This work makes use of redshifts from two different sources: literature

(Section 2.2.1.1) and spectroscopy obtained with Hydra at the WIYN Telescope² (Section 2.2.1.2). The final catalogue contains 1095 spectroscopically confirmed members of the Coma cluster within a 2 deg radius of the cluster centre (58 are new redshifts – see Section 2.2.1.2); 850 of these fall within the WCS footprint (the orange outline in Figure 2.2). The larger catalogue is necessary when looking for substructure within the cluster.

2.2.1.1 Redshifts from the literature

The literature catalogue was collated from a number of published and unpublished catalogues. More than two-thirds of the redshifts were obtained from the Sloan Digital Sky Survey (SDSS) Data Release (DR) 13 (DR13; Albareti et al., 2017). The remainder come from a number of different sources (see Table A.1 for the number of redshifts from the different sources); the reference for each redshift is given in the Coma galaxy catalogue in Appendix C.

Using the VizieR astronomical catalogue database (Ochsenbein et al., 2000), we queried data in published catalogues within a 2 deg radius centred on the Coma cluster. Merging the SDSS redshifts with those obtained from VizieR created a large master catalogue with overlapping sources, some of which had redshifts outside of the Coma volume. To construct our catalogue of unique sources associated with the Coma cluster, we only consider sources with $3000 < cz < 10500 \text{ km s}^{-1}$ as this is the spectral range spanned by the H I data set. Sources within $5''$ radius of each other are considered to be the same source; when multiple sources within the search radius were found, only the redshift with the smallest uncertainty was kept in the catalogue. Every galaxy with multiple redshift measurements was checked by eye so as not to remove the redshifts of real spatially overlapping galaxies.

2.2.1.2 Spectroscopy with Hydra

New spectroscopic data for galaxies in the Coma cluster were obtained using Hydra, the multi-object spectrograph, on the 3.5m WIYN Telescope located at the Kitt Peak National Observatory. Despite being an extremely well-observed cluster, the spectroscopic coverage of Coma drops off for galaxies fainter than $r \sim 17.7$ mag, thus we targeted galaxies fainter than this limit. Since previous targeted spectroscopic surveys have focused on the core of the cluster, we prioritised galaxies with $r > 17.7$ mag on the outskirts of the cluster and with bluer colours ($g - r < 0.6$) as these are the galaxies we expect to contain H I. Figure 2.1 shows the colour magnitude diagram (CMD) for the cluster. The lower right quadrant of the CMD shows very few redshifts from literature, which is another motivation for targeting galaxies in that quadrant of the CMD.

Hydra nominally has 100 fibres feeding the spectrograph, however at the time of the observations, only 80 were accessible. We used the blue cable with the $600@10.1^3$ grating centred on 5300 \AA which covered the wavelength range of $4000\text{--}6700 \text{ \AA}$ at a resolution of 4.63 \AA/pix . This enabled us to target the $H\beta$, OIII, OI, and $H\alpha$ emission lines, as well as the H, K absorption lines. Initially, eight configurations of the five fields were targeted (three of the fields had a second configuration, which was necessary because of the density of targets); however owing to poor weather conditions on the first night, only six configurations were actually observed. In each configuration, 60–65 fibres were assigned to targets, and the remaining 15–20 were assigned as sky fibres. Each configuration was observed in 3×20 min epochs for a total integration time of 1 hour. The data were collected on the nights of 19 – 20 April 2018.

²The WIYN Observatory is a joint facility of the University of Wisconsin-Madison, Indiana University, the National Optical Astronomy Observatory, and the University of Missouri.

³Grooves/mm @ Littrow blaze angle – see www.wiyn.org/instruments/wiynbench.html for more details

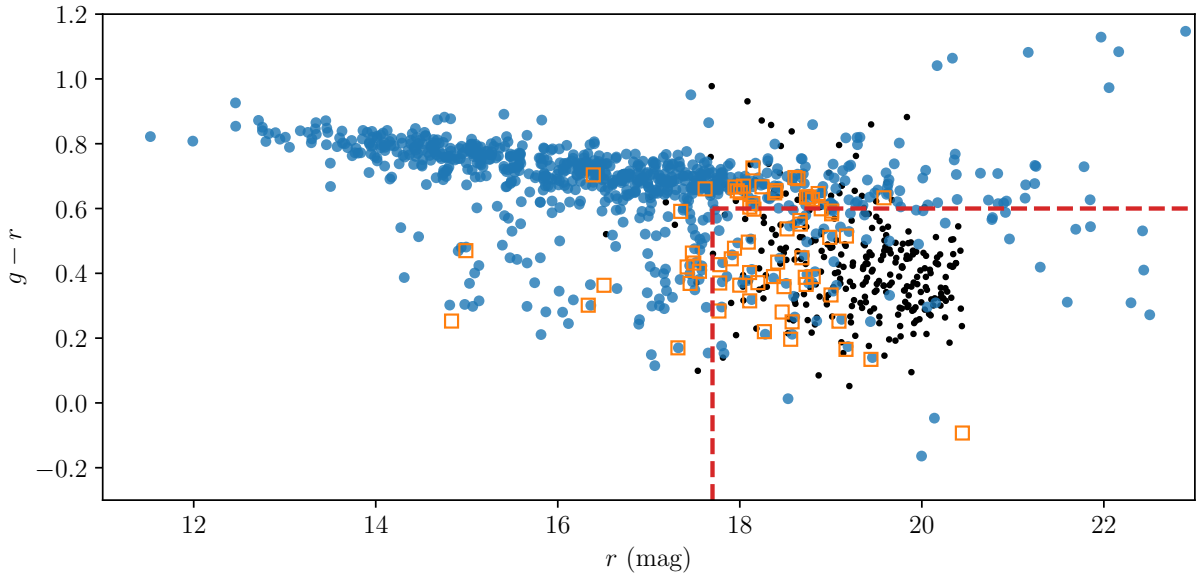


Figure 2.1: Colour magnitude diagram for the Coma cluster. The blue points represent the galaxies in the catalogue of literature redshifts. The black dots represent all galaxies targeted with Hydra, but whose redshifts place them in the foreground or background. The orange open squares represent the galaxies targeted with Hydra with redshifts that place them inside the cluster. Galaxies with $r > 17.7$ mag and $g - r < 0.6$ were prioritised as indicated by the dashed red lines.

All the data reduction was done using IRAF⁴. The first phase of the data reduction after cosmic ray removal using `lacosmic` (van Dokkum, 2001) was done using the `ccdred` package; this took care of the overscan, bias, and dark subtraction. The second phase was guided by the `dohydra` task, which takes care of the flat-fielding, aperture extraction, wavelength calibration, dispersion correction, and sky subtraction. The wavelength-calibrated and sky-subtracted spectra were then matched to template spectra to determine the redshift of the galaxies.

The redshift calculations were performed using the cross-correlation technique that is implemented by the IRAF task `xcsao` (Kurtz et al., 1992) contained within the `rvsao` package. We searched for velocities between 0 km s^{-1} and $100\,000 \text{ km s}^{-1}$ using seven different templates. We used three different types of emission line templates, three different types of absorption line templates, and one composite template so as to make sure we had covered the range in different types of stellar populations. Velocities were only accepted as robust if at least three templates produced results within 100 km s^{-1} , a common uncertainty for a measurement based on absorption lines. The uncertainty on each redshift measurement was determined from the peak of the correlation between the template and observed spectrum. A detailed explanation can be found in Kurtz et al. (1992). All results were also inspected by eye. Three examples of Hydra spectra are shown in Figure 2.3. The spectra have been sky-subtracted, but have not been flux calibrated as this is not necessary to obtain a redshift measurement; the vertical red bands indicate the regions of the spectra for which there are strong sky lines; and the dashed lines and grey regions indicate the wavelength and associated error of the labelled lines. Of the 363 observed galaxies, the spectra of 278 galaxies had high enough S/N to obtain a redshift measurement (see Figure 2.3a); 58 of these redshifts are new measurements of galaxies in the Coma cluster (see the red histogram in Figure 2.4 for redshift distribution of these galaxies). The 85 galaxy spectra from which no redshift measurement could be made were discarded from the sample owing to low S/N (see Figure 2.3b) or poor sky subtraction

⁴IRAF is distributed by the National Optical Astronomy Observatory, which is operated by the Association of Universities for Research in Astronomy (AURA) under a cooperative agreement with the National Science Foundation.

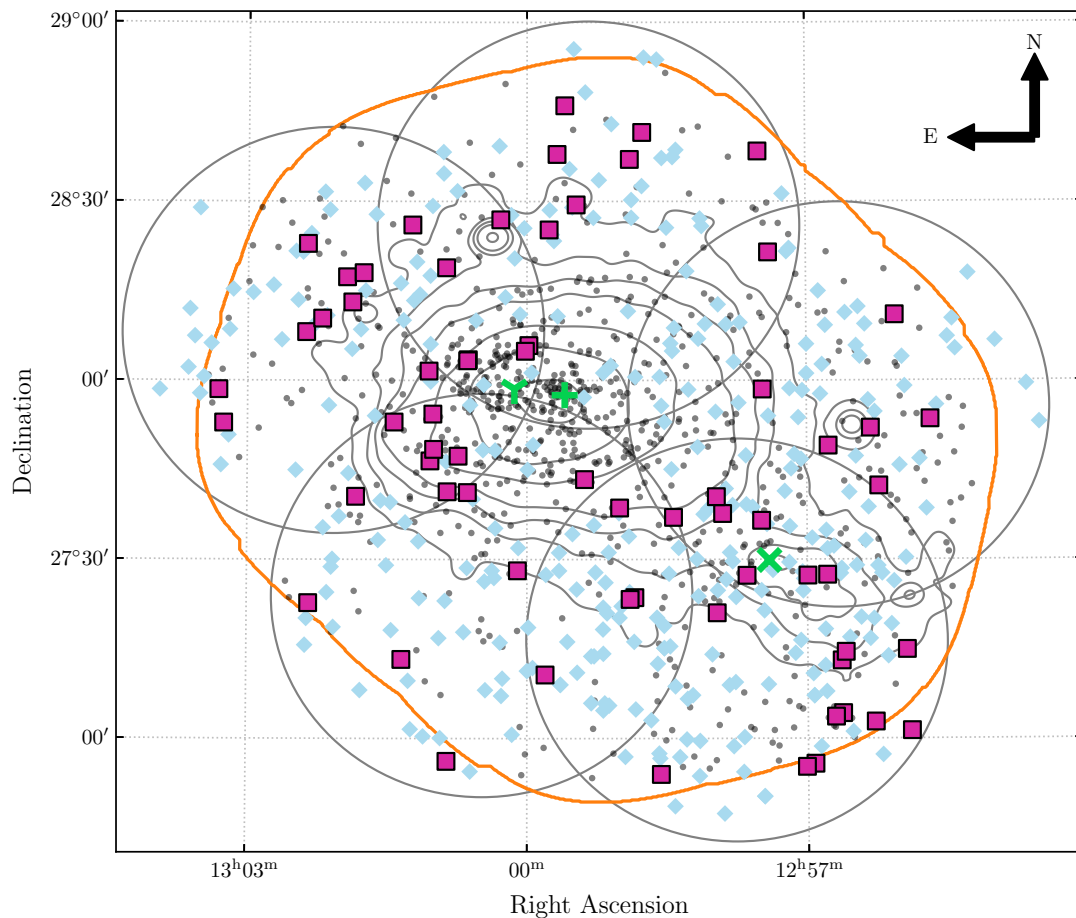


Figure 2.2: WIYN/Hydra targets, and observed sources. The 5 fields (3 of the fields had a second configuration) targeted with WIYN are indicated by the large circles. The square and diamond data points represent the galaxies we targeted with Hydra. The galaxies with redshifts in the Coma volume are represented by the magenta square data points and the foreground and background galaxies are represented by the blue diamond markers. The green markers represent the three cD galaxies in Coma (+–NGC 4874, γ –NGC 4889 and \times –NGC 4839). The 0.4 – 2.4 keV ROSAT X-ray contours are given by the grey contours (outer contours correspond to 3×10^{-5} cts/s, and inner-most contours to 1×10^{-3} cts/s). Other confirmed members of the Coma cluster are represented by the small grey circles. The WCS footprint is indicated by the orange outline.

(there were 29 such galaxy spectra – see Figure 2.3c). The poor sky subtraction is evident in the spectrum shown in Figure 2.3c by the emission line features in the red vertical bands, these bands indicate the regions for which there are known strong sky lines.

2.2.2 Photometric data

Despite Coma being an extremely well-studied cluster, there are no publicly available matched-aperture or total magnitude photometric catalogues that cover the entire region of Coma that we are interested in. It is important when comparing flux (or magnitude) measurements in different photometric bands that the measurements are determined in the same manner (i.e. matched apertures or model fits for total magnitudes). The overlapping sources at the centre of the cluster also provide a challenge to many aperture-based photometric pipelines. Our imaging data include near-

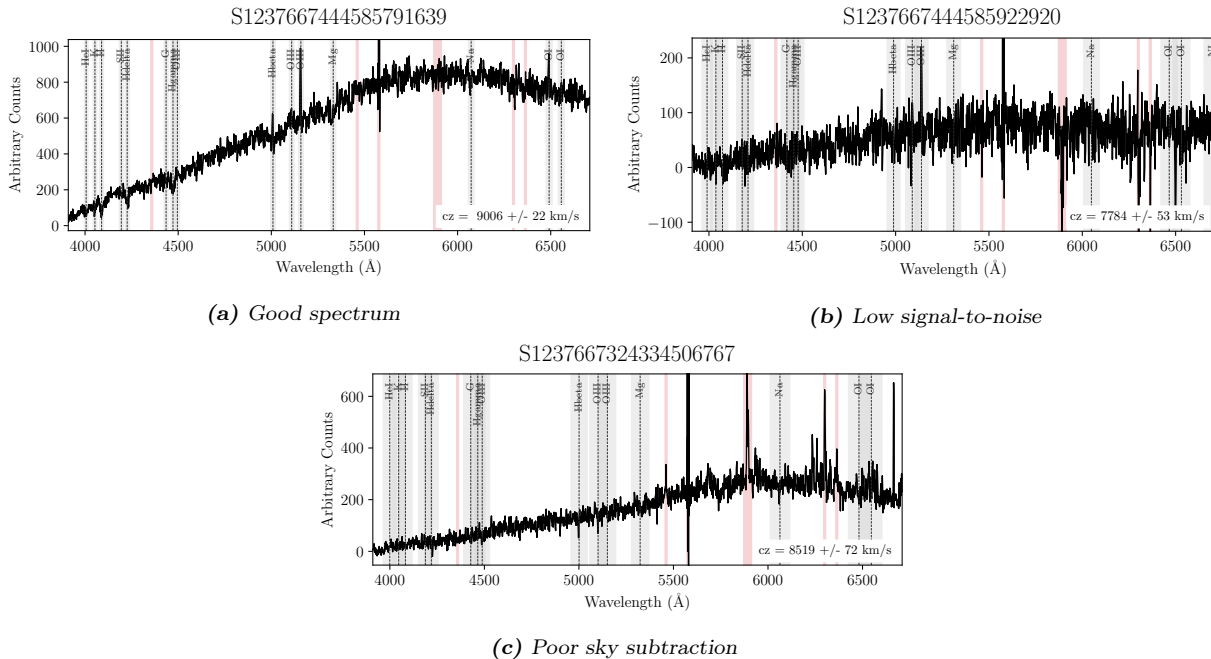


Figure 2.3: Three examples of the cross-correlation results of Hydra spectra. The dashed lines and grey regions indicate the central wavelength and associated error of the labelled line. The red regions indicate those masked out during the cross-correlation process because of strong sky lines.

and far-ultraviolet (UV) data from the Galaxy Evolution Explorer (GALEX, Bianchi & GALEX Team, 2000), five optical bands (*ugriz*) from SDSS (DR12 Alam et al., 2015), and the four mid-infrared bands (W1 - W4) from the Wide-field Infrared Survey Explorer (WISE, Wright et al., 2010). Frames from the 11 bands were mosaicked using SWARP (Bertin, 2010) to create a single $2 \times 2 \text{ deg}^2$ image per band centred on the cluster, all with the same pixel scale ($0.396''/\text{px}$). We also created a pseudo B-band image from the SDSS *g* and *i* bands using the following relation from Cook et al. (2014) for conversion from SDSS to Johnsons magnitude:

$$B - i = (1.27 \pm 0.03)(g - i) + (0.16 \pm 0.01). \quad (2.1)$$

This relation was calibrated using galaxies in the Local Volume Legacy Survey (Dale et al., 2009). It should be noted that this pseudo B-band magnitude is only used to calculate the diameter (D_{25}) of each galaxy at the 25 mag/arcsec^2 isophote, which is required to estimate the expected HI mass (see Section 2.4).

We followed the strategy used by Barden et al. (2012) in the GALAPAGOS pipeline to calculate magnitudes and other morphological properties for each galaxy for which we have a redshift measurement within the WCS footprint. For each galaxy we created a set of postage stamps that are then used to calculate properties such as magnitude and size. The modelling was done using GALFITM (Bamford et al., 2011), which is a modified version of GALFIT created by Peng et al. (2002, 2010). GALFITM is capable of modelling a source across multiple bands simultaneously. It is very sensitive to the initial parameters, and so we therefore calculated the initial values using source characterisation tools in *photutils* (an *AstroPy* package for photometry). We also used the *photutils* image segmentation feature to create masks for each band: any source not associated with our target is masked, with the exception of overlapping sources, which are modelled simultaneously using GALFITM. There are 23 galaxies for which the fit failed or was not possible because the galaxy is too faint (4 of these are known ultra-diffuse galaxies). These galaxies are still included in our spectroscopic sample as they come from spectroscopic surveys that targeted extremely faint dwarf galaxies (e.g. Chiboucas et al., 2010) or ultra-diffuse galaxies (e.g. Alabi et al., 2018).

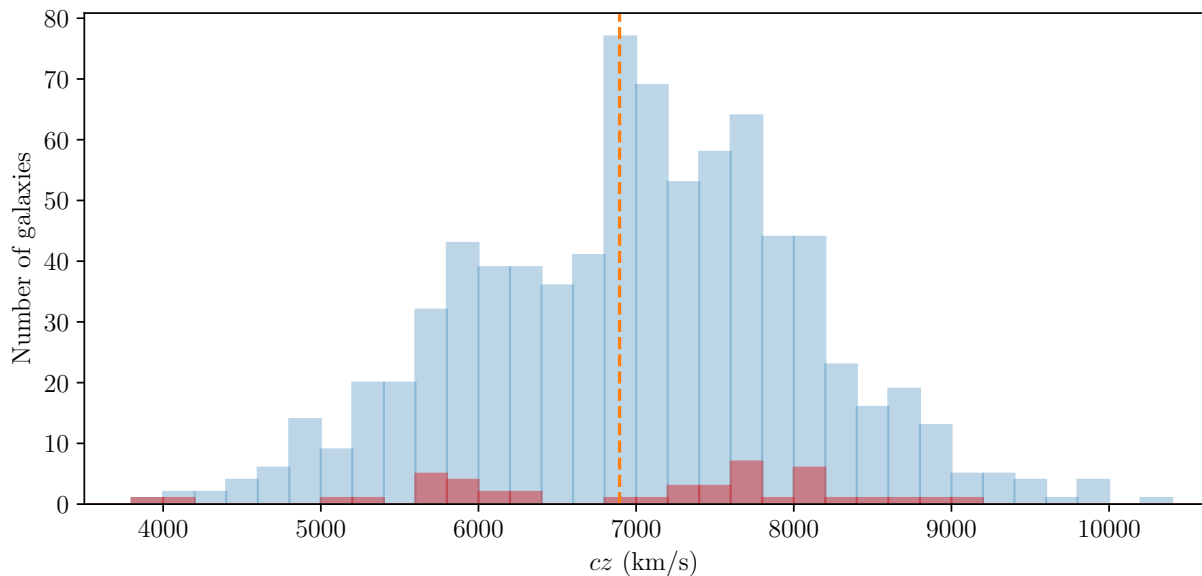


Figure 2.4: Distribution of all redshifts (literature and new) within WCS footprint. The red represents the galaxies whose redshifts were obtained using Hydra/WIYN.

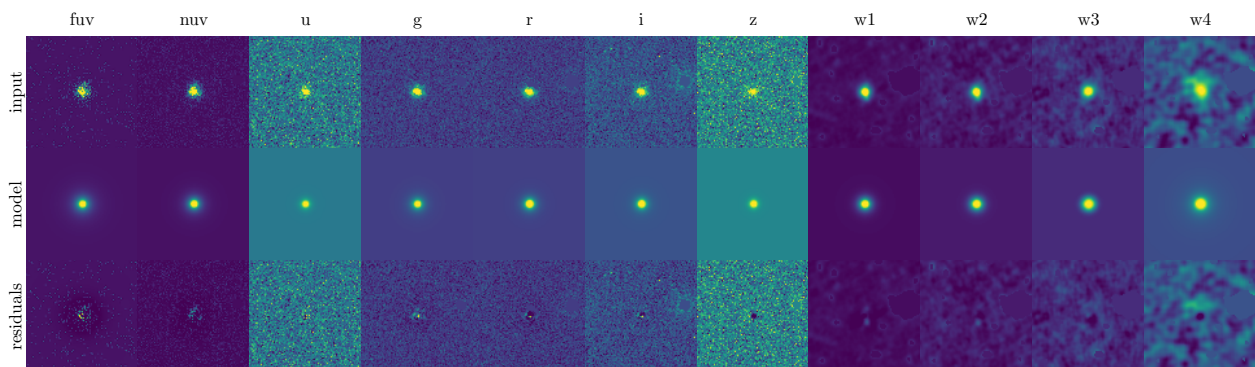


Figure 2.5: Galaxy modelled with a single Sersic profile by GALFITM. The input data are shown in the top row, the model in the second row, and the residuals in the bottom row. The colour scale is set in every column such that each row has the same intensity.

An example of a single Coma galaxy modelled using a single Sersic profile by GALFITM is presented in Figure 2.5. The Sersic profile, one of the most commonly used profiles for modelling galaxies of differing morphologies (Peng et al., 2010), is given by

$$I(r) = I_e \exp \left[-\kappa \left(\left(\frac{r}{r_e} \right)^{1/n} - 1 \right) \right], \quad (2.2)$$

where I_e is the pixel intensity at the effective radius r_e . The κ is tied to the value of n such that when $n = 4$ (making Equation 2.2 consistent with a de Vaucouleurs profile), $\kappa = 7.67$ (Peng et al., 2010). Galaxies better described by an exponential profile have $n = 1$. During the model fitting process, we allow the model parameters to vary across the bands. The full catalogue of properties for Coma galaxies within the WCS footprint is given in Appendix C.

Stellar masses and star formation rates (SFRs) for the Coma galaxies are calculated following the method outlined in Cluver et al. (2014) and using a custom pipeline (Jarrett et al., 2013, 2019). The mass-to-light ratios for each galaxy are calculated from the WISE W1-W2 colour using

$$\log M/L_{W1} = -2.54(W1 - W2) - 0.17, \quad (2.3)$$

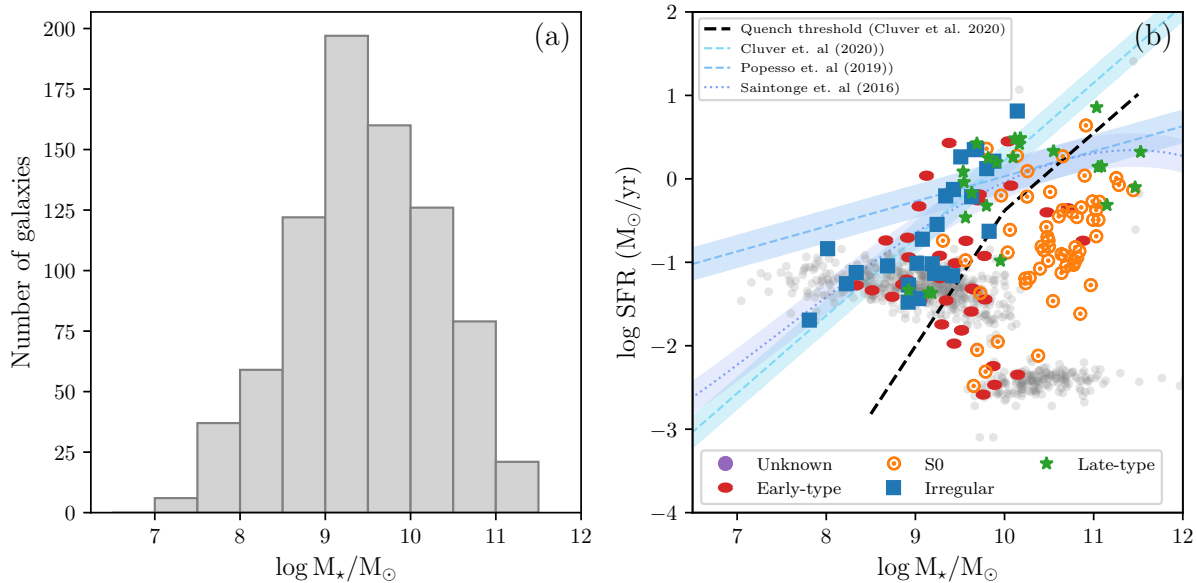


Figure 2.6: Stellar mass and star formation distribution of Coma galaxies in the WCS footprint. *Left:* Stellar mass distribution of Coma galaxies within the WCS footprint. *Right:* Star formation rate as a function of stellar mass for the Coma galaxies. The 2σ upper limit on the star formation rate is shown for galaxies for which there is no detection in the W3 band; these are represented by the light grey points. The step function in the upper limits arises owing to a non-detection in W3 for low-mass galaxies and a non-detection after continuum subtraction in W3 for high-mass galaxies. Also shown for reference are fits to the star formation main sequence by Cluver et al. (2020), Popesso et al. (2019) and Saintonge et al. (2016). The black dashed line indicates the quench threshold (Cluver et al., 2020) below which galaxies are not considered to be actively star forming.

where L_{W1} is the W1 ($3.4\ \mu\text{m}$) in-band luminosity of the galaxy relative to the Sun, and $(W1 - W2)$ is the rest-frame colour (Cluver et al., 2014). The distribution of stellar masses for Coma is shown in panel (a) of Figure 2.6.

As has been shown by Cluver et al. (2014, 2017), the W3 ($12\ \mu\text{m}$) and W4 ($23\ \mu\text{m}$) bands trace the interstellar medium (ISM) emission in galaxies and can thus be used to determine SFRs. The SFRs used in this work are calculated from the $12\ \mu\text{m}$ luminosity (W3) relation determined by Cluver et al. (2017). The W3 flux measurements are separated into the contributions from polycyclic aromatic hydrocarbon (PAH) emission (which is related to the star formation activity) and a contribution from the stellar continuum (Cluver et al., 2017). Panel (b) of Figure 2.6 shows the star formation rate as a function of stellar mass for the sample. Many of the Coma galaxies do not have a measured SFR, and therefore are presented as 2σ upper limits in Figure 2.6. There is a step-distribution in the SFR upper limits, which arises as a result of the low-mass galaxies ($M_* \lesssim 10^{9.5} M_\odot$) not being detected in the W3 band. The higher-mass galaxies ($M_* \gtrsim 10^{9.5} M_\odot$) are detected, but the W3 flux is largely attributed to the stellar continuum that is removed prior to determining the SFR.

2.2.3 H I data

The blind, high-sensitivity and high-resolution WSRT H I observations from Molnar et al. (in prep) provide an opportunity to study the gas content of Coma galaxies located well within the cluster environs, along with those on infall. Like most dense galaxy environments, Coma is well known for being H I deficient, and so we use the H I stacking method to probe the average H I content of groups of galaxies.

The WCS observed Coma in two overlapping 20 MHz bands (1369 – 1389 MHz and 1386 – 1406 MHz) and is comprised of 24 overlapping WSRT pointings of 1×12 h, making the effective integration owing to the overlap, 3×12 h per pointing. The final data cubes were created using the MIRIAD software package (Sault et al., 2011). Details about the data reduction are provided in Molnar et al. (in prep). The two data cubes, together, cover approximately $\sim 5 \text{ deg}^2$ and a velocity range of $\sim 3000 - 10500 \text{ km s}^{-1}$, however, there is a break in the velocity range of $\sim 24 \text{ km s}^{-1}$ at the central cluster velocity of 6925 km s^{-1} due to flagged data in the overlap of the two observed bands. The two HI cubes have a spatial resolution of $26.5 \times 40.3 \text{ arcsec}^2$ ($12.3 \times 18.7 \text{ kpc}^2$ at the distance of the cluster) and a velocity resolution of 16.5 km s^{-1} .

The WCS contains 39 galaxies for which there are direct HI detections, with HI masses greater than $4.4 \times 10^7 M_{\odot}$. The detections were identified using SoFiA (Serra et al., 2015) and confirmed by eye. Details on the source finding and discussion about the properties of the HI detections are provided in Molnar et al. (in prep).

2.3 HI stacking method

The technique utilised in this study to probe the HI content of the galaxies in the Coma cluster is called HI stacking. This statistical technique has become popular to push the HI mass sensitivity below the detection limit. The technique is particularly useful to study the average HI properties of samples of galaxies that are predominantly not directly detected in HI. HI stacking has been successfully used to study the neutral gas content of galaxies in clusters and dense environments (e.g. Chengalur et al., 2001; Fabello et al., 2012; Verheijen et al., 2007; Lah et al., 2009; Brown et al., 2017; Jaffé et al., 2016).

HI stacking uses the optical redshift information for each galaxy to align the HI spectra. The aligned spectra are co-added to create an average spectrum with lower noise statistics than the individual spectra. In this study we make use of the publicly available HI Stacking Software (HISS; Healy et al., 2019)⁵ tool to perform all our stacking experiments.

For every galaxy with a redshift in our catalogue, we extract a spectrum from the HI data cubes. For galaxies where the B-band D_{25} is resolved by the beam, we extract the spectrum using an aperture with the semi-major axis determined from the galaxy diameter at the B-band 25th mag isophote (D_{25}) (see Figure A.1b). For galaxies unresolved by the beam, the corresponding HI spectra are extracted using an aperture the size of the beam ($25'' \times 40''$) (see Figure A.1a). Along with the target spectrum, for every galaxy, we also extract 25 “reference” spectra using the same aperture as the target spectrum. The bottom left panel of Figure A.1a and Figure A.1b show the locations around the target from which the 25 reference spectra are extracted. These reference spectra are stacked in all our analyses in the same manner as the target galaxy spectra. For each target galaxy we extract background spectra from 25 offset positions around it. Taking as input a background spectrum from the same relative offset position around each target galaxy, we produce a background reference spectrum. Using all the offset positions results in 25 separate reference spectra per stacked target spectrum, with each reference spectrum containing the same number of stacked spectra as the target stack. Stacked reference spectra are used to aid in quantifying the signal in the main stacked spectrum. The average of the 25 stacked reference spectra for a well-calibrated dataset should be around zero (e.g. see the grey line in the panels of Figure 2.11). From the spread of the 25 stacked reference spectra, we estimate the uncertainty on the quantity measured from the stacked target spectrum.

Successful stacking relies on the average noise in the stacked spectrum decreasing by a factor

⁵github.com/healytwin1/HISS

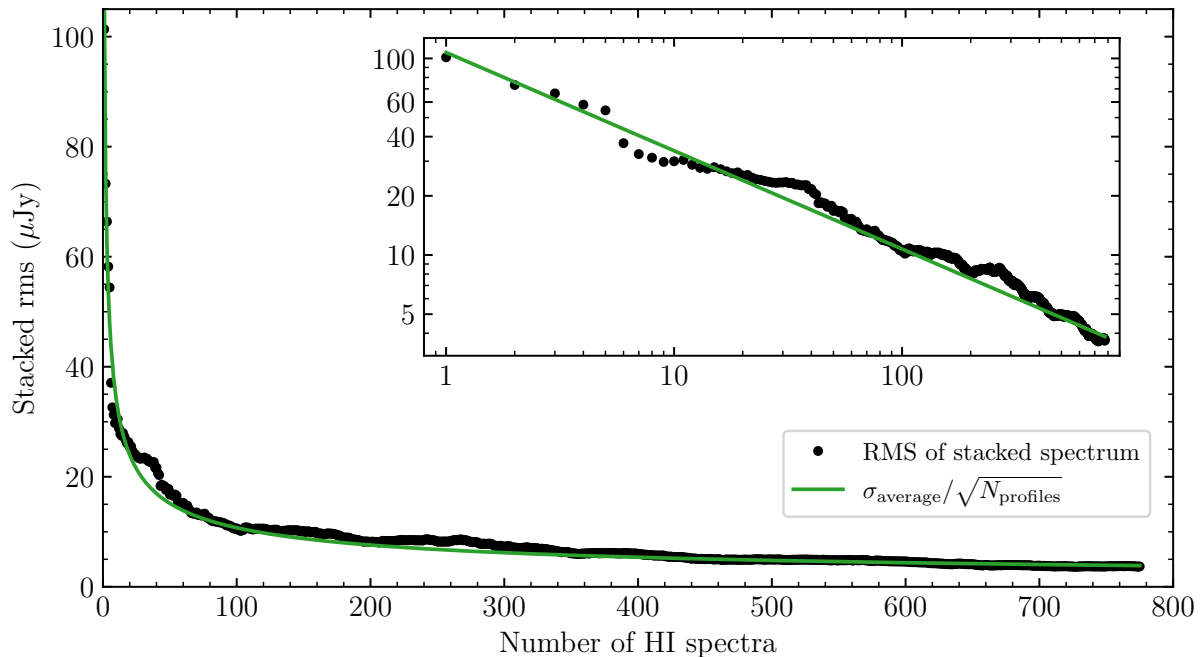


Figure 2.7: Stacked noise as a function of the number of input HI spectra. The black data points represent the measured noise in the stacked spectrum with N input spectra. The green line represents the theoretical change in the stacked noise for a Gaussian distribution, σ/\sqrt{N} where σ is the average noise of all the input spectra. The inset shows the same as the main figure, but in log-log format.

of \sqrt{N} , where N is the number of input spectra. This decrease in the average noise is a property of Gaussian noise. We test that the Coma spectra show the expected change in Gaussian noise by stacking all the HI non-detections in the sample. Figure 2.7 shows the average noise measured in the stacked spectrum as a function of the number of input spectra. The theoretical change in the noise (σ/\sqrt{N}) is indicated by the green line, where σ is the average noise of all the input spectra. It is evident from Figure 2.7 that the noise properties of the input spectra are Gaussian-like and enable the expected decrease in the noise of the stacked spectrum.

2.4 HI in Coma

2.4.1 HI – M_{\star} scaling relation

The stellar mass (M_{\star}) to HI gas fraction (f_{HI} , defined as the HI mass to stellar mass fraction) scaling relations (M_{\star} - f_{HI}) are well characterised for galaxies in the field (e.g. Fabello et al., 2011; Brown et al., 2015; Healy et al., 2019), and have also been used to study the deficiency of HI in galaxies in different density environments including the Virgo cluster (e.g. Cortese et al., 2011; Fabello et al., 2012). However, given the small number of direct HI detections in Coma, there has been no study of the M_{\star} - f_{HI} scaling relation as a method to probe the HI content of the cluster as a whole. In Figure 2.8, we present the M_{\star} - f_{HI} scaling relation for Coma.

We separated the galaxies into samples by stellar mass (indicated by the histogram in Figure 2.8) to probe the f_{HI} - M_{\star} scaling relation. Figure 2.8 shows the Coma direct HI detections in the blue distribution and the HI mass upper limits for the HI non-detections in grey down-pointing triangles. The HI mass upper limits are calculated using the noise from the individual spectra and an upper estimate on the W_{50} line width calculated using the r -band Tully Fisher relation from Ponomareva et al. (2018). The scatter in the distribution of upper limits can also be attributed to

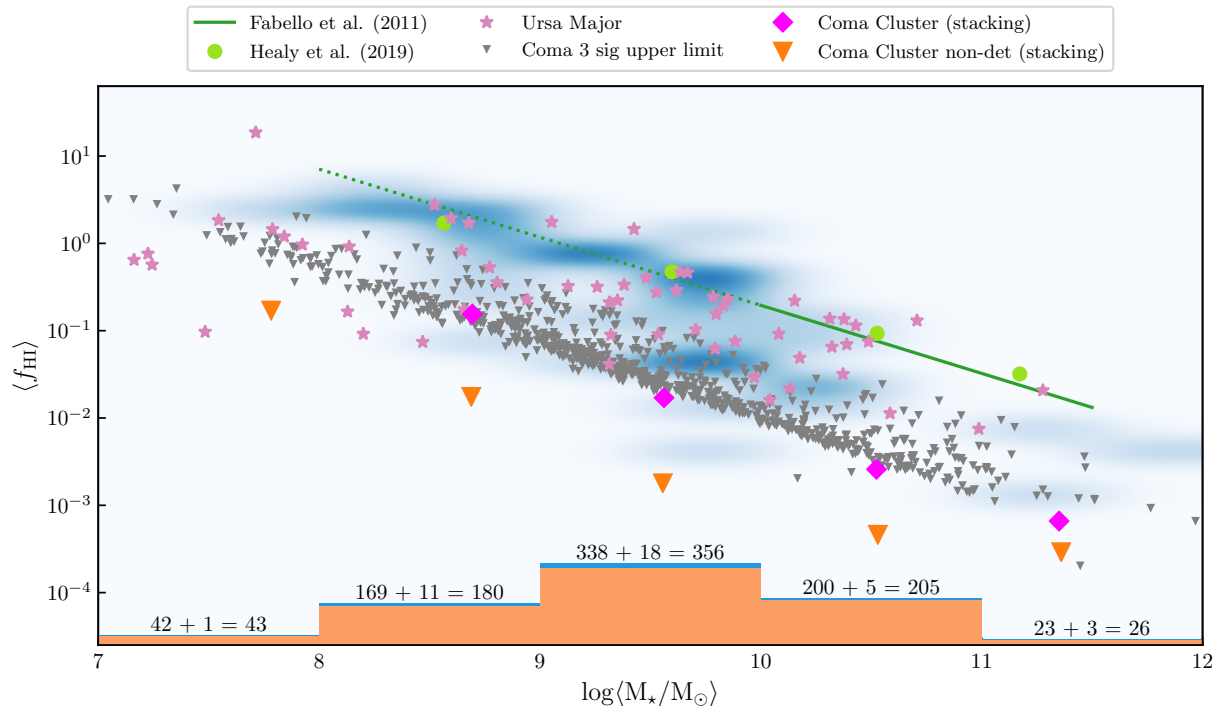


Figure 2.8: Stellar mass (M_*) to HI gas fraction (f_{HI}) scaling relation for the Coma cluster. The individual 3σ upper limits for the Coma HI non-detections are represented by the grey down-pointing triangles, while the distribution of the individual HI detections is shown by the blue density plot. The pink diamond and orange down-pointing triangle symbols represent the stacking of all Coma galaxies and only non-detections, respectively. The pink diamonds show measurements from a detected stacked spectrum, and the orange triangles indicate the 3σ upper limit in the case of a non-detection in the stacked spectrum. The round light green symbols and green line represent the stacking of field galaxies by Healy et al. (2019) and Fabello et al. (2011), respectively; the dashed green line is an extrapolation of the Fabello et al. (2011) results. The individual f_{HI} measurements (pink stars) for galaxies in the Ursa Major cluster are also shown for reference (Verheijen & Sancisi, 2001). Measurements obtained from stacking are presented in Table C.1.

the spread in the noise distribution of the WCS mosaic. Given the number of galaxies that are not detected in HI, we used the HI stacking technique to probe the HI content below the detection threshold.

Utilising the HI stacking technique, we were able to improve the sensitivity in the stacked spectrum by more than an order of magnitude relative to the individual spectra. By stacking HI spectra for the galaxies in each stellar mass bin in units of M_{HI}/M_* , we can determine the average f_{HI} for each sample. We stacked both detections and non-detections, as well as just non-detections. Despite the improved sensitivity of the stacked spectra, there are no detections in the stacked spectra corresponding to the sample with only non-detections; the stacked spectra for each stellar mass bin can be found in Figs. B.1 & B.2. The 3σ upper limits for the stacking results suggest that Coma galaxies on average have at least three orders of magnitude less gas than galaxies at the same stellar mass in the field (indicated by the round light green symbols (Healy et al., 2019) and the dark green line (Fabello et al., 2011)). In comparison, galaxies in Ursa Major cluster (indicated by the pink stars from Bilimogga et al. in prep) have just under an order of magnitude less gas than the field sample and an order of magnitude more than the results from stacking all Coma galaxies (magenta diamonds in Figure 2.8).

Figure 2.8 shows that there is a large spread in HI gas fraction (f_{HI}) values for the Coma galaxies, however looking at the average f_{HI} values for all galaxies in the cluster (the pink diamonds in Figure 2.8, which are measured from the stacked spectrum containing all individual detections

Table 2.1: Values used for a and b in Equation 2.5 for the different morphological types.

Sample	a	b	Reference
All/unknown morphology	7.12	0.88	Haynes & Giovanelli (1984, Table 5)
Early types/ellipticals/S0s	6.88	0.89	Haynes & Giovanelli (1984, Table 5)
Late types	7.51	0.73	Solanes et al. (1996, Table 2)
Irregulars	7.45	0.70	Boselli & Gavazzi (2009, Table 3)

and non-detections in the stellar mass bin), we note that on average, the Coma galaxies have f_{HI} values that are between one and two orders of magnitude lower in each stellar mass bin than the field relations and other individual measurements from less dense environments. However, while the $f_{\text{HI}}-M_*$ scaling relation compares the HI fraction of galaxies of similar stellar mass, galaxies of similar stellar mass but different morphology and size have different HI masses (Haynes & Giovanelli, 1984; Brown et al., 2015; Healy et al., 2019). Thus, it is necessary to use a probe of the HI content that takes morphology and size into account.

2.4.2 HI deficiencies

The HI deficiency parameter (DEF_{HI} , Haynes & Giovanelli, 1984) is a useful quantity to understand how deficient a galaxy (or sample of galaxies) is compared to a field galaxy of the same size and morphology. It is defined as

$$\text{DEF}_{\text{HI}} = \log(M_{\text{HI},\text{exp}}) - \log(M_{\text{HI},\text{obs}}), \quad (2.4)$$

where $M_{\text{HI},\text{exp}}$ is the expected HI mass, which is calculated using an optical–HI scaling relation that takes into account the morphology and size of the galaxy (Haynes & Giovanelli, 1984; Denes et al., 2014).

The expected HI mass ($M_{\text{HI},\text{exp}}$) is derived from a log linear empirical relation, which is calibrated using field galaxies with varying morphologies and sizes (Haynes & Giovanelli, 1984),

$$M_{\text{HI},\text{exp}} = a + b \log(hD_{25})^2 - 2 \log h, \quad (2.5)$$

where D_{25} is the diameter of the galaxy in the B-band at the 25th mag/arcsec², and a and b are empirical constants dependent on the morphology of the galaxy (T type). The quantity h is taken to be 0.7 from $H_0 = 70 \text{ km s}^{-1} \text{ Mpc}^{-1}$. While there have been updates to the scaling relations used to estimate the HI mass of galaxies without using T types (e.g. Denes et al., 2014; Dénes et al., 2016; Jones et al., 2018), the deficiencies presented in this work are calculated using T types.

The Coma galaxies have been separated into broad morphological bins: early-type galaxies, S0s, late-type galaxies, and irregular galaxies; galaxies for which we cannot reliably determine the classification are marked as unknown. The classifications were made by eye (by three adjudicators) using colour optical images from three different surveys (SDSS, PanSTARRS⁶, and DeCALs⁷) and g -band data observed using the Canada-France-Hawaii Telescope (Head et al., 2015). These classifications (where possible) have been cross-matched against the Galaxy Zoo database (Lintott et al., 2008, 2011) and the Third Reference Catalogue of Bright Galaxies (RC3; de Vaucouleurs et al., 1991) and are used to calculate the HI deficiency. The values used in Equation 2.5 for the different morphological types are given in Table 2.1.

We calculated individual measures of the HI deficiency for every galaxy. For the galaxies for which there is no direct HI detection, we used the 3σ upper limit of the measured HI mass. This

⁶Panoramic Survey Telescope and Rapid Response System (Chambers et al., 2016)

⁷The Dark Energy Camera Legacy Survey (Dey et al., 2019)

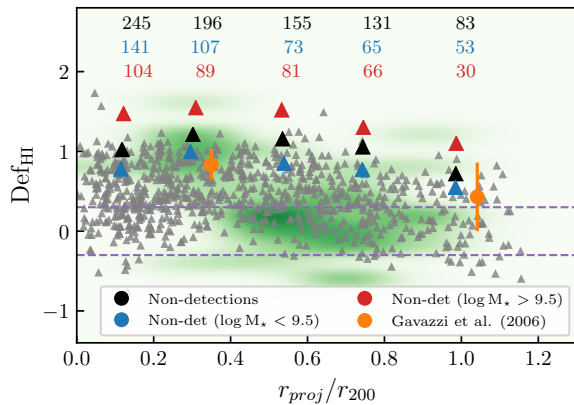


Figure 2.9: HI deficiency of the Coma galaxies as a function of projected radius from the cluster centre. The individual HI deficiency measurements for the Coma galaxies are represented by the green shaded distribution for the HI detections and grey triangles for the lower limits on the HI non-detections. The average HI deficiencies for late-type Coma galaxies from Gavazzi et al. (2006) are shown in orange. The black, blue, and red triangles represent the lower limits from stacking the non-detections in annuli in three samples: all non-detections, $\log M_\star < 9.5$, and $\log M_\star > 9.5$, respectively. The horizontal dashed purple lines set the limit on DEF_{HI} values that indicate a galaxy is HI-normal. Measurements obtained from the stacked profiles are presented in Table C.2.

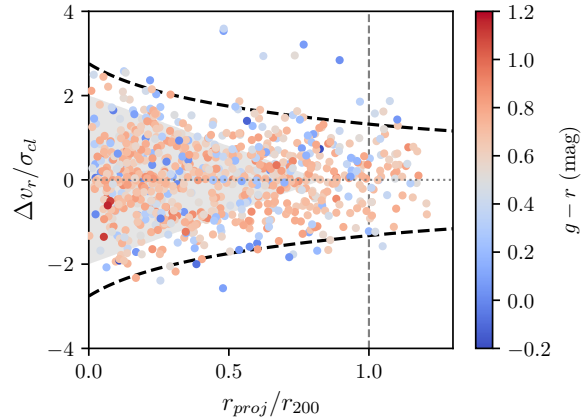


Figure 2.10: Phase-space diagram for Coma. The black dashed lines represent the escape velocity for Coma, calculated using a concentration index (c) of 5, $M_{200} = 5.1 \times 10^{14} M_\odot$ and $R_{200} = 1.8 \text{ Mpc}$ (Gavazzi et al., 2009). Galaxies inside the escape velocity ‘trumpet’ are considered to be within the cluster, while galaxies on the outside edge of the trumpet are considered to be falling into the cluster. The light grey shaded cone represents the virialised zone (Oman et al., 2013). The $g - r$ colour of each galaxy is given by the colour scale in colourbar.

means that the corresponding HI deficiency measurement is a lower limit and the deficiency value is expected to increase in the case of a better sensitivity spectrum.

Denes et al. (2014) used data from the HI Parkes All Sky Survey (HIPASS; Meyer et al., 2004) to map the global HI deficiency across the southern sky. They found that regions that contained an over-density of HI deficient galaxies correlated with known dense galaxy regions. The known galaxy clusters in the southern sky have an average HI deficiency that lies between $0.5 < \text{DEF}_{\text{HI}} < 2$. For the many Coma galaxies where there is no direct HI detection, we measured a lower limit on the HI deficiency. These lower limits for the DEF_{HI} of the Coma galaxies (grey triangles) are predominantly between $0.5 < \text{DEF}_{\text{HI}} < 2$, which indicates that Coma is at least as deficient as the clusters covered in the Denes et al. (2014) sample.

For a sample of 18 clusters, Solanes et al. (2001) studied the HI deficiency of spiral galaxies residing inside one Abell radius compared to those outside. They compare the fraction of HI deficient spirals against different cluster properties. Coma is consistent in the total number of spiral galaxies given its X-ray luminosity, however it is an outlier in the number of HI deficient spirals for its mass, Abell richness, and total number of spiral galaxies. Gavazzi et al. (2006) did a more detailed study on the radial pattern of HI deficiency across the Coma Supercluster. However, like Solanes et al. (2001), the Gavazzi et al. (2006) work only focusses on the late-type galaxies across the cluster.

In this work, we revisit the work by Gavazzi et al. (2006), however we focus on HI non-detections, which cover all galaxy morphologies across the cluster. To calculate the average DEF_{HI} for the HI non-detected galaxies, we used the HI stacking technique to stack the galaxies in annuli with in-

creasing radius from the cluster centre, scaling each input spectrum by the expected HI mass of the galaxy (see Fabello et al. (2011, Eqn. 3.5) for same technique but for HI gas fractions). While there are no clear detections in the stacked spectra (see Figs. B.3. B.4 & B.5), we push the lower limits higher than the individual spectra (see the black triangles in Figure 2.9). These results indicate that the HI content of the Coma galaxies is binary – we either detect HI or the galaxies contain on average at least $\sim 10 - 100$ times less HI than their field counterparts. This suggests an extremely fast and efficient quenching mechanism.

Oman & Hudson (2016) show using N-body simulations of clusters that the time for quenching low-mass galaxies is longer than that of high-mass galaxies. We thus separated the non-detections by stellar mass into a high stellar mass sample ($M_{\star} > 10^{9.5} M_{\odot}$, represented by the red symbols in Figure 2.9) and a low stellar mass sample ($M_{\star} < 10^{9.5} M_{\odot}$, represented by the blue symbols in Figure 2.9). We choose this stellar mass as it is the so-called “gas-richness” threshold (Kannappan et al., 2013): galaxies below this threshold are typically HI gas-rich, while galaxies above this threshold are typically HI gas-poor. For both subsamples, there are no detections in the stacked spectra at any radius. These results set lower limits on the average HI deficiencies for the low- and high-stellar mass populations and we are therefore unable to compare to radial trends in other clusters (e.g. Solanes et al., 2001; Gavazzi et al., 2006) or to quenching times for different mass samples (Oman & Hudson, 2016) with these data.

2.4.3 HI stacking in and around the cluster

In this section we explore the average HI content of the Coma galaxies. The focus is the total galaxy sample, including galaxies without direct detections. The direct HI detections are studied in detail in Molnar et al. (in prep). Figure 2.10 shows the line-of-sight velocity relative to the cluster ($\Delta v_r / \sigma_{cl}$; σ_{cl} is the cluster velocity dispersion, 1180 km s^{-1}) as a function of the projected radius from the centre of the cluster (r_{proj} / R_{200} , where $R_{200} = 1.8 \text{ Mpc}$ is the radius at $200 \rho_{crit}$; Gavazzi et al. 2009); the data points are coloured by their $g - r$ colour. The escape velocities for the cluster are determined using the prescription outlined in Jaffé et al. (2015) assuming a concentration index (c) of 5, and $M_{200} = 5.1 \times 10^{14} M_{\odot}$ (Gavazzi et al., 2009). We refer to Figure 2.10 as the phase-space diagram throughout this work.

We separate the Coma galaxies into four samples, by the regions in the phase-space diagram in Figure 2.10: 1) virialised cone; 2) inside R_{200} which includes all galaxies with $r_{proj} < R_{200}$ and within the escape velocity “trumpet”, but excludes the galaxies in the virialised cone; 3) outside trumpet, which includes all galaxies with $r_{proj} < R_{200}$, but line-of-sight velocities that place them outside of the escape velocity trumpet; and 4) outside R_{200} (all galaxies with $r_{proj} > R_{200}$). The four samples are further separated by $g - r$ colour. Galaxies with $g - r < 0.6$ are considered to be blue, and those with $g - r > 0.6$ are considered to be red. For Coma, $g - r = 0.6$ provides a good separation between the red sequence and the star-forming blue cloud. The stacked spectra for each sample (with direct HI detections excluded) are presented in Figure 2.11. It should be acknowledged that the four samples (virialised zone, inside R_{200} , outside trumpet, and outside R_{200}) contain interlopers due to projection effects especially along the line-of-sight velocity. These projection effects most likely affect the three samples contained within the R_{200} radius of the cluster.

In Figure 2.11 we compare the average HI content of the galaxies for which there are no direct HI detections for the three different regions of the cluster. We also separate the galaxies by colour; the resulting average spectra for the blue and red galaxies in each region are shown in the middle and bottom rows of Figure 2.11. The stacked spectra are smoothed after stacking to a velocity resolution of 40 km s^{-1} to improve the signal-to-noise ratio (S/N). We also stack the 25 reference spectra (see Section 2.3) using the same scheme as the target spectra. From the 25 stacked reference spectra, we create an average reference spectrum represented by the grey spectra in Figure 2.11.

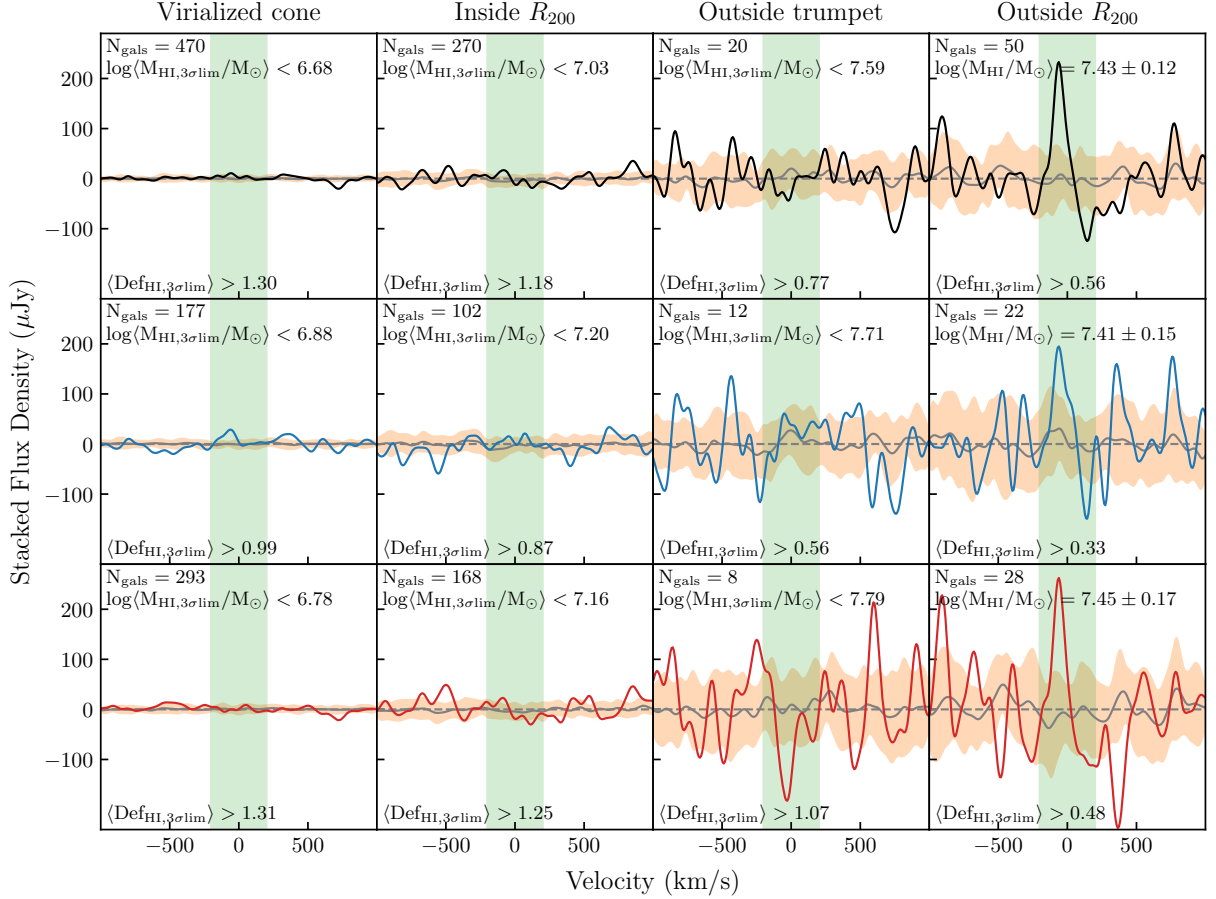


Figure 2.11: Stacked spectra for all (top row), blue (middle row), and red (bottom row) HI non-detections in different regions of the cluster. The average stacked spectrum in each panel is indicated by the solid black, blue, and red lines. The average stacked reference spectrum is represented by the solid grey line. The green band indicates the velocity range $cz \pm 200 \text{ km s}^{-1}$ over which HI emission is expected to be seen. Only the sample of galaxies outside the R_{200} (right-most column) of the cluster appear to contain detectable HI.

Also shown in Figure 2.11 is the variance of the 25 stacked reference spectra; this is represented by the orange band around the grey line. The comparison between the average and variance of the 25 reference spectra, where we do not expect to see a signal, and the stacked target spectrum provides confidence that any signal visible in the target spectrum is real. We consider stacked spectra with a signal in the region $v = 0 \pm 200 \text{ km s}^{-1}$ that has $S/N = 3.5$ to be marginally detected. We feel confident using a $S/N = 3.5$ since there is no corresponding signal in the reference spectrum.

Only the sample of galaxies outside R_{200} shows a possible detection in all three colour samples. Even though both the red and blue samples have roughly the same average HI mass ($\langle M_{\text{HI}} \rangle$), it should be noted that the lower limits on the average HI deficiency ($\langle \text{DEF}_{\text{HI}} \rangle$), which is shown in the bottom left corner of each panel, are different. Despite both the blue and red samples showing lower limits for the HI deficiency, the two samples have similar number of galaxies meaning that the stacked spectra have similar sensitivities making their limits comparable. The difference between the DEF_{HI} for the two samples is not unexpected as red galaxies are well known for being more gas poor than blue galaxies. Unlike what is found by Jaffé et al. (2016) for Abell 963, none of the samples show any possible detections within the R_{200} ; however these authors also do not detect a signal for their red galaxies outside the R_{200} , which we do.

Simulations have shown that quenching begins after some delay time once a galaxy has crossed

$2.5 v_{vir}$ (for reference, $R_{200} \sim 0.73 r_{vir}$, Oman & Hudson 2016) with higher-mass galaxies affected slightly more quickly than lower-mass galaxies (Oman & Hudson, 2016), however once quenching has begun, the time taken for the galaxies to transition from a field-like galaxy to one fully processed by the cluster is very short. Indeed, less than 10 of our galaxies outside R_{200} have measurable SFRs, and most of those are below the star-forming main sequence (see panel b of Figure 2.6 for galaxies with $7 < \log M_{\star}/M_{\odot} < 9.5$).

Gavazzi et al. (2006) show on average Coma galaxies at $r > 5$ Mpc, which is beyond $2 r_{vir}$, are HI normal. We have shown in the previous section, on average, that our Coma galaxies are (at a lower limit) at least 10–100 times more HI deficient than their field counterparts. If we assume that galaxies that are accreted onto the cluster are HI normal and on the star-forming main sequence when they cross $2.5 r_{vir}$, the processes driving the removal of HI in galaxies as they fall into the cluster must be very quick and have a strong influence beyond r_{vir} . In Section 2.6.4 we also compare the average HI content between the Coma galaxies in groups or substructure to those that are not associated with any groups.

2.5 Finding substructure in Coma

Substructure, defined as structure kinematically distinct from the parent halo, is a natural consequence of a hierarchical universe (Hou et al., 2012). As discussed in the introduction, there are many different methods that can identify substructure within a galaxy cluster (e.g. Dressler, 1980; Neumann et al., 2003; Adami et al., 2005; Jaffé et al., 2013). We are interested in how the average HI gas content may change in groups or substructure with different morphologies or possible infall times across the cluster.

To identify these groups/substructure, we chose to use the DS test to identify groups that are kinematically distinct from the cluster. Dressler & Shectman (1988b) applied their test for kinematic deviations to look for substructure in a number of Abell clusters (including Coma). Their conclusion regarding Coma was that there was no substructure within the cluster. Since Dressler (1980), there have been many targeted and blind spectroscopic surveys of the Coma cluster and subsequent studies of Coma have found significant substructure (e.g. Colless & Dunn, 1996; Adami et al., 2005). To detect substructure, one needs ~ 1000 redshifts in a ~ 1 Mpc region (Adami et al., 2005). We apply the DS test, given by

$$\delta_i^2 = \left(\frac{N_{nn} + 1}{\sigma_{cl}^2} \right) [(\bar{v}_{local}^i - \bar{v}_{cl})^2 + (\sigma_{local}^2 - \sigma_{cl}^2)], \quad (2.6)$$

to our redshift catalogue. We used nearest neighbour (N_{nn}) values in increments of 5 from 5 to 30 with a velocity dispersion (σ_{cl}) of 1180 km s^{-1} and a cluster velocity (\bar{v}_{cl}) of 6925 km s^{-1} . Figure A.2 shows the results of the DS Test for $N_{nn} = 25$. Using similar plots for all the N_{nn} values, and two independent judges, we identified groups where there are large overlapping circles (which represent large δ_i values) of similar colour representing similar velocity values. Using the $N_{nn} = 25$ as a reference, galaxies were assigned to groups using a combination of the different N_{nn} runs.

Within the WCS HI data footprint, we find 15 distinct groups. These groups stand out across the six iterations of the DS test, and are highlighted by the different colours in Figure 2.12. The properties of the 15 groups are given in Table 2.2. Despite the difference in the method of identifying substructure, we find some overlap between our groups and those identified by Adami et al. (2005), who use a hierarchical clustering algorithm (see Serna & Gerbal, 1996) which uses a measure of the binding energy to find groups of galaxies that are bound in substructure. Of the 17 groups Adami et al. (2005) found, 14 are within the WCS footprint and seven correspond to groups that we found using the DS Test. The groups overlapping between our work and Adami et al. (2005) are S1, S2, S6, and S11 (combined into one group at the core of the cluster), S8, S9, and S15.

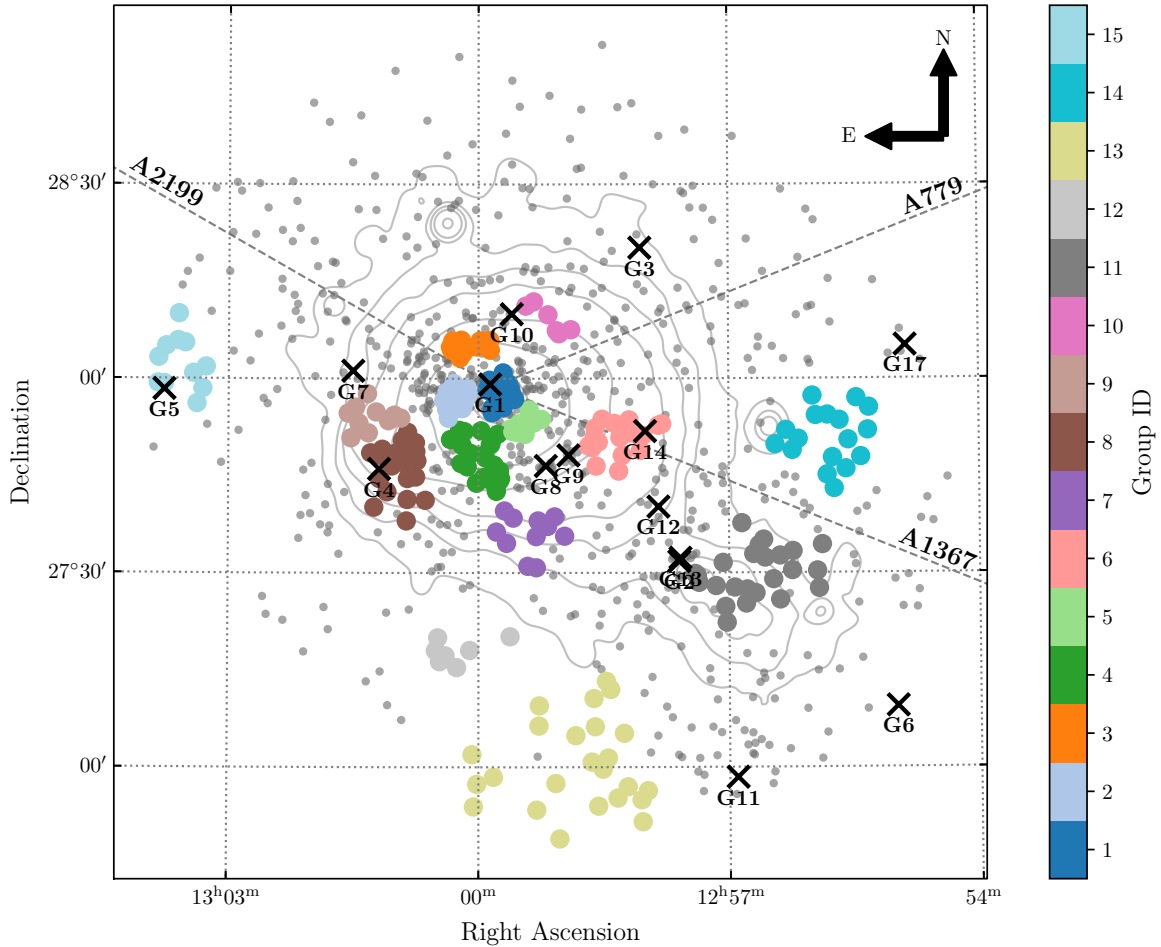


Figure 2.12: Substructure in the WCS footprint. The 15 identified groups are shown in different colours. The background grey contours represent the X-ray emission measured by ROSAT in 0.4 – 2.4 keV. The dashed grey lines indicate the direction to nearby clusters connected to Coma. The groups identified by Adami et al. (2005) are labelled and denoted by black crosses.

2.6 Identified substructures

2.6.1 Core substructures

In the core of the cluster (see Figure 2.12), we identified two groups (groups S1 and S2) around the two cD galaxies (NGC 4874 and NGC 4889) and another two groups surrounding the two central groups: S3 and S5. There is much discussion in the literature surrounding the centre of the Coma cluster. A commonly accepted scenario is that the two cD galaxies eventually merge (e.g. Colless & Dunn, 1996; Adami et al., 2005).

Using the hierarchical clustering method developed by Serna & Gerbal (1996) to identify substructure, Adami et al. (2005) found one group (G1) in the central region of the cluster. These authors later note that with X-ray analysis there are two distinct peaks in the X-ray corresponding to the two galaxies. They postulate that these two groups are in the process of colliding: S1, the larger of the two groups with 27 members, has a mean velocity of 7699 km s^{-1} , and S2 (with 18 members) has a mean velocity of 6113 km s^{-1} . Both the groups have velocity dispersions that are of the order of $\sim 900 \text{ km s}^{-1}$ (see Table 2.2 for more details).

Table 2.2: Details of the 15 groups found within the Coma cluster using the DS test.

Group ID	Members ^a	$\langle v \rangle$ (km s ⁻¹)	σ_{group} (km s ⁻¹)	E:S0:L:I:U ^b	$\log(M_{HI}/M_{\odot})^c$ (M _⊙)	$\log(M_{*}/M_{\odot})$ (M _⊙)	$\langle \text{DEF}_{HI} \rangle^d$	NGC members
S1	27	7699	924	8:10:0:5:4	< 7.20	10.84	> 0.24	NGC4874
S2	18	6113	932	6:6:0:5:1	< 7.43	10.80	> 0.52	NGC4889, NGC4894
S3	14	7626	358	7:3:0:4:0	< 7.34	9.87	> 0.19	
S4	22	7981	899	6:7:1:5:3	< 7.28	10.40	> 0.61	
S5	10	5868	843	5:5:0:0:0	< 7.54	10.25	> 1.09	NGC4869
S6	17	6095	884	9:7:0:1:0	< 7.39	9.82	> 1.09	
S7	11 (2)	6137	1031	4:3:2:2:0	7.35 ± 0.11	9.83	> 0.92	
S8	22 (1)	7386	1238	11:5:1:3:2	7.77 ± 0.03	10.15	> 0.85	NGC4919, NGC4911
S9	11 (1)	6498	942	7:3:1:0:0	8.22 ± 0.02	10.64	1.15 ± 0.07	NGC4923, NGC4921
S10	6 (1)	8355	895	1:4:1:0:0	< 7.71	10.62	0.83 ± 0.04	NGC4860, NGC4858
S11	24	7621	462	12:6:0:2:4	< 7.36	10.52	> 0.64	NGC4839
S12	7	7584	460	4:1:0:2:0	< 7.69	9.68	> 0.76	
S13	24 (3)	7351	691	13:5:1:5:0	8.09 ± 0.03	10.30	0.74 ± 0.07	NGC4859, NGC4892
S14	17	6898	522	10:7:0:0:0	< 7.59	10.25	> 0.97	
S15	11	6436	603	7:3:1:0:0	< 7.93	10.22	> 0.68	NGC4943, NGC4934

^aNumbers in brackets are the number of individual direct detections in the group.

^bNumber of elliptical or early-type galaxies (E), S0/lenticulars (S0), late-types (L), irregular galaxies (I), and galaxies of unknown morphology (U).

^cAverage M_{HI} obtained from stacking, where there is no detection in the stacked spectrum, a 3σ upper limit is used.

^dAverage DEF_{HI} obtained from stacking, where there is no detection in the stacked spectrum, a 3σ lower limit is used.

Located immediately north of S1 and S2 (see Figure 2.13), S3 contains 14 members. The smallest group containing only six galaxies, S5 is located to the south-west of S1. Both the S3 and S5 groups are dominated by early-type and S0 galaxies. None of these groups (S1, S2, S3, or S5) show a detection of HI in their stacked spectra (see Figure B.6), however given the gas removal processes at play in cluster centres, this is unsurprising. The measured upper limits on the HI mass and lower limits on the HI deficiency for the groups can be found in Table 2.2, and the corresponding stacked spectra in Appendix B.

2.6.2 Groups coincident with excess X-ray emission

South-west structure

Using X-ray observations by XMM-Newton, Neumann et al. (2003) studied the dynamical structure within Coma. They fit an elliptical beta model to the X-ray emission where any residuals from this fit may indicate structure within the cluster. Fig. 2 in Neumann et al. (2003) shows that there is X-ray emission not explained by the beta model. Neumann et al. (2003) also found a number of bright galaxies coincident with the peaks in this excess emission. Adami et al. (2005) compared the groups that they found to the excess X-ray emission maps from Neumann et al. (2003), and found a number of overlaps. We used the excess X-ray contours from Adami et al. (2005, Fig. 4) to compare to the location of our groups. Figure 2.13 shows the isocontours residual X-ray emission along with the location of our groups. Figure 2.13 shows that groups S4, S6, S8, S9, and S11 are coincident with X-ray emission, while S10 is slightly offset from the X-ray emission.

Of the groups we identified that are coincident with X-ray emission, S11 is perhaps the most well studied (e.g. Burns et al., 1994; Colless & Dunn, 1996; Neumann et al., 2001; Beijersbergen, 2003; Akamatsu et al., 2013; Lyskova et al., 2019). The S11 group is located to the south-west of the cluster core and is home to NGC 4839. Previously, Beijersbergen (2003) found a group of 18 galaxies within 0.15° of NGC 4839, and using data from their blind WSRT HI survey of the cluster,

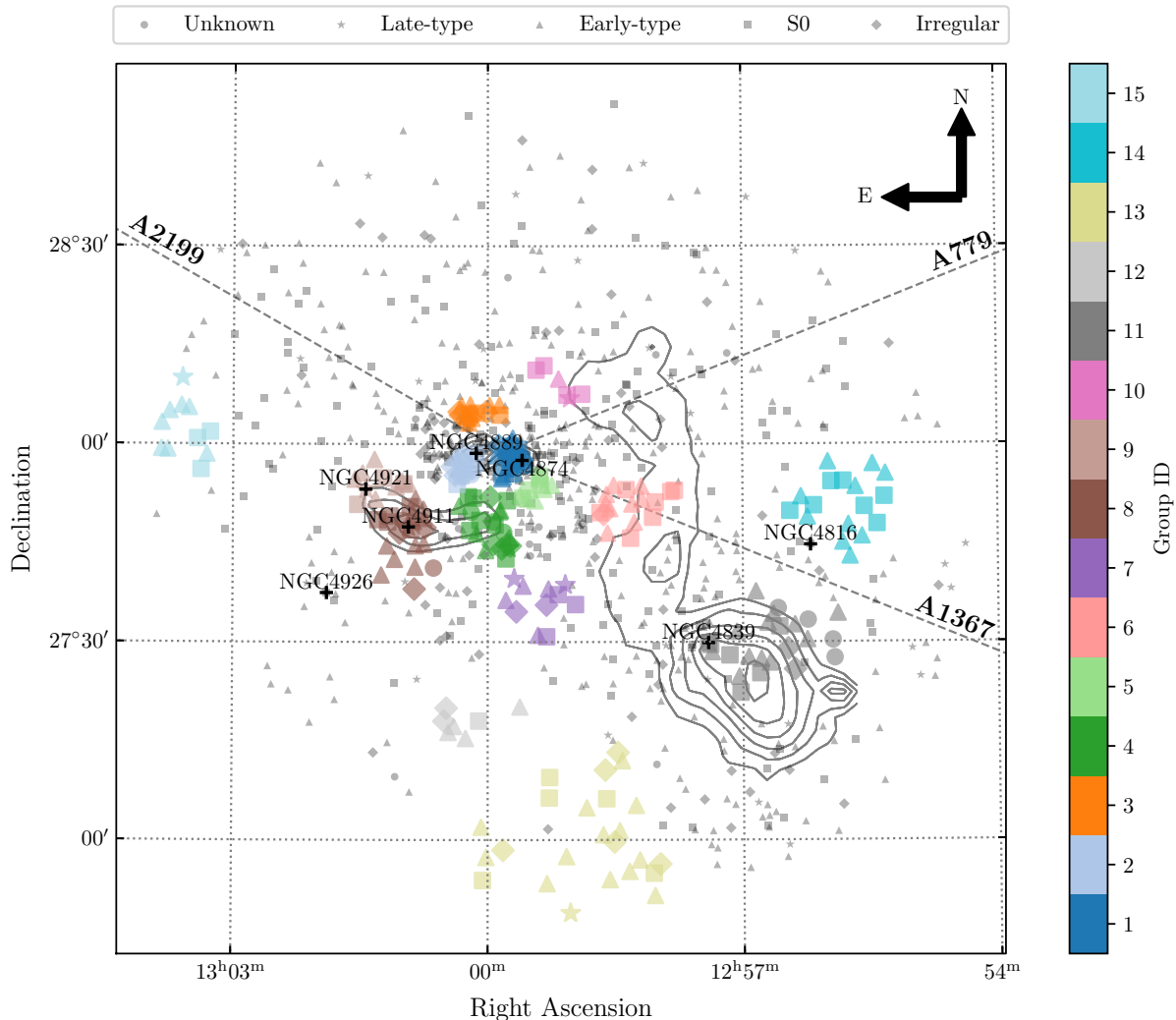


Figure 2.13: Fifteen identified groups within the WCS footprint. The contours (taken from Adami et al. (2005, Fig. 4)) represent the X-ray excess found by Neumann et al. (2003).

calculated for the group, an average H I mass (M_{HI}) 3σ upper limit to be $\langle M_{\text{HI}} \rangle < 7.55 \times 10^8 M_{\odot}$. Within the same radius, we found 26 galaxies, however using the DS test we found 36 galaxies associated with this group. Our average 3σ mass limit is $\langle M_{\text{HI}} \rangle < 2.29 \times 10^7 M_{\odot}$. Many groups have studied this collection of galaxies in an effort to understand if it is still on first infall (e.g. Colless & Dunn, 1996; Neumann et al., 2001; Akamatsu et al., 2013), or has already passed through the centre of the cluster (e.g. Burns et al., 1994; Lyskova et al., 2019).

Lyskova et al. (2019) show using smooth particle hydrodynamical simulations that a post-merger scenario, in which the group has already passed around the centre of the cluster, explains the observed X-ray emission better than the pre-merger scenario where this group is on first infall. In the post-merger scenario, Lyskova et al. (2019) postulate that S11 entered the cluster from a filament on the north-east side of the cluster. Malavasi et al. (2020) use the DisPerSE algorithm to identify filaments connecting to Coma, and while they identify three such filaments (including one joining to the north-east of the cluster), they do not identify the filament known as the “Great Wall” to the south-west of Coma, which connects the cluster to Abell 1367. It is the “Great wall” filament that S11 is thought to be accreted from (Colless & Dunn, 1996; Akamatsu et al., 2013). From our results, we cannot conclude whether these groups are on first infall, or have already passed through the cluster. However, our results indicate that this group is extremely H I deficient and contains an

evolved population of galaxies; this supports the post-merger scenario, but also the first infall scenario under the assumption that this group has been pre-processed. Recent work by Salerno et al. (2020) has shown that filaments can be very effective at quenching star formation. Nevertheless, the question whether the NGC 4839 (S11) group is on first infall or has already passed through the cluster, remains open.

South-eastern structure

Neumann et al. (2003) identified X-ray substructure to the south-east of the core of the cluster (see S4, S8, and S9 in Figure 2.13). Neumann et al. (2003) attributed this X-ray over-density to emission from the intra-group medium of one group of galaxies containing NGC 4911 and NGC 4921. They attributed the bending in the structure due to projection effects by assuming that the direction of the structure motion is to the east with NGC 4921 at the head. They also concluded that NGC 4911 and NGC 4921 are gravitationally bound because they have similar velocities. We do not find these two galaxies to be part of the same group, which can largely be attributed to the differences in their velocities ($\sim 2000 \text{ km s}^{-1}$). The velocity we used for NGC 4926 is taken from SDSS DR13. The SDSS DR13 measurement is in good agreement with other optical and HI redshift measurements of this galaxy (e.g. Dressler & Shectman, 1988a; de Vaucouleurs et al., 1991; Zabludoff et al., 1993; Haynes et al., 1997; Bravo-Alfaro et al., 2000), including the HI measurement from the WCS. Adami et al. (2005) also found NGC 4911 and NGC 4926 to be part of different groups and note that the velocity quoted by Neumann et al. (2003) is incorrect.

We identified three groups (S4, S8, and S9) coincident with this X-ray substructure; S8 and S9 have been previously identified by Adami et al. (2005) as G4 and G7, respectively. The S8 group contains NGC 4911, which appears to be spatially coincident with the peak of the X-ray emission (Neumann et al., 2003; Adami et al., 2005). If the X-ray is associated with these groups, the fact that it is still detectable implies that the groups have not yet passed through the cluster (Adami et al., 2005). However the X-ray emission shows no sign of shock heated gas, which is a signature of radial infall, thus Adami et al. (2005) argued that it is more likely that these groups are on a spiral infall trajectory. Of the three groups, S4 and S8 have mean velocities that are higher than the cluster velocity; S4 and S8 also contain a number of late-type and irregular galaxies (in addition to the E and S0 galaxies), whereas S9 is dominated by early-type galaxies (E or S0) and has only one late-type galaxy (see Table 2.2). Both S4 and S8 are on average extremely HI deficient ($\langle \text{DEF}_{\text{HI}3\sigma \text{ lim}} \rangle > 0.6$, see Table 2.2), thus it is possible that the galaxies have been stripped of their HI, a process that can occur extremely rapidly after crossing into the cluster ($\sim 2.5 r_{\text{vir}}$), but the presence of the bluer galaxies may indicate that they have yet to transition across the ‘green valley’ (Oman & Hudson, 2016). Dominated by an older population of galaxies, S9 has a mean velocity of 6498 km s^{-1} , which is similar to that cluster velocity and could indicate that it is moving in the plane of the sky. The presence of one HI detection in this group would suggest that it could also be a recent infall, however given the difference in mean velocities from S4 and S8, it is unlikely to have followed the same trajectory.

Western filament

The last major X-ray residual is the western filament which is aligned north-south, extending roughly a megaparsec north from NGC 4839. Neumann et al. (2003) discussed possible origins of this structure: the change in X-ray temperature between the western filament and the centre of the cluster suggests that it could be due to heating from compression or shock waves during the infall of a structure onto the core of the cluster. They also discussed the possibility that the two X-ray maxima in the filament are due to a galaxy group that was broken up on infall; they discount the possibility of two groups falling in to the cluster at the same time. However, Neumann et al. (2003) did not find any galaxy over-densities associated with the filament.

Adami et al. (2005) found two groups coincident with the western filament: G12 and G14 (see Figure 2.12). We also found two groups coincident with the filament: S6 and S10 (see Figure 2.13). Located about half way up the filament, S6 is coincident with G14 found by Adami et al. (2005). Our other group that is coincident with the filament, S10, is located at the northern most part of the structure.

Both S6 and S10 lie on lines that connect Coma to other clusters: S6 on the line connecting to Abell 1367, and S10 on the line connecting to Abell 779 (see Figure 2.13). Both of these groups are dominated by early-type and S0 galaxies, however, S10 contains one direct HI detection that dominates the stacked spectrum (see Figure B.6). The S10 group has a higher average velocity ($cz = 8355 \text{ km s}^{-1}$) than Coma which could indicate that it is falling in from the filament connected to Abell 779. The average velocity of S6 is similar to Coma, which like S9, could either indicate that the group is moving slowly or in the plane of the sky.

2.6.3 Groups near the outskirts

There are four groups that can be considered on the outskirts: S12, S13, S14, and S15. Of these four groups, only S15 had been previously identified by Adami et al. (2005) as G5. Adami et al. (2005) identified five other groups on the outskirts of the cluster that we do not identify in this work. It should be noted that two of those groups are outside our HI dataset and the other two are on the edge. Despite using a galaxy catalogue that covered a larger area than our HI dataset, we only identified groups for which we had HI data. The one group contained within our HI dataset by Adami et al. (2005) that we did not find, G11, is located around $\alpha = 12^{\text{h}}57^{\text{m}} \delta = 27^{\circ}00'$. It is clear from Figure A.2, which shows the results of the DS test, that there are no overlapping large circles of similar colour. Given that our redshift catalogue has more redshifts than Adami et al. (2005), in particular in that region owing to our observing campaign with WIYN (see Section 2.2.1.2), it is possible that with the smaller number of redshifts, G11 was artificially highlighted.

The S13 group has a diverse population of galaxies and contains the highest number of direct HI detections, while the other three groups (S12, S14, and S15) are dominated by older early-type or S0 galaxies with no direct HI detections. Both S14 and S15 lie on lines to other clusters (Abell 2199 and Abell 1367, respectively) and have similar velocities to the cluster indicating slow movement or a velocity vector in the plane of the sky. If S14 is being accreted onto Coma, then the average HI deficiency of the group and the evolved galaxy morphologies could indicate that this group underwent advanced evolutionary processes prior to being accreted. The high average velocity of S13 ($cz = 7351 \text{ km s}^{-1}$) could indicate that it is falling into Coma from the foreground, this is supported by the fact that this group is not in line with any of the known filaments connecting to Coma. Given that S13 also contains so many direct detections, this also may suggest that it is being accreted from a low-density environment.

2.6.4 HI in substructure versus the cluster

We explore the HI content of the Coma galaxies in substructure compared to Coma galaxies not in substructure. We separate the Coma galaxies into 0.4 Mpc annuli increasing from the cluster centre. The 15 substructures are also separated into the different annuli: S1-S5 (0 – 0.4 Mpc), S6-S11 (0.4 – 0.8 Mpc), and S12-S15 (> 1.2 Mpc). Figure 2.14 shows the stacked spectra for galaxies in groups in the different annuli (top row) as well as galaxies not in groups (bottom row). There are no possible detections in any of the stacked spectra in Figure 2.14 with the exception of the galaxies with $r > 1.2 \text{ Mpc}$. This is perhaps not surprising as we did not take into account the velocity of the galaxies when separating them into the different annuli. It is possible that there are infalling galaxies in the two innermost annuli; however, this inner region is typically dominated by the oldest

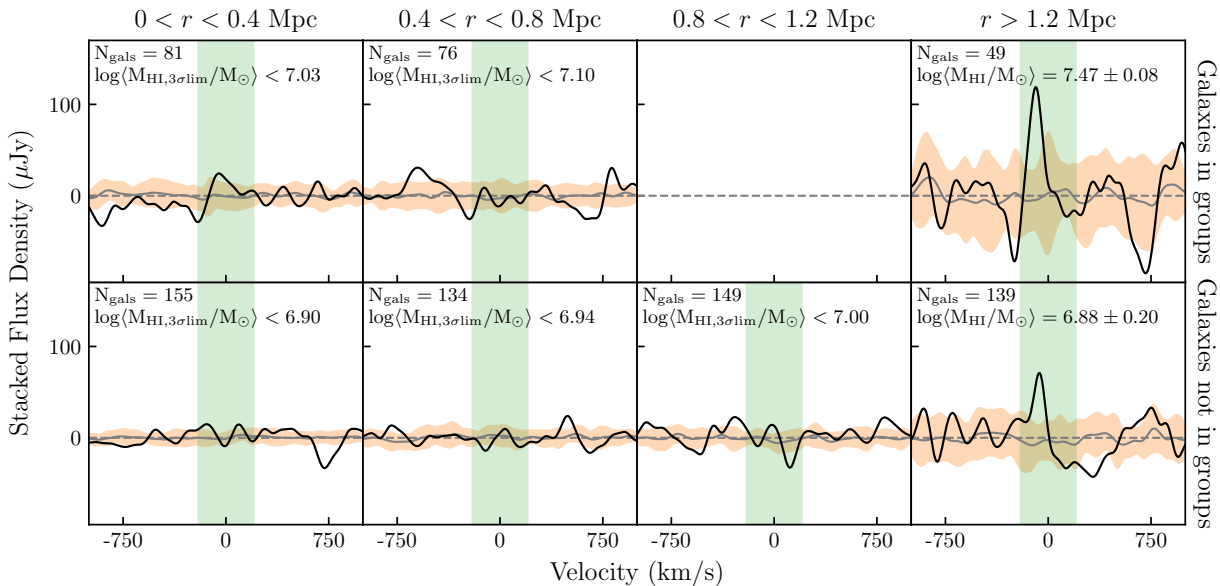


Figure 2.14: Stacked spectra for galaxies in groups (top row), and galaxies not in groups (bottom row) separated into different annuli from the cluster centre. The average stacked spectrum in each panel is indicated by a solid black line. The average stacked reference spectrum is represented by a solid grey line, with the variance of 25 stacked reference spectra surrounding the average reference spectrum in orange. The green band is the velocity range $cz \pm 200 \text{ km s}^{-1}$ over which the HI emission is expected to be seen.

members of the cluster.

In order to explore the difference in HI content between galaxies not associated with any substructure and those that reside in substructure in the different regions of the cluster, we separated the two groups of galaxies into three bins loosely based on the regions of the phase-space diagram (Figure 2.10). The galaxies and substructures that reside predominantly in the virialised cone are assigned to the ‘virialised bin’; galaxies/substructures inside R_{200} are assigned to the ‘inside cluster’ bin, and the remaining galaxies/substructures, which predominantly have $r_{\text{proj}} > R_{200}$, are assigned to the ‘recent infalls’. The resulting stacked profiles for the six samples are presented in Figure 2.15. The top panel of Figure 2.15 shows the stacked spectra from the galaxies in substructure and the bottom panel shows the stacked spectra from the galaxies not associated with any substructure. As with all the previous stacking, we only examine the galaxies for which there are no direct HI detections.

We note detections in the stacked spectra for the ‘recent infalls’ samples, both for galaxies in groups and galaxies not associated with any substructure (right-most panels of Figure 2.15). It is not unexpected that only the ‘recent infalls’ show detections in the stacked spectrum. The average HI deficiency measurement for each sample is given in the bottom left corner of each panel in Figure 2.15. It is interesting to note that while the two samples (galaxies within substructure and galaxies not in substructure) have similar average HI masses, they differ in average HI deficiencies. Galaxies in groups have a lower limit on the average HI deficiency of $\langle \text{DEF}_{\text{HI},3\sigma_{\text{lim}}} \rangle > 0.99$, while the non-group galaxies have an average HI deficiency of $\langle \text{DEF}_{\text{HI}} \rangle = 1.06 \pm 0.56$. The galaxy size, stellar mass, and colour distribution for both samples is similar, and while the $\langle \text{DEF}_{\text{HI}} \rangle$ measurements indicate that both samples are HI deficient, the fact that we can only measure a lower limit on the average HI deficiency for the group galaxies suggests that they are more deficient than the non-group galaxies for which we can measure an average HI deficiency. This could indicate that the gas removal process is more efficient for the group galaxies.

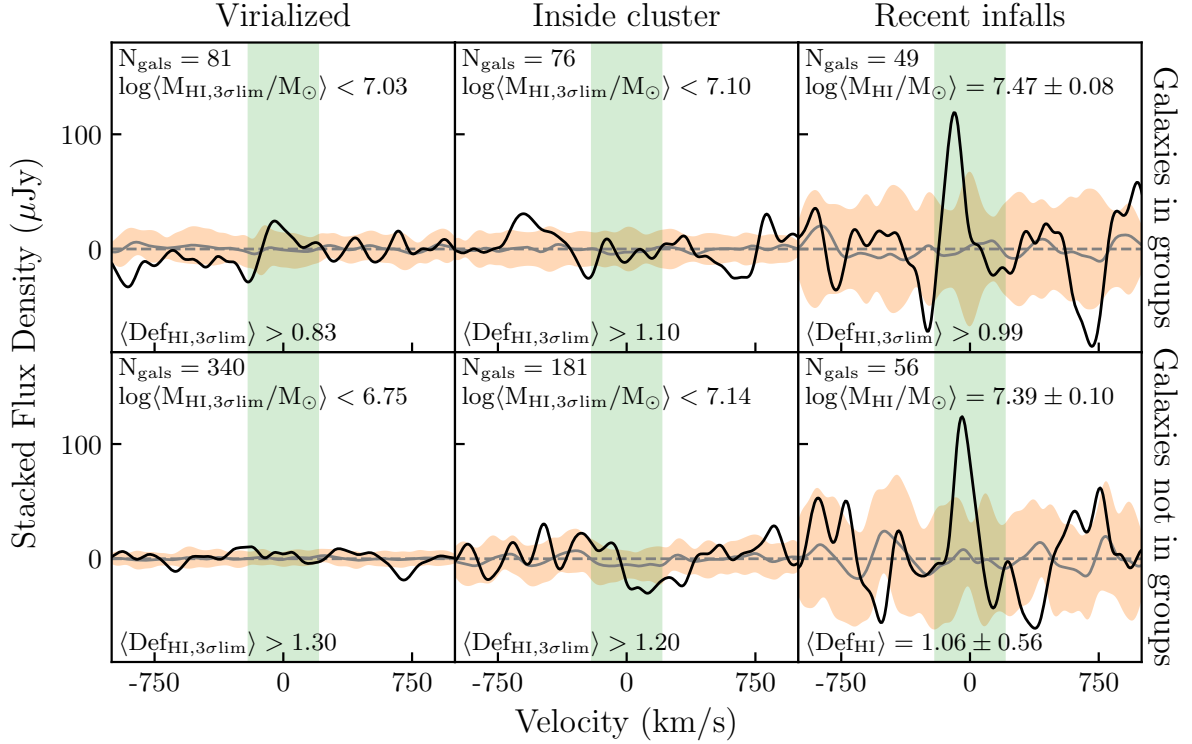


Figure 2.15: Stacked spectra for galaxies in groups (top row), and galaxies not in groups (bottom row) separated into different regions in the cluster. The average stacked spectrum in each panel is indicated by a solid black line. The average stacked reference spectrum is represented by a solid grey line, with the variance of 25 stacked reference spectra surrounding the average reference spectrum in orange. The green band is the velocity range $cz \pm 200 \text{ km s}^{-1}$ over which the H I emission is expected to be seen.

2.7 Summary

In this work we have aimed to study the average H I content and morphologies of galaxies in the substructure of the Coma cluster. We collated a large catalogue of redshifts for the Coma cluster, including 59 new redshifts that we observed with the multi-object spectrometer, Hydra, at WIYN. Using the newly compiled catalogue, we applied the DS test to find substructure within the cluster. Fifteen substructures were found, of which three had not been previously identified.

The WCS provided high-resolution and high-sensitivity H I data that covered both the cluster core and the NGC 4839 group to the south-west. However, with only 39 direct H I detections out of the 850 galaxies that lie within the WCS footprint, we needed an alternate method to study the H I content of the galaxies in the different groups. The H I stacking technique enabled us to probe the average H I content of samples of galaxies.

Using the H I stacking technique, we are able to probe ~ 1 – 2 orders of magnitude lower in H I mass. Despite this improvement in sensitivity, for many of the stacked samples there is no detection in the stacked spectrum. The H I gas fraction to stellar mass relation as well as a study of H I deficiency indicates that Coma galaxies are at least 50 times more H I deficient than their field counterparts. The binary nature of the H I content, where galaxies either have detectable H I content or contain orders of magnitude less H I than expected, supports the theories that favour extremely rapid quenching and gas removal mechanisms.

Given the effectiveness of gas removal processes increases closer to the centre of the cluster,

we expect to see the average HI content increase with distance from the cluster centre. For most samples of galaxies inside the cluster R_{200} , there is no HI detectable in the stacked spectra, however we do detect HI in both blue and red galaxies outside the R_{200} . When we separate the outer galaxies into those that are in groups versus those not in groups, both samples show detections in the ‘recent infall’ galaxies (see Figure 2.15). The average HI masses for the two samples are similar, however we note that there is no detection in the stacked spectrum from which to measure the average HI deficiency for the group galaxies, while there is a measurement of the average HI deficiency for the non-group galaxies, this suggests that the group galaxies are more HI deficient.

Acknowledgements

We thank the anonymous referee for their comments that have improved this work. This project has received funding from the European Research Council (ERC) under the European Union’s Horizon 2020 research and innovation programme (grant agreement no. 679627; project name FORNAX). JH acknowledges research funding from the South African Radio Astronomy Observatory. We thank R Healy for useful comments that improved the readability. Based on observations at Kitt Peak National Observatory, National Optical Astronomy Observatory (NOAO Prop. ID: 2017A-0356; PI: J. Healy), which is operated by the Association of Universities for Research in Astronomy (AURA) under a cooperative agreement with the National Science Foundation. JMvdH acknowledges support from the European Research Council under the European Union’s Seventh Framework Programme (FP/2007-2013)/ERC Grant Agreement no. 291531 (HIStoryNU). MV acknowledges support by the Netherlands Foundation for Scientific Research (NWO) through VICI grant 016.130.338.

Funding for the Sloan Digital Sky Survey IV has been provided by the Alfred P. Sloan Foundation, the U.S. Department of Energy Office of Science, and the Participating Institutions. SDSS acknowledges support and resources from the Center for High-Performance Computing at the University of Utah. The SDSS web site is www.sdss.org.

SDSS is managed by the Astrophysical Research Consortium for the Participating Institutions of the SDSS Collaboration including the Brazilian Participation Group, the Carnegie Institution for Science, Carnegie Mellon University, the Chilean Participation Group, the French Participation Group, Harvard-Smithsonian Center for Astrophysics, Instituto de Astrofísica de Canarias, The Johns Hopkins University, Kavli Institute for the Physics and Mathematics of the Universe (IPMU) / University of Tokyo, the Korean Participation Group, Lawrence Berkeley National Laboratory, Leibniz Institut für Astrophysik Potsdam (AIP), Max-Planck-Institut für Astronomie (MPIA Heidelberg), Max-Planck-Institut für Astrophysik (MPA Garching), Max-Planck-Institut für Extraterrestrische Physik (MPE), National Astronomical Observatories of China, New Mexico State University, New York University, University of Notre Dame, Observatório Nacional / MCTI, The Ohio State University, Pennsylvania State University, Shanghai Astronomical Observatory, United Kingdom Participation Group, Universidad Nacional Autónoma de México, University of Arizona, University of Colorado Boulder, University of Oxford, University of Portsmouth, University of Utah, University of Virginia, University of Washington, University of Wisconsin, Vanderbilt University, and Yale University.

This publication makes use of data products from the Wide-field Infrared Survey Explorer, which is a joint project of the University of California, Los Angeles, and the Jet Propulsion Laboratory/-California Institute of Technology, funded by the National Aeronautics and Space Administration.

A Miscellaneous figures and tables

Table A.1: Number of redshifts obtained from the different literature sources discussed in Section 2.2.1.1.

Redshift source	Number of redshifts
Alabi et al. (2018)	14
Albaret et al. (2017) (SDSS DR13)	773
Biviano et al. (1996)	5
Bravo-Alfaro et al. (2000)	1
Caldwell et al. (1993)	1
Castander et al. (2001)	1
Chiboucas et al. (2010)	38
Chiboucas et al. (2011)	10
Colless & Dunn (1996)	5
Cortese et al. (2003)	2
Davies et al. (1987)	1
Edwards & Fadda (2011)	5
Falco et al. (1999)	2
Gregory & Tifft (1976)	2
Gu et al. (2017)	1
Harrison et al. (2010)	3
Haynes et al. (1997)	1
Huchra et al. (2012)	5
Jangren et al. (2005)	1
Jørgensen et al. (1995)	1
Kadowaki et al. (2017)	2
Karachentsev & Kopylov (1990)	1
Kourkchi et al. (2012)	18
Lucey et al. (1991)	2
Mobasher et al. (2001)	84
Rines et al. (2001)	3
Serra et al. (in prep)	4
Smith et al. (2009)	1
This work	59
Wegner et al. (1990)	1
van Haarlem (in prep.)	49

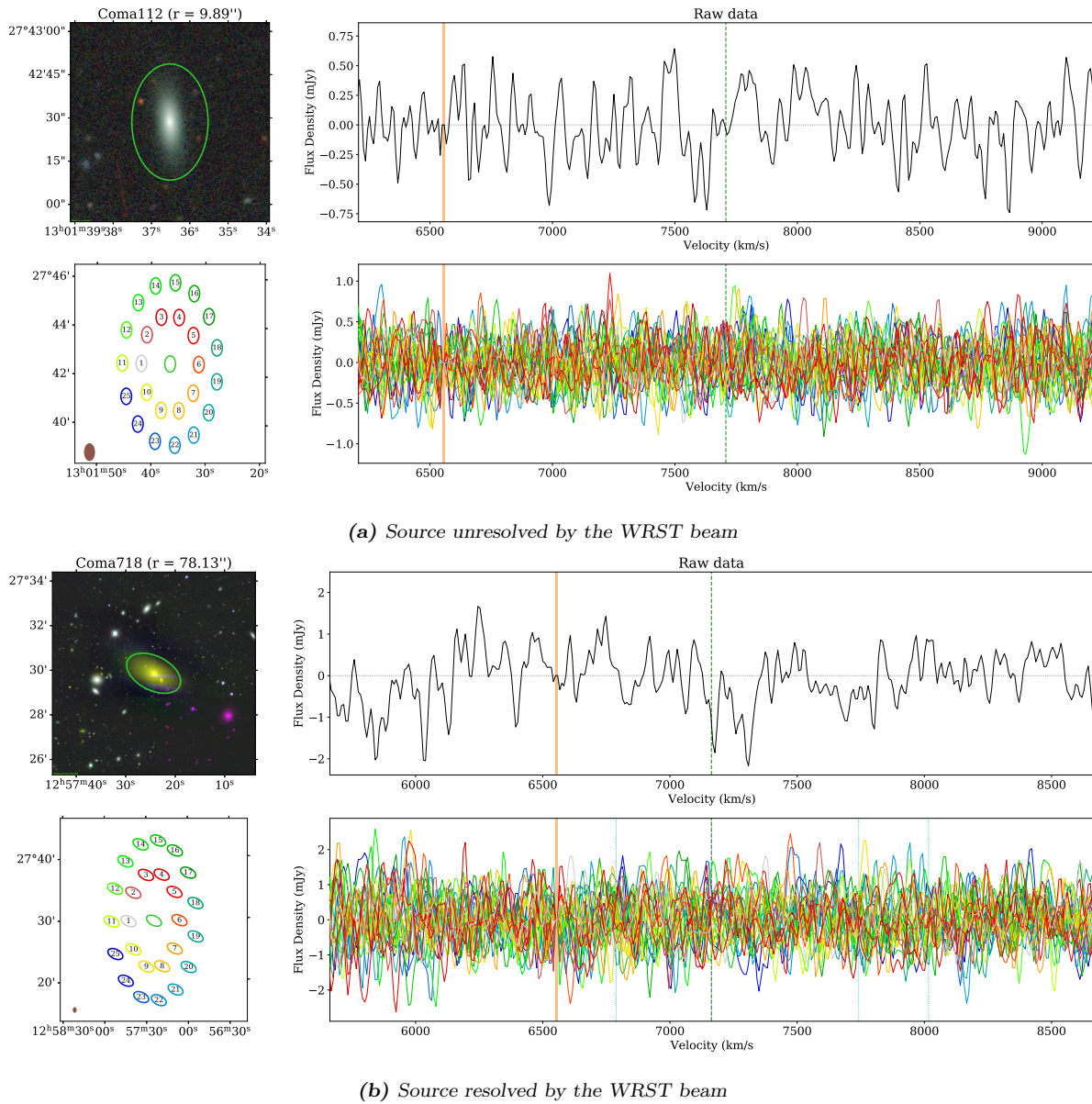


Figure A.1: Method used to extract the 1D HI spectra is presented in the figures above. Figure A.1a presents a galaxy that is unresolved by the WRST beam, and Figure A.1b a galaxy that is resolved by the beam. A colour cut-out of the galaxy with the extraction aperture overlaid in green is shown in the top left panel. The bottom left panel shows the location of the 25 reference spectra relative to the target spectrum. The middle top panel shows the target spectrum, and the middle bottom panel shows the 25 reference spectra. In both middle panels, the vertical dashed green line indicates the redshift of the target galaxy; the orange band represents the gap between the two frequency bands.

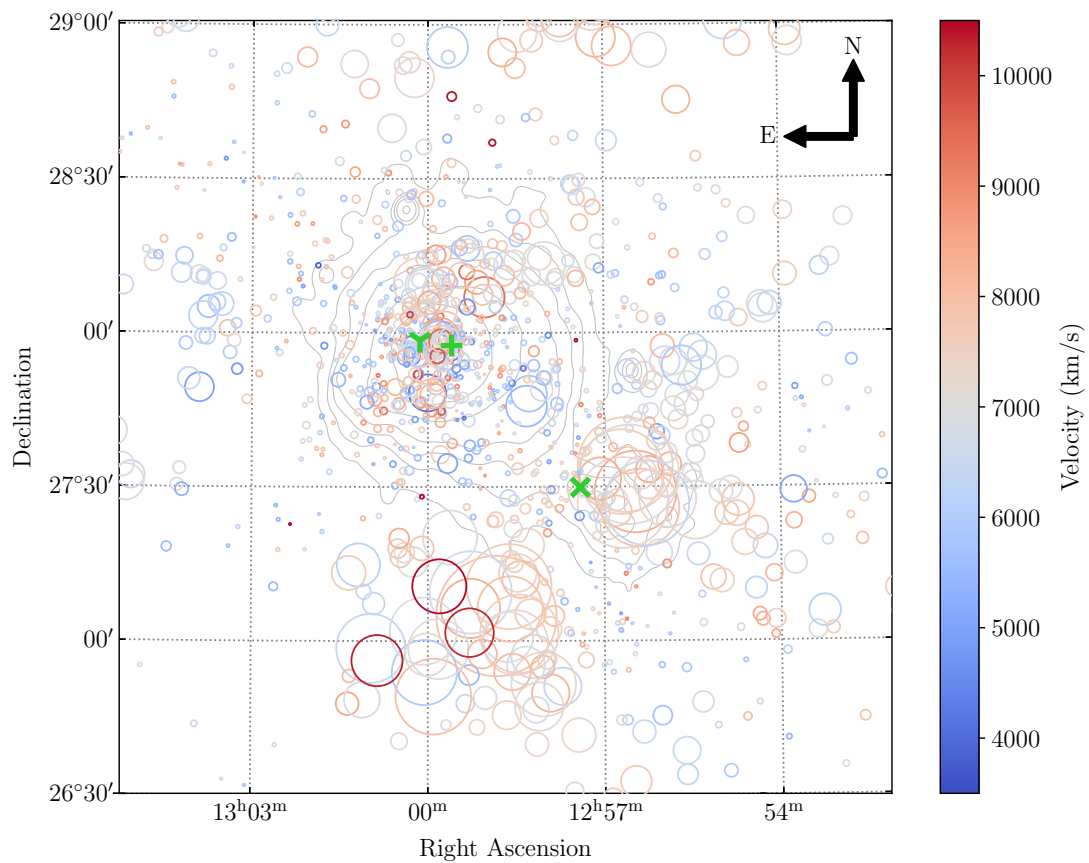


Figure A.2: Bubble plot showing the results of the DS test for the Coma cluster. The δ values are a result of using the 25 nearest neighbours. The red and blue colours indicate the recessional velocity (cz) of each galaxy. The green markers represent the three cD galaxies in Coma (+-NGC 4874, γ -NGC 4889 and \times -NGC 4839). The background grey contours represent the X-ray emission measured by ROSAT in 0.4 – 2.4 keV.

B Stacked spectra

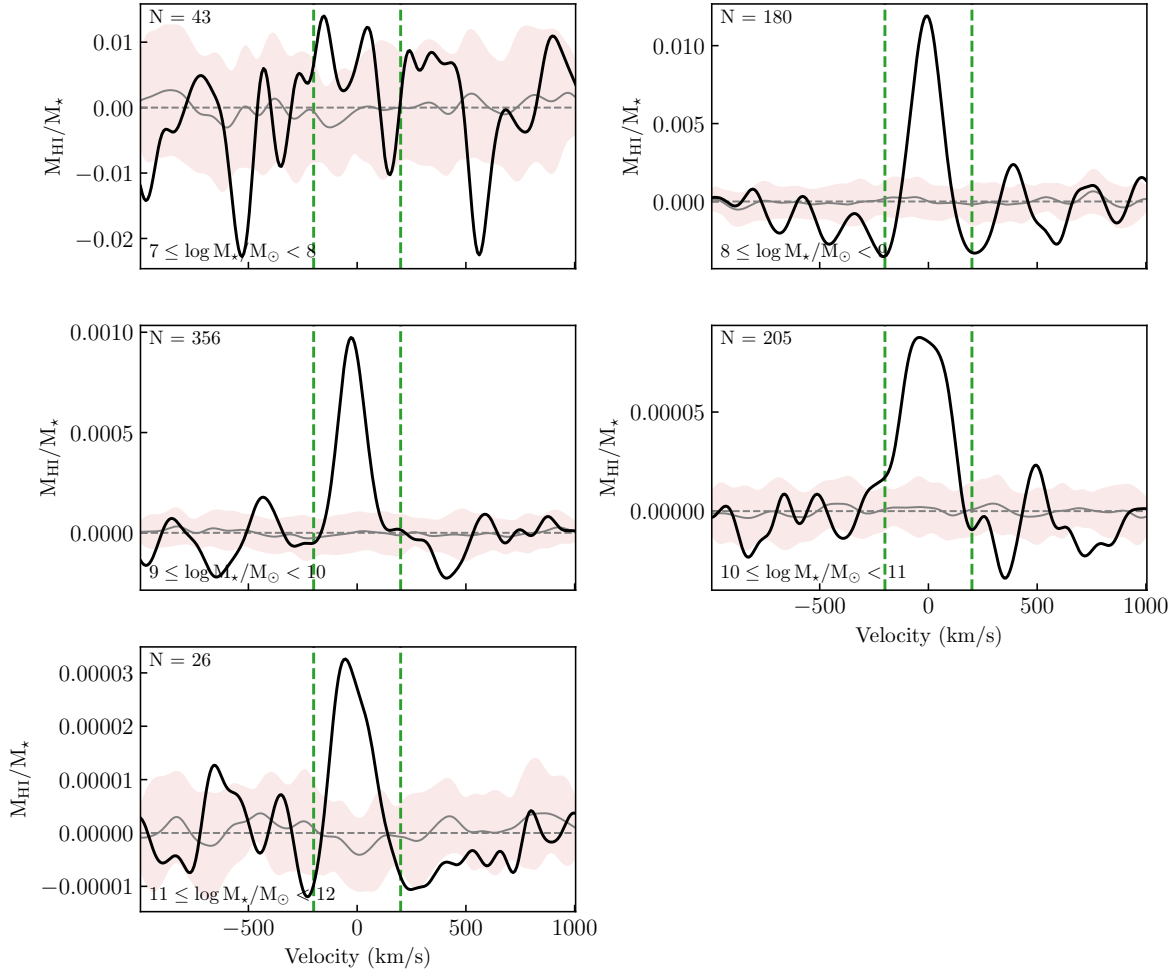


Figure B.1: Stacked spectra from which the full catalogue data points in Figure 2.8 are measured. The stacked spectra (the black line) have been smoothed to a velocity resolution of 80 km s^{-1} . The orange band represents the 1σ distribution from 25 stacked reference spectra. The vertical dashed green lines indicate the range over which the spectra are integrated to determine the average integrated flux density for each sample. Each panel represents a different stellar mass bin. The number of spectra in each bin are given in the top left corner of each panel.

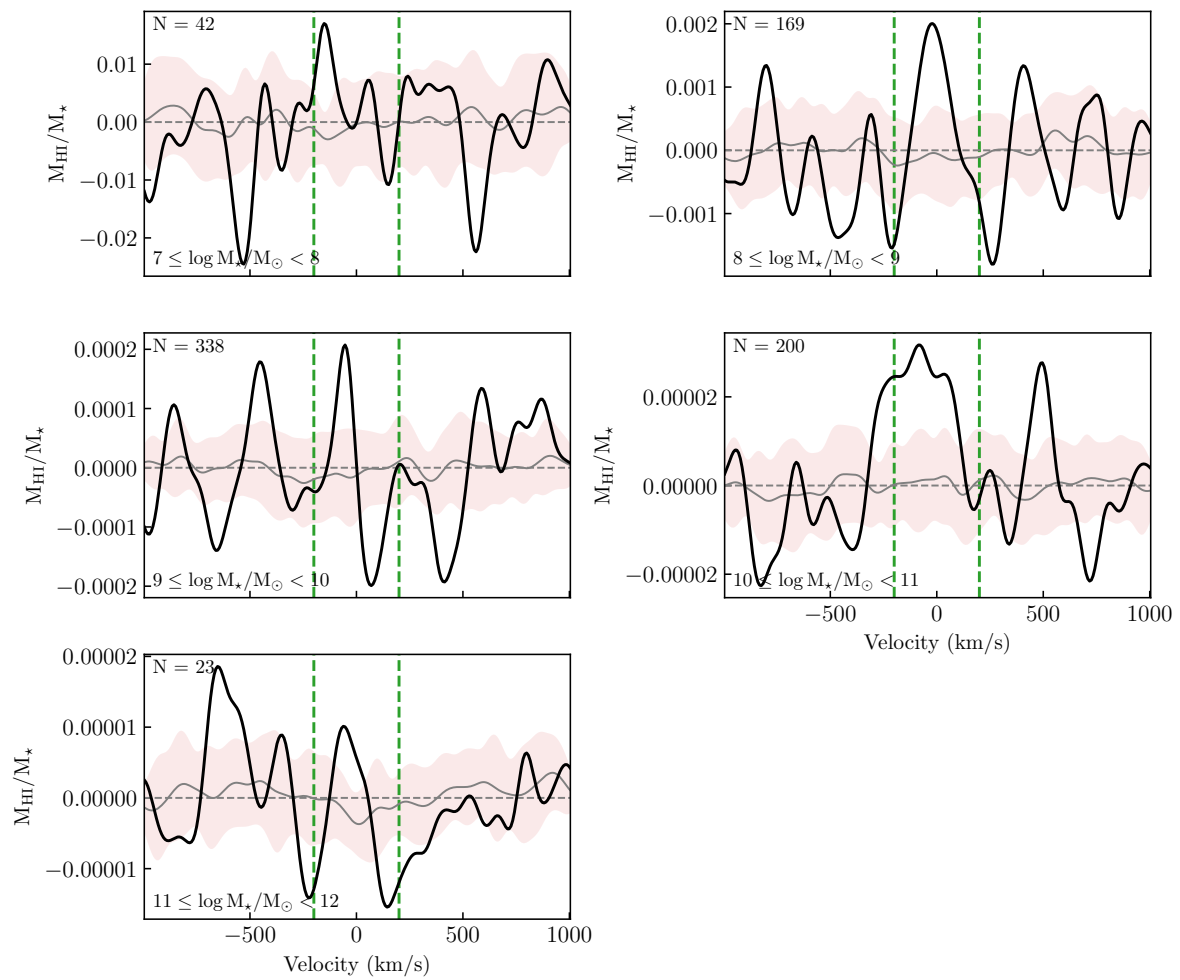


Figure B.2: Same as Figure B.1, for the sample of H I non-detections.

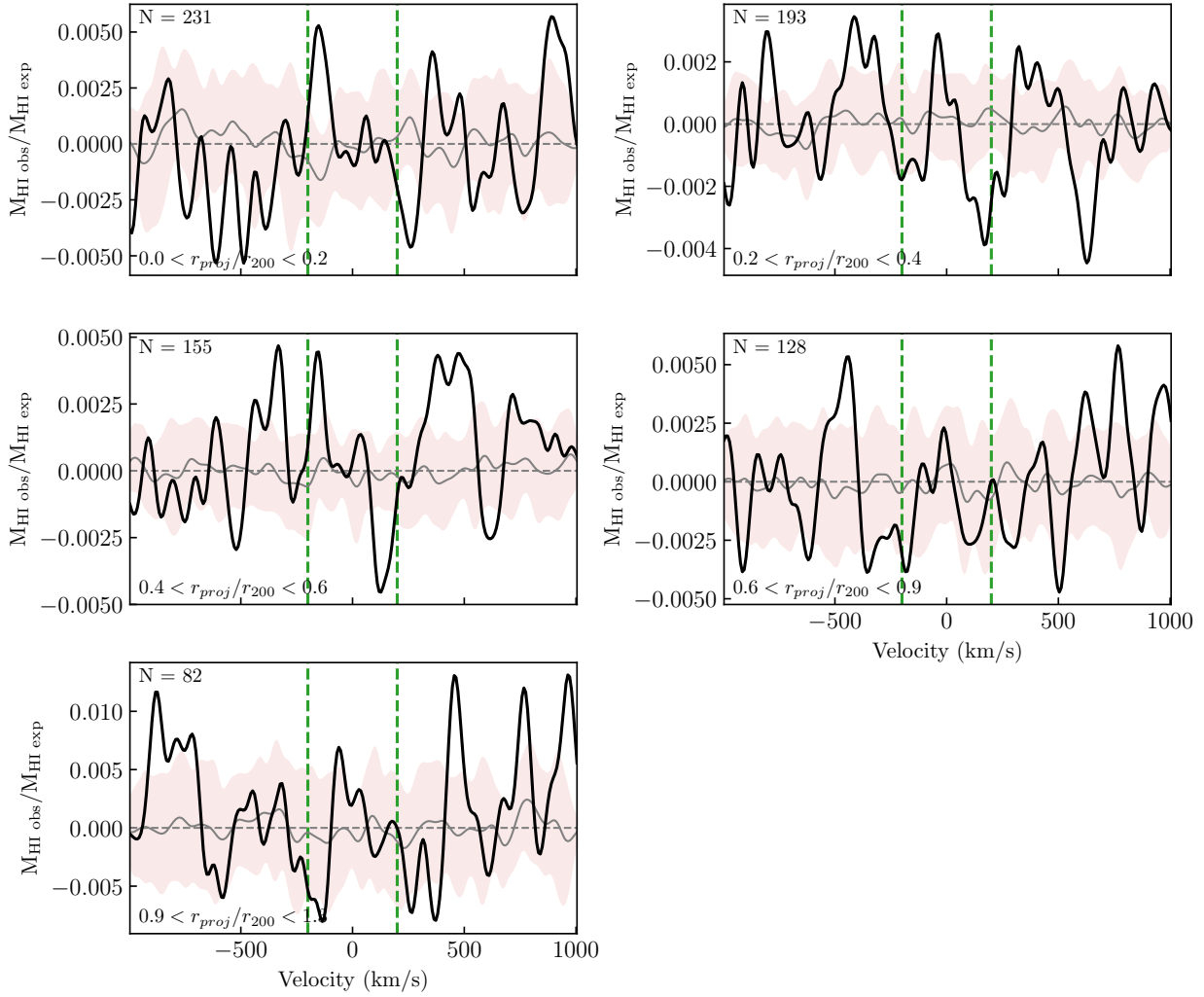


Figure B.3: Coma non-detections stacked in annuli with increasing radius from the cluster centre. The stacked spectra (the black line) have been smoothed to a velocity resolution of 80 km s^{-1} . The orange band represents the 1σ distribution from 25 stacked reference spectra. The vertical dashed green lines indicate the range over which the spectra are integrated to determine the average integrated flux density for each sample. Each panel represents a different stellar mass bin. The number of spectra in each bin are given in the top left corner of each panel. These spectra are used to determine the average DEF_{HI} ($\text{DEF}_{\text{HI}} = \log M_{\text{HI exp}} - \log M_{\text{HI obs}}$) in Figure 2.9.

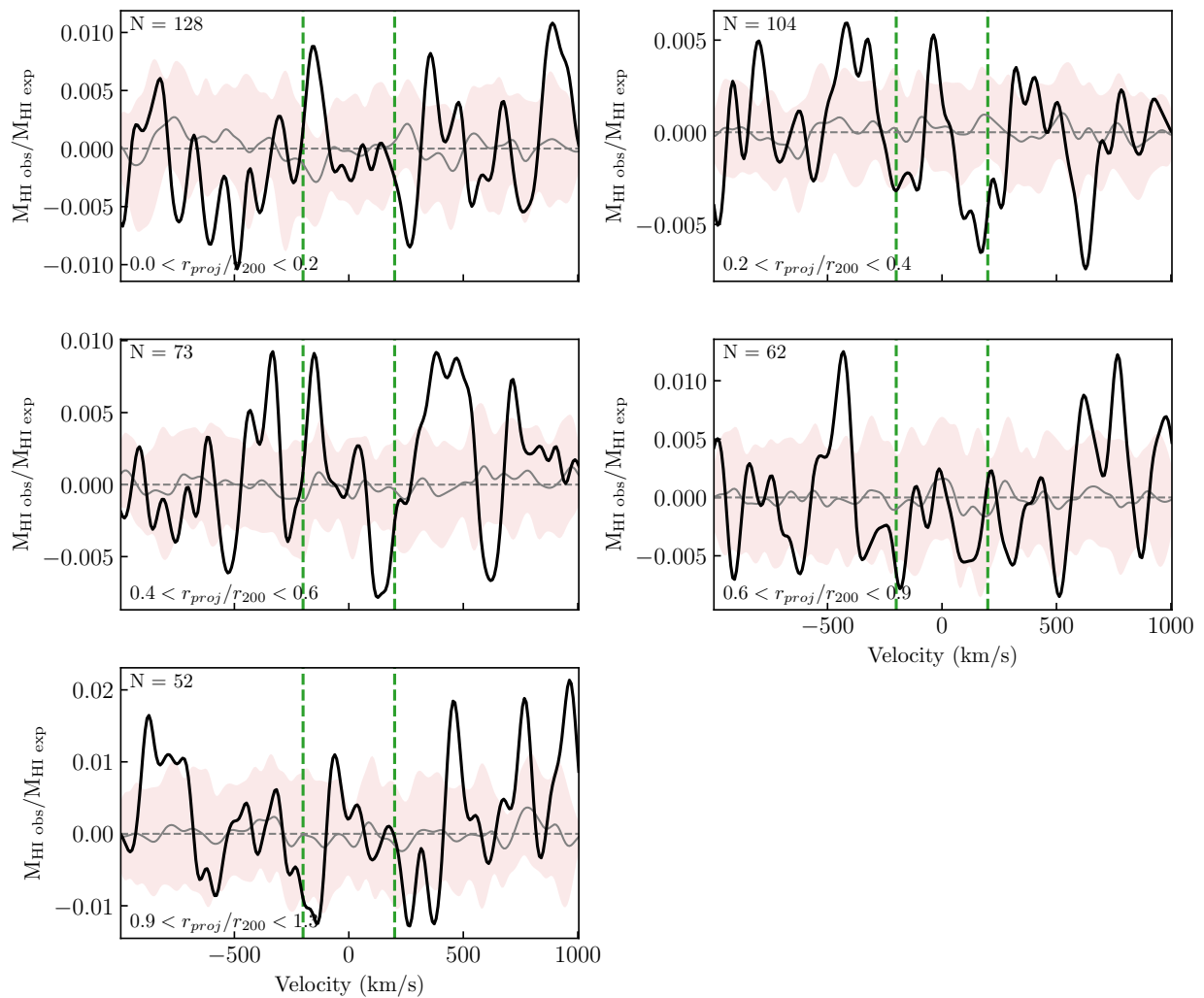


Figure B.4: Same as Figure B.3 for the sample of galaxies with $\log M_\star < 9.5$.

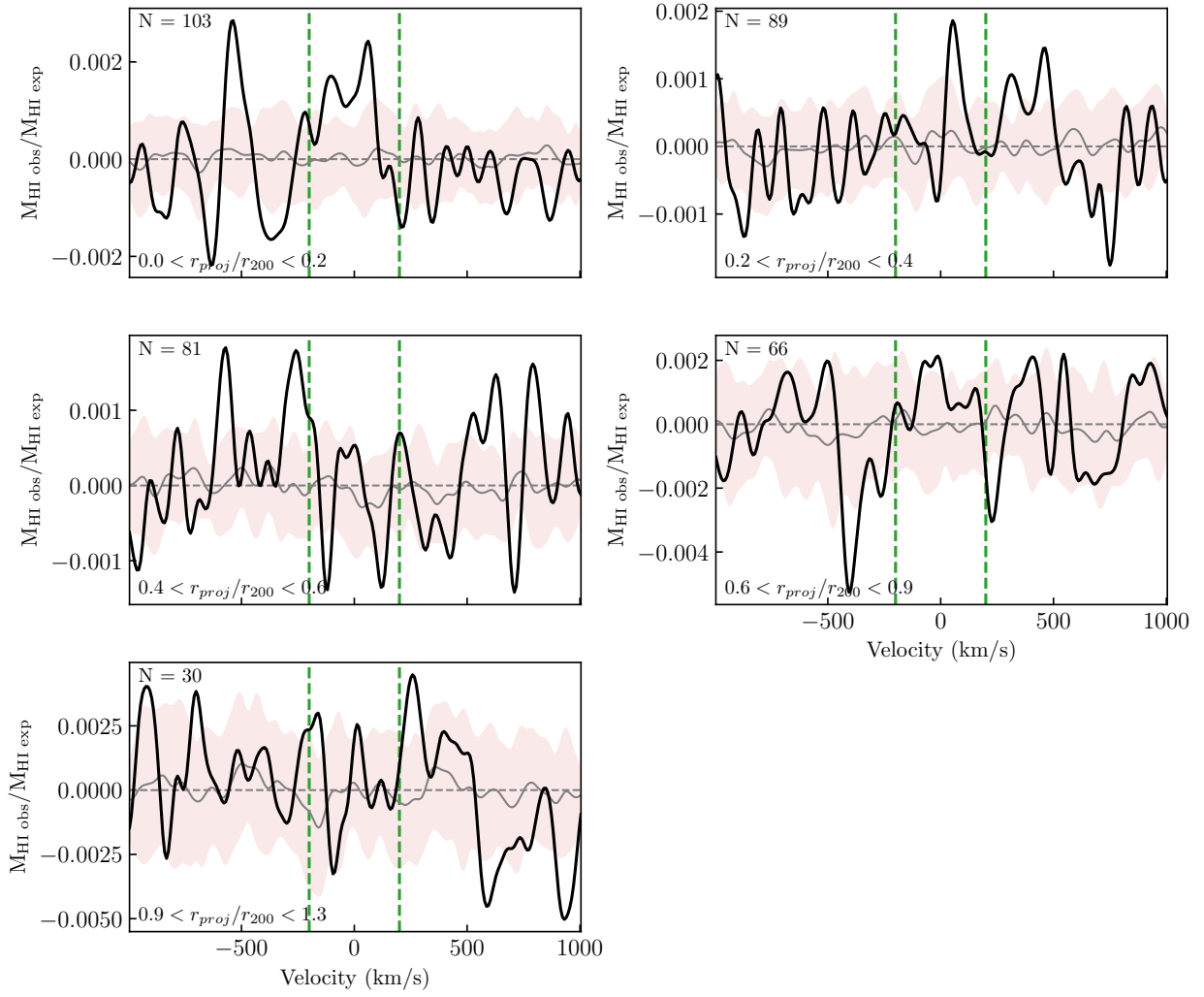


Figure B.5: Same as Figure B.3 for the sample of galaxies with $\log M_{\star} > 9.5$.

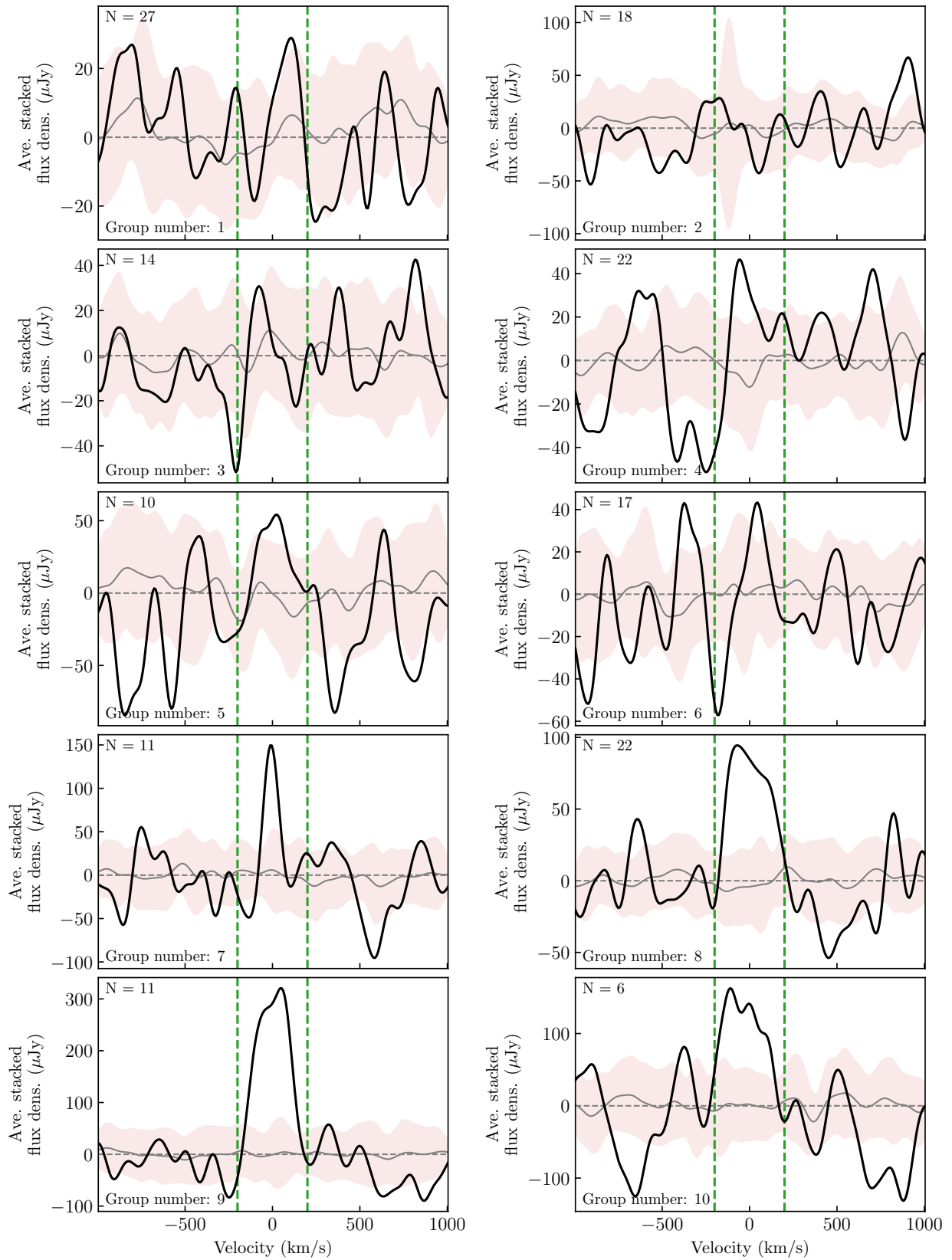


Figure B.6: Stacked spectra for each of the substructures S1–S10. The stacked spectra (the black line) have been smoothed to a velocity resolution of 80 km s^{-1} . The orange band represents the 1σ distribution from 25 stacked reference spectra. The vertical dashed green lines indicate the range over which the spectra are integrated to determine the average integrated flux density for each sample.

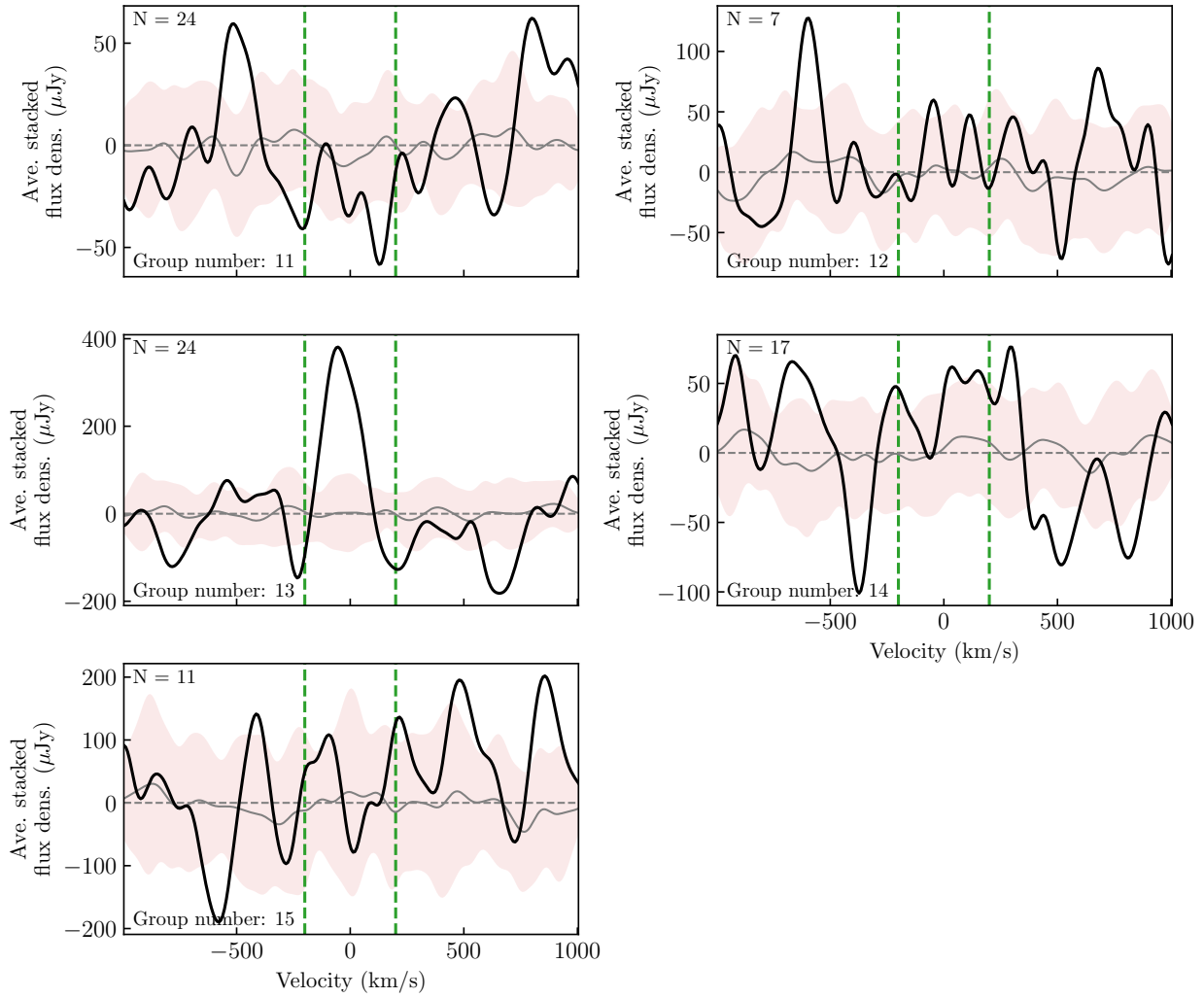


Figure B.7: Same as Figure B.6, but for substructures S11–S15.

C Data tables of measurements from stacking

Table C.1: Average M_* and $f_{\text{H I}}$ measurements for Figure 2.8. Where there is no detection in the stacked spectrum, the the 3σ upper limit is used.

All galaxies			Non-detections only		
$\log\langle M_*/M_\odot \rangle$	$\langle M_{\text{H I}}/M_* \rangle$	N	$\log\langle M_*/M_\odot \rangle$	$\langle M_{\text{H I}}/M_* \rangle$	N
7.78	< 0.47845	43	7.78	< 0.17079	42
8.69	0.15520 ± 0.01045	180	8.69	< 0.01753	169
9.56	0.01704 ± 0.00084	356	9.56	< 0.00180	338
10.52	0.00259 ± 0.00011	205	10.53	< 0.00046	200
11.35	0.00066 ± 0.00007	26	11.36	< 0.00029	23

Table C.2: Average H I deficiency measurements in each radius bin for Figure 2.9. Where there is no detection in the stacked spectrum, the 3σ lower limit is used. The high stellar mass samples have $M_* > 10^{9.5} M_\odot$, and the low stellar mass sample, $M_* < 10^{9.5} M_\odot$.

	All galaxies		High stellar mass		Low stellar mass	
	N	$\langle \text{DEF}_{\text{H I}} \rangle$	N	$\langle \text{DEF}_{\text{H I}} \rangle$	N	$\langle \text{DEF}_{\text{H I}} \rangle$
$0.00 < r_{\text{proj}}/r_{200} < 0.21$	245	> 1.02	104	> 1.47	141	> 0.78
$0.21 < r_{\text{proj}}/r_{200} < 0.43$	196	> 1.21	89	> 1.55	107	> 0.99
$0.43 < r_{\text{proj}}/r_{200} < 0.64$	155	> 1.15	81	> 1.52	73	> 0.85
$0.64 < r_{\text{proj}}/r_{200} < 0.85$	131	> 1.05	66	> 1.30	65	> 0.77
$0.85 < r_{\text{proj}}/r_{200} < 1.17$	83	> 0.72	30	> 1.10	53	> 0.55

D Coma catalogue

Table D.1: Catalogue of Coma galaxies within the *Westerbork Coma Survey*. The full catalogue is available online at <http://cdsarc.u-strasbg.fr/viz-bin/cat/J/A+A/650/A76>.

ID	RA Dec	z	R_{25} (arcsec)	n	b/a	PA (deg)	$f_{uv}, n_{uv}, u, g, r, i, z, W1, W2, W3, W4$ (mag)	M_* ($\log M_{\odot}$)	SFR ($M_{\odot} \text{ yr}^{-1}$)	M_{HI} ($\log M_{\odot}$)	Reference
Coma1001	12:59:57.7 +28:14:48.0	0.02237 ± 0.00001	25.34	4.87	0.96	-54.44	-19.60, 15.69, 13.14, 14.02, 12.50, 12.63, 10.15, 10.02, 8.64, 8.08	11.11 ± 0.10	< 0.00	< 8.29	SDSS DR13
Coma1002	13:00:03.0 +28:14:25.1	0.02569 ± 0.00001	11.95	2.42	0.51	26.41	-17.94, 16.18, 16.41, 15.75, 15.06, 13.95, 13.93, 13.05, 11.93	9.87 ± 0.18	< 0.06	< 7.83	SDSS DR13
Coma1003	12:59:44.6 +28:15:23.5	0.02630 ± 0.00009	6.40	1.61	0.67	-77.99	-19.41, 17.59, 18.33, 17.48, 17.28, 14.95, 14.65, 15.71, 11.94	9.22 ± 0.41	< 0.07	< 7.71	SDSS DR13
Coma1004	13:00:06.2 +28:15:07.9	0.02122 ± 0.00010	11.32	2.89	0.63	-3.22	18.69, 18.28, 20.32, 17.19, 17.65, 16.34, 17.35, 14.58, 14.32, 15.29, -	8.92 ± 0.27	0.03 ± 0.02	9.39	SDSS DR13
Coma1005	13:00:17.9 +28:12:08.6	0.02844 ± 0.00001	42.31	2.86	0.53	-27.50	-16.08, 12.97, 13.77, 12.45, 12.27, 10.26, 10.11, 8.72, 7.08	11.44 ± 0.10	0.73 ± 0.26	< 8.38	SDSS DR13
Coma1008	13:00:30.8 +28:20:46.9	0.01987 ± 0.00001	24.30	4.86	0.52	4.30	18.40, 17.33, 16.11, 12.99, 13.88, 12.78, 11.65, 10.47, 10.39, 9.04, -	10.85 ± 0.10	< 0.00	< 8.32	SDSS DR13
Coma101	13:00:15.6 +27:15:24.0	0.02378 ± 0.00009	6.05	1.28	0.78	11.87	-19.71, 17.55, 18.20, 17.28, 17.13, 15.43, 14.99, 15.35, 12.61, -	8.86 ± 0.35	< 0.07	< 7.88	SDSS DR13
Coma1010	13:00:44.2 +28:20:14.2	0.02639 ± 0.00001	18.17	2.65	0.50	49.73	-19.22, 16.68, 14.64, 15.31, 14.22, 13.67, 11.31, 11.10, 11.21, 9.49	10.74 ± 0.11	< 0.00	< 7.96	SDSS DR13
Coma1012	13:00:22.2 +28:14:49.5	0.02508 ± 0.00002	8.83	1.53	0.31	35.19	-20.17, 16.82, 17.52, 16.37, 16.48, 14.48, 14.24, 12.85, -	9.31 ± 0.19	< 0.04	< 7.77	SDSS DR13
Coma1014	13:00:32.5 +28:15:21.8	0.02102 ± 0.00005	7.35	2.39	0.49	-51.90	-18.98, 16.96, 17.54, 16.57, 16.41, 14.77, 14.83, 16.75, 10.80	9.33 ± 0.28	< 0.04	< 7.80	SDSS DR13
Coma1016	13:01:09.0 +28:21:35.2	0.02301 ± 0.00001	13.71	2.80	0.78	-61.80	-18.89, 17.76, 14.88, 15.63, 14.80, 13.81, 12.36, 12.42, 12.30, -	10.33 ± 0.11	< 0.00	< 8.01	SDSS DR13
Coma1018	13:01:22.8 +28:11:45.7	0.02536 ± 0.00001	18.70	4.93	0.69	-74.98	-16.96, 14.57, 15.25, 14.16, 13.74, 12.08, 11.95, 11.38, 10.30	10.56 ± 0.11	< 0.00	< 7.98	SDSS DR13
Coma102	13:00:27.9 +27:16:18.4	0.02587 ± 0.00003	4.71	1.29	0.63	10.47	-20.47, 17.83, 18.29, 17.26, 17.94, 15.40, 15.30, 13.26, -	9.22 ± 0.31	< 0.05	< 7.87	SDSS DR13
Coma1020	13:01:48.9 +28:10:19.0	0.02542 ± 0.00002	11.52	2.71	0.39	-38.81	-18.47, 16.05, 16.79, 15.60, 15.18, 13.26, 13.08, 12.69, 10.57	9.66 ± 0.15	< 0.03	< 7.86	SDSS DR13
Coma1022	13:02:10.3 +28:11:30.5	0.01914 ± 0.00001	13.95	3.97	0.91	-70.57	-18.12, 15.61, 16.33, 15.12, 14.79, 12.76, 12.71, 12.06, 10.57	10.03 ± 0.12	< 0.00	< 7.99	SDSS DR13
Coma1024	13:01:39.1 +28:14:45.2	0.02534 ± 0.00002	10.38	3.17	0.35	-37.70	-18.87, 16.58, 17.25, 16.47, 16.27, 14.41, 14.12, 14.54, 11.34	9.47 ± 0.36	< 0.07	< 7.84	SDSS DR13
Coma1026	13:01:43.3 +28:17:52.0	0.02566 ± 0.00003	6.25	2.17	0.48	6.51	-20.32, 17.22, 17.85, 16.91, 16.83, 15.01, 15.18, 14.05, 12.69	9.38 ± 0.28	< 0.06	< 7.88	SDSS DR13
Coma1028	13:01:44.2 +28:12:51.7	0.02610 ± 0.00001	8.53	1.80	0.28	-72.36	-19.26, 16.39, 17.02, 15.90, 15.81, 13.84, 13.64, 11.97, -	9.84 ± 0.11	< 0.03	< 7.83	SDSS DR13
Coma103	13:00:23.9 +27:17:12.9	0.02424 ± 0.00009	6.38	1.51	0.57	-12.20	-19.51, 17.67, 18.13, 17.18, 17.07, 15.42, 15.28, 12.57, -	9.11 ± 0.40	< 0.05	< 7.85	SDSS DR13
Coma1030	13:02:12.8 +28:12:53.4	0.02730 ± 0.00001	13.25	1.50	0.81	-8.08	17.14, 17.04, 16.96, 14.93, 15.42, 14.82, 13.58, 12.59, 12.31, 8.20, 6.21	9.82 ± 0.11	1.78 ± 0.62	8.71	SDSS DR13
Coma1032	13:02:21.5 +28:13:50.8	0.01858 ± 0.00001	18.05	3.78	0.47	63.48	-17.11, 14.13, 14.85, 13.66, 13.45, 11.72, 11.57, 10.30, 9.32	10.49 ± 0.38	0.15 ± 0.06	< 8.15	SDSS DR13
Coma1036	13:02:21.7 +28:15:21.5	0.02272 ± 0.00001	16.22	2.48	0.57	59.36	-20.04, 17.38, 14.59, 15.25, 14.12, 13.81, 12.03, 11.89, 10.40, 8.84	10.46 ± 0.10	0.26 ± 0.10	< 8.08	SDSS DR13
Coma104	13:00:30.8 +27:18:00.6	0.02564 ± 0.00012	6.27	2.11	0.63	-23.77	-21.12, 17.39, 17.84, 16.97, 16.80, 15.69, 16.19, 14.78, -	9.07 ± 0.53	< 0.06	< 7.85	SDSS DR13
Coma1040	12:59:59.5 +27:56:26.1	0.02037 ± 0.00005	7.45	2.12	0.91	67.19	-18.76, 16.82, 17.47, 16.73, 16.70, 14.68, 14.92, 17.19, 9.61	9.20 ± 0.29	< 0.04	< 7.76	SDSS DR13
Coma1042	13:00:01.0 +27:56:43.6	0.02282 ± 0.00002	8.13	3.31	0.95	-11.33	-19.99, 19.62, 17.09, 17.11, 16.33, 16.34, 14.55, 14.78, 14.67, 11.35	9.32 ± 0.29	< 0.05	< 7.78	SDSS DR13
Coma105	13:01:10.7 +27:14:47.4	0.02061 ± 0.00004	9.42	2.15	1.00	-90.00	-18.51, 16.16, 16.80, 15.73, 15.65, 14.08, 14.08, 13.52, 11.37	9.59 ± 0.18	< 0.02	< 8.12	SDSS DR13
Coma1051	13:02:11.1 +28:27:23.8	0.02048 ± 0.00005	7.41	2.35	0.88	-41.94	-19.09, 16.63, 17.02, 16.17, 16.07, 14.54, 14.53, 15.39, 12.55	9.42 ± 0.22	< 0.03	< 8.03	SDSS DR13
Coma1052	13:02:32.0 +28:26:21.6	0.01990 ± 0.00002	11.90	2.18	0.81	-72.34	-18.47, 15.55, 16.28, 15.11, 14.95, 13.25, 13.17, 12.23, 10.66	9.93 ± 0.12	< 0.01	< 8.23	SDSS DR13
Coma1053	13:02:38.1 +28:30:06.9	0.01922 ± 0.00003	14.35	1.86	0.34	32.32	-19.29, 16.24, 17.02, 16.24, 15.40, 13.78, 13.62, 12.73, -	9.57 ± 0.17	< 0.02	< 8.25	SDSS DR13
Coma1058	12:56:56.6 +28:37:24.2	0.02186 ± 0.00001	17.64	2.37	0.39	-80.28	-17.52, 14.75, 15.45, 14.29, 14.06, 12.12, 12.06, 10.88, 10.44	10.46 ± 0.11	< 0.00	< 8.56	SDSS DR13
Coma1059	12:58:09.2 +28:42:30.8	0.02537 ± 0.00001	26.74	1.44	0.28	84.81	18.56, 17.22, 16.79, 14.31, 14.79, 13.87, 13.82, 11.55, 11.25, 7.39, 5.92	10.18 ± 0.10	3.06 ± 1.06	9.33	SDSS DR13
Coma1060	12:58:19.3 +28:41:54.6	0.01930 ± 0.00003	9.08	1.75	0.60	-92.42	-19.58, 16.49, 17.27, 16.51, 15.71, 14.28, 14.25, 12.36, -	9.43 ± 0.17	0.01 ± 0.01	< 8.12	SDSS DR13
Coma1061	12:59:08.6 +28:43:41.6	0.02367 ± 0.00003	12.38	1.19	0.35	27.99	-19.44, 16.31, 17.12, 16.32, 15.50, 14.06, 14.01, 13.44, -	9.73 ± 0.16	< 0.04	< 8.16	SDSS DR13
Coma107	13:00:58.4 +27:39:07.5	0.01737 ± 0.00002	17.54	2.96	0.65	-3.28	-17.08, 14.77, 15.54, 14.44, 14.27, 12.73, 12.66, 12.19, 10.08	10.02 ± 0.13	< 0.00	< 7.97	SDSS DR13
Coma1070	13:00:52.1 +28:21:58.1	0.02548 ± 0.00001	24.13	3.30	0.65	13.90	16.45, 18.39, 13.63, 14.48, 13.19, 12.57, 10.84, 10.80, 10.33, -	11.04 ± 0.10	< 0.00	< 8.28	SDSS DR13
Coma1071	13:02:14.3 +28:21:09.5	0.02885 ± 0.00001	17.31	4.13	0.61	82.06	-17.11, 14.64, 15.29, 14.19, 14.15, 12.63, 12.47, 12.11, 10.37	10.47 ± 0.12	< 0.01	< 8.16	SDSS DR13
Coma1076	13:03:30.0 +28:16:28.9	0.02139 ± 0.00002	7.34	2.08	0.48	-80.32	-19.26, 16.52, 17.04, 16.04, 16.51, 14.08, 14.07, 15.02, 11.80	9.55 ± 0.18	< 0.02	< 8.44	SDSS DR13
Coma108	13:01:11.2 +27:44:33.0	0.02458 ± 0.00005	4.99	2.57	0.80	-58.45	-19.81, 17.36, 18.16, 17.14, 17.07, 15.40, 15.37, 13.59, 9.50	9.19 ± 0.37	< 0.10	< 7.72	SDSS DR13
Coma1080	12:57:17.7 +28:26:19.8	0.02304 ± 0.00005	5.87	1.20	0.58	50.95	-20.44, 17.76, 18.43, 17.33, 17.31, 15.01, 14.87, 13.60, -	8.90 ± 0.30	0.06 ± 0.03	< 7.96	SDSS DR13
Coma1081	12:57:27.5 +28:26:22.9	0.02593 ± 0.00002	10.61	1.71	0.53	-82.29	-19.44, 16.38, 17.17, 16.35, 15.48, 14.34, 14.29, 11.38, -	9.65 ± 0.19	0.05 ± 0.02	< 7.96	SDSS DR13
Coma1082	12:59:50.2 +27:54:45.5	0.02417 ± 0.00004	5.82	1.55	0.84	-30.54	-21.16, 17.35, 18.06, 17.04, 16.10, 14.11, 13.37, 17.16, -	10.13 ± 0.11	-	< 7.77	SDSS DR13
Coma1083	13:00:08.1 +27:58:37.0	0.02150 ± 0.00001	92.64	3.25	0.66	78.65	17.76, 16.98, 14.26, 11.15, 12.17, 10.77, 10.35, 12.75, 13.47, 15.00, -	10.13 ± 0.11	< 0.00	< 8.70	SDSS DR13
Coma1085	13:00:16.5 +28:57:03.0	0.01547 ± 0.00001	20.43	4.00	0.53	34.41	-17.23, 14.70, 15.42, 14.23, 14.15, 12.29, 12.12, 11.57, 9.98	11.06 ± 0.10	< 0.00	< 7.96	SDSS DR13
Coma1086	13:00:18.1 +27:57:23.7	0.02127 ± 0.00001	15.47	5.73	0.87	-38.03	-17.53, 14.58, 15.16, 13.72, 13.48, 15.91, 16.36, -, -	11.06 ± 0.10	0.53 ± 0.19	< 7.93	SDSS DR13
Coma1088	13:00:06.1 +27:58:41.9	0.02546 ± 0.00001	12.68	1.61	0.29	-4.00	20.58, 19.78, 18.51, 15.75, 16.46, 15.48, 15.32, 14.85, 15.09, 19.65, -	9.88 ± 0.19	< 0.06	< 7.87	SDSS DR13

E Coma atlas

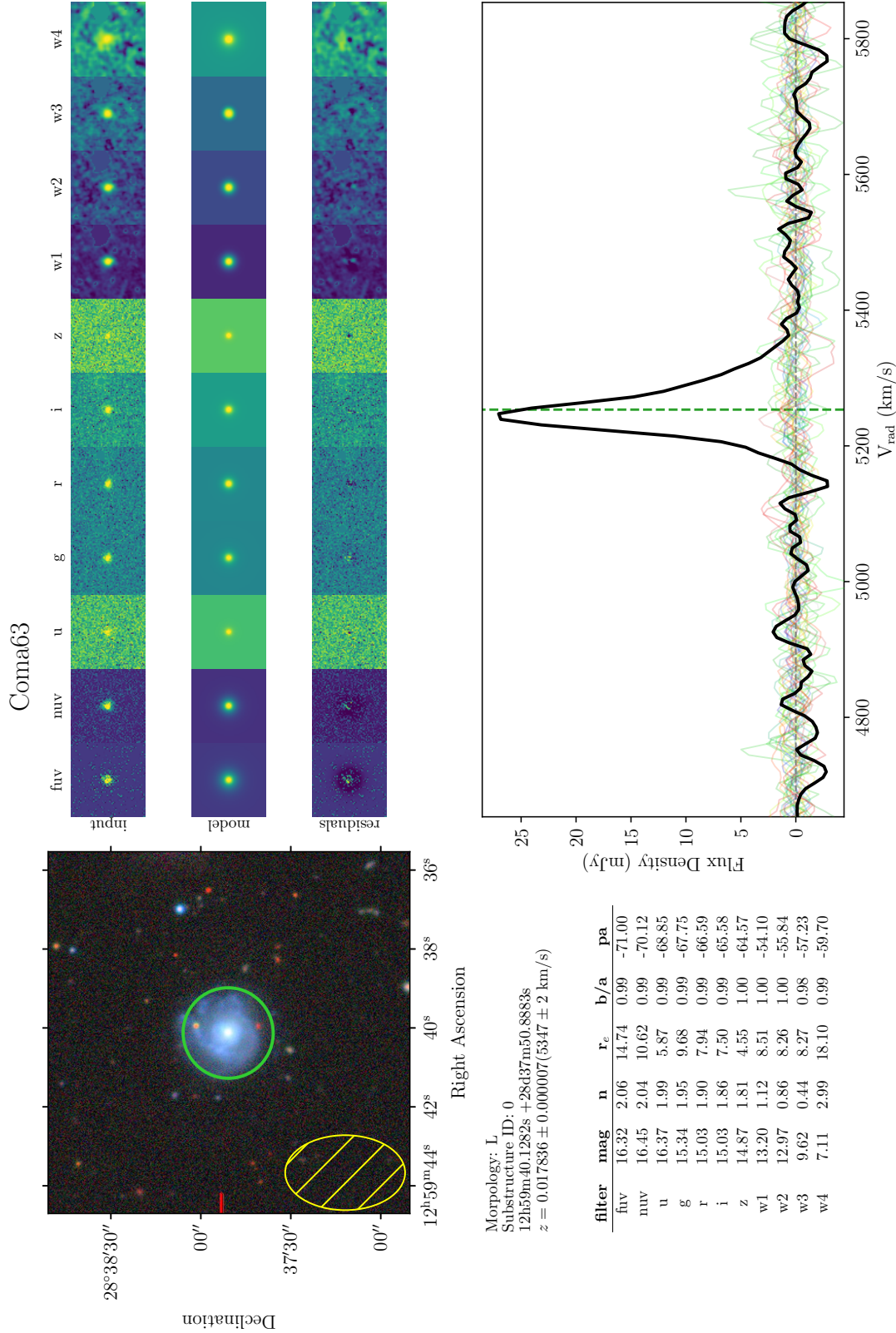


Figure E.1: Atlas page for one galaxy in the WCS. The top left panel shows the colour image of the galaxy from the DECaLS survey. Overlaid in green on the optical image is an aperture defined by the radius at the B-band 25th mag/arcsec² isophote; the yellow hatched ellipse indicates the size of the WRST beam. Below the optical image is a table containing the magnitude, r_{eff} , axis ratio, position angle, and seraic index of the galaxy in each of the 11 bands. To the right of the optical image are the cut-outs of the galaxy in the 11 photometric bands. Shown below the cut-outs are the best-fit GalfitM model and the residual image for each band. The extracted spectrum for the target galaxy is plotted in black in the bottom right panel, with its optical redshift indicated by the dashed green line. The 25 reference spectra are also shown in this panel in the rainbow colours. Atlas pages for the other Coma galaxies can be found at <https://drive.google.com/drive/folders/1sKdnUGcSi6u-Wf11CwRALW4UFYCVgA4?>.

References

- Abramson A., Kenney J. D., Crowl H. H., Chung A., Van Gorkom J. H., Vollmer B., Schiminovich D., 2011, *Astronomical Journal*, 141
- Adami C., Biviano A., Durret F., Mazure A., 2005, *Astronomy and Astrophysics*, 443, 17
- Aguerri J. A. L., 2012, *Advances in Astronomy*, 2012
- Akamatsu H., Inoue S., Sato T., Matsusita K., Ishisaki Y., Sarazin C. L., 2013, *Publications of the Astronomical Society of Japan*, 65
- Alabi A., et al., 2018, *Monthly Notices of the Royal Astronomical Society*, 479, 3308
- Alam S., et al., 2015, *The Astrophysical Journal Supplement Series*, 219, 12
- Albaret F. D., et al., 2017, *Astrophysical Journal, Supplement Series*, 233, 27
- Andrade-Santos F., Nulsen P. E., Kraft R. P., Forman W. R., Jones C., Churazov E., Vikhlinin A., 2013, *Astrophysical Journal*, 766, 107
- Balogh M. L., Morris S. L., 2000, *Monthly Notices of the Royal Astronomical Society*, 318, 703
- Balogh M. L., Navarro J. F., Morris S. L., 2000, *The Astrophysical Journal*, 540, 113
- Bamford S. P., Häußler B., Rojas A., Borch A., 2011, in Ian N. Evans Alberto Accomazzi Douglas J. Mink Arnold H. Rots eds, Vol. 442, *Astronomical Data Analysis Software and Systems XX*. Astronomical Society of the Pacific (ASP), San Fransisco, p. 479, <http://adsabs.harvard.edu/abs/2011ASPC..442..479B>
- Barden M., Häußler B., Peng C. Y., McIntosh D. H., Guo Y., 2012, *Monthly Notices of the Royal Astronomical Society*, 422, 449
- Beijersbergen M., 2003, PhD thesis, University of Groningen, <http://adsabs.harvard.edu/abs/2003PhDT.....236B>
- Bertin E., 2010, SWarp: Resampling and Co-adding FITS Images Together, <https://ui.adsabs.harvard.edu/abs/2010ascl.soft10068B/abstract>
- Bianchi L., GALEX Team 2000, *Memorie della Società Astronomia Italiana*, Vol. 71, p.1117, 71, 1117
- Bird C. M., 1994, *The Astronomical Journal*, 107, 1637
- Biviano A., Durret F., Gerbal D., Le Fèvre O., Lobo C., Mazure A., Slezak E., 1996, *Astronomy and Astrophysics*, 311, 95
- Boselli A., Gavazzi G., 2009, *Astronomy & Astrophysics*, 508, 201
- Bravo-Alfaro H., Cayatte V., van Gorkom J. H., Balkowski C., 2000, *The Astronomical Journal*, 119, 580
- Bravo-Alfaro H., Cayatte V., van Gorkom J. H., Balkowski C., 2001, *Astronomy and Astrophysics*, 379, 347
- Brown T., Catinella B., Cortese L., Kilborn V., Haynes M. P., Giovanelli R., 2015, *Monthly Notices of the Royal Astronomical Society*, 452, 2479
- Brown T., et al., 2017, *Monthly Notices of the Royal Astronomical Society*, 466, 1275

- Burns J. O., Roettiger K., Ledlow M., Klypin A., 1994, *The Astrophysical Journal*, 427, L87
- Caldwell N., Rose J. A., Sharples R. M., Ellis R. S., Bower R. G., 1993, *The Astronomical Journal*, 106, 473
- Carter D., et al., 2008, *The Astrophysical Journal Supplement Series*, 176, 424
- Castander F. J., et al., 2001, *The Astronomical Journal*, 121, 2331
- Chambers K. C., et al., 2016
- Chengalur J. N., Braun R., Wieringa M., 2001, *Astronomy and Astrophysics*, 372, 768
- Chiboucas K., Tully R. B., Marzke R. O., Trentham N., Ferguson H. C., Hammer D., Carter D., Khosroshahi H., 2010, *The Astrophysical Journal*, 723, 251
- Chiboucas K., et al., 2011, *Astrophysical Journal*, 737, 86
- Chung A., van Gorkom J. H., Kenney J. D. P., Crowl H., Vollmer B., 2009, *The Astronomical Journal*, 138, 1741
- Cluver M. E., et al., 2014, *The Astrophysical Journal*, 782, 90
- Cluver M. E., Jarrett T. H., Dale D. A., Smith J. D. T., August T., Brown M. J. I., 2017, *The Astrophysical Journal*, 850, 68
- Cluver M. E., et al., 2020, *The Astrophysical Journal*, 898, 20
- Cocato L., et al., 2020, *Monthly Notices of the Royal Astronomical Society*, 492, 2955
- Colless M., Dunn A. M., 1996, *The Astrophysical Journal*, 458, 435
- Cook D. O., et al., 2014, *Monthly Notices of the Royal Astronomical Society*, 445, 890
- Cortese L., Gavazzi G., Iglesias-Paramo J., Boselli A., Carrasco L., 2003, *Astronomy and Astrophysics*, 401, 471
- Cortese L., Catinella B., Boissier S., Boselli A., Heinis S., 2011, *Monthly Notices of the Royal Astronomical Society*, 415, 1797
- Dale D. A., et al., 2009, *Astrophysical Journal*, 703, 517
- Denes H., Kilborn V. A., Koribalski B. S., 2014, *Monthly Notices of the Royal Astronomical Society*, 444, 667
- Dénes H., Kilborn V. A., Koribalski B. S., Wong O. I., 2016, *Monthly Notices of the Royal Astronomical Society*, 455, 1294
- Dey A., et al., 2019, *The Astronomical Journal*, 157, 168
- Dressler A., 1980, *The Astrophysical Journal*, 236, 351
- Dressler A., Shectman S. A., 1988a, *The Astronomical Journal*, 95, 284
- Dressler A., Shectman S. A., 1988b, *The Astronomical Journal*, 95, 985
- Edwards L. O., Fadda D., 2011, *Astronomical Journal*, 142, 148
- Fabello S., Catinella B., Giovanelli R., Kauffmann G., Haynes M. P., Heckman T. M., Schiminovich D., 2011, *Monthly Notices of the Royal Astronomical Society*, 411, 993

- Fabello S., Kauffmann G., Catinella B., Li C., Giovanelli R., Haynes M. P., 2012, *Monthly Notices of the Royal Astronomical Society*, 427, 2841
- Falco E. E., et al., 1999, *Publications of the Astronomical Society of the Pacific*, 111, 438
- Fitchett M., Webster R., 1987, *The Astrophysical Journal*, 317, 653
- Gavazzi G., O'Neil K., Boselli A., van Driel W., 2006, *Astronomy and Astrophysics*, 449, 929
- Gavazzi R., Adami C., Durret F., Cuillandre J. C., Ilbert O., Mazure A., Pelló R., Ulmer M. P., 2009, *Astronomy and Astrophysics*, 498
- Gregory S. A., Tifft W. G., 1976, *The Astrophysical Journal*, 205, 716
- Gu M., et al., 2017, | 10.3847/1538-4357/aabbae
- Gunn J. E., Gott J. Richard I., 1972, *The Astrophysical Journal*, 176, 1
- Harrison C., Colless M., Kuntschner H., Couch W., De Propris R., Pracy M., 2010, *Monthly Notices of the Royal Astronomical Society*, 409, 1455
- Haynes M. P., Giovanelli R., 1984, *The Astronomical Journal*, 89, 758
- Haynes M. P., Giovanelli R., Herter T., Vogt N. P., Freudling W., Maia M. A. G., Salzer J. J., Wegner G., 1997, *The Astronomical Journal*, 113, 1197
- Haynes M. P., et al., 2018, *The Astrophysical Journal*, 861, 49
- Head J. T., Lucey J. R., Hudson M. J., 2015, *Monthly Notices of the Royal Astronomical Society*, 453, 3729
- Healy J., Blyth S.-L., Elson E., van Driel W., Butcher Z., Schneider S., Lehnert M. D., Minchin R., 2019, *Monthly Notices of the Royal Astronomical Society*, 487, 4901
- Hess K. M., Jarrett T. H., Carignan C., Passmoor S. S., Goedhart S., 2015, *Monthly Notices of the Royal Astronomical Society*, 452, 1617
- Hou A., et al., 2012, *Monthly Notices of the Royal Astronomical Society*, 421, 3594
- Huchra J. P., et al., 2012, *The 2MASS Redshift Survey - Description and data release*, doi:10.1088/0067-0049/199/2/26
- Jaffé Y. L., Poggianti B. M., Verheijen M. A. W., Deshev B. Z., van Gorkom J. H., 2013, *Monthly Notices of the Royal Astronomical Society*, 431, 2111
- Jaffé Y. L., Smith R., Candlish G. N., Poggianti B. M., Sheen Y.-K., Verheijen M. A. W., 2015, *Monthly Notices of the Royal Astronomical Society*, 448, 1715
- Jaffé Y. L., et al., 2016, *Monthly Notices of the Royal Astronomical Society*, 461, 1202
- Jangren A., Wegner G., Salzer J. J., Werk J. K., Gronwall C., 2005, *The Astronomical Journal*, 130, 496
- Jarrett T. H., et al., 2013, *The Astronomical Journal*, 145, 6
- Jarrett T. H., Cluver M. E., Brown M. J. I., Dale D. A., Tsai C. W., Masci F., 2019, *The Astrophysical Journal Supplement Series*, 245, 25
- Jones M. G., et al., 2018, *Astronomy and Astrophysics*, 609

- Jørgensen I., Franx M., Kjaergaard P., 1995, *Monthly Notices of the Royal Astronomical Society*, 276, 1341
- Kadowaki J., Zaritsky D., Donnerstein R. L., 2017, *The Astrophysical Journal*, 838, L21
- Kannappan S. J., et al., 2013, *The Astrophysical Journal*, 777, 42
- Kapferer W., Sluka C., Schindler S., Ferrari C., Ziegler B., 2009, *Astronomy and Astrophysics*, 499, 87
- Karachentsev I., Kopylov A., 1990, *Monthly Notices of the Royal Astronomical Society*, 243, 390
- Knebe A., Mueller V., 1999, *Astronomy and Astrophysics*, 341, 1
- Kourkchi E., et al., 2012, *Monthly Notices of the Royal Astronomical Society*, 420, 2819
- Kurtz M., Mink D., Wyatt W., Fabricant D., Torres G., Kriss G., Tonry J., 1992, in Worrall D., Biemesderfer C., Barnes J., eds, Vol. 25, *Astronomical Society of the Pacific Conference Series*. p. 432
- Lah P., et al., 2009, *Monthly Notices of the Royal Astronomical Society*, 399, 1447
- Lintott C. J., et al., 2008, *Monthly Notices of the Royal Astronomical Society*, 389, 1179
- Lintott C., et al., 2011, *Monthly Notices of the Royal Astronomical Society*, 410, 166
- Lyskova N., Churazov E., Zhang C., Forman W., Jones C., Dolag K., Roediger E., Sheardown A., 2019, *Monthly Notices of the Royal Astronomical Society*, 485, 2922
- Malavasi N., Aghanim N., Tanimura H., Bonjean V., Douspis M., 2020, *Astronomy & Astrophysics*, 634, A30
- McGee S. L., Balogh M. L., Bower R. G., Font A. S., McCarthy I. G., 2009, *Monthly Notices of the Royal Astronomical Society*, 400, 937
- Mellier Y., Mathez G., Mazure A., Chauvineau B., Proust D., 1988, *Astronomy and Astrophysics*, 199, 67
- Meyer M. J., et al., 2004, *The HIPASS catalogue - I. Data presentation*, doi:10.1111/j.1365-2966.2004.07710.x, <http://arxiv.org/abs/astro-ph/0406384>
- Mo H., van den Bosch F. C., White S., 2010, *Galaxy Formation and Evolution*. Cambridge University Press, Cambridge
- Mobasher B., et al., 2001, *The Astrophysical Journal Supplement Series*, 137, 279
- Neumann D. M., et al., 2001, *The NGC 4839 group falling into the Coma cluster observed by XMM-Newton*, doi:10.1051/0004-6361:20000182
- Neumann D. M., Lumb D. H., Pratt G. W., Briel U. G., 2003, *Astronomy and Astrophysics*, 400, 811
- Ochsenbein F., Bauer P., Marcout J., 2000, *Astronomy and Astrophysics Supplement*, 143, 23
- Oman K. A., Hudson M. J., 2016, *Monthly Notices of the Royal Astronomical Society*, 463, 3083
- Oman K. A., Hudson M. J., Behroozi P. S., 2013, *Monthly Notices of the Royal Astronomical Society*, 431, 2307

- Parekh V., Van Der Heyden K., Ferrari C., Angus G., Holwerda B., 2015, *Astronomy and Astrophysics*, 575, 28
- Peng C. Y., Ho L. C., Impey C. D., Rix H.-W., 2002, *The Astronomical Journal*, 124, 266
- Peng C. Y., Ho L. C., Impey C. D., Rix H. W., 2010, *Astronomical Journal*, 139, 2097
- Ponomareva A. A., Verheijen M. A., Papastergis E., Bosma A., Peletier R. F., 2018, *Monthly Notices of the Royal Astronomical Society*, 474, 4366
- Popesso P., et al., 2019, *Monthly Notices of the Royal Astronomical Society*, 483, 3213
- Porter S. C., Raychaudhury S., Pimblet K. A., Drinkwater M. J., 2008, *Monthly Notices of the Royal Astronomical Society*, 388, 1152
- Rines K., Geller M. J., Kurtz M. J., Diaferio A., Jarrett T. H., Huchra J. P., 2001, *The Astrophysical Journal*, 561, L41
- Saintonge A., et al., 2016
- Salerno J. M., et al., 2020
- Sault R. J., Teuben P., Wright M. C. H., 2011, MIRIAD: Multi-channel Image Reconstruction, Image Analysis, and Display, <https://ui.adsabs.harvard.edu/abs/2011ascl.soft06007S/abstract>
- Serna A., Gerbal D., 1996, *Astronomy and Astrophysics*, 309, 65
- Serra P., et al., 2013, *Monthly Notices of the Royal Astronomical Society*, 428, 370
- Serra P., et al., 2015, *Monthly Notices of the Royal Astronomical Society*, 448, 1922
- Smith R. J., et al., 2008, *Monthly Notices of the Royal Astronomical Society: Letters*, 386, L96
- Solanes J. M., Giovanelli R., Haynes M. P., 1996, *The Astrophysical Journal*, 461, 609
- Solanes J. M., Manrique A., García-Gómez C., González-Casado G., Giovanelli R., Haynes M. P., 2001, *The Astrophysical Journal*, 548, 97
- Springel V., et al., 2005, *Nature*, 435, 629
- Van Den Bosch F. C., Aquino D., Yang X., Mo H. J., Pasquali A., McIntosh D. H., Weinmann S. M., Kang X., 2008, *Monthly Notices of the Royal Astronomical Society*, 387, 79
- Verheijen M. A., Sancisi R., 2001, *Astronomy and Astrophysics*, 370, 765
- Verheijen M., van Gorkom J. H., Szomoru A., Dwarakanath K. S., Poggianti B. M., Schiminovich D., 2007, *The Astrophysical Journal*, 668, L9
- Vikhlinin A., Markevitch M., Forman W., Jones C., 2001, *The Astrophysical Journal*, 555, L87
- Wegner G., Thorstensen J. R., Kurtz M. J., Geller M. J., Huchra J. P., 1990, *The Astronomical Journal*, 100, 1405
- White S. D. M., Briel U. G., Henry J. P., 1993, *Monthly Notices of the Royal Astronomical Society*, 261, L8
- Wilman D. J., Oemler A., Mulchaey J. S., McGee S. L., Balogh M. L., Bower R. G., 2009, *Astrophysical Journal*, 692, 298

- Wright E. L., et al., 2010, *The Astronomical Journal*, 140, 22
- Yagi M., Komiyama Y., Yoshida M., Furusawa H., Kashikawa N., Koyama Y., Okamura S., 2007, *The Astrophysical Journal*, 660, 1209
- Yagi M., et al., 2010, *Astronomical Journal*, 140, 1814
- Yoon H., Chung A., Smith R., Jaffé Y. L., 2017, *The Astrophysical Journal*, 838, 81
- Zabludoff A. I., Mulchaey J. S., 1998, *The Astrophysical Journal*, 496, 39
- Zabludoff A. I., Geller M. J., Huchra J. P., Vogeley M. S., 1993, *The Astronomical Journal*, 106, 1273
- Zhang Y. Y., Reiprich T. H., Finoguenov A., Hudson D. S., Sarazin C. L., 2009, *Astrophysical Journal*, 699, 1178
- de Vaucouleurs G., de Vaucouleurs A., Corwin Herold G. J., Buta R. J., Paturel G., Fouque P., 1991, *Third Reference Catalogue of Bright Galaxies*. Springer, New York, <https://ui.adsabs.harvard.edu/abs/1991rc3..book.....D>
- van Dokkum P. G., 2001, *Publications of the Astronomical Society of the Pacific*, 113, 1420



“Try not. Do... or do not. There is no try.” – **Yoda**
(Star Wars V: Empire Strikes Back)

Chapter 3

A radio view of Abell 2626: the H I story

This chapter is adapted from Healy, Deb, Verheijen et al. (accepted for publication in *Astronomy & Astrophysics* on 25 June 2021), and includes work that was done by my collaborators (T. Deb and M. Verheijen).

Abstract

In August 2019, MeerKAT targeted the galaxy cluster Abell 2626 (A2626) for H I observations for a total of 15 hours on source. Host to four candidate “jellyfish” galaxies (galaxies exhibiting tails due to ram pressure stripping), and two confirmed “jellyfish” galaxies, A2626 is an excellent cluster in which to study ongoing environmental evolution. In this chapter, I present the new MeerKAT H I data which are the final piece of the multi-wavelength puzzle for this cluster. I will discuss the observations and data reduction, as well as the imaging steps and quality assurance tests conducted. I will present the H I parameters measured for each galaxy, and compare these to previously published values in the literature.

3.1 Introduction

It has long been known that galaxies that reside in clusters differ from the field galaxy population (Hubble & Humason, 1931). Observed relations such as the morphology-density relation (Dressler, 1980) quantify how the fraction of different galaxy morphologies changes with environmental density – the fraction of early type galaxies increases with galaxy density. Within fixed morphological classes, cluster galaxies tend to have older stellar populations (e.g. Bower et al., 1990; Rose et al., 1994; Cooper et al., 2010) and suppressed star formation (e.g. Balogh et al., 1997; Gomez et al., 2003; Boselli et al., 2020) relative to their field counterparts. The picture that has emerged is one where as a galaxy moves into a dense environment (such as a galaxy cluster), various processes affect the galaxy’s gas content which results in the quenching of star-formation, eventually leading to a morphological transformation. These processes include galaxy-galaxy interactions (e.g. mergers, harassment), interactions between a galaxy’s interstellar medium (ISM) and the hot intra-cluster medium (e.g. ram-pressure stripping), and processes which halt the accretion of cold gas onto a galaxy’s disk (e.g. starvation). Given the link between the removal of the galaxy gas content and the quenching of star formation, a multi-wavelength approach to studying galaxy evolution is required. Optical and infrared emission trace the stellar population and star formation, and radio emission traces the neutral gas content of the ISM.

Up until recently, studies of the environmental impact on the H I in galaxies in clusters have been limited to targeted surveys of galaxies expected to contain H I based on their optical properties, typically late-type galaxies (e.g. Giovanelli et al., 1981; Haynes & Giovanelli, 1986; Gavazzi et al., 2006; Chung et al., 2009). These studies have laid the foundation for what is known about H I in clusters, however blind H I surveys provide a more complete picture of the environmental effects on the H I content of cluster galaxies. Galaxy clusters are known to be H I deficient, particularly in the core of the cluster (e.g. Giovanelli et al., 1982; Bravo-Alfaro et al., 2000; Solanes et al., 2001), requiring high sensitivity observations to enable the detection of H I in the most H I deficient galaxies. Observations and simulations have noted the scatter in the radial trend of H I deficiency (Solanes et al., 2001; Tonnesen et al., 2007) which suggests that even in the outskirts of galaxy clusters, infalling galaxies can be affected by the environmental processes discussed earlier. This highlights the need for wide-area H I cluster surveys. A number of blind H I surveys covering galaxy clusters have already been published (Zwaan et al., 2001; Lah et al., 2007; Verheijen et al., 2007; Kent et al., 2008; Hess et al., 2015; Gogate et al., 2020) with more that are planned or currently being observed by MeerKAT, the Australian SKA Pathfinder (ASKAP) telescope, and Apertif on the Westerbork Synthesis Radio Telescope. In this chapter, I present a blind H I survey of Abell 2626 observed with MeerKAT.

Abell 2626 (hereafter A2626; Abell, 1958), is a moderately sized cluster located in the Pegasus constellation. Despite being part of the WIDE-field Nearby Galaxy-cluster Survey (WINGS; Fasano et al., 2006; Cava et al., 2009), the galaxies in A2626 have not been extensively studied. At the centre of the cluster is an intriguing “kite” source that is visible at radio wavelengths and has been the focus of most of the recent works on this cluster (Rizza et al., 2000; Wong et al., 2008; Gitti, 2013; Ignesti et al., 2018, e.g.). X-ray studies have also shown A2626 to be a cool-core cluster (Wong et al., 2008; McDonald et al., 2018). Despite being located within the Arecibo Legacy Fast ALFA¹ survey (ALFALFA; Haynes et al., 2011, 2018), located at a distance of 250 Mpc, the H I redshift for A2626 falls into the window affected by airport radar making it difficult for many radio telescopes to observe in H I.

The H I data centred on A2626 in combination with existing multi-wavelength data, including complementary optical spectroscopy (see Chapter 4), will shed light on the ongoing environment-driven galaxy evolution within the cluster. A2626 hosts six candidate “jellyfish” galaxies (Poggianti

¹Arecibo L-band Feed Array

et al., 2016), which have undergone extreme ram pressure stripping that has removed gas (of all phases) into tails trailing the galaxy stellar body (e.g. Moretti et al., 2019; Poggianti et al., 2019; Ramatsoku et al., 2019; Deb et al., 2020). The only confirmed jellyfish galaxy, JW100, has been at the centre of multi-wavelength (radio–X-ray) studies aimed at understanding how the stripping processes affect the stellar and gas components of the galaxy (e.g. Moretti et al., 2019; Poggianti et al., 2019). A2626 has also been shown to contain substructure (Mohr et al., 1996; Mohr & Wegner, 1997), and shows evidence in the X-ray of a group merging with the cluster core (Wong et al., 2008).

In this chapter, I present the new MeerKAT observations of A2626. I will describe the calibration and imaging process (Section 3.2–Section 3.3.2), as well as the tests carried out to evaluate the quality of the calibration (Section 3.3.1.1 and Section 3.4.3). I also discuss how the source finding was performed on the H I spectral line cube (Section 3.4.1), and present the global properties of the detected H I sources (Section 3.4.2). Throughout this chapter, I use $H_0 = 70 \text{ km s}^{-1}$ and $\Omega_m = 0.3$.

3.2 MeerKAT Observations

Observations of Abell 2626 were carried out using the L-band receivers on MeerKAT (Jonas & MeerKAT Team, 2016) over the nights of 15–17 July 2019. I imaged a single pointing centred on the cluster. The MeerKAT primary beam full width half max (FWHM) gives us a field-of-view (FoV) of 1 deg^2 at $z \sim 0$ which encompasses the R_{200} ($1.64 \text{ Mpc} \approx 25'$ at $z \sim 0.05$) of the cluster (Cava et al., 2009). Due to the sensitivity of MeerKAT, it is possible to image past the FWHM $2 \times 2 \text{ deg}^2$ (see Section 3.3.2 for details).

Abell 2626 achieves a maximum elevation of $35 - 40 \text{ deg}$ above the northern horizon of the MeerKAT site. The field was observed for a total of 3×5 hours on source. Scans of bandpass calibrator (J1939-6342) were made at the start and end of the observations for 10 min per scan, while phase calibrator scans of J2253+1608 were made every 20 min for 2 min. The data were observed using the SCARAB correlator in 4K mode; the total MeerKAT bandwidth was 856 MHz, with 4096 channels of width 207 kHz corresponding to 45 km s^{-1} at $z \sim 0$. Thus far, I have only processed two subsets of the total bandwidth as follows: 960 – 1160 MHz, and 1300 – 1520 MHz for the continuum imaging (see Section 3.3.1); and 1300 – 1430 MHz for the H I data (see Section 3.3.2). The velocity range covered by the H I data cube spans -2011 km s^{-1} to 27766 km s^{-1} , which corresponds to a volume depth of 420 Mpc.

Under the guidelines of the first open call for MeerKAT observations, proposals could ask for a maximum of 16 hours, including overheads. The large FoV of MeerKAT meant that the cluster could be observed using a single pointing, thus enabling the devotion of all the allocated time to obtaining data as sensitive as possible. With effectively 15 hours on source, the 3σ H I mass detection limit for a galaxy with a line width of 300 km s^{-1} is $M_{\text{HI}} = 2 \times 10^8 M_{\odot}$, and the 5σ H I column density sensitivity is $N_{\text{HI}} = 2 \times 10^{19} \text{ cm}^{-2}$ when the data are smoothed to $30''$ resolution. The observational parameters can be found in Table 3.1.

3.3 Data processing

In order to limit the compute resources required to calibrate and image the dataset, I only processed a limited subset of the 856 MHz total bandwidth. For the H I data cube (see Section 3.3.2 for details) I processed 1300 – 1430 MHz, and for the continuum image (see Section 3.3.1) we processed two chunks: 1300 – 1520 MHz and 960 – 1160 MHz. For both the continuum and H I data, we only processed the XX and YY correlations. The calibration of the data was done on the ilifu compute cluster hosted by IDIA² using the CARACal pipeline (formerly MeerKATHI, Józsa et al. 2020).

²Inter-University Institute for Data Intensive Astronomy

Table 3.1: MeerKAT observations and imaging parameters

Observing parameters	
Observation dates	15, 16, 17 July 2019
Flux/bandpass calibrator	J1939-6342
Phase/gain calibrator	J2253+1608
Pointing centre	23:36:31.00 +21:09:35.9
Total integration time	15 hr (3×5 hr)
Number of active dishes	61
Shortest-longest baselines	40 – 7709 m
Correlator mode	4k, dual polarisation
Primary beam FWHM	$58'$ at 1420.406 MHz
Total bandwidth	856 MHz
Frequency range	900–1670 MHz
Spectral resolution	208.966579 kHz
Continuum imaging properties	
Imaged area	2×2 deg ²
Frequency ranges	960 – 1160 MHz (LF image) 1300 – 1520 MHz (HF image)
Synthesised beam	$10.7'' \times 12.9''$ (LF image, robust= –1) $8.5'' \times 13.2''$ (HF image, robust= –1)
Image rms	$11.0 \mu\text{Jy}$ (LF image, robust= –1) $7.5 \mu\text{Jy}$ (HF image, robust= –1)
HI imaging properties	
Imaged area	2×2 deg ²
Frequency range	1300 – 1430 MHz
Velocity coverage	–2011 to 27766 km s ^{–1}
Velocity resolution	$44.1 \times (1 + z)$ km s ^{–1}
Synthesised beam	$6.2'' \times 13.7''$ (Robust= –0.5 at 1420 MHz)
Cube rms	$80 \mu\text{Jy}/\text{beam}$

I followed the same general strategy as Serra et al. (2019) to do the cross-calibration using

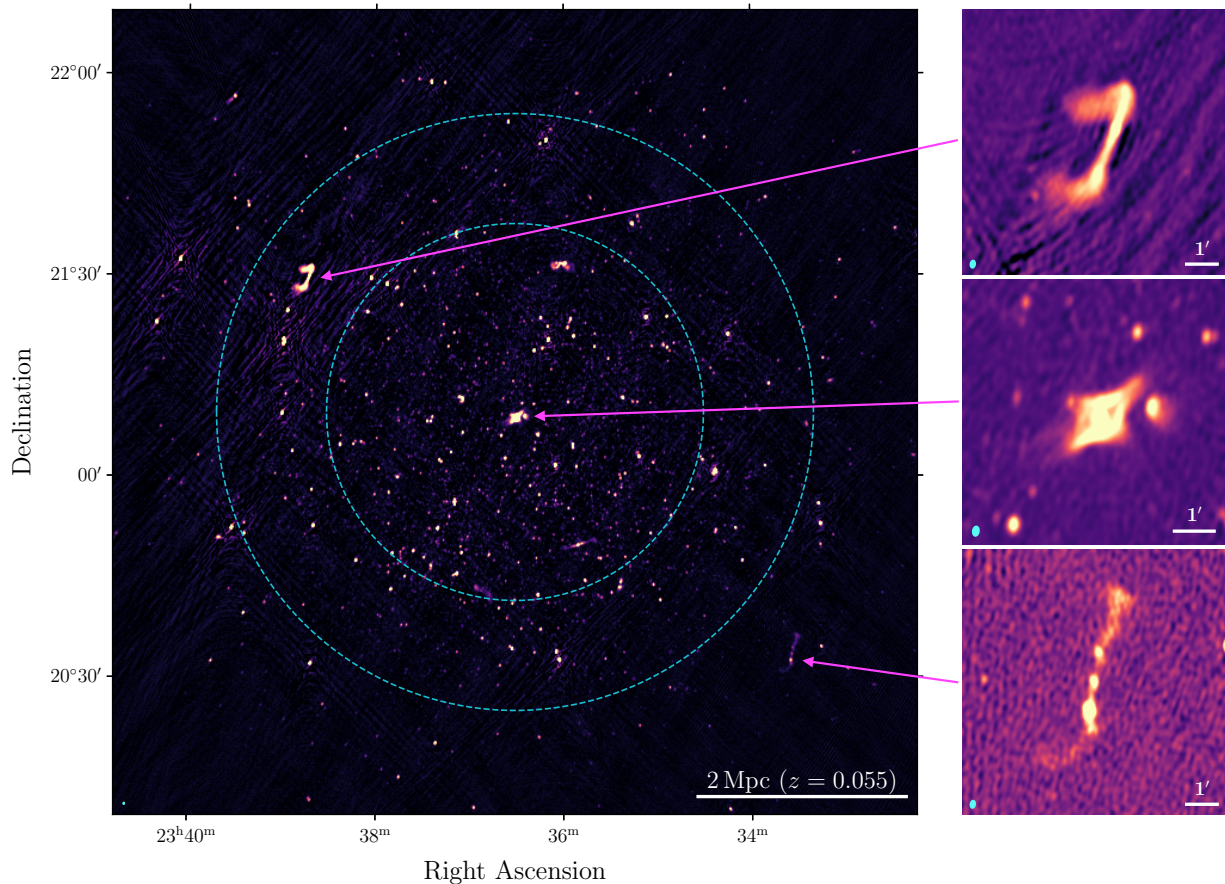


Figure 3.1: $2 \times 2 \text{ deg}^2$ L-band multi frequency synthesis continuum image centred on Abell 2626. This image covers a frequency range of 960–1160 MHz and 1300–1520 MHz, and was imaged with a robust weighting of -1. The image has not been primary beam corrected, however the FWHM of the primary beam at 1520 MHz (the high frequency limit of the image) is given by the inner dashed cyan circle and the outer dashed cyan circle represents the primary beam at 960 MHz (the low frequency limit of the image). The horizontal white bar in the bottom right corner indicates 2 Mpc at the distance of A2626 ($z = 0.058$). The synthesised beam ($8.6'' \times 12.3''$) is shown by the filled light blue ellipse in the bottom left corner. The three stacked panels on the right are zoomed in on interesting sources. The colour stretch in the three zoom-in images is tailored to each source. The synthesised beam is represented by the solid light blue ellipse in the lower left corner of each of the zoom-in panels and the horizontal white bar in each panel indicates 1' for scale.

CARAcad. Given the low altitude of A2626 at the MeerKAT site, the data were flagged for possible shadowing. Possible radio frequency interference (RFI) in the calibrator data was flagged using **AOflogger** (Offringa et al., 2012). I used a flagging strategy that is based only on the Stokes Q data, which is the default ‘first pass’ strategy bundled with **CARAcad**. The next step was to derive the antenna-based complex bandpass for the primary calibrator (J1939-6342). The bandpass solutions were bootstrapped to the secondary calibrator (J2253+1608) to determine the flux scale. The phase corrections based on each scan of the secondary calibrator were applied to the target field. It is important to note here, that the phase solutions of the secondary calibrator were determined using only the baselines in which the calibrator was unresolved, this means that all baselines longer than $7\text{ k}\lambda$ were excluded. With all cross calibration solutions applied to the target field, the target field was also flagged for RFI using the same firstpass **AOflogger** strategy.

3.3.1 L-band continuum imaging

Using the cross-calibrated visibilities, I iteratively imaged and self-calibrated the target field using **WSClean** (Offringa et al., 2014) and **CubiCal** (Kenyon et al., 2018). I performed three rounds of

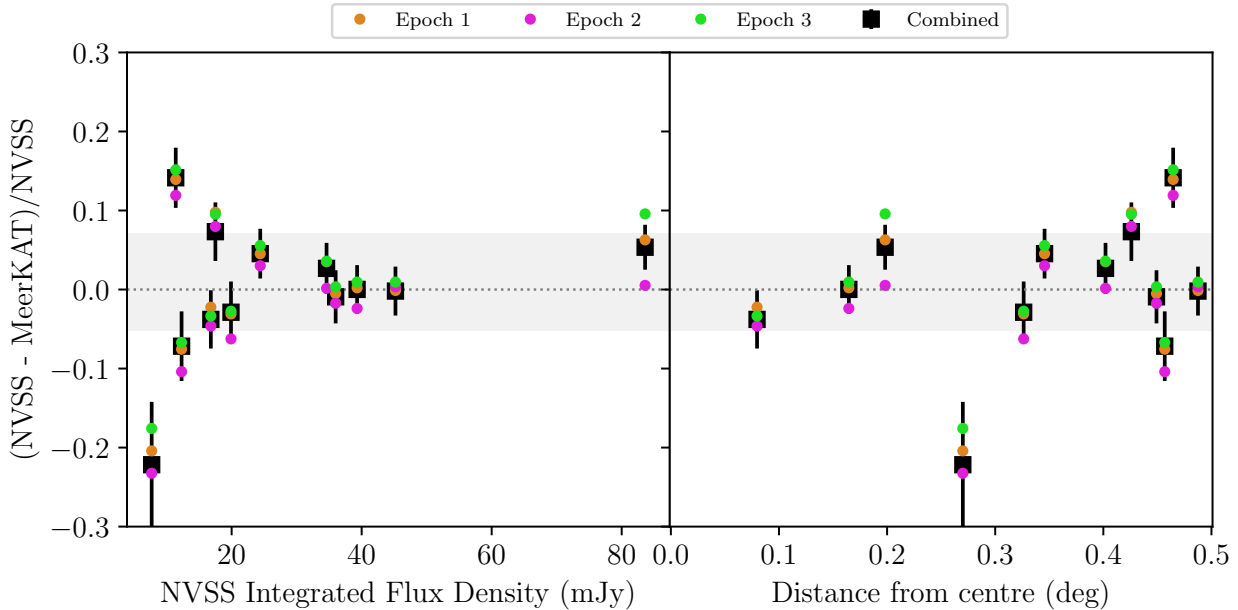


Figure 3.2: Comparison between the integrated fluxes from NVSS and MeerKAT (1300–1520 MHz) for 12 sources unresolved by NVSS. **Left:** the fractional difference as a function of NVSS integrated flux. **Right:** fractional difference as a function of radius from the centre of the pointing. The grey horizontal band in each panel indicates the standard deviation of the differences. Measurements from the combined 3-epoch image are represented by the black squares with errorbars. The coloured circles represent the integrated fluxes measured on the individual epoch images.

self-calibration with solution intervals of two minutes: two rounds of phase only followed by one round of amplitude and phase.

I used multi frequency synthesis (MFS) in `WSClean` to image the radio continuum of the target field for three frequency ranges: *i*) 960 – 1160 MHz (LF image), *ii*) 1300 – 1520 MHz (HF image), and *iii*) 960 – 1160, 1300 – 1520 MHz (full image). Shown in Figure 3.1 is a $2 \times 2 \text{ deg}^2$ MFS image covering 960 – 1160, 1300 – 1520 MHz and imaged with a Briggs robust weighting of $r = -1$, giving a resolution of $8.6'' \times 12.3''$. The sensitivity of the continuum images are close to the confusion limit of MeerKAT making it difficult to determine the RMS noise in the centre of the image. However, at the edge of the images where the thermal noise dominates, the RMS of the HF image is $7.4 \mu\text{Jy}$, the LF image is $11 \mu\text{Jy}$, and the full image is $7.5 \mu\text{Jy}$. The FWHM of the primary beam for the high frequency subset and the low frequency subset are indicated by the dashed cyan circles in Figure 3.1, where the inner circle represents the high frequency primary beam, and the outer circle represents the low frequency primary beam.

To correct the images for the primary beam, I obtained a model of the primary beam at the centre frequency of each frequency chunk using `eidors` (Asad et al., 2021). The centre frequency used for the LF image is 1060 MHz, for the HF image is 1410 MHz, and for the full image I used the average between the primary beam at 1320 MHz and 1160 MHz. I use an average primary beam rather than the measured primary beam to approximate the primary beam at the centre frequency for the full image because I have effectively used a hard RFI mask between 1160 – 1300 MHz and thus do not have data at the centre frequency (1240 MHz).

3.3.1.1 Continuum flux calibration assessment

In order to assess the flux calibration, I compared the continuum source fluxes from the MeerKAT data to previously published continuum measurements in the literature. The first step is to identify

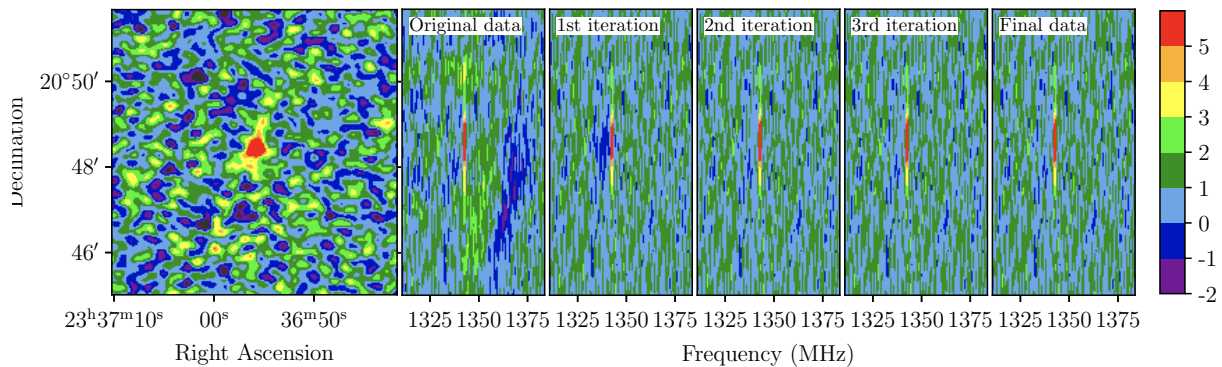


Figure 3.3: The left-most panel shows the spatial extent of an H I detection in one channel. The second panel from the left shows the declination vs frequency centred on the H I detection – the ripple is noticeable through the correlated noise. The subsequent panels also show the declination versus frequency, however highlighting the improvement in the cube with each iteration of the 15th order polynomial spline fit and subsequent subtraction from the data. The right-most panel indicates the final cube.

the point sources in the HF image, I did this using PyBDSF (Mohan & Rafferty, 2015).

PyBDSF is a Python-based source-finding and -characterisation package used to identify sources in radio continuum images. It identifies “islands” of emission above a certain threshold, and then fits 2D Gaussian profiles to the emission in pixels above a second threshold in order to determine the flux density of the source. In order to identify the continuum sources, I set the island threshold to 2.5σ and the pixel threshold to 3.5σ . After fitting, any sources that are smaller than the area of the beam are discarded. The source finding is done on a “detection image”, which in this case is the continuum image prior to primary beam correction. Once all the islands are found, the Gaussians are fitted to the continuum image that has been primary beam corrected so that the correct fluxes can be determined.

I cross-matched the catalogue of continuum sources to a subset of unresolved sources in the NRAO VLA Sky Survey (NVSS, Condon et al., 1998); the sources are cross-matched within a radius of $3''$. This cross-match yielded 12 sources within the FWHM of the MeerKAT primary beam. Using the integrated flux measurements from the PyBDSF catalogue, I compared the fractional difference between the NVSS fluxes and those from the MeerKAT continuum images. In Figure 3.2, the errorbars on each point represent the uncertainty of the integrated flux in the MeerKAT image. I find good agreement between the NVSS and MeerKAT integrated fluxes (see Figure 3.2) at all distances from the pointing centre and at all flux values. The offset and scatter between the MeerKAT and NVSS integrated fluxes are 0.9% and 6% respectively.

3.3.2 H I line data reduction

Using the calibrated visibilities, I subtracted the sky-model created during the self-calibration process (see Section 3.3.1). I then subtracted a 4th order polynomial fit to the visibilities to remove any residual continuum. The data were doppler corrected to a barycentric reference frame and then imaged channel by channel using `WSClean` with a Briggs robust weighting $r = -0.5$, a pixel scale of $2.5''$, and no tapering. I imaged the data over a frequency range of 1300 – 1430 MHz, which covers the cluster at ~ 1342 MHz, the foreground (including Milky Way emission), and some background structures out to $z \sim 0.09$.

After applying the previous data reduction steps, the dirty H I cube appeared to still contain a significant ripple in the data along the frequency axis (see Figure 3.3). My collaborators, T.

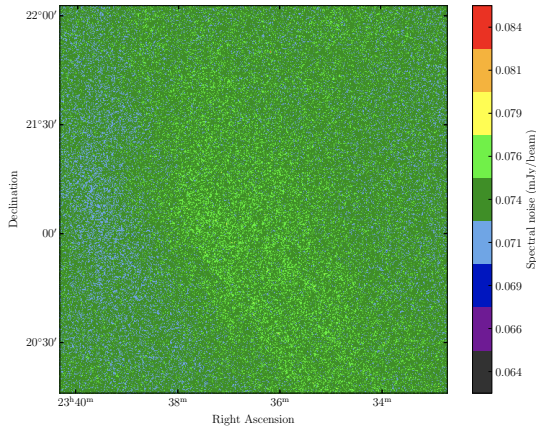


Figure 3.4: Spectral noise map showing the rms noise in the spectrum of each pixel.

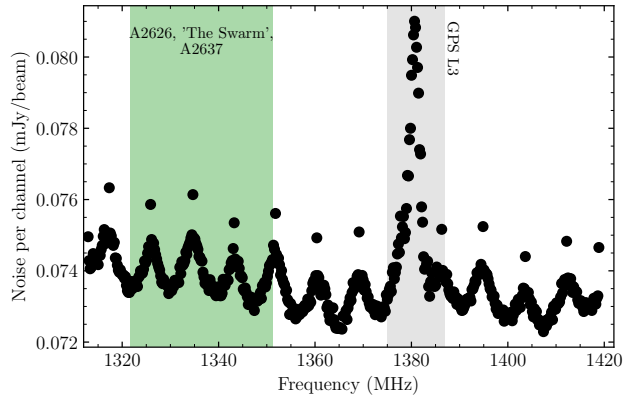


Figure 3.5: Noise per 207 kHz channel as a function of frequency.

Deb and M. Verheijen, and I investigated possible sources of the ripple: the data were flagged for antenna shadowing and the bandpass solutions were stable, but it is still unclear what the origin of it is. Thus, the decision was taken to remove the ripple in the image domain.

In order to remove the ripple, M. Verheijen used the Groningen Image Processing System (GIPSY; Allen et al., 1985; van der Hulst et al., 1992), to fit a 15th order spline to the spectrum of each pixel. The order of the cubic spline was tuned to the 130 MHz bandwidth of the processed HI cube, thus locally, a 2nd order polynomial was fit to 8.7 MHz. This was done over three iterations where the spline was fitted to and subtracted from the data. The initial ripple is evident in the second panel of Figure 3.3. Each iteration of the spline fit and subtraction process is shown in Figure 3.3, with the final “de-rippled” cube shown in the right-most panel. Following the de-rippling procedure, a number of detections were checked for any negative ‘bowls’ on either side of the detection along the frequency axis; as can be seen in the right-most panel of Figure 3.3, there is no negative bowl. From this, we are confident that the fidelity of the HI data is not affected by the spline fit, further evidence to this is the comparison with the ALFALFA detections in Section 3.4.3. It is possible, however, that any residuals from this fit could appear when stacking the global profiles in Chapter 5.

The native resolution of the dirty cube, measured from the antenna pattern (created during the imaging process) varied with increasing frequency from 14.7'' to 13.5'' in the north-south direction, and 6.7'' to 6.1'' in the east-west direction. Based on this information, the de-rippled dirty cube was smoothed to a circular resolution of 15'' independent of frequency. Cleaning of the HI cube was done twice using GIPSY: the first round was done using a mask created by the **Source Finding Application** (SoFiA; Serra et al., 2015) which was run using a clip threshold of 5σ , the cube was re-cleaned to a depth of 0.3σ using masks created after detailed source finding (see the next section).

3.4 Galaxies with HI

3.4.1 HI Source finding

HI source finding in a blind survey is an art – there is no single method or set of criteria that works for every telescope or even across surveys with a single telescope. Thus, the source finding method is typically tailored to the particular data set and the science case of those performing the source finding. For this survey, my collaborators and I chose to use the **SoFiA**³ software package (Serra et al., 2015) to do the source finding. **SoFiA** was designed specifically to automate reliable

³<https://github.com/SoFiA-Admin/SoFiA>

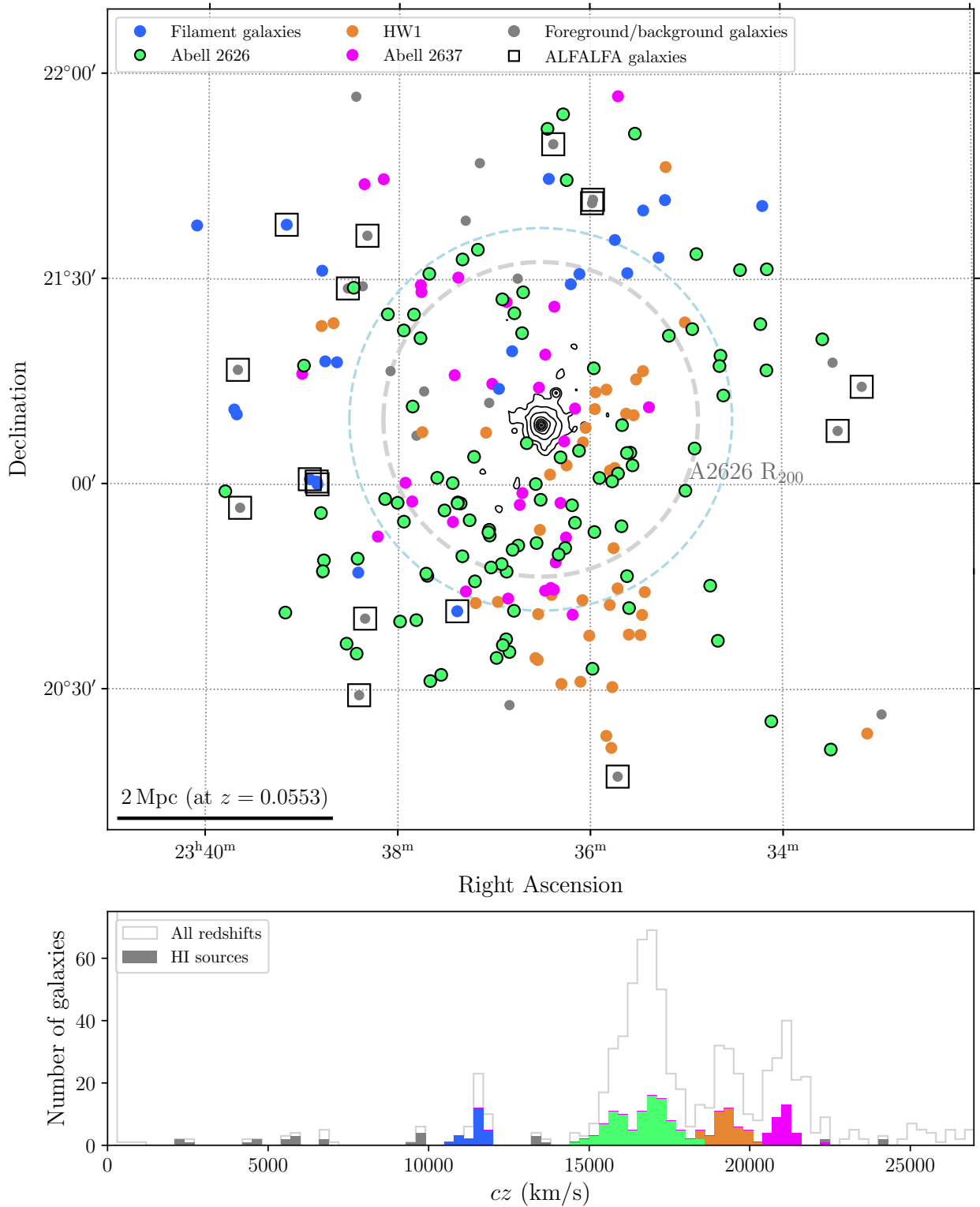


Figure 3.6: **Top:** Sky distribution of the H I detections identified with SoFia. The inner dashed grey circle represents the R_{200} of A2626, and the outer light blue dashed circle represents the primary beam FWHM at the frequency of the cluster. The black contours represent the x-ray emission from A2626 taken from ROSAT images. The data points representing the H I detections are coloured by the spectral over-density of which they are a member. The open squares represent the galaxies also detected by ALFALFA that are used in the H I flux comparison in Section 3.4.3. **Bottom:** Redshift histogram of the H I detections. The filled histogram represents the H I detections. Also shown for reference, by the open grey histogram, is the optical redshift catalogue for the field from Healy et al. (submitted) (see Chapter 4).

source finding in HI spectral line data cubes. We chose to use `SoFiA` as it has proven to be very adept at detecting real sources that are very close to the noise (Serra et al., 2015), `SoFiA` is also publicly available which means that the inclusion of the parameter file used in this source finding run would make our results easy to reproduce. The version of `SoFiA` my collaborators, T. Deb and M. Verheijen, used to perform the source finding was `SoFiA-2`⁴ (Westmeier et al., 2021); this version of the application is written in C.

`SoFiA` has the ability to perform spatial and spectral smoothing using a number of different kernels, and then combine all the identified sources into one source list. To optimise the column density sensitivity, the cube was smoothed to four different spatial resolutions (15", 20", 25", and 30") and three velocity resolutions (45 km s⁻¹, 90 km s⁻¹, and 180 km s⁻¹). Note that 15" spatial and 45 km s⁻¹ spectral are the native resolutions of the cube used to perform the source finding. `SoFiA-2` was run four times (once for each of the spatial resolutions), each time smoothing the cube spatially in increments of 5" from 15" up to the desired resolution as well as smoothing spectrally. Sources were identified using a 3.5 σ threshold and requiring the reliability value to be above 90%.

Each source finding run produced a catalogue of detections that was then manually combined to create a single catalogue of 404 unique HI detections. Each detection was then checked for a possible optical counterpart. An optical source was considered to be the counterpart to the HI detection if the optical redshift of the galaxy coincided with the redshift of the detection. The redshift catalogue used is discussed in Chapter 4. Where there was no optical redshift to confirm the link between an optical source and the HI detection, optical counterparts were associated with the detection based on proximity to the HI centre (typically the optical source had to be located within the mask of the HI detection), and colour – HI rich galaxies tend to be blue from ongoing star formation, however red galaxies are known to contain detectable HI (e.g. Serra et al., 2012). Possible counterparts were only excluded on the basis of colour if the galaxy was redder than the red sequence of A2626, HW1, or A2637. Where there were multiple possible counterparts for a single HI detection, preference was given to the bluer galaxy. Of the 404 unique detections identified by `SoFiA` based on the detection criteria, 219 have optical counterparts – 161 of which have an optical redshift confirming the HI detection.

It is possible that the 185 HI detections excluded from the final source catalogue are real, however using a 3.5 σ threshold and 90% reliability limit increased the number of false detections. Pushing the `SoFiA` settings to such low thresholds came at the cost of an increased probability of false detections, however in order to detect the low surface brightness HI emission in the cluster galaxies, this was a necessary cost. In a blind survey such as this, and with such a large spectral resolution (45 km s⁻¹), it is difficult to assess the reliability of the detections without other information such as the optical images and spectroscopy. In a cluster environment, it is highly possible that HI has been stripped from galaxies falling into the cluster and is thus free-floating without an optical counterpart; however, in the context of the analysis presented in the later chapters of this thesis, excluding such detections does not change the scientific results.

Many of the final list of 219 detections were detected at multiple spatial resolutions. The masks for the final list of sources were thus based on the largest resolution where the galaxy was detected so as to not exclude the lower surface density emission typically located in outskirts of the HI disk. The masks were also manually dilated by a pixel in all directions. These dilated optimum masks were then used to re-clean the cube from which the global profiles and global properties could then be determined. The sky positions of the 219 detections, as well as the redshift distribution of the sources is presented in Figure 3.6. It is clear from the histogram in Figure 3.6 that many of the detected HI sources are associated with A2626 (highlighted in the light green).

⁴<https://github.com/SoFiA-Admin/SoFiA-2>

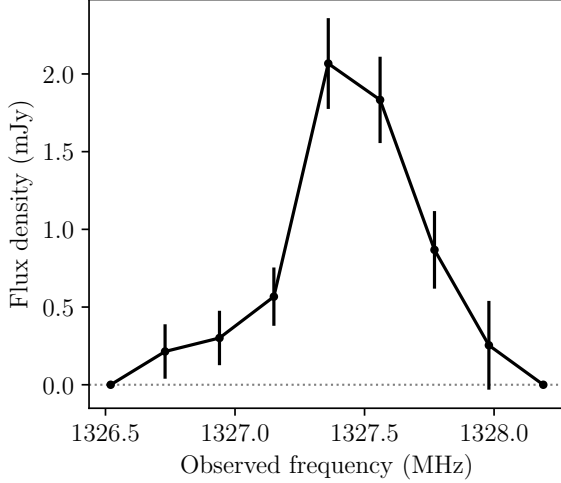


Figure 3.7: A global profile (black line) of one of the HI detections identified by SoFiA. The errorbars are determined from the variance of the flux density from 24 reference spectra.

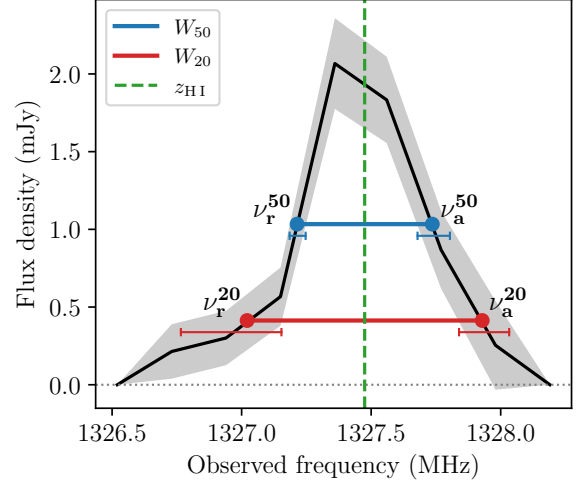


Figure 3.8: Global profile (black line) of the HI detection in Figure 3.7. The grey band represents the upper and lower limits of the spectrum set by the flux density errors per channel. The vertical dashed green line indicates the frequency of the redshift determined from the spectrum. The red and blue horizontal lines show the line width at 20% and 50% of the peak flux, the intervals on the approaching (ν_a) and receding (ν_r) sides indicate the uncertainty on the frequency of the two sides.

3.4.2 HI global properties

Using the `flux` task in GIPSY, the global HI profiles for each galaxy were extracted from the primary beam corrected cube. Only the flux contained within the masks created by SoFiA was considered to be part of the galaxy. The flux errors for each channel were determined from the variance in the same channel of 24 “reference” spectra. The reference spectra were extracted in the same manner as the target spectrum from HI line-free regions around the target galaxy. An example HI spectrum with the flux errors in each channel is shown in Figure 3.7.

The global profile enables the measurement of a number of important global properties: the integrated flux (S_{HI}), the HI redshift (z_{HI}), and the line width which is measured at both the 50% (W_{50}) and 20% (W_{20}) peak flux level. From the integrated flux and the redshifts, the HI mass can also be determined. The integrated flux and line widths are important properties that can be compared to measurements made of the same galaxy by other telescopes, thus verifying the quality of the data calibration (see Section 3.4.3).

The line width for each galaxy is determined by the difference between the approaching (ν_a) and receding (ν_r) side of the spectrum. Due to the coarseness of the MeerKAT HI spectra, it was necessary to interpolate the flux values between channels in order to determine the frequency at which 20% and 50% of the peak flux occurs. I used a simple linear interpolation routine to determine the flux values between channels. The ν_r and ν_a were determined by starting from outside the spectrum emission and moving towards the centre of the spectrum where the emission peaks. The points for 20% and 50% of the peak flux level are indicated in Figure 3.8 by red and blue circles respectively. The galaxy’s W_{50} and W_{20} are thus given in the rest-frame by:

$$W = \frac{|\nu_a - \nu_r|}{\nu_e} c(1 + z), \quad (3.1)$$

where ν_e is the rest-frame frequency of the 21-cm HI line (1420.4057517667 MHz), c is the speed of

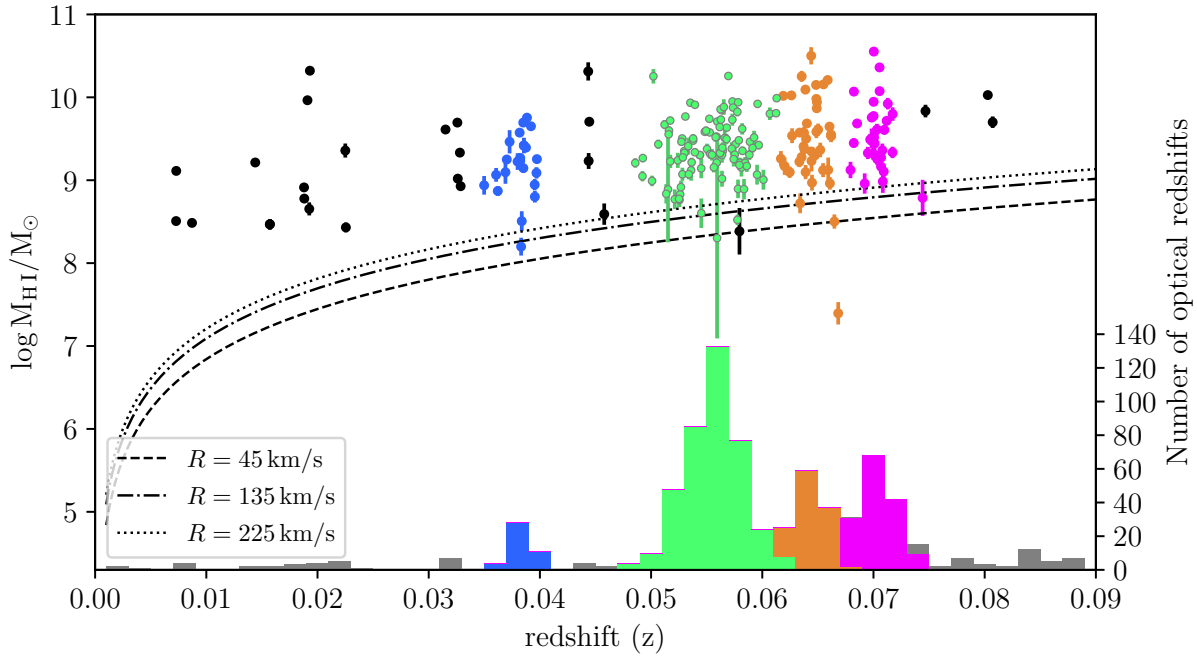


Figure 3.9: HI mass as function of redshift. The coloured round data points indicate the 219 HI detections; the colours correspond to the spectral over-densities highlighted in the histogram, and the black data points correspond to the grey histograms, these sources are not associated with any over-density. The dashed, dot-dashed, and dotted lines represent the 3σ HI mass limit of the different velocity resolutions (45 km s^{-1} , 135 km s^{-1} , and 225 km s^{-1} respectively) used in the source finding.

light ($299792.458 \text{ km s}^{-1}$), and z is the HI redshift determined at the frequency half way between ν_r^{20} and ν_a^{20} (shown by the dashed green vertical line in Figure 3.8). The errors on ν_a and ν_r were calculated by determining the frequencies where

$$p_{\text{level}} = f \pm u(f). \quad (3.2)$$

p_{level} is the value of 20% or 50% of the peak flux, f is the flux density of the spectrum and $u(f)$. $f \pm u(f)$ is represented by the shaded grey region in Figure 3.8, and the frequency errors are shown by the coloured intervals below the $\nu_{a/r}$ markers. The error on the line widths are determined by combining the individual errors on ν_a and ν_r in quadrature.

The integrated flux is determined by

$$S_{\text{HI}} = \int S_v dv \quad (3.3)$$

which in practice becomes $S_{\text{HI}} = \sum S_i \Delta v$, where S_i is the flux density in each channel and Δv is the channel velocity width. The error on S_{HI} was calculated by propagating the individual flux errors per channel and adding in quadrature. Having determined S_{HI} , I can also determine the HI mass of each galaxy based on the formulation from Wieringa et al. (1992) under the assumption that the HI cloud is spherical and optically thin with a uniform internal velocity distribution:

$$\frac{M_{\text{HI}}}{M_{\odot}} = \frac{2.36 \times 10^5}{1+z} \left(\frac{D_L(z)}{\text{Mpc}} \right)^2 \left(\frac{\int S_v dv}{\text{Jy km s}^{-1}} \right) \quad (3.4)$$

where z is the redshift of the galaxy, $D_L(z)$ is the luminosity distance, and $\int S_v dv$ is the rest-frame integrated flux.

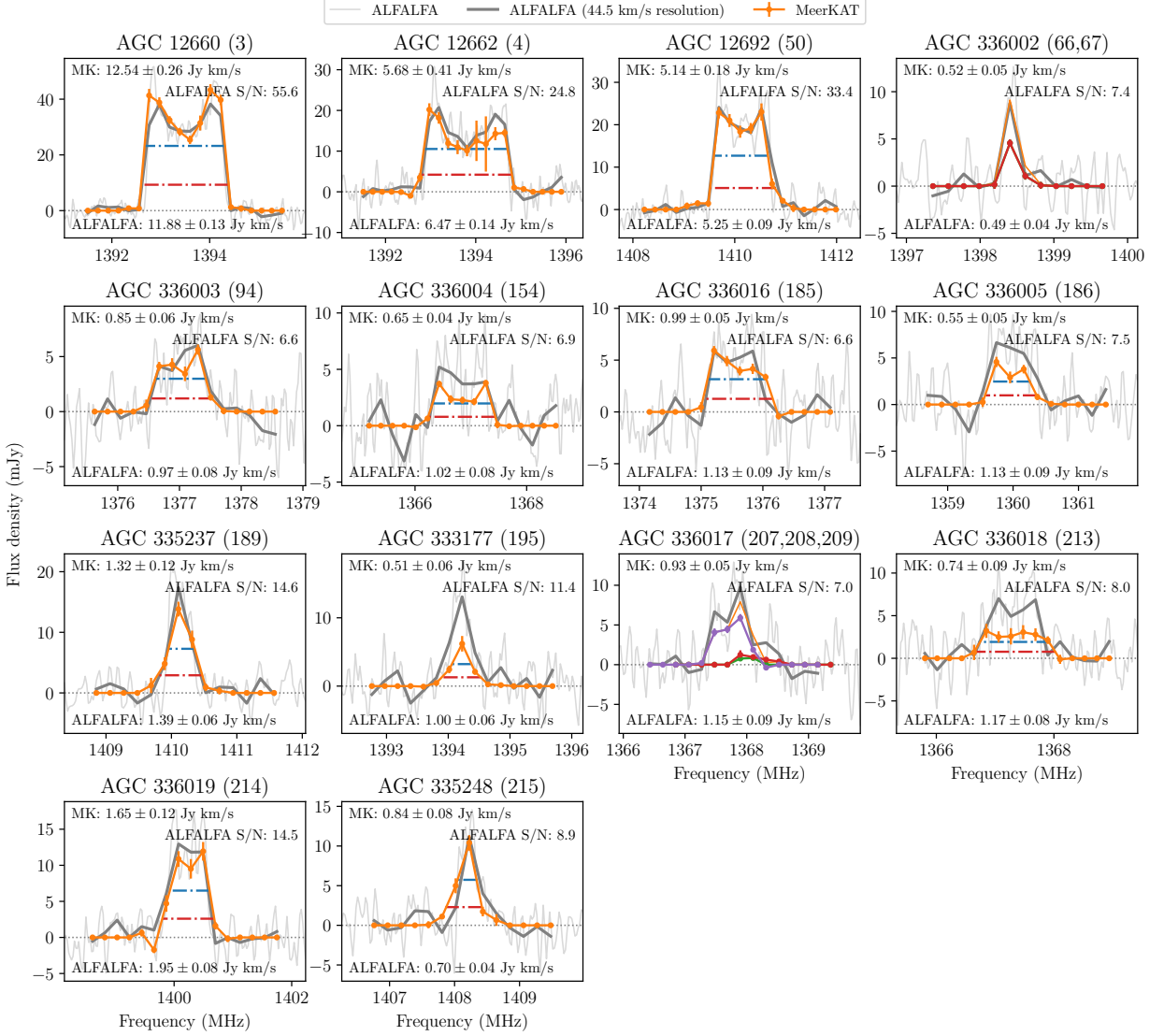


Figure 3.10: Global profiles for the 14 galaxies identified in the ALFALFA survey that are also identified in the MeerKAT HI data. The MeerKAT spectra are shown in orange, the ALFALFA spectra in light grey (original spectral resolution) and dark grey (MeerKAT spectral resolution). The red and blue horizontal dot-dash lines indicate where the W_{20} and W_{50} respectively are measured for the MeerKAT spectra. AGC 336002 and AGC 336017 are cross-matched multiple MeerKAT detections within the Arecibo beam; the orange spectrum represents the sum of the individual MeerKAT spectra which are plotted in red, purple, and green.

As mentioned in Section 3.2, based on the theoretical properties of the instrument and the observation time, the expected 3σ HI mass limit for a galaxy with a line width of 300 km s^{-1} at the distance of the cluster was $M_{\text{HI}3\sigma \text{ lim}} = 2 \times 10^8 M_{\odot}$. Figure 3.9 shows the distribution of the HI masses for the detected sources as a function of redshift. The dashed and dotted grey and red lines indicate mass limits based on the source finding criteria (grey) and the predicted mass limit (red).

3.4.3 HI data quality checks

The final data quality check to be performed was the comparison of the integrated fluxes and line widths with values in the literature. A2626 is located in the footprint of the ALFALFA, a large-area blind HI survey using the Arecibo Radio Telescope. Cross-matching the 219 HI detections from MeerKAT with the $\alpha.100$ catalogue, there are 14 ALFALFA galaxies which have MeerKAT counterparts. Only 12 of the ALFALFA galaxies had one MeerKAT counterpart within the large

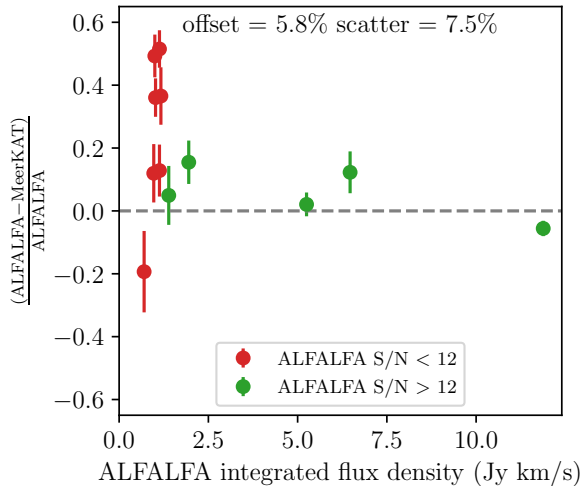


Figure 3.11: Fractional difference between ALFALFA and MeerKAT integrated fluxes as a function of the ALFALFA integrated flux for 12 non-blended galaxies. The green symbols represent galaxies with an ALFALFA S/N value greater than 12, red symbols represent profiles with a lower S/N value.

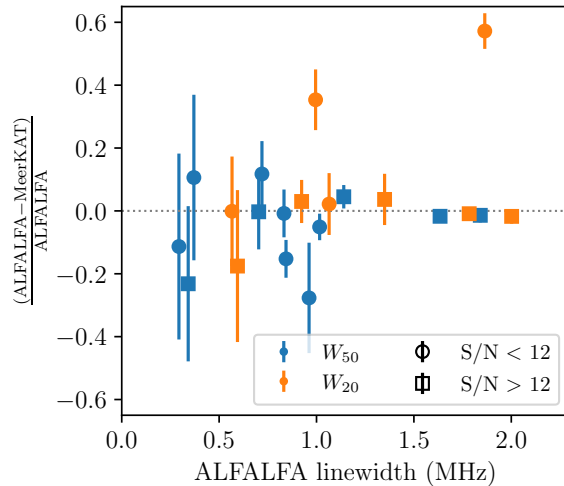


Figure 3.12: Fractional difference between the W_{50} (blue) and W_{20} (orange) line widths for the 12 non-blended galaxies observed by both ALFALFA and MeerKAT. The square symbols represent galaxies with an ALFALFA S/N value greater than 12, circle symbols represent profiles with a lower S/N value.

3.3' Arecibo beam. For this comparison, it was very important not to have any possible confusion between HI sources as this could lead to an unfair comparison. All 12 non-blended sources are located at distances beyond the FWHM of the MeerKAT primary beam from the centre of the cluster, Figure 3.6 shows the locations of these 12 galaxies through the positions of the open squares. The direct comparison between the MeerKAT HI spectra and all 14 ALFALFA HI spectra (including the 2 blended ALFALFA sources) is shown in Figure 3.10.

I quantify the comparison between the MeerKAT and ALFALFA integrated fluxes using the fractional offset between the two as shown in Figure 3.11. There is good agreement between the MeerKAT and ALFALFA measurements for the galaxies which have an ALFALFA S/N > 12: no significant offset (in this case, I do not consider the 5.8% offset as significant), and a scatter of 7.5%. Given that all 12 galaxies lie outside the FWHM of the primary beam, the consistency of the fluxes indicates that there are no issues with either the primary beam correction or the general calibration.

Lastly, I compared the measured line widths. In order to do this, I re-sampled the higher resolution ALFALFA spectra ($\Delta v = 11 \text{ km s}^{-1}$) to the same coarse resolution as the MeerKAT spectra ($\Delta v = 44.5 \text{ km s}^{-1}$) so that I could avoid introducing any possible offset between the line widths due to the differences in velocity resolution. I also measured the ALFALFA line widths in the same way as the MeerKAT line widths (see Section 3.4.2). Figure 3.12 shows the fractional difference comparisons between the W_{50} and W_{20} line widths for MeerKAT and ALFALFA. With the exception of a few low S/N detections (determined as ALFALFA S/N < 12), the measurements of the line widths from the two surveys are consistent.

The analysis represented by Figures 3.11 and 3.12 shows that the calibration of the MeerKAT HI data presented in this chapter is consistent with previously published data covering this field.

3.5 Summary

This chapter has discussed the calibration, imaging, and source finding of new H I observations of the galaxy cluster A2626 with MeerKAT. The data quality and images I have presented highlight the impressive sensitivity of MeerKAT. And the high number of H I detections in the cluster suggest an environment that is richer in H I than expected based on previous observations of other clusters. As discussed in Section 3.4.1, 219 reliable H I detections were found with optical counterparts using the SoFiA source finding software. The comparison of the continuum fluxes to NVSS (Section 3.3.1), as well as the H I integrated fluxes and line widths to ALFALFA (Section 3.4.3), show that the MeerKAT data are consistent with previously published surveys.

The sky distribution (Figure 3.6) and redshift distribution of the H I masses (Figure 3.9) paint a picture of an environment around A2626 that is rich with H I detections. The measured 3σ H I mass sensitivity for a galaxy with a 300 km s^{-1} line width at the distance of the cluster ($\sim 3.6 \times 10^8 M_{\odot}$) makes this dataset comparable to the Westerbork Coma Survey in Chapter 2. In the following chapters, I present the optical redshift catalogue for this field (Chapter 4), as well as an analysis of the global and local cosmic environments around A2626. I then use the identified environments in Chapter 5 and probe the gas content of galaxies not directly detected in H I to understand how the different local environments and the cluster affect the evolution of the galaxies.

References

- Abell G. O., 1958, *The Astrophysical Journal Supplement Series*, 3, 211
- Allen R. J., Ekers R. D., Terlouw J. P., 1985, in Gesù V. D., Scarsi L., Crane P., Friedman J., Leivaldi S., eds, *Data Analysis in Astronomy, Proceedings of the 1st Workshop held in Erice, Italy, 1984*, Ettore Majorana International Science Series. Plenum Press, New York, p. 271, <https://ui.adsabs.harvard.edu/abs/1985daa.conf..271A/abstract>
- Asad K. M., et al., 2021, *Monthly Notices of the Royal Astronomical Society*, 502, 2970
- Balogh M. L., Morris S. L., Yee H. K. C., Carlberg R. G., Ellingson E., 1997, *The Astrophysical Journal*, 488, L75
- Boselli A., et al., 2020, pp 1–26
- Bower R. G., Ellis R. S., Rose J. A., Sharples R. M., 1990, *The Astronomical Journal*, 99, 530
- Bravo-Alfaro H., Cayatte V., van Gorkom J. H., Balkowski C., 2000, *The Astronomical Journal*, 119, 580
- Cava A., et al., 2009, *Astronomy and Astrophysics*, 495, 707
- Chung A., van Gorkom J. H., Kenney J. D. P., Crowl H., Vollmer B., 2009, *The Astronomical Journal*, 138, 1741
- Condon J. J., Cotton W. D., Greisen E. W., Yin Q. F., Perley R. A., Taylor G. B., Broderick J. J., 1998, *The Astronomical Journal*, 115, 1693
- Cooper M. C., Gallazzi A., Newman J. A., Yan R., 2010, *Monthly Notices of the Royal Astronomical Society*, 402, 1942
- Deb T., et al., 2020, *Monthly Notices of the Royal Astronomical Society*, 494, 5029
- Dressler A., 1980, *The Astrophysical Journal*, 236, 351

- Fasano G., et al., 2006, *Astronomy and Astrophysics*, 445, 805
- Gavazzi G., O'Neil K., Boselli A., van Driel W., 2006, *Astronomy and Astrophysics*, 449, 929
- Giovanelli R., Haynes M. P., Chincarini G. L., 1981, *The Astrophysical Journal*, 247, 383
- Giovanelli R., Haynes M. P., Chincarini G. L., 1982, *The Astrophysical Journal*, 262, 442
- Gitti M., 2013, *Monthly Notices of the Royal Astronomical Society: Letters*, 436, L84
- Gogate A. R., Verheijen M. A. W., Deshev B. Z., van Gorkom J. H., Montero-Castaño M., Hulst J. M. v. d., Jaffé Y. L., Poggianti B. M., 2020, *Monthly Notices of the Royal Astronomical Society*, 496, 3531
- Gomez P. L., et al., 2003, *The Astrophysical Journal*, 584, 210
- Haynes M. P., Giovanelli R., 1986, *The Astrophysical Journal*, 306, 466
- Haynes M. P., et al., 2011, *The Astronomical Journal*, 142, 170
- Haynes M. P., et al., 2018, *The Astrophysical Journal*, 861, 49
- Healy J., Willner S., Verheijen M., Blyth S.-L., 2021, *Astronomical Journal*
- Hess K. M., Jarrett T. H., Carignan C., Passmoor S. S., Goedhart S., 2015, *Monthly Notices of the Royal Astronomical Society*, 452, 1617
- Hubble E., Humason M. L., 1931, *The Astrophysical Journal*, 74, 43
- Ignesti A., Gitti M., Brunetti G., O'Sullivan E., Sarazin C., Wong K., 2018, *Astronomy and Astrophysics*, 610, 89
- Jonas J. L., MeerKAT Team 2016, in Taylor R., Camilo F., Leeuw L., Moodley K., eds, *MeerKAT Science: On the Pathway to the SKA. Proceedings of Science*, Stellenbosch, p. 1, doi:10.22323/1.277.0001, <http://pos.sissa.it/>
- Józsa G. I. G., et al., 2020, *ASPC*, 527, 635
- Kent B. R., et al., 2008, *Astronomical Journal*, 136, 713
- Kenyon J. S., Smirnov O. M., Grobler T. L., Perkins S. J., 2018, *Monthly Notices of the Royal Astronomical Society*, 478, 2399
- Lah P., et al., 2007, *Monthly Notices of the Royal Astronomical Society*, 376, 1357
- McDonald M., Gaspari M., McNamara B. R., Tremblay G. R., 2018, *The Astrophysical Journal*, 858, 45
- Mohan N., Rafferty D., 2015, *Astrophysics Source Code Library*, p. ascl:1502.007
- Mohr J. J., Wegner G., 1997, *The Astronomical Journal*, 114, 25
- Mohr J. J., Geller M. J., Wegner G., 1996, *The Astronomical Journal*, 112, 1816
- Moretti A., et al., 2019, *The Astrophysical Journal*, 889, 9
- Offringa A. R., Van De Gronde J. J., Roerdink J. B., 2012, *Astronomy and Astrophysics*, 539, 95
- Offringa A. R., et al., 2014, *Monthly Notices of the Royal Astronomical Society*, 444, 606

- Poggianti B. M., et al., 2016, *The Astronomical Journal*, 151, 78
- Poggianti B. M., et al., 2019, *The Astrophysical Journal*, 889
- Ramatsoku M., et al., 2019, *Monthly Notices of the Royal Astronomical Society*, 487, 4580
- Rizza E., Loken C., Bliton M., Roettiger K., Burns J. O., Owen F. N., 2000, *The Astronomical Journal*, 119, 21
- Rose J. A., Bower R. G., Caldwell N., Ellis R. S., Sharples R. M., Teague P., 1994, *The Astronomical Journal*, 108, 2054
- Serra P., et al., 2012, *Monthly Notices of the Royal Astronomical Society*, 422, 1835
- Serra P., et al., 2015, *Monthly Notices of the Royal Astronomical Society*, 448, 1922
- Serra P., et al., 2019, *Astronomy & Astrophysics*
- Solanes J. M., Manrique A., García-Gómez C., González-Casado G., Giovanelli R., Haynes M. P., 2001, *The Astrophysical Journal*, 548, 97
- Tonnesen S., Bryan G. L., van Gorkom J. H., 2007, *The Astrophysical Journal*, 671, 1434
- Verheijen M., van Gorkom J. H., Szomoru A., Dwarakanath K. S., Poggianti B. M., Schiminovich D., 2007, *The Astrophysical Journal*, 668, L9
- Westmeier T., et al., 2021, *Monthly Notices of the Royal Astronomical Society*, pp 1–16
- Wieringa M. H., de Bruyn A. G., Katgert P., 1992, *Astronomy and Astrophysics*, 256, 331
- Wong K.-W., Sarazin C. L., Blanton E. L., Reiprich T. H., 2008, *The Astrophysical Journal*, 682, 155
- Zwaan M., van Dokkum P., Verheijen M., Briggs F., 2001, *Gas and Galaxy Evolution*, 240, 640
- van der Hulst J. M., et al., 1992, in Worrall D. M., Biemesderfer C., Barnes J., eds, Vol. 25, *Astronomical Data Analysis Software and Systems I*, A.S.P. Conference Series. p. 131, <https://ui.adsabs.harvard.edu/abs/1992ASPC...25..131V/abstract>



“ ‘Out-of-the-box’ is where I live.” – Lt. Kara ‘Starbuck’ Thrace
(Battlestar Galactica, Season 1: The Hand of God)

Chapter 4

Abell 2626 and friends: large and small scale structure

J. Healy,^{1,2} S.P. Willner³, M.A.W. Verheijen¹ and S-L. Blyth²

Based on Healy, Willner, Verheijen & Blyth, accepted for publication in the *Astronomical Journal* on 14 June 2021

¹ Kapteyn Astronomical Institute, University of Groningen, Landleven 12, 9747 AV Groningen, the Netherlands

² Department of Astronomy, University of Cape Town, Private Bag X3, Rondebosch 7701, South Africa

³ Center for Astrophysics | Harvard & Smithsonian, 60 Garden Street, Cambridge, MA 02138, USA

Abstract

New MMT/Hectospec spectroscopy centred on the galaxy cluster A2626 and covering a ~ 1.8 deg² area out to $z \sim 0.46$ more than doubles the number of galaxy redshifts in this region. The spectra confirm four clusters previously identified photometrically. A2625, which was previously thought to be a close neighbour of A2626, is in fact much more distant. The new data show six substructures associated with A2626 and five more associated with A2637. There is also a highly collimated collection of galaxies and galaxy groups between A2626 and A2637 having at least three and probably four substructures. At larger scales, the A2626–A2637 complex is not connected to the Pegasus–Perseus filament.

4.1 Introduction

Large, wide-area spectroscopic surveys such as the Sloan Digital Sky Survey (SDSS; Strauss et al., 2002; Smee et al., 2012), 2dF Galaxy Redshift Survey (2dFGRS; Colless et al., 2001), and VIMOS Public Extragalactic Survey (VIPERS; Guzzo et al., 2013) have revealed the distribution of galaxies in the Universe. The emerging picture, now referred to as the “Cosmic Web,” is a complex and interconnected set of structures (de Lapparent et al., 1986; Bond et al., 1996). These include megaparsec-long one-dimensional structures (“filaments”), thin two-dimensional sheets (“walls”), and vast empty spaces (“voids”) surrounded by walls. Galaxy clusters are located where multiple filaments intersect (e.g., Aragón-Calvo et al., 2010; Cautun et al., 2014; Malavasi et al., 2017).

The early catalogues of galaxy clusters (Abell, 1958; Zwicky et al., 1961) were constructed by identifying apparent over-densities of galaxies on photographic plates. Lucey (1983) and Struble & Rood (1987) estimated that as many as 25% of such identified clusters may be chance superpositions. The only way to confirm cluster members or even the existence of clusters at all is through extensive spectroscopy or at least multi-band imaging. Identifying cluster members can become particularly problematic when foreground and background galaxy over-densities overlap spatially, e.g., when the line of sight is along a cosmic filament. Early spectroscopy of Abell clusters was usually limited to the brightest galaxies in the field (for a summary, see Struble & Rood and references therein). Struble & Rood commented that within their collation, as many as 5% of the cluster redshifts may be incorrect and warned about the reliability of cluster redshifts determined from 1–3 galaxies. They endorsed the recommendation from Postman et al. (1986) that reliable cluster redshift measurements need to be made from at least five galaxies.

In the hierarchical structure-formation scenario, large structures such as galaxy clusters are built through successive merging and accretion of galaxies and groups of galaxies. The imprint of this accretion is told through the kinematic substructure within the cluster (e.g. Dressler & Shectman, 1988; Hou et al., 2012). Identifying and studying substructure is an important step to uncovering how galaxy clusters form. Analysis of substructures can help to understand the local environments in which galaxies are located. The interaction between the cluster proper and the smaller group or substructure environment affects the evolution of the constituent galaxies. Processes such as galaxy–galaxy interactions are more likely to occur in the more compact environments, whereas processes such as ram-pressure stripping are more common in cluster environments where the intracluster medium (ICM) is denser. Understanding these effects may shed light of the causes of observed phenomena such as the morphology–density relation (Dressler, 1980) in which dense environments such as clusters show a majority of red, quiescent galaxies whereas low-density environments have a majority of bluer star-forming galaxies.

The galaxy cluster at the centre of this work is Abell 2626 (officially ACO 2626 but hereafter A2626; Abell, 1958). A2626 is thought to be undergoing a merger between the main cluster and an accreted sub-cluster (Mohr et al., 1996; Mohr & Wegner, 1997). Using ~ 150 new redshifts, Mohr et al. (1996) found evidence for a potential sub-cluster southwest of the A2626 core. Newer spectroscopy from the WIder-field Nearby Galaxy cluster Survey (WINGS; Fasano et al., 2006; Cava et al., 2009) improved the redshift coverage for A2626, but Ramella et al. (2007) found no evidence of substructure in the cluster. These conflicting results are not surprising: different substructure algorithms are sensitive to different types of clustering (spatial or spectral) as well as the number of galaxies in the input catalogue.

If A2626 is really undergoing a merger, it can act as a natural laboratory for the effects of mergers on constituent galaxies. At a distance of 250 Mpc and in a part of the sky that is not well surveyed, this cluster has not been extensively studied. Most of the recent interest in this cluster has focused on the intriguing “kite” source, visible at radio wavelengths at the centre of the cluster (Ignesti et al., 2018). The cluster has been observed in X-rays, initially by Rizza et al. (2000),

and Wong et al. (2008); both combined detailed X-ray observations with observations of the radio continuum to study the interplay between the physical processes that emit in both wavelength regimes. They found X-ray enhancements to the northeast and southwest of the cluster centre and a significant jump in the radial gas temperature profile, which they suggested may be due to a past or ongoing merger event. The cluster is also home to six candidate “jellyfish” galaxies (Poggianti et al., 2016), extreme examples of galaxies undergoing ram-pressure stripping. One of the six, JW 100, a confirmed jellyfish galaxy, has been the centre of a multi-wavelength (X-ray–radio) study to understand the interplay between the stripping processes and the stellar and gas components of the galaxy (e.g., Moretti et al., 2019; Poggianti et al., 2019). These studies have shown how important multi-wavelength data are to understand how the environmentally driven processes affect the evolution of galaxies, but equally important is a thorough census of the galaxies in the environment.

This chapter presents new and deep spectroscopy of A2626 and its surroundings. The redshifts identify new members of A2626 and the nearby A2637 (Abell, 1958) and reveal more of the large-scale structure in which these two clusters are embedded. The redshifts also identify a number of new structures in this region out to $z \sim 0.46$.

The new spectroscopy presented in this chapter complements new radio observations with MeerKAT centred on A2626 (Healy et al., 2021a), which have added the previously unattainable neutral hydrogen (HI) measurements of galaxies in the cluster and its surrounds. The MeerKAT data can facilitate the study of HI in galaxies out to $z \sim 0.46$ due to MeerKAT’s wide bandwidth. While HI has yet to be directly detected beyond $z \sim 0.376$ (Fernández et al., 2016), optical redshifts can be used for HI stacking—a technique where the HI line spectra of a sample of galaxies are aligned and coadded to create an average spectrum with a higher sensitivity than the individual spectra (e.g., Healy et al., 2019; Chowdhury et al., 2020).

The chapter is organised as follows: Section 4.2 presents the new spectroscopy. Section 4.3 uses the new redshifts along with published ones to update the picture of the large-scale structure centred on A2626 at $z \lesssim 0.46$. Section 4.4 provides updated measurements of the cluster size, and Section 4.5 describes substructures in and around A2626 and A2637. This chapter uses throughout a standard, flat Λ CDM cosmology with $H_0 = 70 \text{ km s}^{-1} \text{ Mpc}^{-1}$, $\Omega_M = 0.3$, $\Omega_\Lambda = 0.7$, and $h = 0.7$. All magnitudes are given in the AB system.

4.2 Spectroscopy

4.2.1 Literature redshifts

WINGS (Fasano et al., 2006) is a multi-wavelength imaging and spectroscopic survey of 77 galaxy clusters at Galactic latitude $|b| \geq 20^\circ$ selected from three flux-limited X-ray surveys. The main target of this work, A2626, is one of the clusters in the WINGS sample. WINGS used existing literature redshifts for the clusters in their sample in combination with their own follow-up spectroscopy survey (WINGS-SPE, Cava et al., 2009) to determine cluster membership. The targets for the WINGS-SPE were selected from the WINGS imaging survey (Varela et al., 2009), which for A2626, only extended to $r = 0.7 R_{200}$. (R_{200} is the radius inside which the mean density of the cluster is 200 times the critical density of the Universe. For A2626, $R_{200} = 1.64 \text{ Mpc} = 25'.27$ at $z = 0.0557$, Cava et al. 2009.) We are interested in the substructure of the cluster as a whole and understanding how the average gas content varies across the cluster based on local environment. For this, we need to be able to characterise the environment of the cluster beyond the R_{200} .

We supplemented the WINGS-SPE spectroscopy with redshifts by performing searches through the SDSS spectroscopic survey and the SIMBAD Astronomical database within a radius of 1.5 from A2626. The radius of 1.5 was chosen so that we could identify the known galaxies that are

located in the area covered by the MeerKAT HI cube (Healy et al., 2021a), which covers $2 \times 2 \text{ deg}^2$ centred on A2626. Despite falling into the SDSS spectroscopic footprint, as well as being part of the WINGS-SPE, the spectroscopic coverage across the entire $2 \times 2 \text{ deg}^2$ field was very sparse and incomplete, especially for $R > 0.7 R_{200}$ from the cluster center. We therefore targeted A2626 for follow-up spectroscopy using the multi-object fibre-fed spectrograph Hectospec on the MMT.

4.2.2 MMT Spectroscopy

4.2.2.1 Target selection

The galaxies targeted for Hectospec followup were selected from the SDSS photometric catalogue. The first step was to identify all extended sources that did not already have a redshift. We classified sources as extended if they satisfied the criterion

$$r_{\text{psf}} - r_{\text{petro}} > 0.1 \text{ mag} \quad , \quad (4.1)$$

where r_{psf} is the PSF magnitude, and r_{petro} is the Petrosian magnitude (an aperture-based magnitude, Blanton et al. 2001). All sources that matched this criterion were cross-matched to the catalogue of literature redshifts. Photometric sources within $5''$ of an existing redshift were assumed to be part of the same galaxy and removed from the target catalogue. The distribution of literature redshifts indicated three spectral over-densities at $cz \sim 20\,000 \text{ km s}^{-1}$, one of which corresponds to A2626 (left panel in Figure 4.1). The highest-redshift over-density was at $cz \sim 125\,000 \text{ km s}^{-1}$ and is centred around $0^\circ 7$ east-southeast of A2626. It is within the MeerKAT primary beam at that redshift. Based on the $g-r$ colour, total r magnitude, and locations of the noted four over-densities (see right panel of Figure 4.1), we further restricted the target catalogue to:

$$\begin{aligned} 0 < g - r < 2, \\ r < 20.4 \text{ mag, and} \\ R < 0^\circ 75. \end{aligned} \quad (4.2)$$

The colour and magnitude limits are shown in Figure 4.1. We also imposed a brightness limit on the ‘‘fibre magnitude’’, the magnitude within a $2''$ aperture, only including sources that had $r_{2''} < 21.5 \text{ mag}$. This criterion enabled us to maximise the success rate of the observations. The colour distribution of the prime target catalogue of ~ 2500 sources is shown in Figure 4.1. For the last three configurations observed, fainter targets were added in order to utilise more fibres. These galaxies were observed only when no brighter source could be targeted.

4.2.2.2 Observations

Hectospec (Fabricant et al., 2005) is a fibre-fed spectrograph operating at the MMT in Arizona, USA. Its 300 fibres, each subtending a $1''.5$ diameter on the sky, patrol a circle of radius $0^\circ 5$ with the constraint that the distance between fibres must be at least $20''$. The 270 lpm grating gave wavelength coverage $3725\text{--}9150 \text{ \AA}$ with spectral resolution 6 \AA .

The A2626 field was observed with nine Hectospec configurations designed to maximise the number of galaxies, and especially the number of bright galaxies, observed. The plan was to observe five configurations with 45 minutes exposure time and four with 105 minutes, but in some cases longer exposures were obtained. Objects with SDSS g fibre magnitudes > 21 were preferentially assigned to configurations with longer exposure times. This led to ~ 280 galaxies being targeted twice. Each configuration was observed with three individual exposures to allow cosmic-ray removal. Table 4.1 shows positions, dates, and total exposure times of the configurations. (Configuration labels are arbitrary.) Each configuration measured about 250 targets and included 20–30 sky fibres. Remaining fibres were unassigned because of position conflicts.

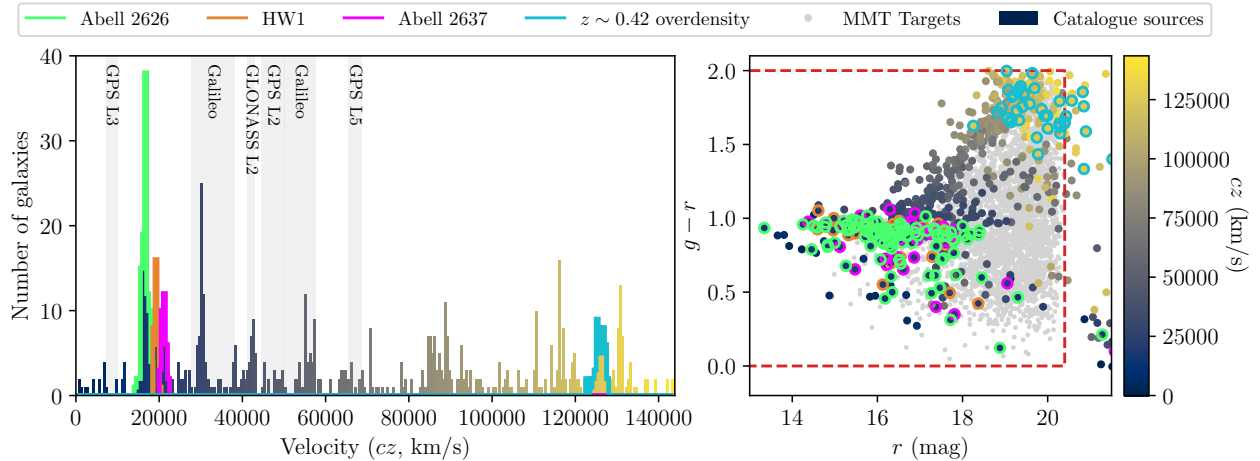


Figure 4.1: *Left:* histogram showing the known redshifts of galaxies within a 1° radius of A2626. The green, orange, and pink outlines indicate the distribution of galaxies in A2626, a newly identified structure we are calling HW1, and A2637 respectively. The blue outline indicates a background over-density at $z \sim 0.42$. grey vertical bands mark the redshift ranges where radio-frequency interference makes it difficult to identify galaxies in the MeerKAT H I data. Only over-densities outside these bands are coloured. *Right:* colour-magnitude diagram for the galaxies in the field. The colour scale of the circles represents the redshifts as indicated in the colour bar to the right. The four over-densities are outlined in the same colours as the histogram. The grey dots within the dashed red bounding box represent the sources we targeted with Hectospec. The dashed red box represents the colour and magnitude limit for the target catalogue.

4.2.2.3 Redshift measurements

MMT spectra were reduced with the IDL Hectospec pipeline HSRED 2.1, originally written by R. Cool (http://mmt.org/~rcool/data_tools.html). The pipeline, a re-implementation of the one described by Mink et al. (2007), combined the separate spectra while rejecting cosmic rays, subtracted the sky, and corrected the wavelengths to barycentric values. The pipeline then cross-correlated each target spectrum with eight spectral templates representing a variety of galaxy spectra. The template with highest correlation coefficient was chosen as the initial redshift guess, and the location and width of the correlation peak gave the redshift and its uncertainty. Table 4.2 lists the galaxy templates and the number of times the pipeline chose each one. It also gives the additional uncertainty because the assigned template may not best represent the true galaxy velocity. These uncertainties should be added in quadrature to the individual redshift uncertainties in Table 4.3.

All spectra were examined by eye and the correlations re-run with XCSAO, the original cross-correlation routine. Redshifts from HSRED and XCSAO were consistent within their uncertainties. For about 10% of targets, a template other than the initial guess looked to be a better representation of the spectrum, and the initial guess was replaced with the HSRED redshift for the better template. In most cases, the replacement template was chosen for better agreement with emission line velocities than the initial one. For ~ 10 targets, none of the HSRED redshifts matched the spectrum, and an XCSAO fit was used. Most of these were spectra with large noise spikes that confused the pipeline but could be deleted manually.

The visual examination gave each fit a quality ranking Q to code whether the template had correctly identified the spectral features. $Q = 4$ designates an unambiguous redshift based on multiple features of high S/N . $Q = 3$ designates a reliable redshift, but the number of features and their S/N is insufficient for $Q = 4$. $Q = 2$ designates a probable redshift but one with a reasonable chance of features being misidentified. $Q = 1$ designates some indication of a redshift, often a single, weak emission line or multiple features that could be absorption or could be noise. $Q = 0$ indicates no

Table 4.1: Hectospec Configurations

Config	R.A.	Dec.	Date	Exp. time
	J2000		UT	minutes
c1	23:38:02.6	21:19:45	2019-09-03	105
c2	23:37:25.6	20:47:21	2019-09-04	105
b1	23:37:31.0	21:34:02	2019-10-24	45
b2	23:38:16.9	21:05:37	2019-10-24	54
a2	23:36:03.6	20:43:19	2020-06-20	45
d1	23:35:09.4	20:53:36	2020-06-22	114
e2	23:35:21.3	21:24:28	2020-09-11	60
f1	23:35:00.3	21:20:06	2020-10-07	120
e1	23:37:55.3	21:15:48	2020-10-08	45

Table 4.2: Template Uncertainties

Template	N	Δcz^a	Δz
SPTEMP	1011	17	0.000057
M31_K_TEMP	364	19	0.000063
ELTEMP	294	25	0.000083
HEMTEMP0.0	282	14	0.000047
HABTEMP90	190	24	0.000080
EATEMP	69	29	0.000097
M31_F_TEMP	46	23	0.000077
M31_A_TEMP	11	31	0.000103

^aHere and throughout this chapter $c \equiv 299792.5$.

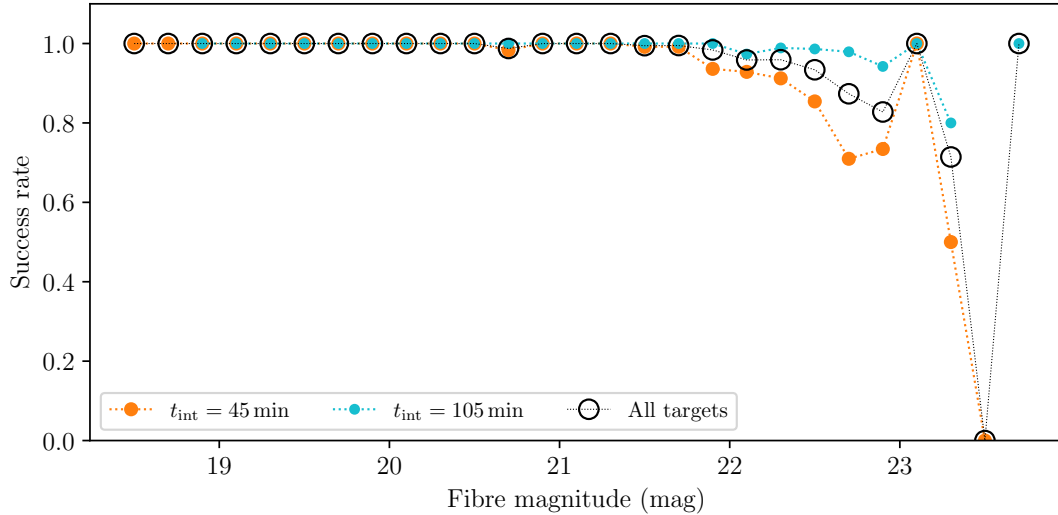


Figure 4.2: Fraction of targeted galaxies from which a redshift could be measured. The orange (blue) show the galaxies observed with $t_{\text{int}} = 45$ min ($t_{\text{int}} = 105$ min). The full target list is represented by the open black circles. The horizontal (x) axis is SDSS g magnitude in a $2''$ diameter (“fibre2Mag_g”).

spectral information, usually very low S/N . Only $Q \geq 3$ redshifts are used in this work, though others are included in Table 4.3 for completeness.

4.2.2.4 Data quality and success rate

The success rate is given as a function of the magnitude by

$$S(m) = \frac{N_z}{N_{\text{targ}}}(m) \quad , \quad (4.3)$$

where N_z is the number galaxies of magnitude m for which a redshift could be measured, and N_{targ} is the number of galaxies that were targeted and a spectrum obtained. Figure 4.2 shows the success rate as a function of the fibre magnitude.

Table 4.3: MMT Redshifts

Name	RA	Dec	petroMag_g	PetroMag_r	fiber2Mag_g	cModel_g-r	Q	z	Δz	alt	template	R	config	fibre	Comment
MMT_1192	23:33:03.49	+21:11:03.6	20.15	19.26	21.50	0.91	4	0.101908	0.000136		m31_f_temp	6.6	f_1	096	
MMT_0441	23:33:03.74	+21:19:11.2	17.82	16.90	19.91	0.93	4	0.057972	0.000074		eltemp	16.7	f_1	109	
MMT_1977	23:33:04.98	+20:58:04.5	20.02	18.53	21.52	1.61	4	0.248916	0.000089		eltemp	17.3	d_1	169	
MMT_1185	23:33:06.15	+21:07:32.3	19.01	17.92	20.85	0.99	4	0.101535	0.000041		hemtemp0	13.9	f_1	017	
MMT_1979	23:33:06.39	+21:00:30.7	18.96	18.04	21.07	0.92	4	0.099553	0.000125	a	eltemp	9.2	d_1	161	
MMT_0443	23:33:10.49	+21:15:37.7	19.14	17.96	20.58	1.22	4	0.162603	0.000058		m31_k_temp	16.6	f_1	093	
MMT_0448	23:33:10.76	+21:17:27.2	20.59	19.14	22.04	1.46	4	0.224653	0.000096		sptemp	13.3	f_1	106	
MMT_2430	23:33:11.54	+20:43:39.4	20.42	20.01	21.67	0.40	4	0.141438	0.000018		hemtemp0	24.9	d_1	147	
MMT_2156	23:33:11.59	+21:25:35.4	19.79	18.94	21.48	0.86	4	0.192463	0.000065		sptemp	17.5	f_1	116	
MMT_1196	23:33:11.86	+21:09:40.8	20.35	19.43	21.69	0.83	4	0.169041	0.000087		sptemp	12.5	f_1	013	
MMT_0457	23:33:12.29	+21:23:58.7	19.47	18.44	21.61	0.93	4	0.265598	0.000090		sptemp	13.5	f_1	112	
MMT_1198	23:33:13.62	+21:12:07.5	21.49	19.66	22.81	1.59	4	0.282104	0.000147		eltemp	9.2	f_1	098	
MMT_1983	23:33:13.68	+20:55:35.8	20.13	19.46	22.13	0.62	4	0.142830	0.000040	a	hemtemp0	9.0	d_1	164	
MMT_1989	23:33:14.20	+20:54:01.2	19.22	18.54	21.74	0.67	4	0.161680	0.000061	a	hemtemp0	5.7	d_1	151	
MMT_0458	23:33:14.69	+21:20:10.2	21.25	19.97	23.00	1.17	3	0.284297	0.000171		habtemp90	7.1	e_2	094	
MMT_1980	23:33:14.70	+20:53:05.3	19.38	18.39	20.90	1.01	4	0.099837	0.000053		m31_k_temp	17.7	d_1	155	
MMT_2323	23:33:15.32	+21:05:11.0	19.28	18.62	21.35	0.68	4	0.146221	0.000062		sptemp	18.6	d_1	176	
MMT_2319	23:33:15.91	+21:04:43.1	21.08	19.15	22.24	1.74	4	0.412846	0.000156		sptemp	5.3	f_1	087	
MMT_2463	23:33:16.04	+20:52:21.4	18.60	17.59	20.28	1.01	4	0.099018	0.000050		m31_k_temp	20.6	d_1	157	
MMT_2462	23:33:16.28	+20:49:40.1	17.56	16.90	19.40	0.69	4	0.054066	0.000033	a	hemtemp0	11.3	d_1	152	
MMT_1348	23:33:16.47	+21:29:37.0	17.59	17.21	19.23	0.37	4	0.038449	0.000025		hemtemp0	15.6	e_2	107	
MMT_1194	23:33:16.56	+21:07:34.0	20.20	19.46	21.58	0.60	4	0.100518	0.000096		sptemp	10.5	f_1	081	
MMT_0462	23:33:17.47	+21:22:12.6	19.84	18.96	21.36	0.88	4	0.057187	0.000083		m31_k_temp	10.3	f_1	026	
MMT_2464	23:33:17.48	+20:50:08.8	18.83	17.76	20.41	1.06	4	0.133259	0.000077		eltemp	17.5	d_1	154	
MMT_1199	23:33:17.58	+21:09:45.3	19.78	19.00	21.70	0.64	4	0.019790	0.000081		sptemp	10.5	f_1	015	
MMT_0451	23:33:17.58	+21:23:29.8	18.13	17.19	19.84	0.94	4	0.057222	0.000051		m31_k_temp	18.0	e_2	095	
MMT_2322	23:33:17.79	+21:03:31.9	19.11	17.96	20.44	1.14	4	0.132217	0.000081		eltemp	17.5	d_1	271	
MMT_1981	23:33:17.82	+20:55:55.9	19.66	18.95	21.71	0.66	4	0.248011	0.000057		sptemp	20.8	d_1	166	
MMT_0461	23:33:18.24	+21:16:19.8	20.42	19.32	21.70	1.10	4	0.165881	0.000093		sptemp	13.4	f_1	091	
MMT_0463	23:33:18.74	+21:22:39.6	21.54	19.84	22.75	1.72	4	0.290004	0.000146		eltemp	9.1	f_1	028	

Magnitudes are from SDSS and are in AB units. An ‘a’ in the alt column indicates the pipeline template choice was

overridden. Only a portion of this table is shown here to demonstrate its form and content. A machine-readable version of the full table is available.

4.2.3 Spectroscopic Completeness

Understanding the completeness of our spectroscopic samples is important for the reliability identifying substructure and groups. Following the colour and luminosity cuts outlined in Section 4.2.2.1, we examined the spectroscopic completeness across the entire $2 \times 2 \text{ deg}^2$ region covered by the MeerKAT HI observations and centred on A2626. The completeness is defined in the same way as Cava et al. (2009):

$$C(m) = \frac{N_z}{N_{\text{ph}}}(m) \quad (4.4)$$

where N_{ph} is the number of sources of magnitude m in our target catalogue. Figure 4.3 shows the spectroscopic completeness as a function of the SDSS r -band magnitude, which was used to select the targets for the MMT observations (Section 4.2.2.1).

While Figure 4.3a provides the global overview at what magnitude the completeness begins to drop off, with a non-uniform spatial spectroscopic coverage it is important to understand how the completeness varies across the field. Figure 4.3b shows the spectroscopic completeness determined in annuli with increasing radii from the centre of the cluster. The spatial variation of the spectroscopic completeness in six magnitude bins is shown in Figure 4.4. The completeness is relatively uniform and above 50% across most of the field.

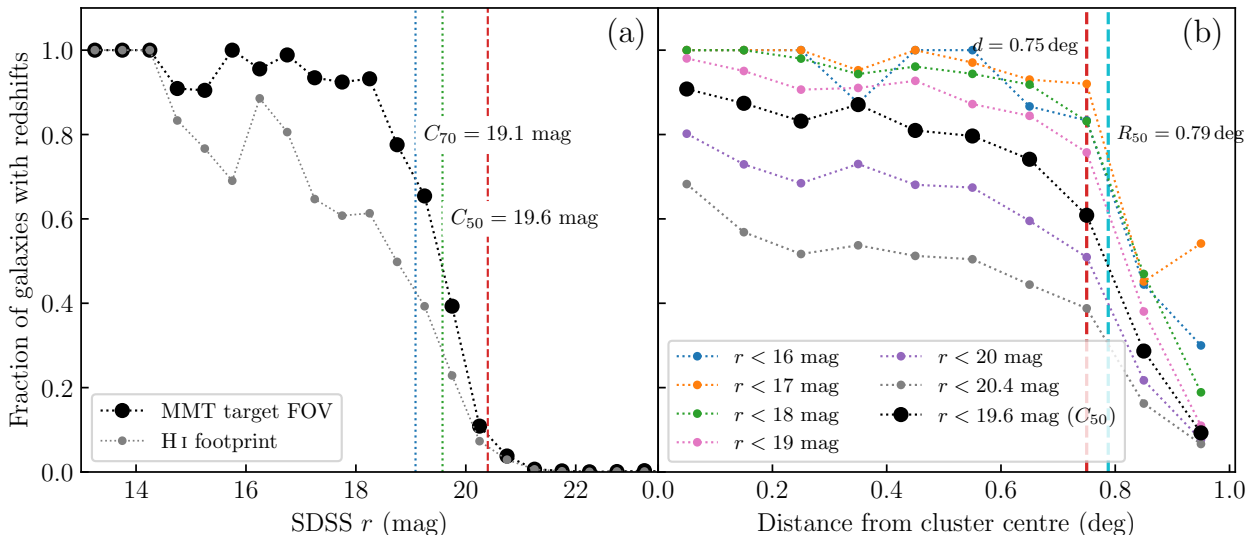


Figure 4.3: (a) Spectroscopic completeness as a function of SDSS r across the A2626 field. Black points show the completeness for the MMT target field, and grey points show it for the entire 2×2 deg² MeerKAT H I footprint. The blue and green dotted vertical lines indicate magnitudes for 70% and 50% completeness for the MMT field. The red dashed line indicates the limiting magnitude for the MMT target catalogue before the faint targets were added. (b) Spectroscopic completeness in annuli as a function of distance from the cluster center. The black points represent the completeness for galaxies brighter than the 50% completeness magnitude ($r < 19.6$ mag), and the grey points represent all galaxies in the MMT target catalogue ($r < 20.4$ mag). The blue, orange, green, pink, and purple points represent the completeness for the sample with increasingly fainter limiting magnitudes as indicated in the legend. The vertical dashed red line indicates the radius of the MMT survey region, and the vertical dashed cyan line indicates the radius at which the black points (galaxies brighter than $r = 19.6$ mag) fall below 50% completeness.

4.3 Large-scale structure

4.3.1 Large scale structure in the MMT volume

There are at least 11 known clusters or over-densities within $0^{\circ}.8$ of A2626 and at $cz < 138000$ km s⁻¹. These are listed in Table 4.4. The MMT observations yielded 1858 new redshifts with $cz < 138000$ km s⁻¹ and 20 with $cz > 138000$. With the addition of the MMT redshifts (Figure 4.5), many of these over-densities stand out as shown by the histogram in Figure 4.1. The three Abell clusters (Abell et al., 1989) were found as surface over-densities of galaxies on the sky. The seven clusters identified as ‘‘RM’’ were identified using the RedMaPPer algorithm (Rykoff et al., 2014), which searched for surface over-densities of red galaxies. ZwCL 2332+2027 was identified by Zwicky et al. (1961), again as a galaxy surface over-density, and 1RXS J233354.3+214052 was identified by Bohringer et al. (2000) from its X-ray emission.

The sky distributions of eight over-densities are shown in the bottom part of Figure 4.5. The two clusters A2625 and ZwCl 2332+2027, which were identified from photographic plates, had previous cluster redshifts from only a few bright galaxies around the central position. Our new spectroscopy suggests that those galaxies are actually in the foreground, and updated cluster redshifts are shown in the figure legend and listed in Table 4.4.

4.3.2 Identifying A2625

The ACO catalogue (Abell et al., 1989) identified galaxy surface over-densities. These were later spectroscopically confirmed by measuring the redshifts of the brightest galaxies in the field (sometimes as few as three galaxies, see Struble & Rood 1999). A2625 was one of the clusters identified photographically, and the published cluster redshift was based the redshifts of three galaxies. Fig-

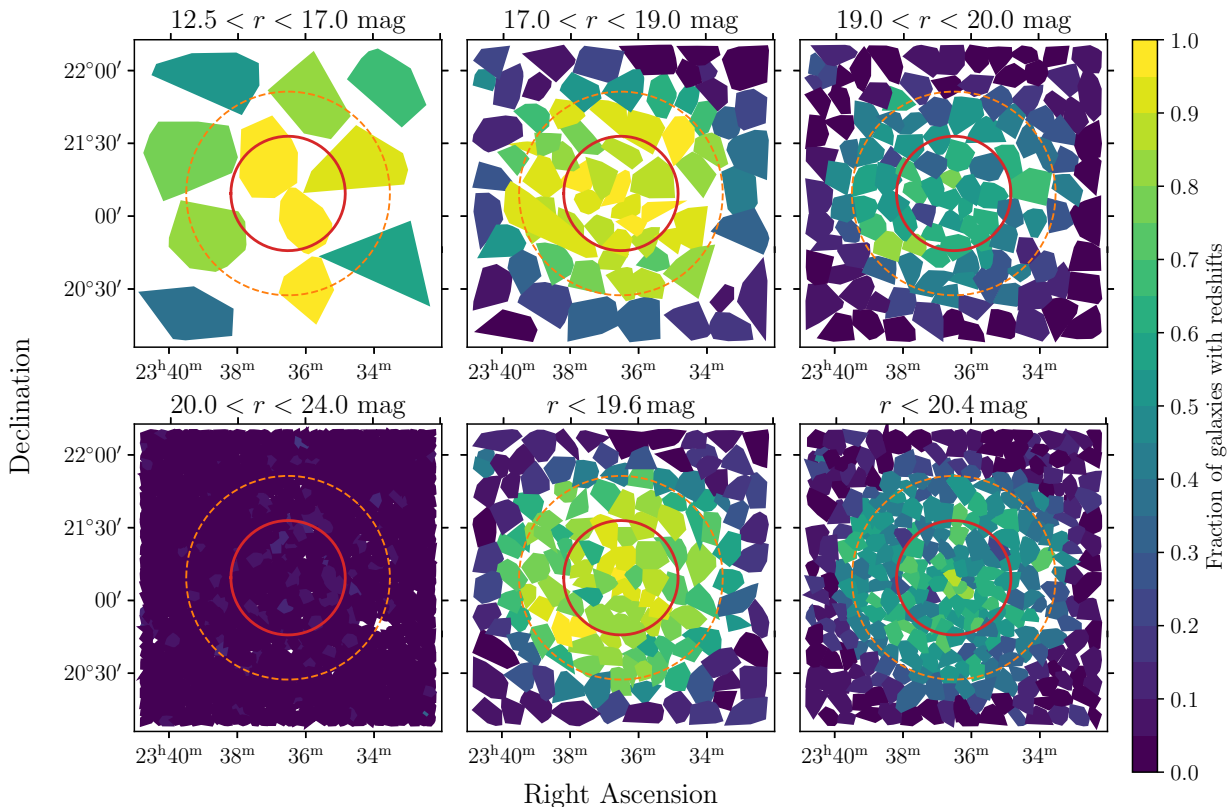


Figure 4.4: Spatial distribution of spectroscopic completeness across the A2626 field. The colour of each tile indicates the completeness fraction $C(m)$ (Equation 4.4) of that subset of sources according to the colour bar on the right. The solid red circle represents R_{200} of A2626 at the centre of the field. The dashed orange circle indicates the outline of the MMT survey footprint. The irregular shapes of each tile are defined by the minimum area spanned by the positions of the galaxies represented by that tile. In order to minimise the effects of stochasticity, each tile contains roughly the same number of sources.

ure 4.6 shows a clear over-density of galaxies at the A2625 location in both previously published and new redshifts.

The previous redshift assigned to A2625 places it in velocity space between A2626 at $\sim 16600 \text{ km s}^{-1}$ and the over-density around 19100 km s^{-1} . As it was based on only three galaxies, the published redshift was uncertain, and the three galaxies could be associated with the spectral over-density at $cz \sim 19100 \text{ km s}^{-1}$ (Figure 4.5b). The spatial distribution of that over-density’s galaxies shows no significant spatial clustering but rather a more linear distribution stretching up the west side of A2626 (Figure 4.6). There is also no X-ray emission associated with any of the localised clustering of galaxies in this over-density. Although the ACO position for A2625 is on the edge of the MMT survey area, there is enough coverage to have seen a cluster if it were there. Evidently the spectral over-density around $\sim 19100 \text{ km s}^{-1}$ is not associated with A2625, and we will henceforth refer to this over-density as HW1.

Piffaretti et al. (2011) used *ROSAT* to identify X-ray emission of a galaxy cluster at A2625’s position. There are two bright galaxies near the X-ray position and within an arcminute of each other: LEDA 97482 and LEDA 1630451. Owen et al. (1995) found $cz = 30130 \pm 90 \text{ km s}^{-1}$ for LEDA 97482, and we found $cz = 17829 \pm 15 \text{ km s}^{-1}$ for LEDA 1630451 (Section 4.2.2). The LEDA 1630451 redshift places it in HW1. This galaxy’s spiral morphology and detection in H I (Healy et al., 2021a) suggest that it is probably not close to the centre of a cluster. LEDA 97482, on the other hand, is a cD galaxy (Yuan et al., 2016). The X-ray emission and cD galaxy are clear evidence of a cluster. Additional evidence is the over-density of red galaxies known as RM J233602.7+203245.1 (Bohringer

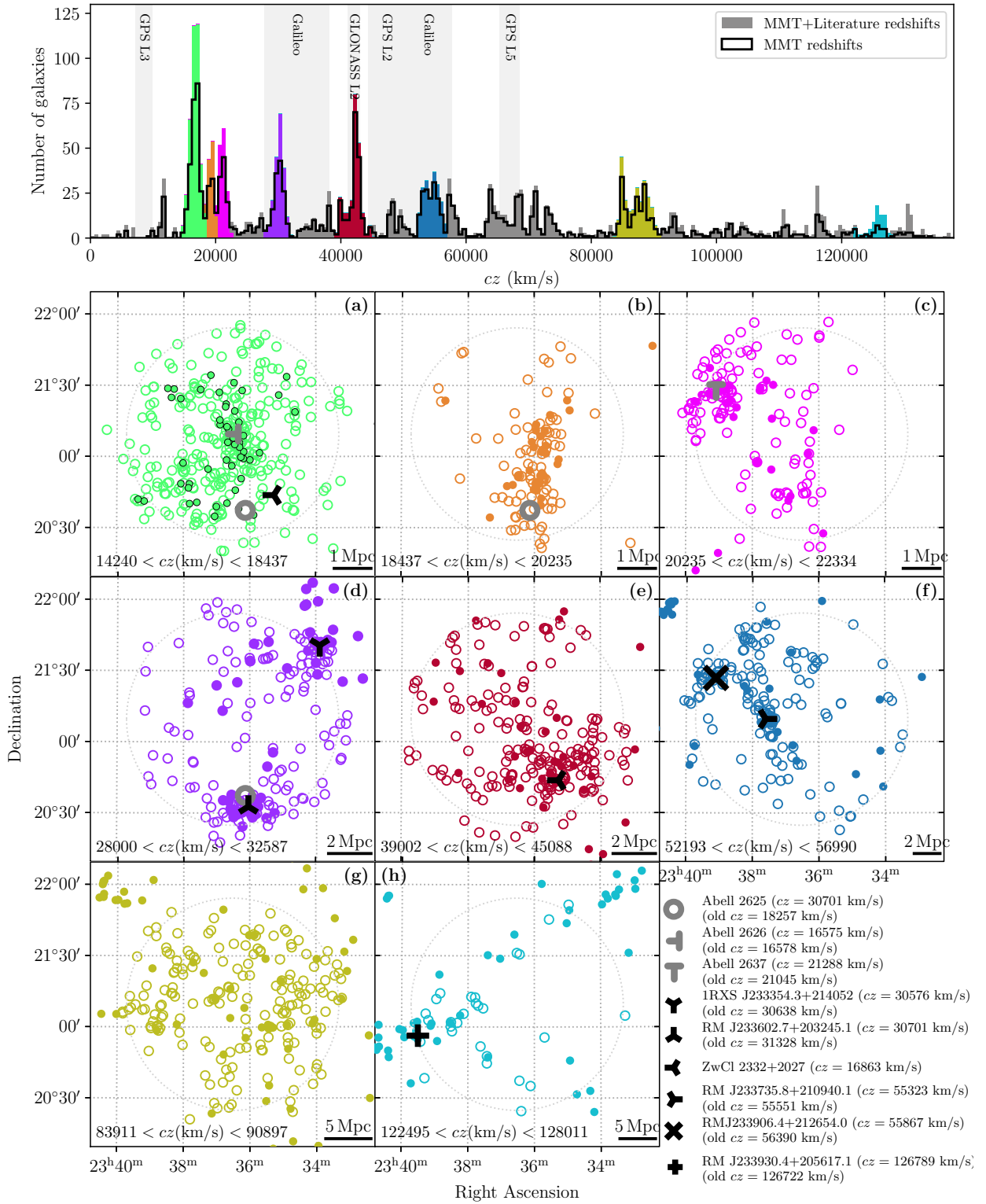


Figure 4.5: *Top:* redshift histogram of all redshifts $z < 0.46$ ($cz < 137\,900\text{ km s}^{-1}$) in a $2 \times 2\text{ deg}^2$ region centred on A2626. The grey and coloured histograms represent all known redshifts in this region, while the black open histogram represents our new MMT redshifts. *Bottom:* sky distribution of eight of the spectral over-densities. Small circles represent galaxies with redshifts in the range indicated in each panel. Open circles represent galaxies with MMT redshifts while filled circles represent galaxies with redshifts from the literature. colours in each panel a–h are the same as the corresponding over-density in the histogram above. The light grey dotted circles indicate the approximate outline of the union of MMT footprints (Table 4.1). Known clusters in the region are indicated by markers as shown in the legend at bottom right.

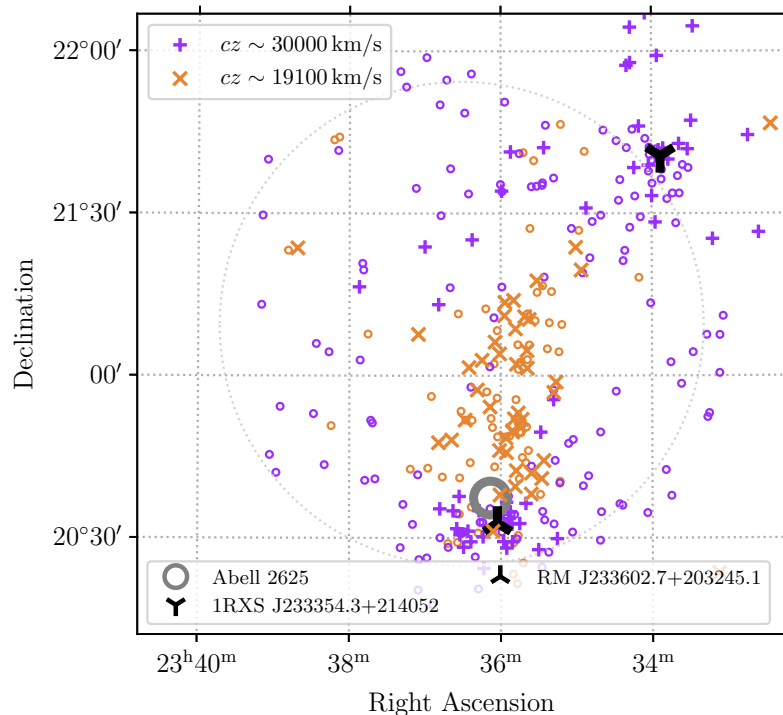


Figure 4.6: Sky distribution of the galaxies in the $cz \sim 19100 \text{ km s}^{-1}$ over-density (orange) and $cz \sim 30000 \text{ km s}^{-1}$ over-density (purple). The small open circles in the two colours represent the new MMT redshifts, while the orange ‘x’ and purple ‘+’ symbols represent measurements from literature. The black markers indicate the position of the two clusters associated with the two $cz \sim 30000 \text{ km s}^{-1}$ over-densities. The position of A2625 is indicated by the open grey circle.

et al., 2000), now shown to be a cluster in redshift space as well (Figure 4.5d). Taken together, the clustering of galaxies, the X-ray emission at the centre of the cluster, and the proximity to the original location of A2625 imply that A2625 and RM J233602.7+203245.1 are the same cluster at $cz = 30519 \text{ km s}^{-1}$. Table 4.4 gives cluster properties.

4.3.3 Large scale structure beyond the MMT Volume

Batuski & Burns (1985) identified a filament of galaxies extending over 425 Mpc from the Perseus–Pisces supercluster. Figure 4.7 shows a recreation of the Batuski & Burns (1985, their Fig. 1) plot of the large scale structure using the most recent position and redshift information for the clusters in this region. Einasto et al. (2001) identified groups of galaxy clusters with $cz < 39000 \text{ km s}^{-1}$ in a compilation of the ACO catalogue and a sample of X-ray-detected clusters from Ebeling et al. (1998). Using a friends-of-friends algorithm, Einasto et al. identified the superclusters using a linking length of 37–54 Mpc. A number of these superclusters are located in the Perseus–Pegasus filament (Figure 4.8). One includes the Perseus cluster, which Einasto et al. claimed, is connected to SCL 211 and SCL 215 by “free-floating” clusters. Another Einasto et al. supercluster is SCL 213, which is home to A2626, A2637, and four other clusters.

Additional redshifts gathered since 2001 change the picture. From the left panel of Figure 4.7, the black symbols could represent a coherent filament. However, when one rotates the figure (right panel), there is a separation between SCL 211 (the triangles) and SCL 213 (the black circles). It appears that the closer part of the filament (containing Perseus, SCL 211, and SCL 215) is veering away from the direction of SCL 213.

This separation becomes more evident from the sky distribution shown in Figure 4.8. The filament is traced from the top left of the figure by the light blue through to the purple and then pink points coming down the centre of the figure and is outlined by the grey “hockey stick.” On the outer

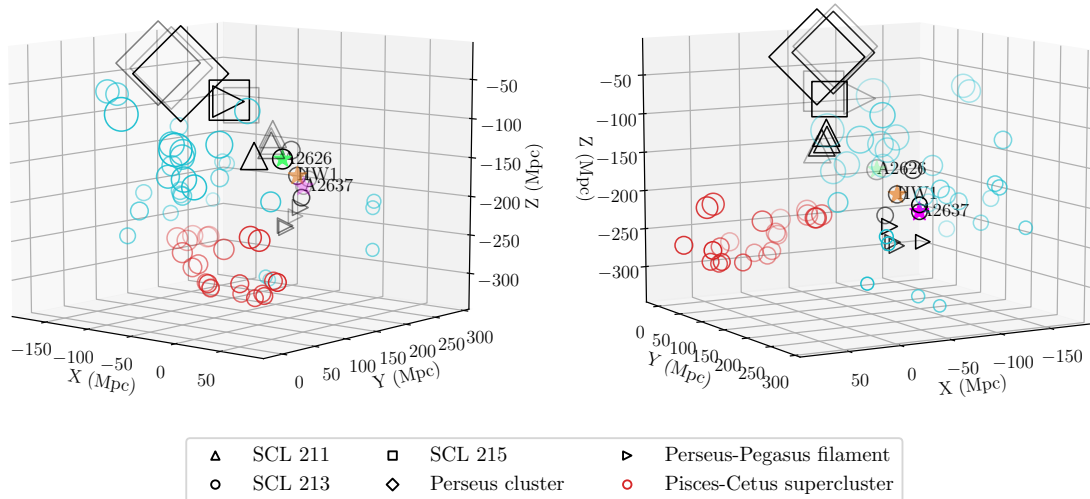


Figure 4.7: 3-D distribution of the galaxy clusters in and around the Perseus–Pegasus filament. Coordinates are a Cartesian frame with the Galactic centre at its origin. The left and right panels show two different azimuth angles. The filament is represented by the black shapes (diamonds = Perseus cluster; squares = SCL 211; upward triangles = SCL 215, circles = SCL 213, sideward triangles = other clusters in the filament). The red circles represent the Pisces–Cetus supercluster, and the blue circles represent other clusters in the field. The three clusters or over-densities in the low-redshift MMT volume are labelled and indicated by the green (A2626), orange (HW1), and pink (A2637) stars. Batuski & Burns (1985) included HW1 in their original version of this plot, labelling it A2625. The cluster marker sizes are scaled by the inverse of their redshifts and coloured by structure: red is the Pisces–Cetus supercluster (Tully, 1986, 1987); black is the Perseus–Pegasus filament; and light blue is unassigned.

edge of the hockey stick, we see a relatively smooth transition in colours likely indicating that the galaxies and clusters are part of the same structure. Given the available data, there appears to be no connection between the outer and inner parts of the hockey stick, the inner part being dominated by dark green colours corresponding to significantly higher recession velocities. Batuski & Burns (1985) described the filament as following the plane of the sky, twisting to a line-of-sight direction around A2593. That would predict a structure around 15000 km s^{-1} that would connect the plane of the sky portion to the line of sight. However, the transition of colours in Figure 4.8 shows no such structure. Based on the available data, we conclude that the A2626 complex is separate from the Perseus–Pegasus filament.

4.3.4 Large scale structure around A2626

Within a 1 deg radius around A2626 and at similar redshifts, there is one other Abell cluster: A2637 (Abell et al., 1989). These two clusters are evident in the redshift histogram for the field (Figure 4.5), where the two clusters stick out as distinct peaks with another over-density, HW1, between them. Aside from the central region of A2626 (Struble & Rood, 1999; Cava et al., 2009), this region has not been extensively surveyed, and many of the existing measurements for HW1 and A2637 have been based on a handful of redshifts and X-ray detections.

Despite Einasto et al. (2001) identifying A2626, HW1, and A2637 as part of SCL 213, the currently available redshift data for galaxies in this supercluster are sparse. Within our data, there are hints of how the three structures connect to the other clusters, but given the complexity of the cosmic web, it is not possible to show the links. Even with our limited field-of-view, there are still three interesting over-densities.

A2626 itself shows an extended distribution of galaxies (Figure 4.5a). If we exclude the virialised population within 1.5 Mpc of the cluster center, there is a smooth distribution of sources.

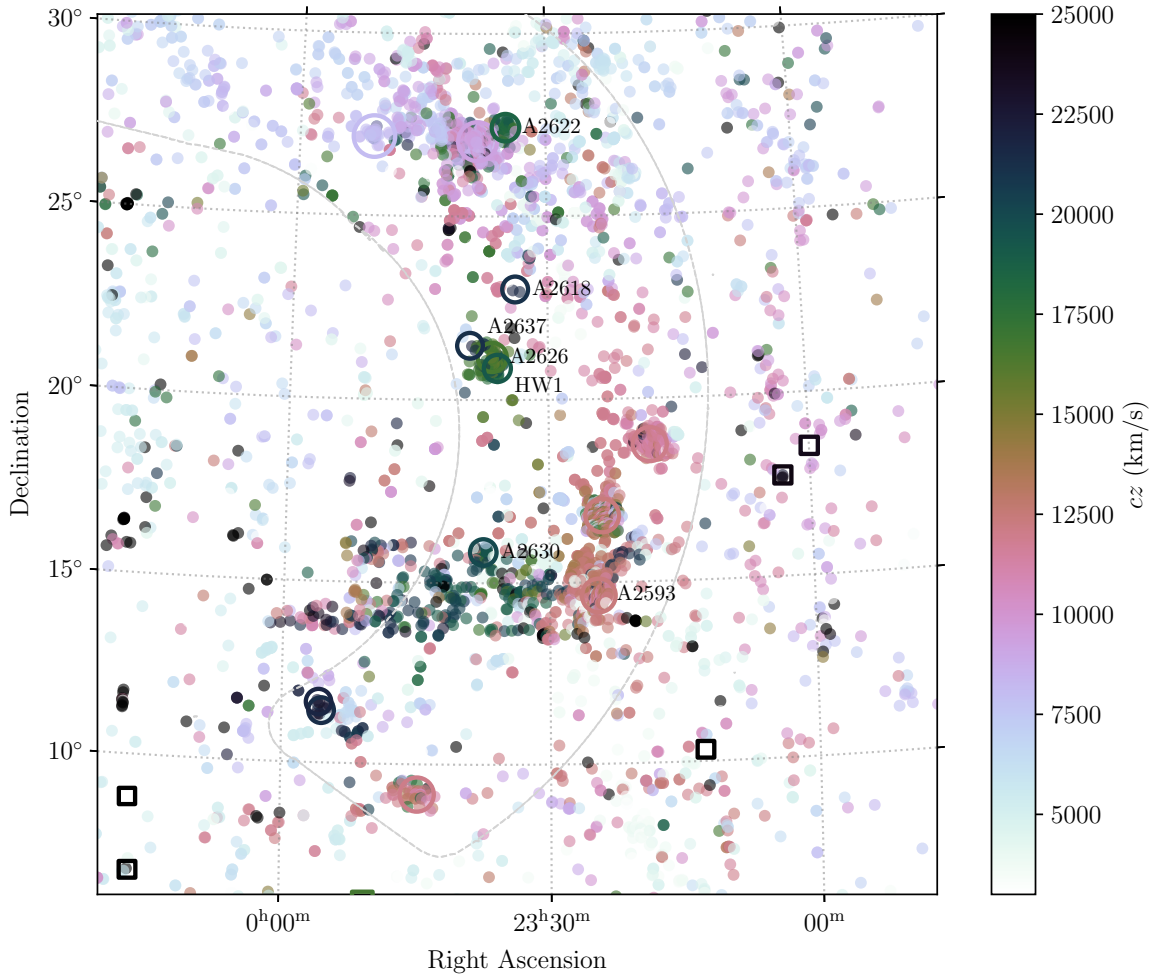


Figure 4.8: Sky distribution of the Perseus–Pegasus filament based on Batuski & Burns (Fig. 3, 1985). The filament is outlined by the light grey dashed line that resembles the bottom end of a field hockey stick. The small coloured points indicate galaxies in the region with redshifts from a combination of the CfA2, the Updated Zwicky catalogues, and targeted searches around the clusters in the SIMBAD database. The open circles represent Abell clusters identified by Batuski & Burns (1985) as part of the filament, while the open squares represent clusters not in the filament. The size of the open markers is inversely proportional to the redshift of the cluster. The colours (as indicated by the colour bar on the right) represent the recessional velocity of the object.

This implies that the A2626 cluster is embedded within a wall as sketched in Figure 4.9.

A2637, another of the SCL 213 clusters in our field, is only half covered by the MMT survey footprint. Nevertheless, the data show a central, dense region of galaxies with a radial decrease in the density of sources. A2637 is well separated from A2626 in both position and velocity.

The final member of SCL 213 in our field is what we refer to as HW1. Einasto et al. (2001) assigned this over-density to SCL 213 under the name A2625. As discussed above, HW1 is not A2625, but more important, it does not appear to be a cluster. There is no X-ray emission associated with any part of HW1. Moreover, the distribution of the HW1 galaxies has no central, dense region. Instead the structure seems to be linear, almost like a filament. The HW1 structure starts around the same declination as A2626 but more to the east (Figure 4.5b) and stretches south to the limit of our field. The highly collimated distribution of the HW1 galaxies also stands out.

Table 4.4: Clusters and over-densities in the MMT footprint.

Cluster	RM ^h (J2000)	RA Dec	cz_{cl} km s ⁻¹	σ_{cl} Mpc	R_{200}	N_z
A2626	...	23:36:31.00 +21:09:36.3 ^a	16576	660 ± 26	1.59	163
HW1 ^b	...	23:35:55.26 +20:51:43.2	19247	397 ± 22	0.95	54
A2637	...	23:38:57.80 +21:25:55.2 ^c	21288	610 ± 46	1.46	74
A2625	J233602.7+203245.1	23:36:08.20 +20:37:23.0 ^e	30702	369 ± 36	1.51	38
1RXS J233354.3+214052	...	23:33:53.00 +21:40:36.0 ^f	30577	635 ± 66	1.49	39
ZwCl 2332+2027	J233524.3+204336.1	23:35:18.00 +20:44:00.0 ^g	42615	437 ± 22	1.01	59
...	J233735.8+210940.1	23:37:35.80 +21:09:40.0 ^h	55323	553 ± 62	1.25	28
...	J233906.4+212654.0	23:39:06.38 +21:26:54.0 ^h	52972	458 ± 35	1.04	30
...	J233502.7+210205.3		(119000)			
...	J233930.4+205617.1	23:39:30.40 +20:56:17.0 ^h	126789	–	–	7
...	J233905.9+210125.2		(132600)			

^aCava et al. (2009) ^bover-density but not a cluster (Section 4.3.4). Position given is luminosity-weighted mean. ^cPatel et al. (2006) ^fBohringer et al. (2000) ^gZwicky et al. (1961) ^hRykoff et al. (2014)

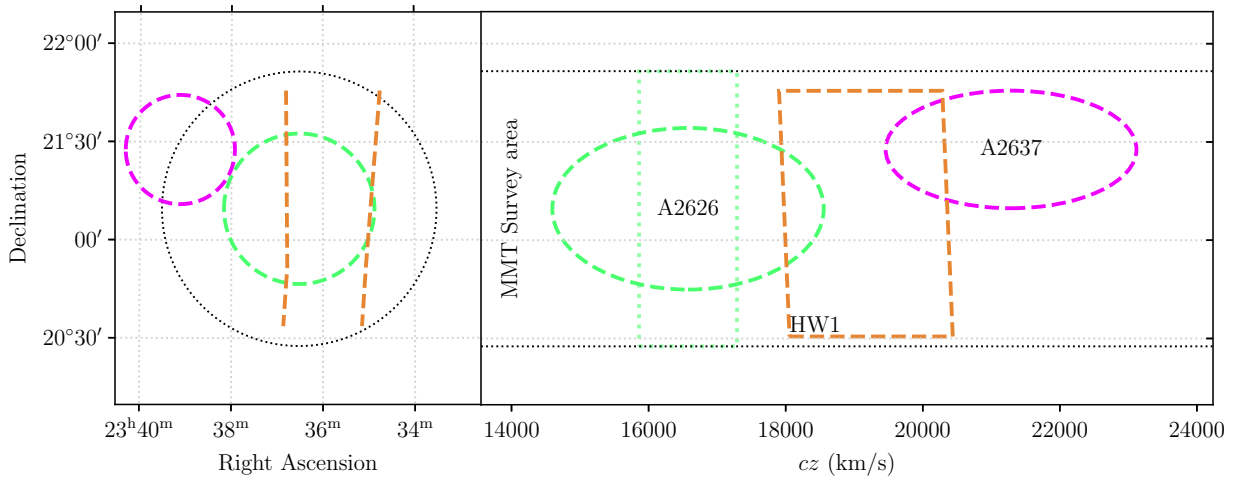


Figure 4.9: Schematic of how A2626, HW1, and A2637 fit together. The coloured circles/ellipses represent A2626 (green) and A2637 (pink). The orange rectangular shapes represent HW1, and the MMT survey area is indicated by the black circle and horizontal dashed lines. The wall in which A2626 is embedded is represented in the right panel by the light green vertical rectangle.

Figure 4.9 shows a schematic of the sky and redshift distributions of the three structures. The three overlap in the plane of the sky, but in redshift space, A2626 and A2637 are distinct from each other. While HW1 overlaps with A2626 in the plane of the sky, and both clusters in redshift space, we do not believe that HW1 is connected to either cluster. Section 4.5.3 discusses this further.

4.3.5 Background clusters

Table 4.4 listed seven clusters well separated from the A2626 complex. One is the cluster 1RXS J233354.3+214052 (Rykoff et al., 2014) in the northeast of the field (Figure 4.5d). While it is at almost the same redshift as A2625, its projected separation is 8.0 Mpc. ZwCl 2332+2027 (=RM J233524.3+204336.1) is shown in Figure 4.5e, and RM J233735.8+210940.1 is shown in Figure 4.5f. Updated parameters for both clusters are given in Table 4.4. RM J233906.4+212654.0 is also visible in Figure 4.5f, and there is an additional galaxy concentration to its northwest. These three clusters may be part of a larger structure with size scale ~ 5 Mpc.

At still larger distances, there are three over-densities defined by clusters of red galaxies (Rykoff et al., 2014). These have too few redshifts to say much about them, but Table 4.4 gives an updated redshift for RM J233930.4+205617.1, though based on only seven galaxies. The other two over-densities (J233502.7+210205.3 and J233905.9+210125.2) do not have enough redshifts to spectroscopically confirm the positions. Figure 4.5h shows a diffuse, linear structure, but the spectra are not deep enough to provide a good sample of galaxies at this redshift.

4.4 A2626 and friends

A goal of this work is to identify substructures within the clusters as well as groups that may be a “bridge” between any of the clusters in the large-scale environment. This requires reliable measures of the cluster redshift (z_{cl}) and velocity dispersion (σ_{cl}). The redshift histogram in Figure 4.10 gives estimates for z_{cl} and σ_{cl} for the three over-densities shown. In the rest frame of the over-density,

$$v = c \frac{z - z_{\text{cl}}}{1 + z_{\text{cl}}}, \quad (4.5)$$

where c is the speed of light, z is the redshift of the galaxy, and z_{cl} is the redshift of the cluster. To determine z_{cl} , we selected all galaxies within a radius of 1.5 Mpc of the cluster centre and with $-3\sigma_{\text{cl}} < v < 3\sigma_{\text{cl}}$. We discarded all galaxies detected in HI (Healy et al., 2021a) because they do not typically trace the virialised population of a cluster (Colless & Dunn, 1996). We applied the biweight location estimator to the redshifts of the sample of galaxies representing the virialised galaxy population (Beers et al., 1990) to determine z_{cl} . Using the updated z_{cl} , we recalculated the rest-frame velocities, v , for each galaxy using Equation 4.5. We determined σ_{cl} by fitting a Gaussian to the histogram of rest-frame velocities, fixing the mean of the Gaussian to the cluster redshift. Our $\sigma_{\text{cl}} = 660 \pm 26 \text{ km s}^{-1}$ for A2626 is fully consistent with the $679 \pm 60 \text{ km s}^{-1}$ measured by Cava et al. (2009).

The cluster velocity dispersion determines R_{200} , the radius inside which the mean density of the cluster is 200 times the critical density of the universe. From Finn et al. (2005) for $h = 0.7$,

$$R_{200} = 2.47 \left(\frac{\sigma_{\text{cl}}}{1000 \text{ km s}^{-1}} \right) \times (\Omega_{\Lambda} + \Omega_M(1 + z_{\text{cl}})^3)^{-1/2} \text{ Mpc}. \quad (4.6)$$

The calculated z_{cl} , σ_{cl} , and R_{200} for the three over-densities are listed in Table 4.4. HW1 is not a cluster nor is it a virialised system, but the numbers are useful for determining which galaxies may belong to the over-density.

The newly calculated z_{cl} , σ_{cl} , and R_{200} for A2626, A2637, and HW1 show how galaxies in these systems relate to each other in angular distance and velocity. Figure 4.11 shows the phase space plots for the three systems. The virial mass M_{200} was calculated from R_{200} via

$$M_{200} = \frac{4}{3} \pi R_{200}^3 200 \rho_c. \quad (4.7)$$

Figure 4.11 shows that the three over-densities are distinct systems. The large velocity separation coupled with the distance between the three systems’ centres of mass suggests that they are not even interacting with each other. The HW1 panel of Figure 4.11 reinforces that HW1 is not a cluster because galaxies do not fill the flare of the trumpet at small radii. The A2637 trumpet also does not fill up at small radii, but this could be due to the lack of redshift coverage as A2637 is on the northeastern edge of the MMT survey area.

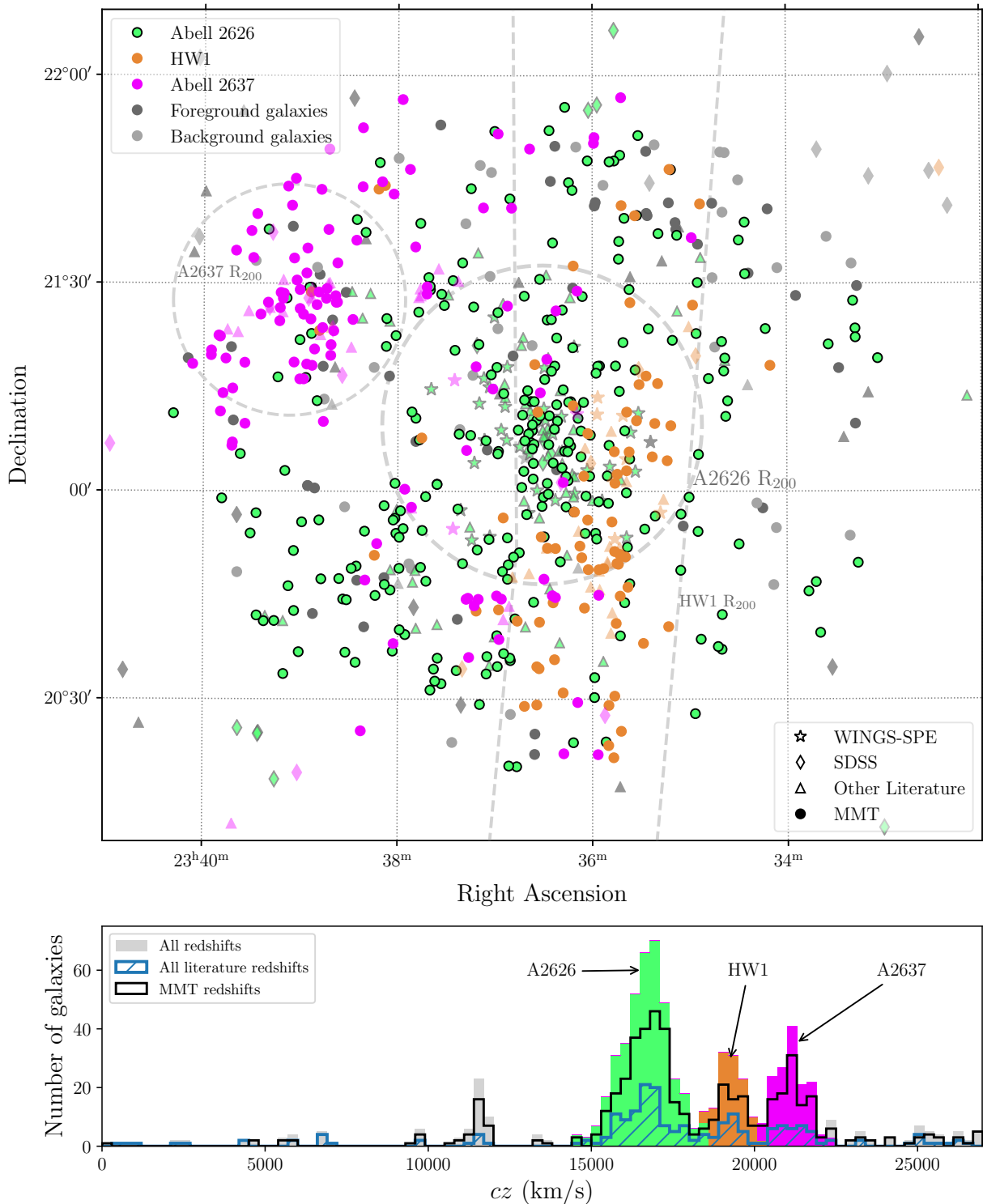


Figure 4.10: Top: sky distribution of all galaxies with $z < 0.09$ in a $2 \times 2 \text{ deg}^2$ region centred on A2626. The dashed grey circles indicates R_{200} for the different over-densities as labelled. The different symbols represent the different sources from which the redshifts were obtained, and the colours represent the large scale structure to which the galaxies belong. Bottom: redshift histogram of all the galaxies in the upper panel. The solid histogram represents the entire catalogue, while the open histograms indicated what portion of the total catalogue comes from literature (hatched blue) and from the MMT observations (black).

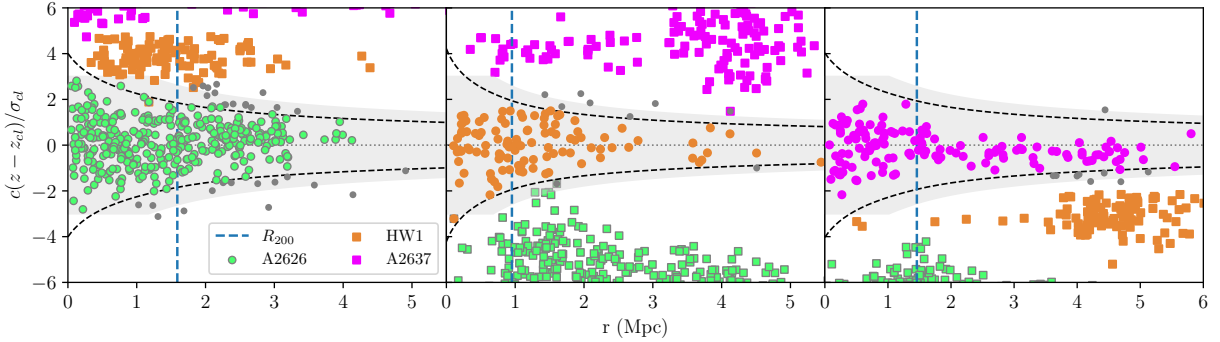


Figure 4.11: Phase space diagram for A2626 (left), HW1 (middle), and A2637 (right). The black dashed lines indicate the escape velocity for each over-density. This was calculated using the formalism from Jaffé et al. (2015), assuming a concentration index $C = 6$ and the mass enclosed by R_{200} from Equation 4.7. Galaxies located within the escape velocity trumpet for each over-density are represented by the coloured data points. The grey circles represent galaxies that satisfy $-3\sigma_{cl} < v < 3\sigma_{cl}$ (Eq. 4.5) but are not located within the escape-velocity trumpet for the particular over-density. The vertical dashed blue line indicates R_{200} for each cluster. The grey shaded region shows the galaxies used in the DS test for each cluster.

4.5 Substructure in A2626

Mohr et al. (1996) identified three sub-components with distinct velocities within 2.1 Mpc of A2626. Their Groups A, B, and C match our definitions of A2626, HW1, and A2637, respectively. Applying the Dressler-Shectman (DS, Dressler & Shectman, 1988) test to their 159 redshifts, Mohr et al. (1996) found no substructure within any of the three groups. This is perhaps not too surprising as the DS test (like many substructure finding methods) is sensitive to the number of redshifts used. More recently, using new data from the WINGS survey, Ramella et al. (2007) applied a non-parametric clustering algorithm to A2626 and also found no significant substructure. This is also unsurprising given that the WINGS spectroscopy is limited to $R < 0.7 R_{200}$ and redshifts of 76 galaxies. Early work on clusters such as the Coma cluster found no significant substructure within the cluster (Dressler & Shectman, 1988), but later works with more redshifts found the Coma cluster to contain a significant amount of substructure (Adami et al., 2005; Healy et al., 2021b).

4.5.1 Identifying substructures

To identify groups of galaxies that are kinematically distinct from their parent cluster, we used the DS test, which has been successful in many other clusters (e.g., Hess et al., 2015; Healy et al., 2021b). The DS test parameter is defined as

$$\delta_i^2 = \left(\frac{N_{nn} + 1}{\sigma_{cl}^2} \right) [(\bar{v}_{local}^i - \bar{v}_{cl})^2 + (\sigma_{local}^2 - \sigma_{cl}^2)], \quad (4.8)$$

where σ_{cl} is the cluster velocity dispersion, v_{cl} is the mean velocity of the cluster (given in Table 4.4), and σ_{local} and v_{local} are the velocity dispersion and mean velocity of a putative group with N_{nn} nearest neighbours. We used $N_{nn} = 5, 10, 15, 20,$ and 25 and identified groups that consistently appear with multiple N_{nn} values.

We ran the DS test on all three of the over-densities in the field. A simple $\pm 3\sigma_{cl}$ cut in velocity results in contamination from the neighbouring over-densities, and we therefore assigned galaxies to the different over-densities based on their location in the distance–velocity phase space (Figure 4.11). To assign galaxies, we widened the trumpet by doubling M_{200} and selected all galaxies within the wider trumpet and having velocities within $3\sigma_{cl}$ of the cluster velocity.

Figure 4.12 reveals six groups associated with A2626, four groups with HW1, and five groups associated with A2637. The identified groups are shown by the different symbols and coloured

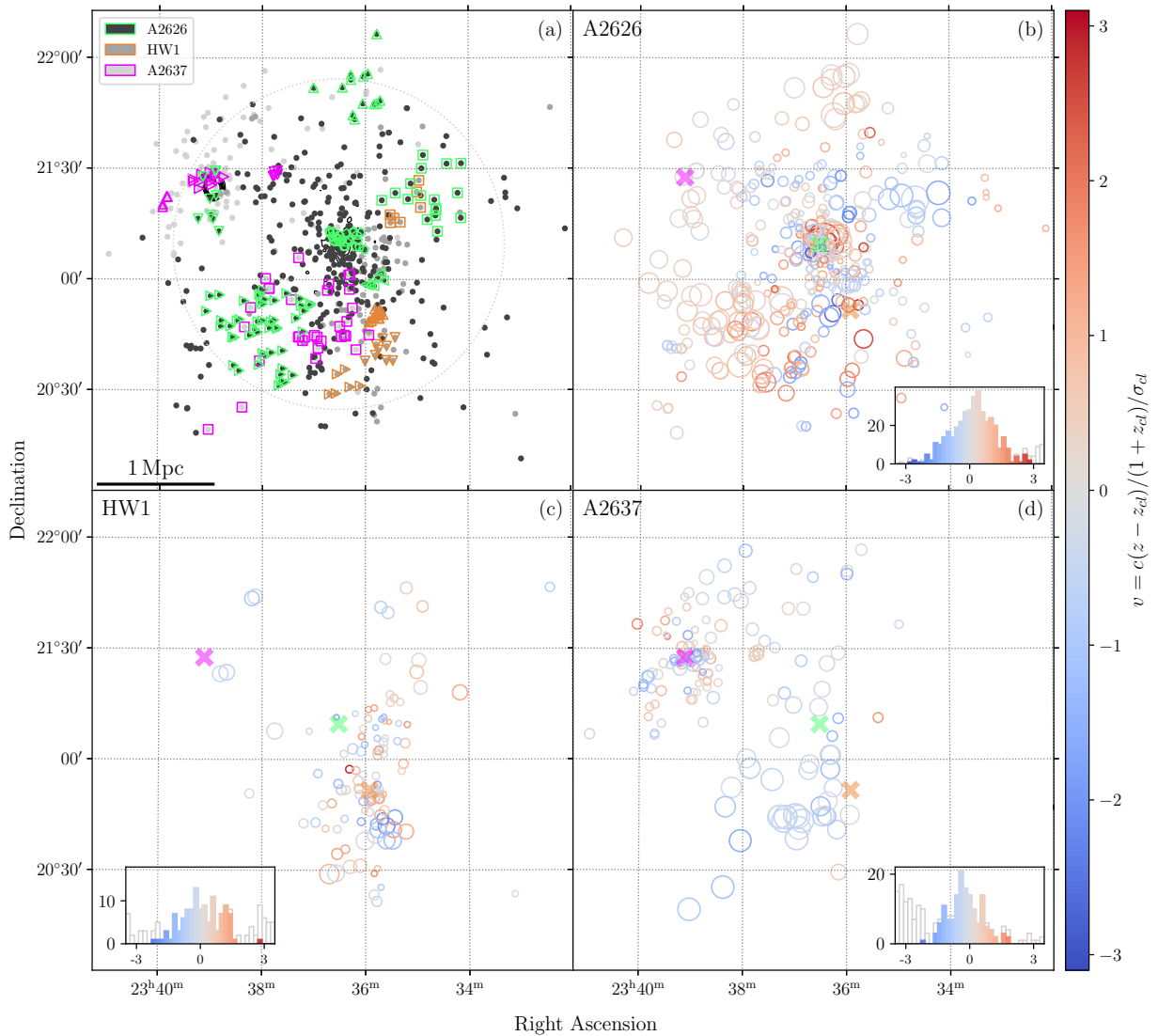


Figure 4.12: Sky distribution of galaxies in the over-densities. Colours in each panel mark related substructures. Panel (a) shows all three main structures A2626, HW1, and A2637 as marked by the colours of the open symbols. The open symbol shapes indicate group membership within the main structure. The black, grey, and light grey points represent the galaxies not associated with substructure in A2626, HW1, and A2637 respectively. Panels (b), (c), and (d) show the results from the DS test for A2626, HW1, and A2637 respectively. The size of each symbol is scaled by e^{δ_i} where δ_i is calculated by Equation 4.8 for $N_{\text{m}} = 10$. The large crosses mark the three main over-density centres. The histograms in the lower corners of the panels show the velocity distribution of the sources in that panel with colours indicating velocity relative to the mean velocity of the over-density. Horizontal units are σ_{cl} as given in Table 4.4.

by their parent cluster in panel (a) of Figure 4.12. More detailed sky distribution and velocity histogram plots of the identified groups are shown in Figure 4.13. The H I information is useful here as groups that are H I rich are more likely to be recent additions to the cluster environment.

4.5.2 Substructure in A2626

The locations and velocity distributions of the six groups identified within A2626 are shown in Figure 4.12, and the details are given in Table 4.5. Four of the groups (A1, A2, A3, and A4) are located outside R_{200} of the cluster and contain between 10 and 60% H I detections. This suggests these groups are on first infall into the cluster. The two smaller groups A2 and A3 have mean velocities similar to the cluster velocity (16576 km s^{-1}) consistent with being accreted from the wall

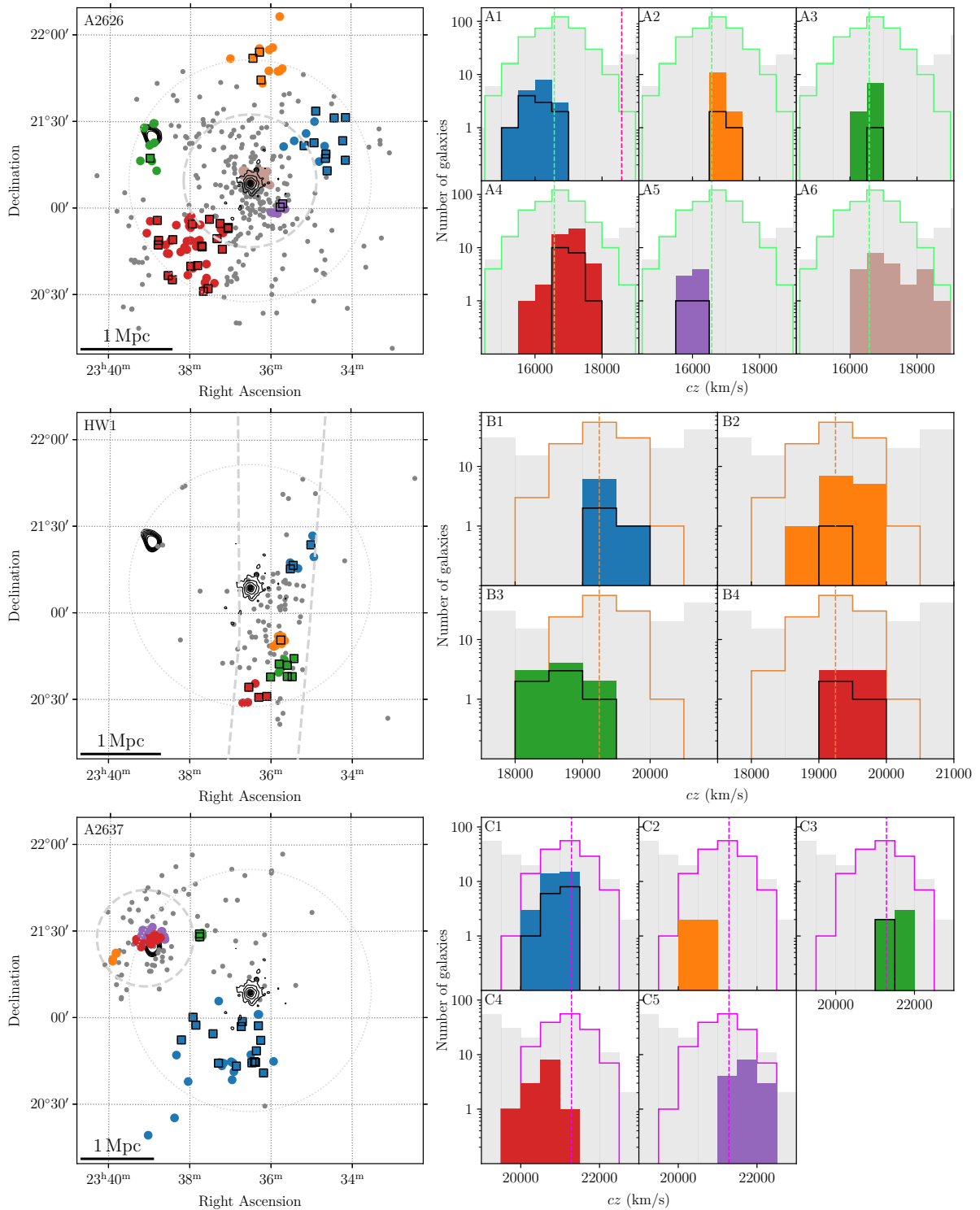


Figure 4.13: Sky distribution and velocity histograms of identified groups in A2626, HW1, and A2637. The large faint grey dotted lines show R_{200} of the clusters and over-density. Contours show X-ray emission from ROSAT at the centre of A2626 and A2637. The groups identified using the DS test are indicated by the coloured points. Black outlines indicate galaxies detected in H I (Healy et al., 2021a). Grey points show galaxies associated with the over-density but not part of any identified substructure. The velocity histograms of the identified groups are shown in the panels on the right. In the histogram panels, the background grey histogram shows the velocity distribution of the entire sample, and the open histograms outlined by green (A2626), orange (HW1), and pink (A2637) represent the galaxies identified as part of the clusters. The coloured histograms correspond to the groups highlighted in the sky distribution plot. The black open histograms in each panel show the velocity distributions of the H I-detected galaxies (Healy et al., 2021a) in each group.

Table 4.5: Groups identified in A2626 using the DS test

Group ID	N_m	\bar{v} (km s^{-1})	σ_g (km s^{-1})
A1	17	16130	339
A2	13	16868	151
A3	9	16660	156
A4	49	17051	402
A5	7	16104	161
A6	24	17216	685

Table 4.6: Groups identified in HW1 using the DS test

Group ID	N_m	\bar{v} (km s^{-1})	σ_g (km s^{-1})
B1	7	19409	79
B2	13	19433	282
B3	9	18731	325
B4	6	19560	248

in which A2626 is embedded and therefore moving in the plane of the sky. Groups A1 and A4 have mean velocities respectively lower and higher than the cluster velocity. This could mean that A1 is falling into the cluster from behind, while A4 is falling in from the front. While there are no known filaments connecting to A2626, A2622 (another member of SCL 213) is nearby to the north of A2626. However A1 and A4 are coming in from the northeast and southwest respectively, suggesting, along with the high fraction of H I detections, that these groups are not being accreted along a filament but rather from the field.

The two groups located inside R_{200} (A5 and A6) tell us something about the recent accretion onto the cluster. A5 still has 25% of its galaxies detected in H I, suggesting this is a group new to A2626. A5's velocity relative to the cluster suggests falling in from behind the cluster. Group A6 is near the cluster centre (offset 250 kpc northwest) and has no H I detections. Presumably it was accreted early.

The overall picture that A2626 has undergone a merger (Mohr et al., 1996; Mohr & Wegner, 1997; Wong et al., 2008) is supported by the X-ray observations. Wong et al. (2008) found a significant change in the X-ray temperature at a radius of 260 kpc from the centre of the cluster. They suggested an ongoing or previous merger as the likely explanation. The offset position of A6 from the centre of the cluster is consistent with the echo of a group merging with the cluster center. The projected distance between A6 and the centre of A2626 roughly is consistent with the radius of the change in X-ray temperature. A6 includes the emission-line galaxy IC 5337, which Wong et al. (2008) suggested is infalling from the west of the cluster.

4.5.3 Substructure in HW1

HW1, as discussed above, is probably not a cluster but rather a collimated collection of galaxies and galaxy groups. The DS test identified four distinct groups in this over-density. B3 might be on an infall trajectory towards A2626, its mean velocity being only $3.2 \sigma_{A2626}$ higher than the cluster velocity of A2626 and located just beyond A2626's R_{200} . In this scenario, the higher relative mean velocity of B3 would suggest it is approaching A2626 from in front. While most of B3 was not included in the DS test for A2626 due to the galaxy velocities being greater than $3 \sigma_{cl}$ from A2626, we see hints of the eastern and lower-velocity side of this group in Figure 4.12b around $23^{\text{h}}36^{\text{m}} +20^{\circ}35'$.

The three groups B1, B2, and B4 all have mean velocities that differ too much from A2626's for them to be associated. B1, B2, and B4 are also linearly aligned and have mean velocities that are within 150 km s^{-1} . However it is unclear whether this is a chance alignment or a result of the

Table 4.7: Groups identified in A2637 using the DS test

Group ID	N_m	\bar{v} (km s ⁻¹)	σ_g (km s ⁻¹)
C1	32	20905	242
C2	4	20521	97
C3	5	21527	180
C4	13	20572	287
C5	15	21755	329

underlying large scale structure. B1, B3, and B4 include >40% H I detections, implying that these groups have been little-affected by stripping.

4.5.4 Substructure in A2637

Our substructure analysis of A2637 is not as complete as for A2626 or HW1 because A2637 is on the edge of the MMT survey. This cluster is also outside the MeerKAT FWHM, which means the H I sensitivity for this cluster is not as good as for A2626 and HW1. Despite this, we identified four groups C2, C3, C4, and C5 associated with the cluster and one group, C1, at a similar redshift but >1 Mpc from the cluster. C2 and C3 both appear to be infalling or recently accreted (particularly C2). However, the paucity of H I data leaves the gas-stripped fractions uncertain.

There are two groups, C4 and C5, near the centre of A2637. The two are similar in size but have mean velocities differing by >1100 km s⁻¹. At the heart of C5 is 2MASXI J2338533+212752, identified as a brightest cluster galaxy (BCG) (Lauer et al., 2014). Based on this, we hypothesise that C5 is at the centre of the cluster, and C4 has been accreted and is merging with C5. Similar substructure is seen, for example, at the centre of the Coma cluster, where there are separate X-ray emission peaks coinciding with the BCGs associated with two substructures (Adami et al., 2005; Healy et al., 2021b). It is also widely accepted that the two groups at the centre of the Coma cluster are merging (e.g. Colless & Dunn, 1996; Adami et al., 2005). In the case of groups C4 and C5 in A2637, no such detailed X-ray analysis has yet been carried out.

The diffuse group C1, which contains nearly 50% H I detections, does not appear to be associated with A2637. Its centre is $\sim 3 R_{200}$ from A2637, and there are no galaxies between C1 and A2637 which could hint at a connection. This raises the question of how C1 fits into the large scale structure of the system, but the limited field of view of the MMT survey and the lack of available redshifts outside it make it difficult to speculate on the possible origins of C1.

4.6 Summary

There are now over 2900 redshifts in a $2^\circ \times 2^\circ$ field centred on the cluster A2626. The A2626 complex is made up of A2626 itself ($z \approx 0.055$), the cluster A2637 ($z \approx 0.071$), and an apparent wall or at least an extended structure designated here as HW1 ($z \approx 0.064$). The structure is linear rather than centrally concentrated, and its origins and connections to the large scale structure around the clusters remain unclear. On a larger scale, the A2626–HW1–A2637 complex appears not connected to the Perseus–Pegasus filament.

At much larger distances than A2637, the cluster A2625, formerly thought to be at roughly the same redshift as A2626 (Struble & Rood, 1999), is in fact the same cluster as RM J233602.7+203245.1 at $z \approx 0.102$ ($cz = 30519 \text{ km s}^{-1}$). There are at least three and probably four other clusters in the background, the most distant at $z \approx 0.42$.

The greater numbers of confirmed members of A2626, A2637, and HW1 have revealed substructures within these systems. There are six substructures within A2626, five within A2637, and probably four within HW1, although one of these last could instead be a group associated with A2626. The new redshifts have also decreased the uncertainties in the systems' velocity dispersions and sizes, which are now known to better than 10%.

This work has shown the importance of extensive spectroscopy in identifying large-scale structure and linking components together. Even with the existing data, though, some questions remain: how is HW1 connected to the structure around it? And how do A2626 and A2637 connect to the other members of the supercluster SCL 213? Answering these questions will require spectra over a still wider area on the sky than observed here, and we look to the future of wide-area spectroscopic surveys such as the WEAVE Wide-field Cluster Survey (Jin et al. 2021, in prep.) to be able to answer some of the outstanding questions about the environment in which A2626 is embedded. Wider-field H I observations will also be valuable.

Acknowledgements

JH acknowledges research funding from the South African Radio Astronomy Observatory, which is a facility of the National Research Foundation, an agency of the Department of Science and Innovation. We thank K Hess for useful discussions about groups and filaments. We thank the UCT Writing Circle for suggestions that improved the readability of this work. MV acknowledges support by the Netherlands Foundation for Scientific Research (NWO) through VICI grant 016.130.338. This paper uses data products produced by the OIR Telescope Data Center, supported by the Smithsonian Astrophysical Observatory. The authors thank Nelson Caldwell for help with the Hectospec configuration design and queue scheduling processes, Sean Moran for maintaining the Hectospec data pipeline, and Jessica Mink for help with XCSAO. This research has made use of the SIMBAD database, operated at CDS, Strasbourg, France. Funding for the Sloan Digital Sky Survey IV has been provided by the Alfred P. Sloan Foundation, the U.S. Department of Energy Office of Science, and the Participating Institutions. SDSS-IV acknowledges support and resources from the centre for High-Performance Computing at the University of Utah. The SDSS web site is www.sdss.org. SDSS-IV is managed by the Astrophysical Research Consortium for the Participating Institutions of the SDSS Collaboration including the Brazilian Participation Group, the Carnegie Institution for Science, Carnegie Mellon University, the Chilean Participation Group, the French Participation Group, Harvard-Smithsonian centre for Astrophysics, Instituto de Astrofísica de Canarias, The Johns Hopkins University, Kavli Institute for the Physics and Mathematics of the Universe (IPMU)/University of Tokyo, the Korean Participation Group, Lawrence Berkeley National Laboratory, Leibniz Institut für Astrophysik Potsdam (AIP), Max-Planck-Institut für Astronomie (MPIA Heidelberg), Max-Planck-Institut für Astrophysik (MPA Garching), Max-Planck-Institut für Extraterrestrische Physik (MPE), National Astronomical Observatories of China, New Mexico State University, New York University, University of Notre Dame, Observatório Nacional/MCTI, The Ohio State University, Pennsylvania State University, Shanghai Astronomical Observatory, United Kingdom Participation Group, Universidad Nacional Autónoma de México, University of Arizona, University of Colorado Boulder, University of Oxford, University of Portsmouth, University of Utah, University of Virginia, University of Washington, University of Wisconsin, Vanderbilt University, and Yale University.

References

- Abell G. O., 1958, *The Astrophysical Journal Supplement Series*, 3, 211
- Abell G. O., Corwin Harold G. J., Olowin R. P., 1989, *The Astrophysical Journal Supplement Series*, 70, 1
- Adami C., Biviano A., Durret F., Mazure A., 2005, *Astronomy and Astrophysics*, 443, 17
- Aragón-Calvo M. A., Van De Weygaert R., Jones B. J., 2010, *Monthly Notices of the Royal Astronomical Society*, 408, 2163
- Batuski D. J., Burns J. O., 1985, *Astrophysical Journal*, 299, 5
- Beers T. C., Flynn K., Gebhardt K., 1990, *The Astronomical Journal*, 100, 32
- Blanton M. R., et al., 2001, *The Astronomical Journal*, 121, 2358
- Bohringer H., et al., 2000, *The Astrophysical Journal Supplement Series*, 129, 435
- Bond J. R., Kofman L., Pogosyan D., 1996, *Nature*, 380, 603
- Cautun M., Van De Weygaert R., Jones B. J., Frenk C. S., 2014, *Monthly Notices of the Royal Astronomical Society*, 441, 2923
- Cava A., et al., 2009, *Astronomy and Astrophysics*, 495, 707
- Chowdhury A., Kanekar N., Chengalur J., Sethi S., Dwarakanath K. S., 2020, *Nature*, 586, 369
- Colless M., Dunn A. M., 1996, *The Astrophysical Journal*, 458, 435
- Colless M., et al., 2001, *Monthly Notices of the Royal Astronomical Society*, 328, 1039
- Dressler A., 1980, *The Astrophysical Journal*, 236, 351
- Dressler A., Shectman S. A., 1988, *The Astronomical Journal*, 95, 985
- Ebeling H., Edge A. C., Böhringer H., Allen S. W., Crawford C. S., Fabian A. C., Voges W., Huchra J. P., 1998, *Monthly Notices of the Royal Astronomical Society*, 301, 881
- Einasto M., Einasto J., Tago E., Müller V., Andernach H., 2001, *The Astrophysical Journal*, 122, 2222
- Fabricant D., et al., 2005, *Publications of the Astronomical Society of the Pacific*, 117, 1411
- Fasano G., et al., 2006, *Astronomy and Astrophysics*, 445, 805
- Fernández X., et al., 2016, *The Astrophysical Journal Letters*, 824, 7
- Finn R. A., et al., 2005, *The Astrophysical Journal*, 630, 206
- Guzzo L., et al., 2013, *ESO Messenger*
- Healy J., Blyth S.-L., Elson E., van Driel W., Butcher Z., Schneider S., Lehnert M. D., Minchin R., 2019, *Monthly Notices of the Royal Astronomical Society*, 487, 4901
- Healy J., Deb T., Verheijen M., Blyth S.-L., Serra P., Ramatsoku M., Vulcani B., 2021a, *Astronomy & Astrophysics*
- Healy J., et al., 2021b, *Astronomy & Astrophysics*, 650

- Hess K. M., Jarrett T. H., Carignan C., Passmoor S. S., Goedhart S., 2015, *Monthly Notices of the Royal Astronomical Society*, 452, 1617
- Hou A., et al., 2012, *Monthly Notices of the Royal Astronomical Society*, 421, 3594
- Ignesti A., Gitti M., Brunetti G., O'Sullivan E., Sarazin C., Wong K., 2018, *Astronomy and Astrophysics*, 610, 89
- Jaffé Y. L., Smith R., Candlish G. N., Poggianti B. M., Sheen Y.-K., Verheijen M. A. W., 2015, *Monthly Notices of the Royal Astronomical Society*, 448, 1715
- Lauer T. R., Postman M., Strauss M. A., Graves G. J., Chisari N. E., 2014, *Astrophysical Journal*, 797, 82
- Lucey J. R., 1983, *Monthly Notices of the Royal Astronomical Society*, 204, 33
- Malavasi N., et al., 2017, *Monthly Notices of the Royal Astronomical Society*, 465, 3817
- Mink D. J., Wyatt W. F., Caldwell N., Conroy M. A., Furesz G., Tokarz S. P., 2007, *Astronomical Data Analysis Software and Systems XVI ASP Conference Series*, 376, 249
- Mohr J. J., Wegner G., 1997, *The Astronomical Journal*, 114, 25
- Mohr J. J., Geller M. J., Wegner G., 1996, *The Astronomical Journal*, 112, 1816
- Moretti A., et al., 2019, *The Astrophysical Journal*, 889, 9
- Owen F. N., Ledlow M. J., Keel W. C., 1995, *The Astronomical Journal*, 109, 14
- Patel P., Maddox S., Pearce F. R., Aragón-Salamanca A., Conway E., 2006, *Monthly Notices of the Royal Astronomical Society*, 370, 851
- Piffaretti R., Arnaud M., Pratt G. W., Pointecouteau E., Melin J. B., 2011, *Astronomy and Astrophysics*, 534, A109
- Poggianti B. M., et al., 2016, *The Astronomical Journal*, 151, 78
- Poggianti B. M., et al., 2019, *The Astrophysical Journal*, 889
- Postman M., Huchra J. P., Geller M. J., 1986, *The Astronomical Journal*, 92, 1238
- Ramella M., et al., 2007, *Astronomy and Astrophysics*, 470, 39
- Rizza E., Loken C., Bliton M., Roettiger K., Burns J. O., Owen F. N., 2000, *The Astronomical Journal*, 119, 21
- Rykoff E. S., et al., 2014, *Astrophysical Journal*, 785, 104
- Smee S., et al., 2012, *Astronomical Journal*, 146, 2013
- Strauss M. A., et al., 2002, *The Astronomical Journal*, 124, 1810
- Struble M. F., Rood H. J., 1987, *The Astrophysical Journal Supplement Series*, 63, 543
- Struble M. F., Rood H. J., 1999, *The Astrophysical Journal Supplement Series*, 125, 35
- Tully R. B., 1986, *The Astrophysical Journal*, 303, 25
- Tully R. B., 1987, *The Astrophysical Journal*, 323, 1

- Varela J., et al., 2009, *Astronomy and Astrophysics*, 497, 667
- Wong K.-W., Sarazin C. L., Blanton E. L., Reiprich T. H., 2008, *The Astrophysical Journal*, 682, 155
- Yuan Z. S., Han J. L., Wen Z. L., 2016, *Monthly Notices of the Royal Astronomical Society*, 460, 3669
- Zwicky F., et al., 1961, *Catalogue of galaxies and of clusters of galaxies, Vol. I*. California Institute of Technology (CIT), Pasadena, <https://ui.adsabs.harvard.edu/abs/1961cgcg.book.....Z/abstract>
- de Lapparent V., Geller M. J., Huchra J. P., 1986, *The Astrophysical Journal*, 302, L1



"This is the way."
(The Mandalorian)

Chapter 5

H I beyond the detection threshold in Abell 2626

Abstract

In Chapter 3, I presented new H I observations of the galaxy cluster Abell 2626, and in Chapter 4, using a combination of literature and new MMT redshifts, I identified six kinematic substructures within the cluster. In this chapter, I use the H I stacking technique to probe the average H I content of the cluster galaxies. Using the substructure information, I compare the average H I content of the cluster galaxies not in substructure to that of the cluster galaxies in substructures in order to investigate whether the processes removing the H I from the galaxies (e.g. ram-pressure stripping, harassment, starvation) occur preferentially in either environment. I also explore the global optical and H I properties of the cluster, comparing the average H I properties of the Abell 2626 galaxies to galaxies in the Virgo and Coma clusters.

5.1 Introduction

In the current cosmological paradigm of Λ cold dark matter, the hierarchical merging of structures is responsible for the building of successively larger structures (Springel et al., 2005). This means that large cosmological structures such as galaxy clusters are formed through the successive merging and accretion of individual galaxies and galaxy groups. Roughly 30% of galaxy clusters are known to contain kinematic substructure (e.g. Dressler & Shectman, 1988; Bird, 1994; Hou et al., 2012). This implies that group environments can play an important role in the evolution of cluster galaxies prior to infall onto the cluster (McGee et al., 2009).

Since galaxies were first systematically classified according to their visual morphology, it has been known that galaxies of different morphological classes in the cluster environment differ from galaxies of similar morphologies in the field (Hubble & Humason, 1931). Dressler (1980) later noted that dense cosmic environments, such as galaxy clusters, had a higher fraction of early-type galaxies than the less dense cosmic environments, and the opposite trend was noted for late-type galaxies – these tended to be found in less dense cosmic environments. This observation became known as the morphology-density relation (Dressler, 1980). Follow-up work by Dressler et al. (1997) showed that centrally concentrated, regular clusters have the spiral fraction increasing outward with radius, while the elliptical fraction increased inward, and the S0 population tends to be flat. The morphology-radius (T-R) relation is also present in the Coma cluster, but with different fractions (Beijersbergen, 2003, Chap 4) than what is presented in Dressler et al. (1997). Dressler et al. (1997) explored whether the same T-R relation is seen in more distant clusters ($z \sim 0.4$), separating the cluster sample into regular (centrally concentrated) and irregular. They found that the elliptical fraction is high no matter the concentration of the cluster; they suggest that the elliptical galaxies pre-date the virialisation of the cluster. This has shown to be true for early-type galaxies in the Coma cluster, which are suggested to have formed at $z \gtrsim 2$ (Bower et al., 1990, 1992). However this does not answer the question as to why the late-type galaxy population decreases towards the centre of the cluster.

In populations of field galaxies, it has been shown that there are two evolutionary tracks, one for late-type galaxies and one for early-type galaxies, that occur over very different timescales (Schawinski et al., 2014; Peng et al., 2010). The evolutionary track for late-type galaxies is the longer of the two, occurring on Gyr timescales and triggered by a shutoff in the cold gas supply that leads to a drop in the specific star formation rate as the remainder of the gas reservoir is depleted (Schawinski et al., 2014). This sequence of events has been shown to hold, albeit on shorter timescales, in galaxies experiencing an evolutionary change as a result of environmental processing (Oman et al., 2021). Environmental processing speeds up the evolutionary process as mechanisms such as ram-pressure stripping (Gunn & Gott, 1972) and galaxy harassment (e.g. Moore et al., 1996; Jaffé et al., 2016) have been shown to remove the cold gas from cluster galaxies. While ram-pressure stripping has been observed in less dense group environments (Vulcani et al., 2018), it is extremely effective at stripping the HI from galaxies. Some models have shown that by peri-centric passage, the galaxies are completely quenched (e.g. Roediger & Brüggen, 2007; Oman & Hudson, 2016). There is mounting evidence that while the cluster environment is very effective at galaxy quenching, the process has already started in the group environment prior to cluster infall (e.g. Hess et al., 2015; Yoon et al., 2017; Dzudzar et al., 2019; Kleiner et al., 2021), this is known as “pre-processing”.

Abell 2626 (A2626; Abell, 1958), is a moderately sized (Cava et al., 2009; Healy et al., 2021a) galaxy cluster that provides an ideal environment in which to study ongoing galaxy evolution: the cluster is home to six galaxies identified by Poggianti et al. (2016) as exhibiting ‘jellyfish’ morphologies, a result of ongoing ram-pressure stripping (e.g. Moretti et al., 2019; Poggianti et al., 2019). A2626 has also been shown to contain significant substructure (e.g. Healy et al., 2021a; Mohr et al., 1996), with some identified groups located outside R_{200} that are believed to still be on first infall. This provides an opportunity to study whether or not pre-processing plays a role in removing the

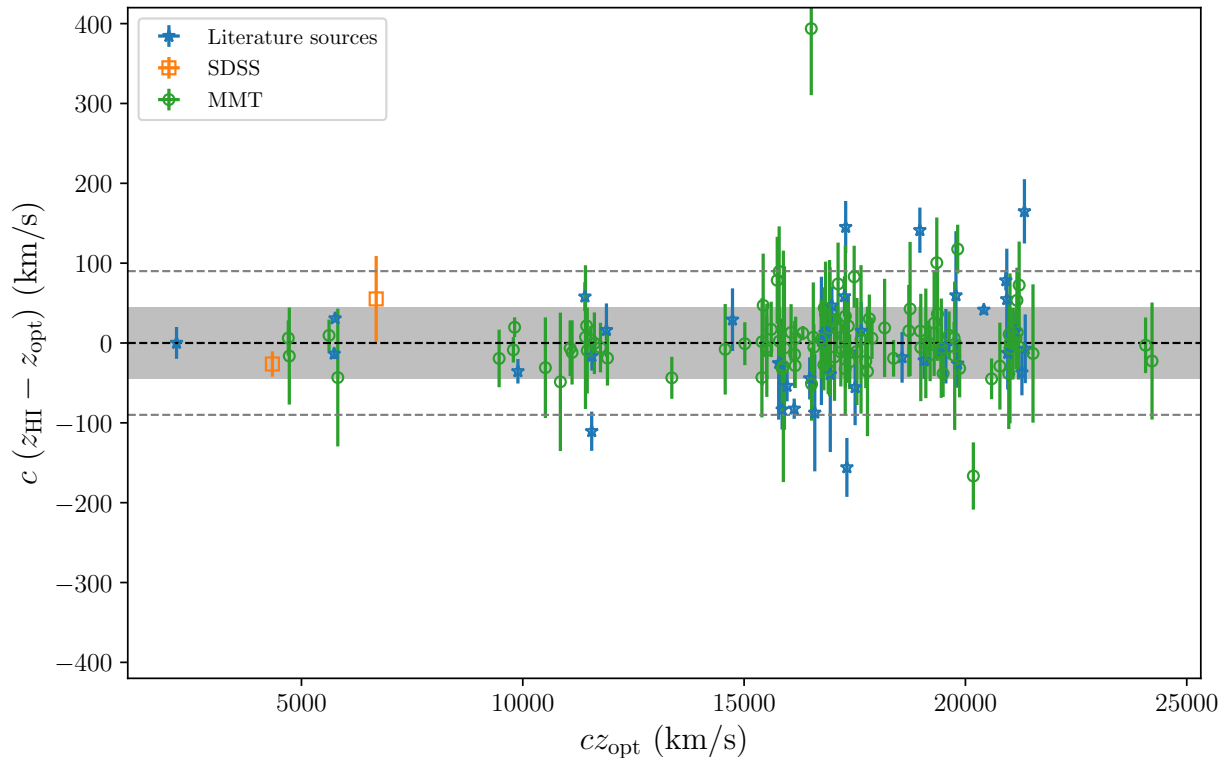


Figure 5.1: Comparison between the optical and H I redshifts for 161 H I detections in the MeerKAT H I cube. The colour and shapes of the data points indicate from where the redshifts were obtained. The grey band indicates ± 1 channel ($\pm 45 \text{ km s}^{-1}$) and the horizontal dashed lines are at ± 2 channels ($\pm 90 \text{ km s}^{-1}$).

H I content from the group galaxies. A2626 was observed by MeerKAT in 2019, which provided deep H I observations for the cluster galaxies (Healy et al., in prep). However, despite the sensitive MeerKAT H I data only a quarter of the cluster galaxies (out to $\sim 2 R_{200}$) are detected in H I. Thus using deep, complementary optical spectroscopy centred on the cluster, I can use the H I stacking technique as a method to probe the average H I content of samples of galaxies in different regions of the cluster. H I stacking has been successfully used to study the average H I content of cluster galaxies (e.g. Verheijen et al., 2007; Jaffé et al., 2016; Healy et al., 2021c), and can be an important tool in identifying H I just below the detection threshold.

This chapter is organised into two parts. In the first part, I characterise the cluster galaxy population using visually identified morphologies, and optical photometry from the DECam Legacy Surveys (DECaLS; Dey et al., 2019) to determine the richness class of the cluster. I also explore the radial-H I deficiency relation of the cluster galaxies, and compare it to other nearby clusters. In the second part, I explore which cosmic environment, the local group environment or the global cluster environment, plays a stronger role in removing the H I from the member galaxies. Throughout this chapter, I use $H_0 = 70 \text{ km s}^{-1} \text{ Mpc}^{-1}$, $\Omega_M = 0.3$, $\Omega_\Lambda = 0.7$, and $h = 0.7$.

5.2 Multi-wavelength data

5.2.1 Spectroscopy

The key technique used in this chapter to study the gas content in the A2626 galaxies, is the H I stacking technique. This requires the redshift information of the galaxies so that the H I line spectra can be aligned and co-added. In Chapter 4, I presented new and deep spectroscopy of a $\sim 1.8 \text{ deg}^2$ field centred on A2626, adding to the existing spectroscopic catalogues in the literature. The full catalogue presented in Chapter 4 contains galaxies with redshifts from $0 < z \lesssim 0.46$, and is 50%

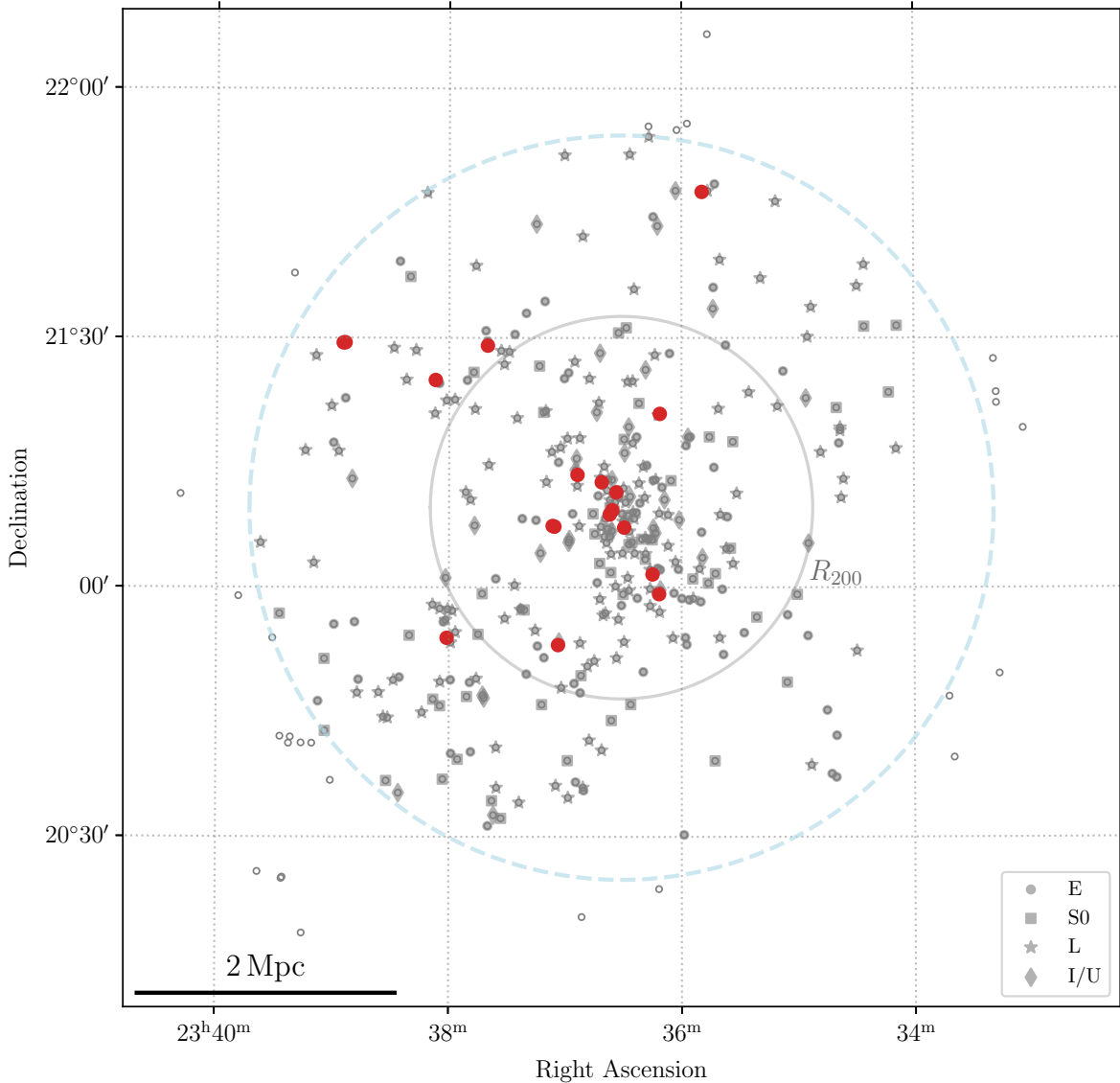


Figure 5.2: Spectroscopically confirmed members of Abell 2626. The dashed light blue circle has a radius of 0.79 deg – the radius at which spectroscopic completeness is 50%. The inner grey circle represents the R_{200} of the cluster. The open grey symbols represent cluster galaxies not included in the stacking sample, and the filled grey symbols representing the cluster galaxies in the stacking sample indicate the visual morphology listed in the legend. The filled red circles represent the 18 galaxies that have a nearby neighbour within a $45''$ radius with a recessional velocity within $cz \pm 500 \text{ km s}^{-1}$.

complete in SDSS r at $C_{50} = 19.6$ mag within a radius of $R_{50} = 0.79$ deg.

A key assumption of H I stacking is that the optical redshift is an accurate proxy for the H I redshift. The redshift accuracy can also play a role in broadening the stacked profile, thus lowering the signal to noise ratio of any possible detections in the stacked spectrum. This is not a concern with this particular H I data set as the average redshift uncertainty in the optical catalogue is 22 km s^{-1} which is less than the width of a single channel (45 km s^{-1}). Given that most of the galaxies in the cluster are not directly detected, the only way to determine how well this assumption holds for this sample is to compare the measured H I redshifts of galaxies with a corresponding optical redshift. Figure 5.1 shows the difference between the optical and H I redshifts as a function of the optical redshift. The data points representing the galaxies are coloured by the source of the optical redshift. The measured offset between the two redshift types is -0.9 km s^{-1} and the scatter is 32 km s^{-1} .

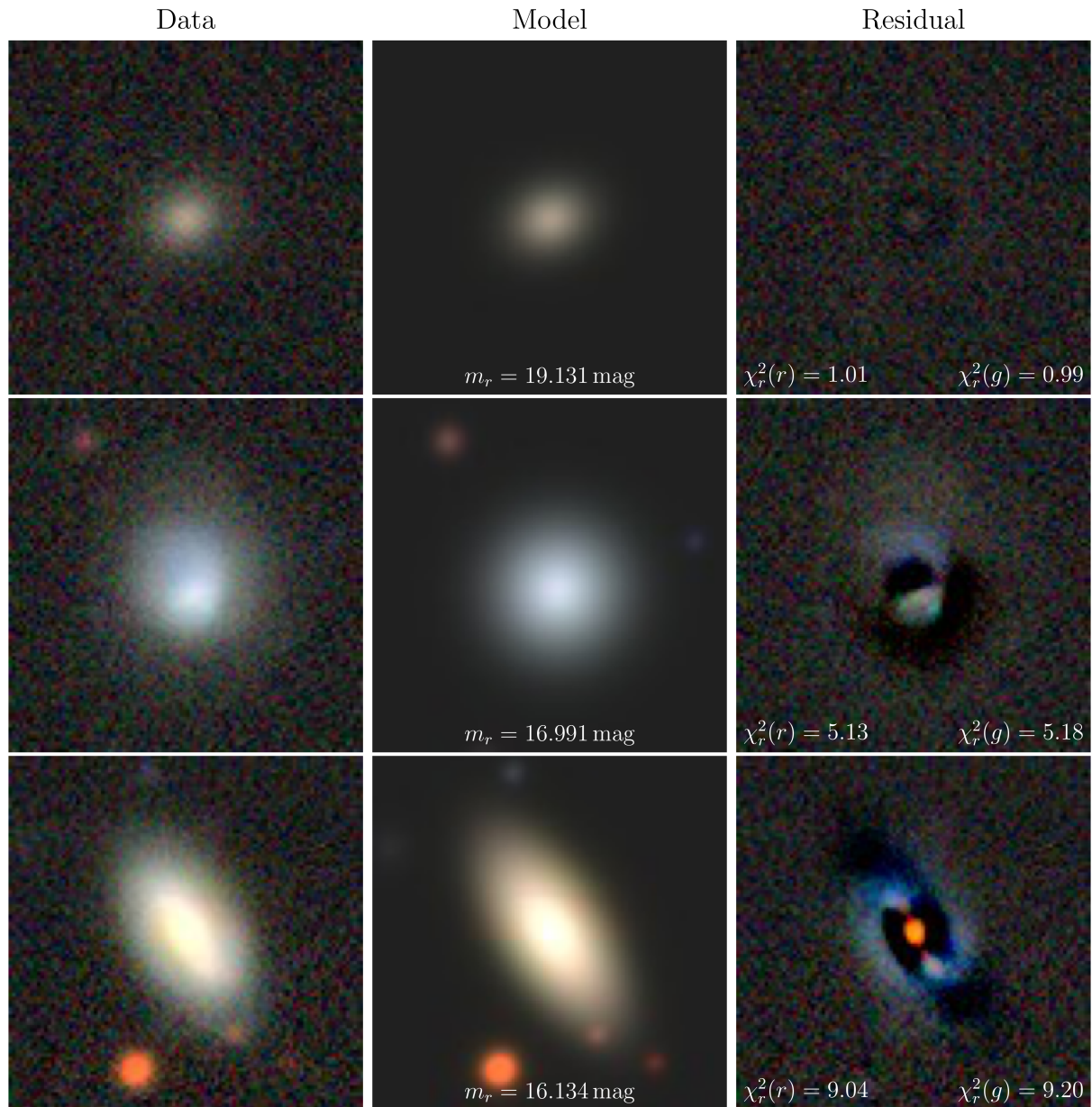


Figure 5.3: Examples of fits to the DECaLS data resulting in different χ_r^2 values. The cutouts are downloaded as is from the Legacy Surveys sky viewer. Left: the grz colour image of the data from DECaLS. Middle: best-fit model to the data. Right: residual image (data-model). The χ_r^2 values in the g - and r -band are printed in the bottom corners of the residual column.

The channel width of 45 km s^{-1} means that the scatter is contained within a channel, and from Figure 5.1, the majority of the galaxies are contained within $\pm 90 \text{ km s}^{-1}$. Individual galaxies with a larger offset between optical and HI redshifts may result in a broader stacked spectrum (Maddox et al., 2013).

This chapter focuses only on the 347 galaxies that are known to be part of A2626 and are within the projected R_{50} radius. Also included are the six substructures identified using the Dressler-Shectman (Dressler & Shectman, 1988) test in Chapter 4. Figure 5.2 shows the spatial distribution of all galaxies associated with A2626, where the filled grey symbols within the dashed blue circle ($R_{50} = 0.79 \text{ deg}$) represent the galaxies used in this chapter.

5.2.2 Optical photometry

A2626 is located within the footprints of a number of publicly accessible wide-area imaging surveys (e.g. SDSS, PANSTARRS, DECaLS). For this work, I have used g - and r -band photometry from Data Release (DR) 8 of the DECaLS survey. The galaxy fluxes are obtained directly from the DECaLS **Tractor** (Dey et al., 2019) catalogue. **Tractor** is a source detection and measurement software package. For each source, five models are fit to the image: a de Vaucouleurs (DEV) profile, an exponential profile (EXP), a rounded exponential profile (REX), a point source model (PSF), and a composite model (COMP) comprised of an exponential+de Vaucouleurs profile. The DEV profiles typically describe the elliptical galaxies, while the EXP/REX profiles typically describe the spiral galaxies. The integrated fluxes and morphological information from the best fit profile are contained in the **Tractor** catalogues which can be found at www.legacysurvey.org/dr8/catalogs.

I cross-matched the **Tractor** catalogue to the A2626 redshift catalogue within a $3''$ radius. Figure 5.3 shows the model fits and residuals for three galaxies in the cluster. Only sources where the fits in both the g - and r -band have a $\chi_r^2 < 10$ are used in this work. A comparison between the model magnitudes from DECaLS and Petrosian (aperture) magnitudes from SDSS shows no significant discrepancy for sources with a $\chi_r^2 \sim 9$ (as in the lower panel of Figure 5.3), compared to those with a lower χ_r^2 value. In galaxies (particularly the brighter galaxies), in which significant structure is present (e.g. spiral arms or asymmetries in the light distribution), the models will not be a good representation of the light distribution. The cutouts in Figure 5.3) are taken directly from the legacy survey sky viewer¹, and the imaging scaling and colouring is optimised for RGB colour images in the sky viewer. I converted the integrated fluxes from nanomaggies (as given in the catalogue) to AB magnitudes using:

$$m = 22.5 - 2.5 \log_{10}(f), \quad (5.1)$$

where f is the integrated flux (in nanomaggies) in the g - and r -band given in the catalogue. The magnitudes were Galactic extinction corrected using the Schlegel et al. (1998) dust maps.

Morphological types

One of the goals of this chapter is to understand how the HI content of galaxies changes as a function of environment for different morphological types. I use visually identified morphological classifications made by a collaborator, Jaco Brink. He visually classified the sample using imaging from DECaLS to separate the galaxy sample into Early types (E), Late types (L), Irregulars (I), and Lenticulars/S0s (S0). Galaxies, for which a classification was not possible (usually very faint galaxies), were marked as Unknown (U). Examples of the five morphological classifications are shown in Figure 5.4. I have compared the visual classifications to the model fit morphological classifications (see Figure 5.5). The comparison shows that most late types are modelled by an exponential profile, and most early types by a de Vaucouleurs profile. The S0s are split between the exponential and de Vaucouleurs profiles. This is consistent with the split theories on the formation of S0 galaxies (e.g. Deeley et al., 2020, and references therein). In the analysis that follows, I have used the visual classifications.

Galaxy sizes

Another parameter that I determined from the r -band DECaLS images are the sizes of the galaxies. For this, I measured the radius at the 25 mag/arcsec^2 isophote. This was done by fitting ellipses (allowing the central position, position angle, and ellipticity to vary) to the r -band DECaLS images using the Elliptical Isophote Analysis routines in **photutils**², an AstroPy affiliated package for photometry. Figure 5.6 illustrates the method I used to determine the R_{25} for one galaxy.

¹www.legacyviewer.org/viewer

²photutils.readthedocs.io

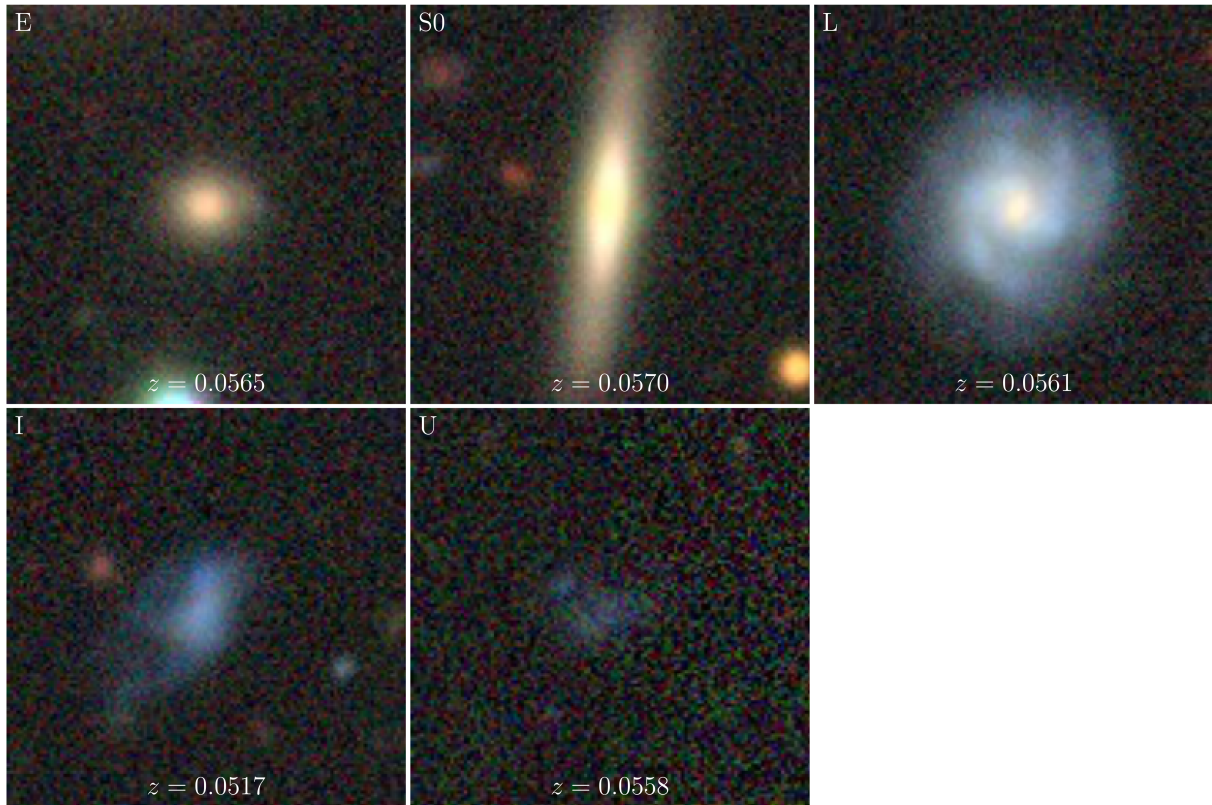


Figure 5.4: Examples of the visual morphological classifications for five galaxies in the cluster. The classification is printed in the top left corner of each panel. All five panels are on the same scale.

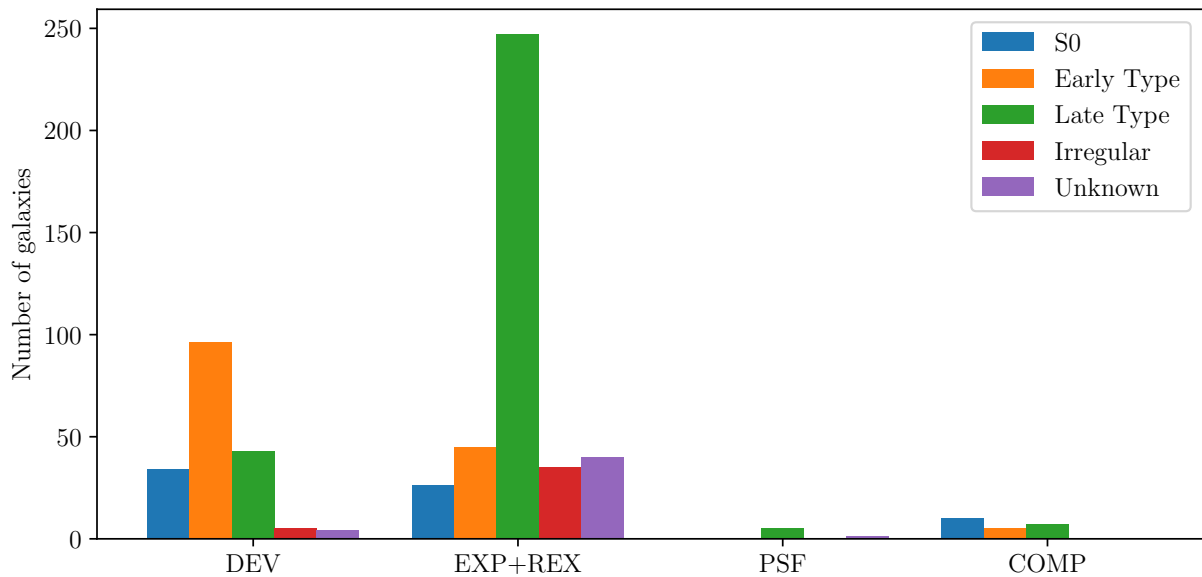


Figure 5.5: Comparison between visually identified galaxy morphologies and model-based morphologies. The labels on the x-axis indicate the best-fit model, while the colours of the bars indicate the visual morphology.

All the galaxy fits were inspected by eye, 14 of the 347 fits failed. There were two main reasons for failed fits: the source was too small/faint, or there were too many overlapping neighbouring sources making it difficult to determine the edge of the target galaxy. This exercise also provided

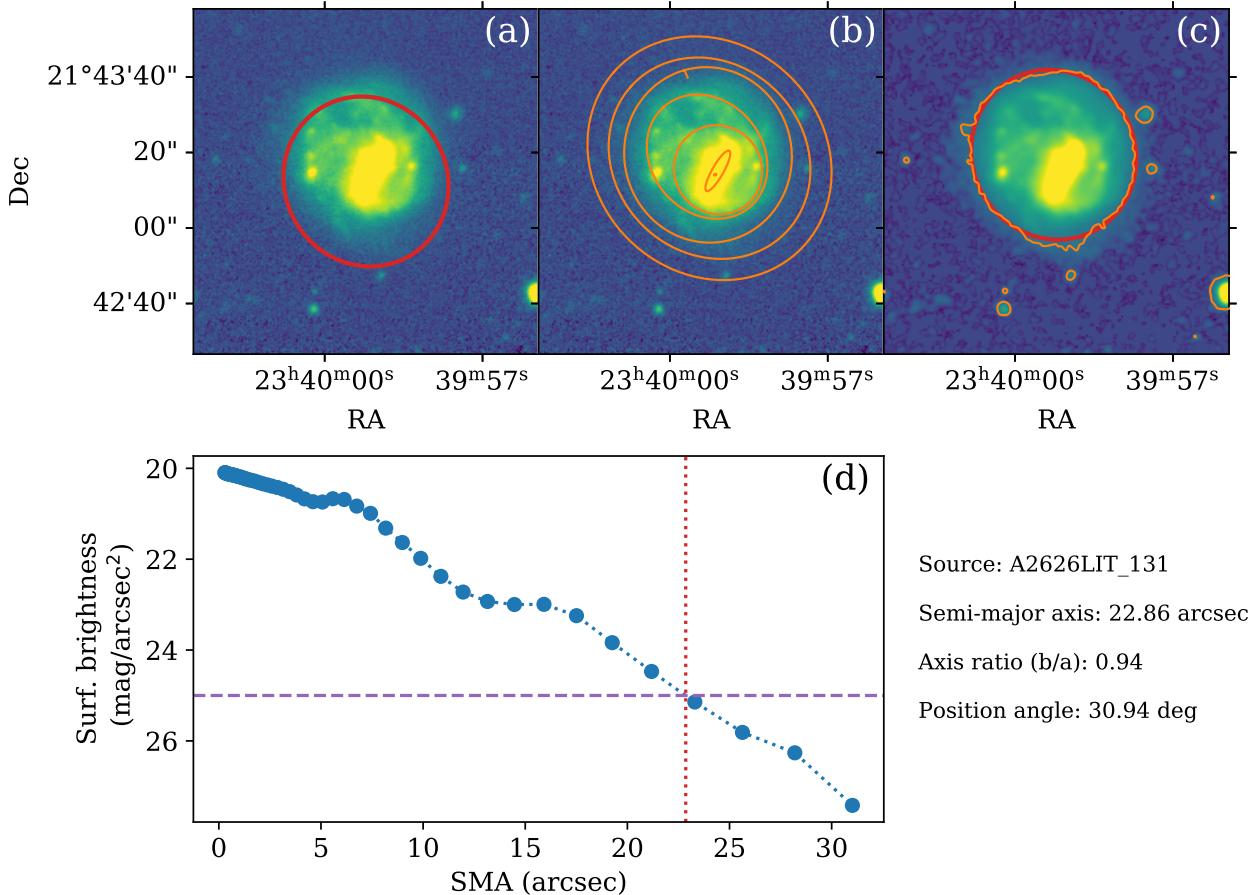


Figure 5.6: Panels (a)–(c) show DECaLS r -band cutouts centred on the target galaxy, in units of flux density (nanomaggies) for (a) and (b), and in surface brightness units ($\text{mag}/\text{arcsec}^2$) for (c). The thick red ellipse in (a) represents the size of the galaxy at the $25 \text{ mag}/\text{arcsec}^2$ isophote, and is centred on the position at which the galaxy redshift is measured. The orange ellipses in (b), which were allowed to vary in centre position, position angle, and axis ratio, represent annuli at which the surface brightness was measured to create the surface brightness profile plotted in panel (d). The orange contours in (c) connect regions along the $25 \text{ mag}/\text{arcsec}^2$ isophote; the thick red ellipse represents the size of the galaxy measured at the $25 \text{ mag}/\text{arcsec}^2$ isophote and is centred based on the centre of the region the isophote subtends. The surface brightness profile created by fitting ellipses to the isophotes is presented in panel (d). From this profile, the radius at the $25 \text{ mag}/\text{arcsec}^2$ isophote is measured. The final measured parameters (semi-major axis, position angle and axis ratio) for the galaxy are presented to the right of panel (d).

the position angle, ellipticity, and the optical centre of the galaxy defined by the $25 \text{ mag}/\text{arcsec}^2$ isophote, which is sometimes offset from the position at which the galaxy redshift is measured. The 14 galaxies for which the fitting failed, have no measured radius or position angle, and the centre of the galaxy is adopted to be the position of the measured redshift.

5.2.3 HI data

In Chapter 3, I presented new HI data for A2626 observed using MeerKAT. The sensitivity of MeerKAT made it possible to detect HI in galaxies beyond the 1 deg full width half maximum (FWHM) of the MeerKAT primary beam. In this chapter, the HI data cube I use has been cleaned with a $15'' \times 15''$ Gaussian beam which is set to be independent of frequency. The cube is $2 \times 2 \text{ deg}^2$ with a pixel scale of $2.5''$. The success of the HI stacking technique, used in this chapter (explained in Section 5.3), relies on the average signal-to-noise ratio (SNR) improving as the average noise decreases with $1/\sqrt{N}$ (N is the number of spectra in the stack). In the case of a single

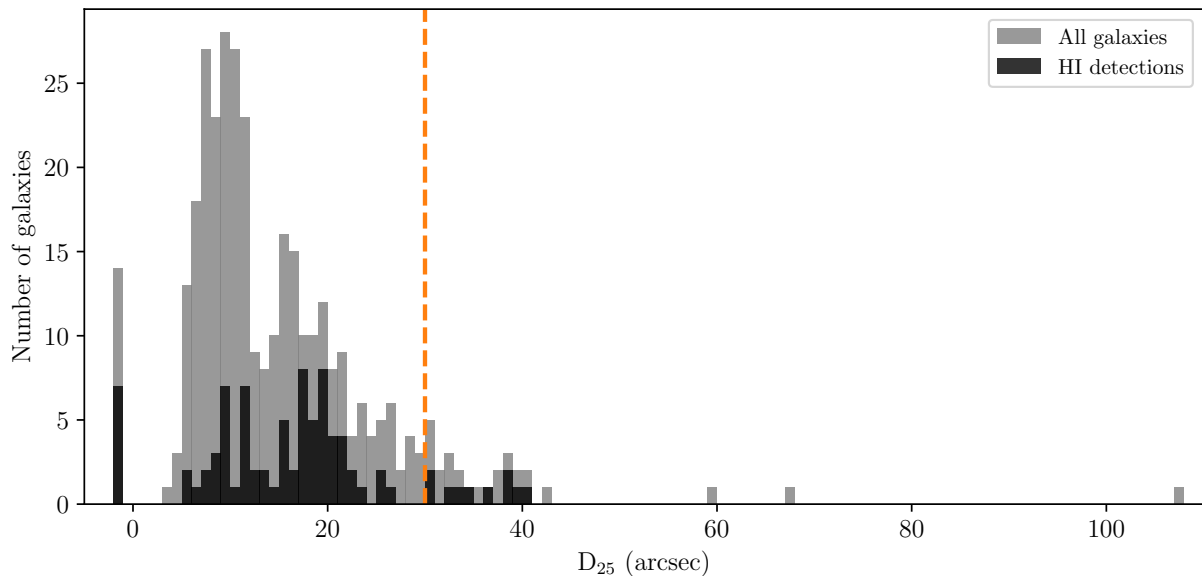


Figure 5.7: Distribution of the diameters of the A2626 galaxies at the $\mu_r = 25 \text{ mag/arcsec}^2$ isophote. Galaxies with a negative size have no measured size (the fitting routine failed). The orange line indicates $30''$ which is twice the size of the major axis of the synthesised beam at the native resolution of the HI data. The grey represents all galaxies in the sample, and the black the HI detections.

pointing observation (like this one), the noise near the edges of the cube corrected for primary beam attenuation is higher than the centre of the cube. The increase in the noise follows the primary beam pattern: it is higher where the beam is less sensitive. I thus only use the spectra of galaxies that are contained within the size of the beam at 20% of the peak power. This corresponds to a radius of 0.85 deg , however because of the earlier requirement of only including redshifts of galaxies inside the 50% completeness radius, this new restriction does not change the number of galaxies in the cluster sample.

In the HI cube, there are 87 cluster galaxies that are directly detected in HI with masks created during the SoFiA source finding process (see Section 3.4.1) that have been `cleaned`. The other 259 cluster galaxies not detected by SoFiA do not have emission masks, and are not `cleaned`. To extract the global HI profiles, I used two different types of apertures depending on whether the source was detected or not. For the detected sources, I flattened the 3D masks (from SoFiA) to create a 2D mask aperture that outlines the known HI emission, I then use the mask aperture to extract the global HI profile. The flux density is corrected for the beam by dividing the flux density per channel by the integral over the clean beam which is determined by projecting the 2D mask aperture onto the beam and adding up all the beam pixels within the aperture. For the non-detections, I use the optical size of the galaxy (as defined by the R_{25}) to determine the circular or elliptical aperture within which to extract the HI spectrum. Galaxies for which 1.2 times the optical size is contained within a circular aperture with a diameter of $30''$ (twice the synthesised beam FWHM) are extracted using a $30''$ diameter circular aperture. Galaxies that are larger and are not contained within the $30''$ aperture are extracted using an elliptical aperture that is defined by the optical size, $1.2 R_{25}$, the position angle, and the ellipticity measured in Section 5.2.2. In the same way as the detections, the non-detected HI spectra are corrected for the beam, however in the case of the non-detections, which have not been `cleaned`, I use the integral of the central part of the dirty beam. Figure 5.7 shows the distribution of galaxy sizes, the black histogram represents the portion of HI detected galaxies in each bin.

In flattening the 3D SoFiA masks to 2D apertures, the integrated flux of the HI detections is

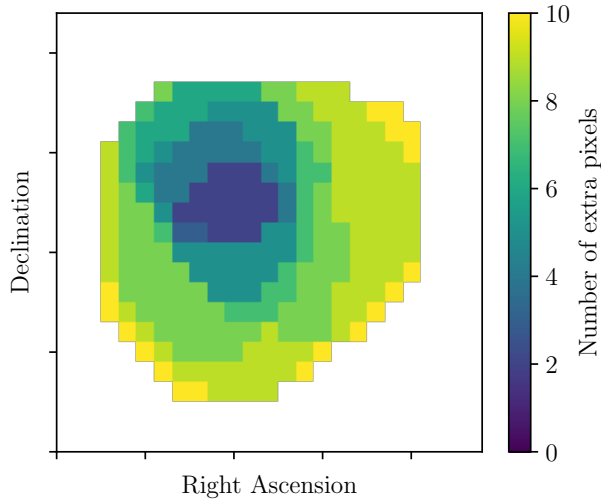


Figure 5.8: Example of a flattened SoFiA mask. The colour scale represents the number of extra pixels included in the aperture.

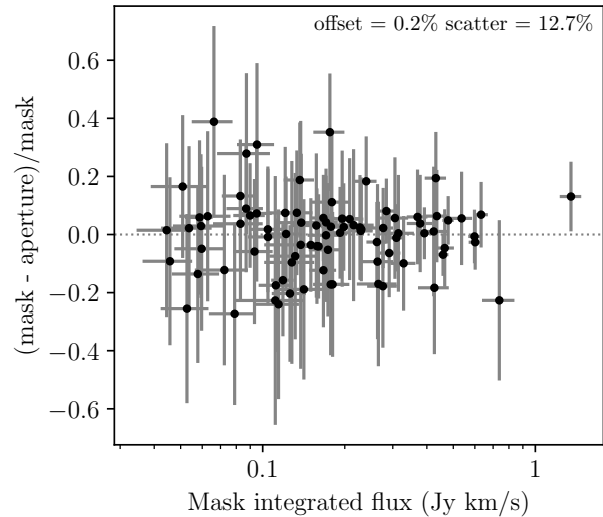


Figure 5.9: Fractional offset between mask flux and aperture flux for direct detections identified by SoFiA.

likely to be affected as more noise pixels are included in the aperture. Figure 5.8 shows the extra pixels added to the 2D aperture. There is no bias in the 3D mask towards positive pixels, thus the extra pixels in the aperture also do not have a bias towards either positive or negative pixels. Examining the fractional difference between the integrated fluxes determined from the 3D mask spectra and the aperture-extracted spectra (see Figure 5.9), there is no offset between the two flux measurements, and the scatter is Gaussian noise. Fitting a single Gaussian to the distribution of the fractional differences, I find a mean value of 0.2% and a scatter of 12.7%.

For each galaxy in the cluster, I extract a spectrum centred on the optical centre of the galaxy (for the direct detections, this is based on the HI mask). I also extract 25 reference spectra using the same aperture as for the target spectrum, but offset from the target position. Figure 5.10 shows an example of the reference spectra locations for a detection and a non-detection. Given the distance between the reference aperture centres and the centre of the target, the reference spectra do occasionally contain emission from other galaxies. Confusion for the target sources is not a concern in this study: Figure 5.2 shows the locations of the 18 galaxies that have a neighbour within a $45''$ radius and $\pm 500 \text{ km s}^{-1}$.

Optically selected HI detections

Visual inspection of all the extracted spectra showed that there were a number of clear HI detections that were missed by SoFiA. I will refer to these “missed” detections as optically selected HI detections henceforth. Despite being missed by SoFiA, these optically selected HI detections are still considered reliable detections as they are identified with the prior knowledge of the optical redshift which corresponds to the HI redshift. The SoFiA-identified HI sources were identified without any prior knowledge. For some HI detected galaxies there is no corresponding optical redshift but there is an optical counterpart spatially coincident with HI emission. The optically selected HI detections are identified as such if the HI spectrum has:

- $\text{SNR} \geq 3$, and
- smoothed to 90 km s^{-1} resolution, $\text{SNR} \geq 3.5$.

The SNR is the peak signal-to-noise ratio, where the noise is determined by the standard deviation of the reference spectra (represented by the orange band in Figure 5.11) in a $\pm 200 \text{ km s}^{-1}$ window

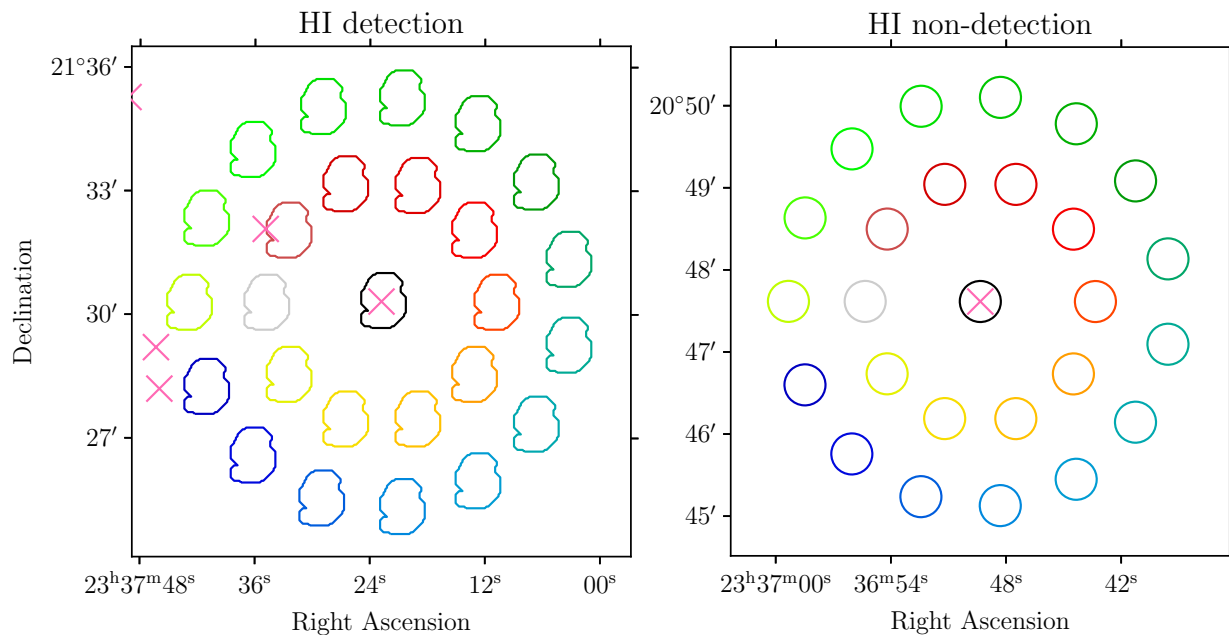


Figure 5.10: Example of target and reference spectra extraction apertures. The black apertures at the centre of the figure represent the aperture used to extract spectrum of the target galaxy. The coloured apertures indicate the locations at which the 25 reference spectra are extracted. **Left:** a detection, **right:** a non-detection.

(represented by the vertical green band in Figure 5.11) centred on the optical redshift of the galaxy. Figure 5.11 shows an example of two of the identified optical detections. There are 15 HI detections in the cluster that were missed by SoFiA and identified based on coincidence with the optical redshift.

5.3 HI stacking

As mentioned in Section 5.2.3, the primary method of HI analysis used in this chapter is HI stacking. As Chapter 2, I use HISS³ (Healy et al., 2019) to perform the stacking discussed later in this chapter. HI stacking has been shown to be effective in obtaining average HI measurements for samples of galaxies that are not individually detected (e.g. Chengalur et al., 2001; Lah et al., 2009; Brown et al., 2015; Jaffé et al., 2016; Bera et al., 2019; Chowdhury et al., 2020).

For every sample of galaxies I stacked, 26 stacked spectra were created: the target stacked spectrum and 25 stacked reference spectra. The 25 stacked reference spectra each correspond to one of the coloured apertures around the target (see Figure 5.10). The uncertainty on the quantity measured from the stacked target spectrum is calculated from the variance of the 25 reference spectra. The reference spectra are also used to determine whether or not signal is detected in the target spectrum.

The average noise of the HI data used in this chapter increases towards the edges, following the primary beam attenuation pattern. The effectiveness of stacking relies on the average noise of the stacked spectrum decreasing as σ/\sqrt{N} , where N is the number of individual spectra in the stack. Thus, I use a $1/\sigma_{rms}^2$ weighting factor, where σ_{rms} is the rms noise of the individual input spectra, applied to each spectrum included in the stack. This weighting factor down-weights the higher rms spectra typical of galaxies on the edges of the field. Figure 5.12 shows how the rms in the stacked

³<https://github.com/healytwin1/HISS>

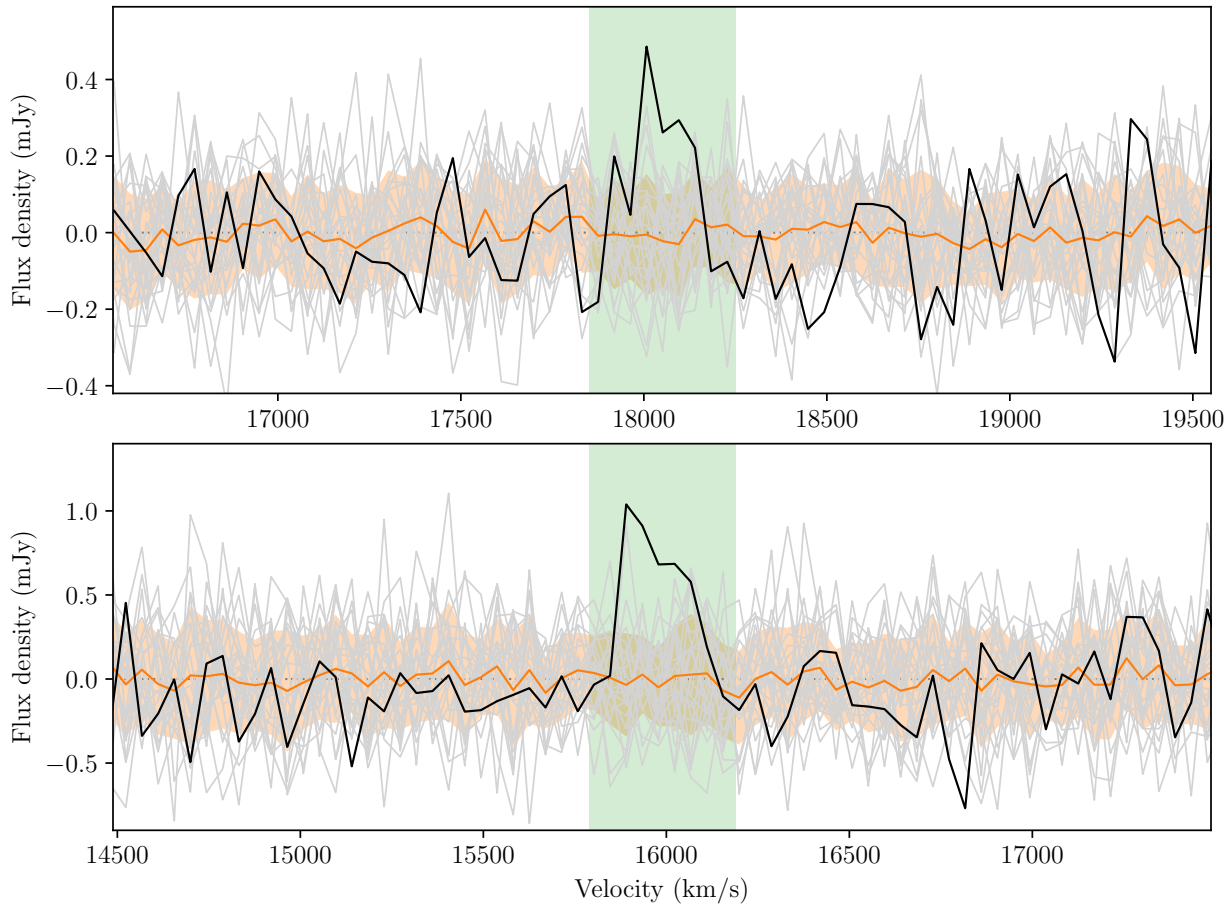


Figure 5.11: Two examples of HI detections (black) missed by *SoFiA*. The orange band represents the standard deviation of the 25 reference spectra (shown in light grey), the orange line indicates the mean of the reference spectra, and the green vertical band indicates the window ± 200 km s⁻¹ centred on the galaxy’s optical redshift.

A2626 spectra decrease with a factor of \sqrt{N} as expected for Gaussian spectra.

The velocity resolution of the MeerKAT data is 45 km s⁻¹ which means that in some low HI mass samples the HI emission may only appear in one or two channels, especially given the accuracy of the redshifts used for the stacking. With stacking, there is a prior on any peak within the ± 200 km s⁻¹ window that this is real HI emission, even if there are similar S/N peaks elsewhere in the stacked spectrum. As mentioned in Section 3.3.2, it is possible that the residuals from the ‘de-ripple’ process may appear in the stacked spectra – these would appear in two ways: as a negative baseline which would be obvious from the average of the reference spectra, or peaks in the spectra were the nodes from the spline fit happen to coincide which would also be apparent in the rms of the 25 reference spectra.

5.4 Characterising the cluster

5.4.1 The galaxy population

Except for a few interesting galaxies and radio sources in the cluster, A2626 has not been extensively studied. In Chapter 4, I presented new spectroscopy my team obtained of the cluster using Hectospec on the MMT. This enabled us to more than double the spectroscopically confirmed members of the cluster. In this chapter, I have matched the DECaLS photometry to the spectroscopically

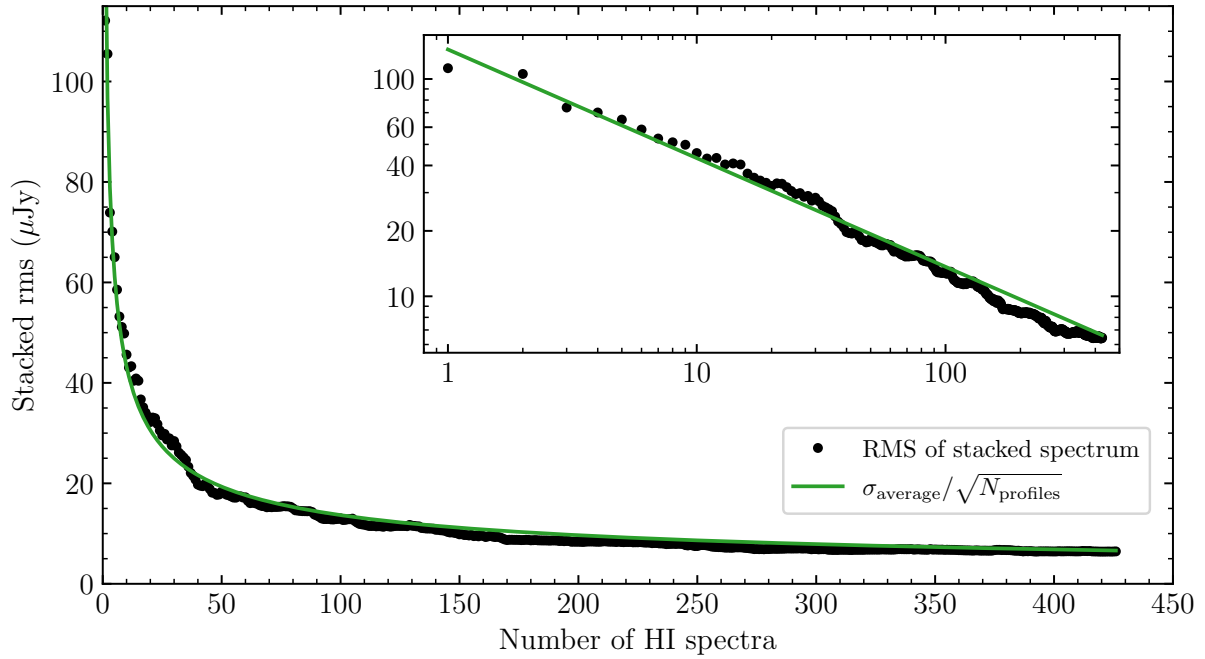


Figure 5.12: Stacked noise as a function of the number of input HI spectra. The black data points represent the measured noise in the stacked spectrum with N input spectra. The green line represents the theoretical change in the stacked noise for a Gaussian distribution, σ/\sqrt{N} where σ is the average noise of all the input spectra. The inset shows the same as the main figure, but in log-log format.

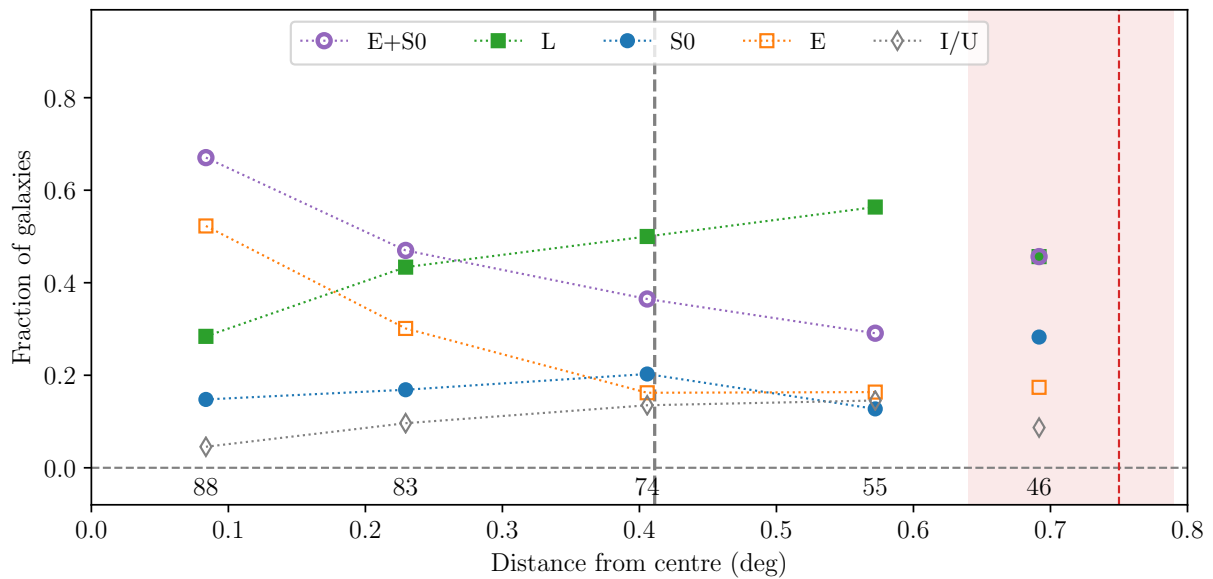


Figure 5.13: Morphology-radius relation for A2626. The coloured symbols represent the fraction of galaxies for the different morphology classifications as indicated in the legend. The vertical dashed grey line indicates the R_{200} for A2626, and the vertical dashed red line represents the radius at which the data are 70% complete. The shaded red region indicates the bin which contains data where the completeness fraction is less than 70%.

confirmed cluster members which, in conjunction with the visually identified morphologies, has enabled me to characterise the cluster and investigate whether the constituent galaxies follow similar radial trends as in other clusters.

Table 5.1: Number of galaxies for each morphological classification in annuli increasing from the cluster centre.

Annuli (deg)	E	S0	L	I/U	Total
$0.00 < r < 0.16$	46	13	25	4	88
$0.16 < r < 0.32$	25	14	36	8	83
$0.32 < r < 0.48$	12	15	37	10	74
$0.48 < r < 0.64$	9	7	31	8	55
$0.64 < r < 0.80$	8	13	21	4	46

The richness class of a cluster, a classification introduced by Abell (1958), states that a rich cluster consists of no less than 50 members “that are not more than 2 mag fainter than the third brightest member” within a radius of $R_A = 1.5 h^{-1}$ Mpc (the Abell radius). In the “catalog of rich clusters”, Abell et al. (1989) classified A2626 as a poor cluster with richness class 0. Clusters with a richness class of 0 have 30–50 members that satisfy the Abell (1958) criterion. Since the richness class of a cluster contains information about the cluster population, it can be a baseline for comparisons with other clusters; for reference, the Virgo cluster has a richness class of 1 (Binggeli et al., 1985), and the Coma cluster has a richness class of 2 (Beijersbergen, 2003, and references therein). Using the “clean” (see Section 5.2.2) r -band photometry from DECaLS, I find 54 galaxies within an $R_A = 2.1$ Mpc (assuming $h = 0.7$) radius of the cluster centre that satisfy the Abell (1958) criterion. This suggests that A2626 is not a poor cluster, but rather a rich cluster with richness class of 1.

Dressler et al. (1997) showed for centrally concentrated, regular clusters that the spiral fraction of galaxies increases outward from the cluster centre, while the elliptical fraction increases towards the cluster centre. Beijersbergen (2003) showed this was true (with different relative fractions) for the Coma cluster. In Figure 5.13, I show the relative fractions of early type (E) galaxies, S0/Lenticular (S0) galaxies, and late type (L) galaxies as a function of radius from the centre of A2626. The numbers for Figure 5.13 are presented in Table 5.1. As with other clusters, A2626 has a high fraction of early-type galaxies at the cluster centre but the fraction decreases with increasing radius. Also, as expected, the late-type galaxies follow the inverse trend – an increasing fraction with increasing radius. The S0 fraction shows a flat distribution at all radii from the cluster centre. This is consistent with the clusters in the Dressler et al. (1997) sample, as well as with Coma (Beijersbergen, 2003).

5.4.2 HI deficiency in the cluster

Galaxy clusters have long been known to be HI deficient (e.g. Haynes & Giovanelli, 1984; Solanes et al., 2001; Denes et al., 2014). The HI deficiency parameter (DEF_{HI}) is defined as the ratio of the HI mass expected based on the size, luminosity or morphology of a similar isolated galaxy, to the measured HI mass for the galaxy. This is formulated as,

$$\text{DEF}_{\text{HI}} = \log M_{\text{HI}exp} - \log M_{\text{HI}obs}. \quad (5.2)$$

In Chapter 2, I discussed some of the different methods of calculating the expected HI mass of a galaxy. In this chapter, I use the Denes et al. (2014)⁴ scaling relations based on the r -band diameter to calculate the expected HI mass for the A2626 galaxies. I use the Denes et al. (2014) relations, which do not require morphological information, because I do not have B -band photometry (or a proxy) which was used in Chapter 2. Optical diameters measured in the B -band are typically used

⁴see Table 3 in Denes et al. (2014)

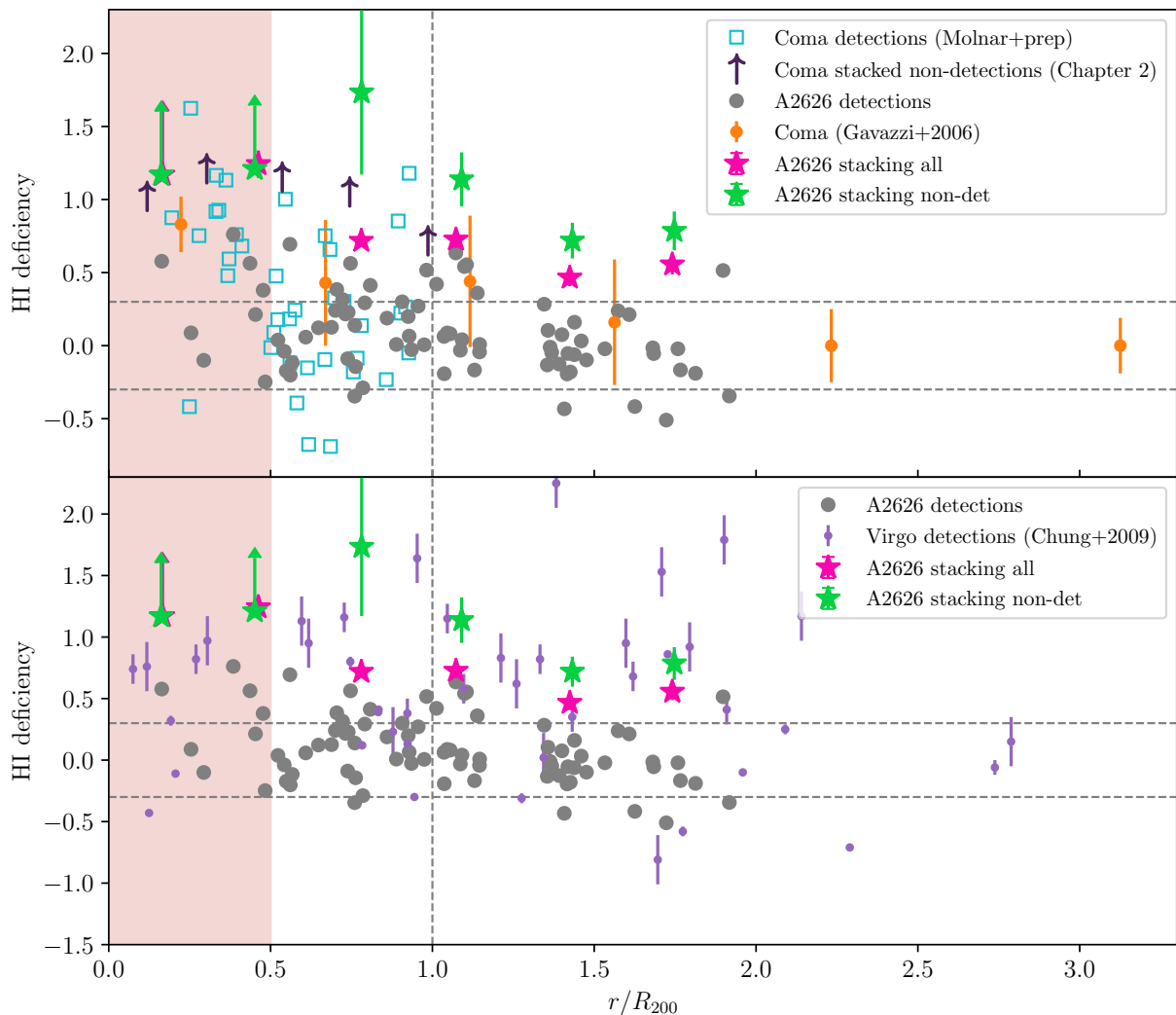


Figure 5.14: H I deficiency as a function of projected radius from the cluster centre. The grey circles represent the measurements of the A2626 direct detections, while the pink (green) stars represent the average H I deficiency calculated by stacking all galaxies (only H I non-detections). The other data points represent H I deficiency measurements for galaxies in other clusters as indicated in the legend. The horizontal dashed lines indicate the H I deficiency for a galaxy that has half (the upper line) or double (the lower line) the H I mass expected based on a field galaxy of similar type. The top panel shows the comparison with the Coma cluster, and the bottom panel is the comparison with the Virgo cluster.

in all the morphology-calibrated diameter- $M_{\text{H I exp}}$ relations (e.g. Haynes et al., 1984; Solanes et al., 1996).

It is well known that H I deficiency has a radial dependence in clusters (e.g. Giovanelli et al., 1981; Bravo-Alfaro et al., 2000; Solanes et al., 2001; Chung et al., 2009), with gas-poor galaxies more likely to be found near the centre of clusters than the outskirts. Solanes et al. (2001) studied the H I deficiency in 1900 spiral galaxies around 18 clusters. They found that the fraction of H I deficient spiral galaxies (these are galaxies which have $\text{DEF}_{\text{H I}} > 0.3$, meaning that the measured H I mass is less than half the expected mass) starts increasing from around $r/R_A \sim 2$. In their Fig 4 (shown in Figure 1.4), Solanes et al. (2001) also show the H I deficiencies of the galaxies as a function of Abell radius for their sample – the average H I deficiency starts increasing around $r/R_A \sim 1$. If the same trend were to hold for A2626, this would be around $r/R_{200} \sim 1.3$. For Coma, this would be $r/R_{200} \sim 1.2$, and for Virgo this would correspond to $r/R_{200} \sim 1.4$ (based on R_{200} from Yoon et al. 2017 and references therein).

Using HISS to stack the A2626 galaxies in radial bins, I can study how the average HI deficiency of the cluster galaxies changes as a function of radius. The galaxies are stacked in units of $M_{\text{HI},\text{obs}}/M_{\text{exp}}$ so that each galaxy spectrum is weighted by the expected HI mass for that galaxy. This is necessary as $\langle M_{\text{HI},\text{obs}}/M_{\text{exp}} \rangle \neq \langle M_{\text{HI},\text{obs}} \rangle / \langle M_{\text{exp}} \rangle$. I stack all the A2626 galaxies in one group, and only the HI non-detections in the second group. The average DEF_{HI} ($\langle \text{DEF}_{\text{HI}} \rangle$) measured from the stacks are represented by the pink (all A2626 galaxies) and green (only non-detections) stars in Figure 5.14. Where there is no detection in the stacked profile, as defined by peak $S/N > 2.5$ (the noise here is determined by the variance in the stacked reference spectra), the 1σ lower limit is used – these are represented by the upward-pointing arrows. The stacked profiles are presented in Figure A.1, and the measured data in Table B.1.

5.4.2.1 A comparison with the Coma cluster

As expected, there are no detections in the average measurements of the HI deficiency within the core of A2626 ($r/R_{200} < 0.5$). It should be noted that while there are a handful of direct HI detections at $r < 0.5R_{200}$, it is possible that this is a result of projection as I have used the projected radius to determine distance from the cluster centre. However, in comparing the A2626 detections to the Coma detections outside of $0.5R_{200}$ (Gavazzi et al. 2006, Molnar et al., in prep), the A2626 galaxies are more HI normal. On average, the A2626 detections do show the same increasing HI deficiency from $r/R_{200} \sim 1.3$ towards the centre of the cluster as shown in Solanes et al. (2001). Considering only the average DEF_{HI} for the non-detections, I note that these start to diverge from the global average around $r/R_{200} \sim 1.3$, until there are no more detections in the stacked spectra for $r/R_{200} < 0.5$. This is not the same for Coma, where the average DEF_{HI} measurements for the Coma non-detections (the dark purple arrows) show only lower limits at all radii. I have also included the average DEF_{HI} measurements for late-type galaxies in the Coma cluster from Gavazzi et al. (2006) and the individual HI detections from the Westerbork Coma Survey (Molnar et al., in prep).

In Chapter 2, we suggested that this bimodality in the HI measurements was due to an extremely rapid gas removal mechanism. While it is evident that the HI non-detections in A2626 start increasing in HI deficiency at larger radii than the HI non-detections in Coma, there is not the same bimodality in the HI measurements as with Coma. It should be noted that the Coma and A2626 HI surveys have comparable HI detection thresholds, and a similar number of direct detections within R_{200} : 40 for Coma (Healy et al. 2021c, Molnar et al. in prep.), and 46 for A2626. Compared to Coma, the A2626 non-detections, are not as deficient. Coma has only lower limit DEF_{HI} measurements. However, for A2626 it is possible to measure the average DEF_{HI} between $0.5R_{200}$ and R_{200} from the stacked spectra (Figure A.1). The A2626 non-detections are still HI deficient (10–30 times less HI than their field counterparts), but with the Coma galaxies (with a similar HI mass sensitivity), however no measurement could be made.

5.4.2.2 A comparison with the Virgo cluster

The bottom panel of Figure 5.14 shows the radial DEF_{HI} comparison between A2626 and the Virgo cluster. There is no equivalent blind HI survey of Virgo, thus the comparison between A2626 and Virgo is not a complete one. The Virgo DEF_{HI} measurements are taken from Chung et al. (2009), who targeted selected spiral galaxies in the cluster with the VLA. Another comment on the comparison between the HI deficiency measurements for the two clusters is that the deficiencies were calculated differently. Chung et al. (2009) calculated the HI deficiencies for the Virgo galaxies using a morphology-independent method which is based on the mean HI surface density (Haynes et al., 1984), however the uncertainties quoted on all the Virgo measurements are determined from the difference between the morphology-dependent relation and the morphology independent relation. I compared the HI deficiency measurements for the Coma cluster galaxies in Chapter 2 with

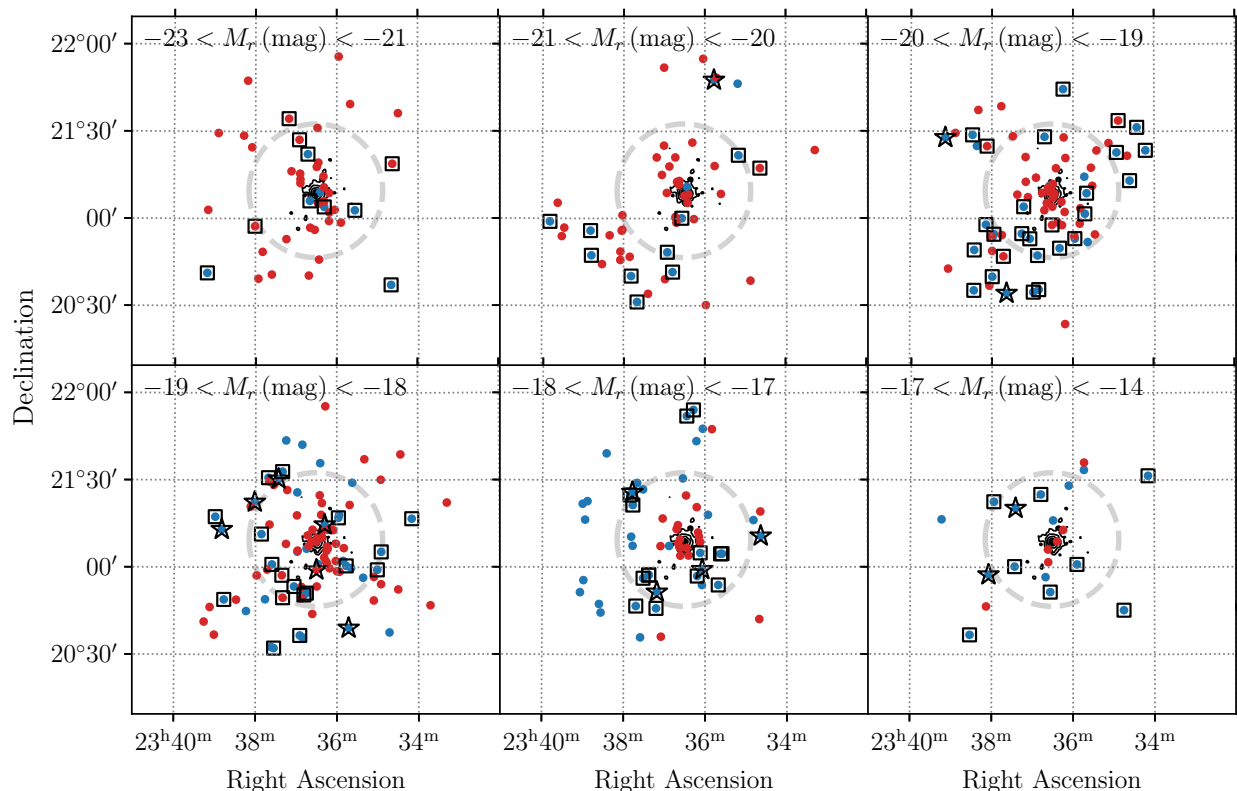


Figure 5.15: Spatial distribution of the cluster galaxies in increasingly fainter magnitude bins. The thick grey dashed circle represents the R_{200} . The galaxies are coloured based on their $g-r$ colour: blue for bluer galaxies, and red for redder galaxies. The black open squares and stars indicate the galaxies that are directly detected in H I and detected in H I after optical selection.

morphology information and without, and found that, while there was an offset, the measurements made without morphological information tended to have a higher H I deficiency value. However, this offset was on average 0.2 dex, which is more than the average difference between A2626 and Virgo.

There is no trend in the Virgo galaxies, but it is interesting to note that Virgo galaxies presented here are systematically more deficient than the A2626 detections. A2626 and Virgo are comparable clusters: both have a richness class of 1, similar R_{200} radii, and similar velocity dispersions, which would imply similar masses. Based on the comparison between the H I deficiencies of the two clusters shown in the lower panel of Figure 5.14, it could be speculated that cluster mass has no impact on H I deficiency; recall that Solanes et al. (2001) found no correlation between the fraction of H I deficient spirals and richness count (a measure of cluster size), or X-ray luminosity (a measure of cluster mass).

5.4.3 Optical luminosity and H I

Galaxies of different morphologies and masses have been shown to lose their H I content at different rates. Schawinski et al. (2014) used a sample of “green valley” galaxies across different cosmic environments to show that early-type galaxies are quenched on much faster timescales compared to late-type galaxies ($t_q < 250$ Myr for early-types and $t_q \gtrsim 1$ Gyr for late-types). Oman & Hudson (2016) found that quenching typically occurs 3.5–5 Gyr after galaxies have crossed $2.5 r_{\text{vir}}$ ($\sim 3.4 R_{200}$) of clusters with host masses of 10^{13} – $10^{15} M_{\odot}$ ($M_{A2626,200} \sim 5 \times 10^{15} M_{\odot}$). They also found that low mass galaxies have a longer delay between crossing $2.5 r_{\text{vir}}$ and the onset of quenching than high mass galaxies, and that once quenching begins, the timescale over which the galaxy is transformed

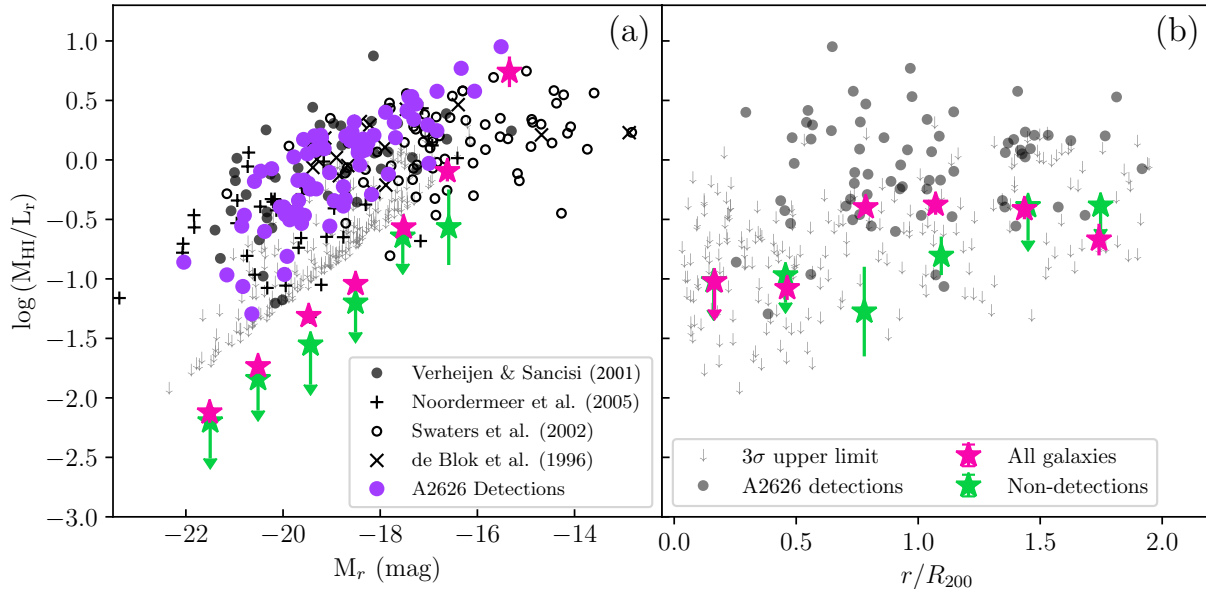


Figure 5.16: (a) M_{HI}/L_r as a function of absolute r magnitude. The black symbols represent a field sample: filled circles for the Ursa Major galaxies, open circles for the late-type and irregular galaxies in the WHISP survey (Swaters et al., 2002), ‘+’ symbols for the early-type galaxies in the WHISP survey (Noordermeer et al., 2005), and ‘x’ symbols for the low surface brightness galaxies from De Blok et al. (1996). The A2626 detections are shown as solid purple circles, and the 3σ upper limits for the A2626 non-detections are indicated by the grey arrows. The average M_{HI}/L_r ratios measured from the stacked profiles are represented by pink (green) stars for all A2626 galaxies (only non-detections). (b) M_{HI}/L_r vs cluster radius. Stacked results in colour, individual limits/measurements in grey. The corresponding stacked profiles are presented in Figures A.2 and A.3, and the measured values in Tables B.2 and B.3.

from its field-like properties to being fully processed by the cluster is quick ($\lesssim 2$ Gyr). For reference the crossing time of A2626 is calculated to be $t_{\text{cross}} \sim 2.5$ Gyr.

Using r -band luminosity as a proxy for the baryonic mass of the galaxies, and the $g-r$ colour as a proxy for star formation, I explore the distribution of the red ($g-r > 0.7$) and blue ($g-r < 0.7$) galaxies as a function of luminosity, and investigate how the M_{HI}/L_r ratio varies as a function of projected radius from the cluster centre. Figure 5.15 shows the spatial distribution of the A2626 galaxies separated into six magnitude bins. The galaxies are coloured based on their $g-r$ colour, and the HI detections (both the SoFIA and the optically selected HI detections) are marked by different symbols. From Figure 5.15, two observations can be made: 1 – the blue galaxies tend to avoid the centre of the cluster, and the number of blue galaxies also increases as the galaxies become fainter; 2 – while the number of faint blue galaxies directly detected in HI is higher than the bright blue sample, the fraction of HI detected blue galaxies is higher for the bright blue sample. In a later section, I will separate the galaxies into bright and faint as a proxy for high and low mass respectively, bright galaxies have $M_r < -19$ mag and faint galaxies $M_r > -19$ mag (i.e the top and bottom rows). This separation was chosen so that the brightest bin of the faint sample would contain Large Magellanic Cloud type galaxies. It is worth noting that the 50% spectroscopic completeness limit corresponds to $M_r = -17.36$ mag (using a distance modulus for the cluster of 36.96), thus the faintest two magnitude bins (the lower right two panels in Figure 5.15) are spectroscopically incomplete.

Figure 5.16a presents the M_{HI}/L_r as a function of the absolute r -band magnitude of the A2626 galaxies compared to similar measurements made of other galaxies in different cosmic environments. The four comparison samples are: the Ursa Major association of galaxies (Verheijen & Zwaan, 2001); spiral and irregular galaxies from the Westerbork HI survey of spiral and irregular

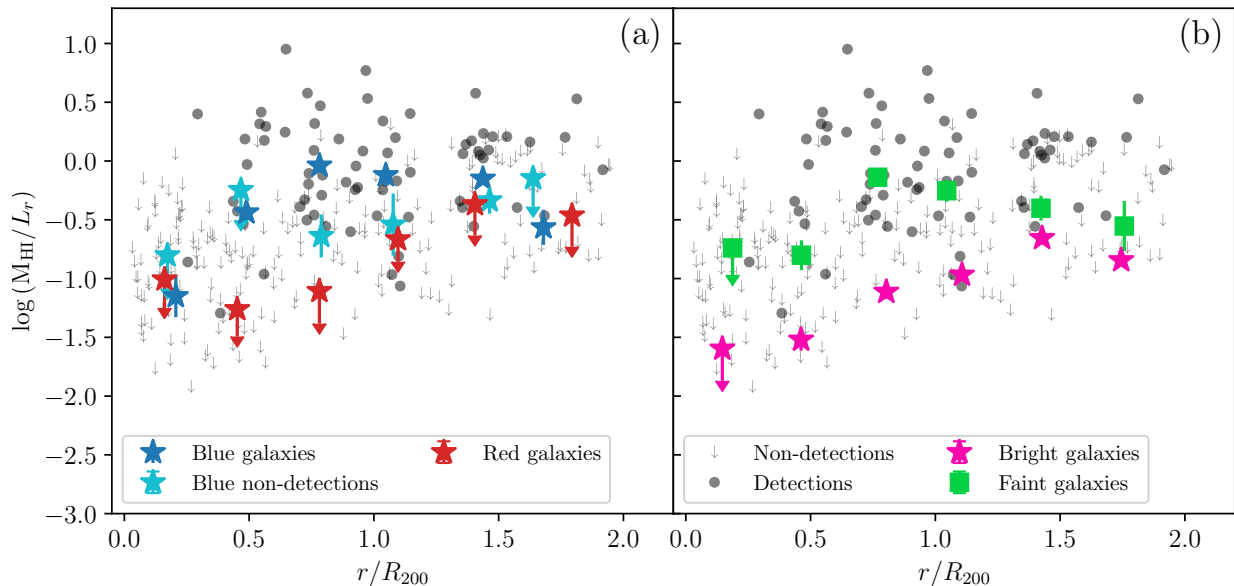


Figure 5.17: Both panels show the M_{HI}/L_r as a function of projected radius from the cluster centre. The grey symbols in both panels represent the measurements of the individual cluster galaxies: solid circles for the H I detections and arrows indicating the 3σ upper limit for the non-detections. (a) The coloured stars represent the average M_{HI}/L_r measured from stacked profiles of all blue galaxies (dark blue), H I non-detected blue galaxies (light blue), and red galaxies (red). (b) The green squares represent the average M_{HI}/L_r of faint galaxies ($M_r > -19$ mag) and the pink stars indicate the average M_{HI}/L_r of the bright galaxies ($M_r < -19$ mag). The corresponding stacked profiles are presented in Figures A.4, A.5, A.6 and A.7, and the measured values in Tables B.4, B.5 and B.6.

galaxies (WHISP Swaters et al., 2002); early-type disk galaxies from WHISP (Noordermeer et al., 2005); and low surface brightness galaxies in low-density environments (De Blok et al., 1996). The H I detections (represented by the filled purple circles in Figure 5.16a) have comparable M_{HI}/L_r to the other galaxies from different cosmic environments shown in the plot. This demonstrates that the direct H I detections are largely H I normal. The 3σ upper limits of the H I non-detections are shown as grey arrows, and these trace a sharp edge at the lower edge of the envelope outlined by the detections. The sharp edge is due to the noise limits of the H I data.

Stacking the A2626 galaxies in bins of magnitude (see Table B.2) shows the average M_{HI}/L_r of all A2626 galaxies per magnitude bin (pink stars in Figure 5.16a) to be 0.5 dex below the direct detections. Separating out only the non-detections (green stars in Figure 5.16a) shows that only in the faintest magnitude bin is a measurement possible from the stacked spectrum (all the brighter bins are upper limits). The galaxies in this faintest bin ($-17 < M_r$ (mag) < -16) have an average M_{HI}/L_r that is consistent with the faintest late-type and irregular galaxies in the Swaters et al. (2002) WHISP sample.

Given that the centres of clusters are known to be H I-poor, Figure 5.16b shows the average M_{HI}/L_r as a function of radius from the cluster centre. The individual measurements of M_{HI}/L_r from the direct detections are shown as solid grey circles, and the upper limits for the non-detections are shown as grey arrows. Figure 5.17a shows the same as Figure 5.16b, but with the galaxies separated into blue and red populations – a proxy for star-forming and non-star forming. The blue galaxies show constant average M_{HI}/L_r for $r > R_{200}$, at smaller clustercentric distances the average M_{HI}/L_r decreases and the limits on the measurements make it difficult to draw definitive conclusions. Since star formation is correlated with H I surface density (e.g Kennicutt, 1989; Walter et al., 2008), I speculate that the change in M_{HI}/L_r around R_{200} is consistent with the delay timescales that Oman & Hudson (2016) predict for the onset of quenching after crossing $\sim 3R_{200}$. The non-

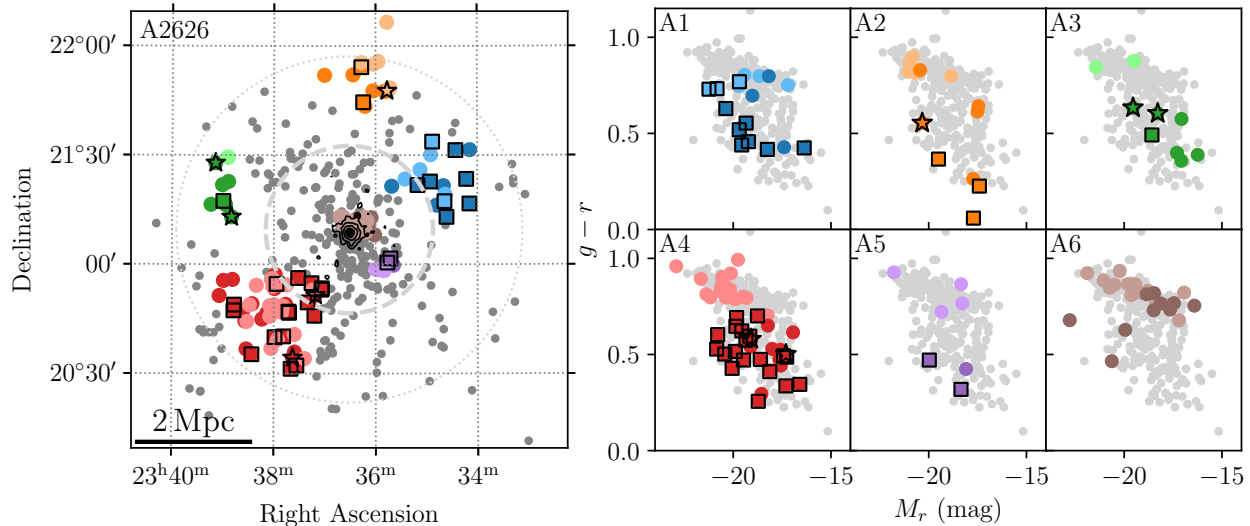


Figure 5.18: Left: spatial distribution of the six substructures in A2626. Right: the colour magnitude diagrams for each substructure. The background grey points in each panel represent the cluster galaxies, and the coloured data points, the substructure galaxies. The darker colours for the substructure galaxies represent the late-type galaxies, while the lighter colours represent early-type galaxies. The black open squares indicate the galaxies detected in H I by SoFiA and the open stars, the optically selected H I detections.

detection of the blue galaxies in the inner region of the cluster ($r < 0.5R_{200}$) is also consistent with observations made by Oman et al. (2021) regarding the timing of different stages of environmental processing: first the galaxies are no longer detected in H I, this is followed a few Gyr later by a drop in the specific star formation rate, and then on the time scales of stellar evolution (\lesssim Gyr), the galaxy becomes redder. Caveat: these are projected clustrocentric distances and blue galaxies seen at $r < 0.5 R_{200}$ are not necessarily in the cluster core

In contrast to the blue galaxies, the red galaxies contain on average no detectable H I at all radii out to $2R_{200}$ (Figure 5.17a). This could suggest that the red galaxies in the cluster have lost their gas and ceased forming stars long before arriving in the cluster environment. This is consistent with what is suggested by Dressler et al. (1997): the formation of early type (typically red) galaxies predates cluster virialisation.

In Figure 5.17b, I separated the galaxies into a faint ($M_r > -19$ mag) sample and a bright ($M_r < -19$ mag) sample. The bright galaxies (pink stars) have systematically lower $\langle M_{\text{H I}}/L_r \rangle$ than the faint galaxies (green squares), but this is to be expected as is shown in Figure 5.16a: the brightest galaxies have $M_{\text{H I}}/L_r$ ratios that are an order of magnitude or more lower than the faintest galaxies. What is not necessarily expected (but is predicted by Oman & Hudson 2016) is that the decrease in $\langle M_{\text{H I}}/L_r \rangle$ for the bright galaxies starts at larger clustrocentric distances than for the faint galaxies which only start decreasing around $r/R_{200} \lesssim 1$.

5.4.4 H I in cluster substructures

In Chapter 4, I presented new identified substructures in A2626 based on the DS test. I also speculated about possible origins of the substructures (see Section 4.5.2). However, these speculations were lacking the colour, morphological and H I information that is presented in this chapter. Figure 5.18, presents a new version of Figure 4.13 which includes the colour-magnitude relation for the galaxies, as well as the galaxies' morphologies which is encoded into the colour of the data points for each substructure – late-type galaxies are represented by the darker colours, while early-type and S0 galaxies are indicated by the lighter colours. For each of the substructures, I have determined

Table 5.2: Details of the six substructures associated with A2626.

ID	N_{mem}^a	$\langle v \rangle$ (km s^{-1})	σ_{group} (km s^{-1})	E:S0:L:I/U	$\log\langle M_{\text{HI}}/M_{\odot} \rangle$	$\langle \text{DEF}_{\text{HI}} \rangle$	$\langle M_r \rangle$ (mag)
A1	17 (10)	16130	322	2:5:8:2	8.77 ± 0.05	0.76 ± 0.09	$-19.10_{0.58}^{0.65}$
A2	13 (4)	16868	143	2:3:7:1	9.14 ± 0.04	0.35 ± 0.08	$-19.25_{1.32}^{1.64}$
A3	9 (3)	16660	148	0:2:5:2	8.82 ± 0.09	0.22 ± 0.09	$-17.98_{0.53}^{0.84}$
A4	49 (21)	17051	381	10:7:29:3	8.83 ± 0.03	0.55 ± 0.04	$-19.08_{1.01}^{1.01}$
A5	7 (2)	16104	153	4:0:3:0	8.40 ± 0.11	0.91 ± 0.11	$-19.30_{0.51}^{1.00}$
A6	24 (0)	17216	650	11:3:9:1	< 8.25	> 0.84	$-19.02_{1.07}^{1.10}$

^a the number in parentheses indicates the number of HI detections (SoFIA and optical detections)

the average M_{HI} and the average DEF_{HI} . The stacked spectra for each of the substructures are presented in Figure A.8 and Figure A.9, and the measured quantities in Table 5.2.

Substructures A1, A2, A3 and A4 are speculated to be on first infall based on their locations and the percentage of member galaxies that are detected in HI. The addition of the information provided in this chapter enables a richer interpretation of the groups' current status. While A1 has a rather clear separation between early- and late-type galaxies that follows the blue/red separation, it does not have a clearly defined red sequence. It is also worth noting that this group is the most HI deficient of the four groups outside R_{200} , as it has $\langle \text{DEF}_{\text{HI}} \rangle = 0.76 \pm 0.09$ while the average deficiency for only the non-detections is $\langle \text{DEF}_{\text{HI}} \rangle > 0.73$ (see Figure A.9). Given the large fraction of direct detections, it is unlikely that this group has already passed through the cluster, thus it is probable that the high HI deficiency is due to the group environment prior to interaction with the cluster. If this is true, then the onset of the HI deficiency is likely to be relatively recent as the colour and morphological transformations have not caught up yet. The galaxy populations of A2 and A3 show clear separations of early- and late-type galaxies that correspond to colour separations, and like A1 there does not appear to be a clustering of early-type galaxies at the centres of the groups. Unlike A1, both A2 and A3 are HI normal for both the group average and for only the HI non-detections.

The final group of the outer four is A4, this group is the largest of the six, and has the largest fraction of late-type galaxies. Unlike the other three outer groups, the early-types are clustered towards the centre of the group while the outer galaxies are mostly late-types. This morphology-density relation for group environments has been seen before (e.g. Postman & Geller, 1984). The average HI deficiency for this group is $\langle \text{DEF}_{\text{HI}} \rangle = 0.55 \pm 0.04$, which within the error could be considered HI normal. The average HI deficiency for only the non-detections is $\langle \text{DEF}_{\text{HI}} \rangle = 1.04 \pm 0.15$. The non-detections in this group are situated at the centre of the group and are located on the red sequence (see the light pink points not outlined by black in Figure 5.18), this is suggestive of pre-processing in the group environment prior to cluster infall.

A5, one of the two groups inside R_{200} , has an even split between early- and late-type galaxies that also follow the red/blue split. This group still has two galaxies directly detected in HI, but has a high average HI deficiency ($\langle \text{DEF}_{\text{HI}} \rangle = 0.91 \pm 0.11$). The high HI deficiency might not be surprising given the projected distance between this group and the cluster centre.

The final group of the six, A6, is the group thought to have recently merged with the cluster core. Out of all the substructures, A6 shows the most similar properties to the cluster itself. It has

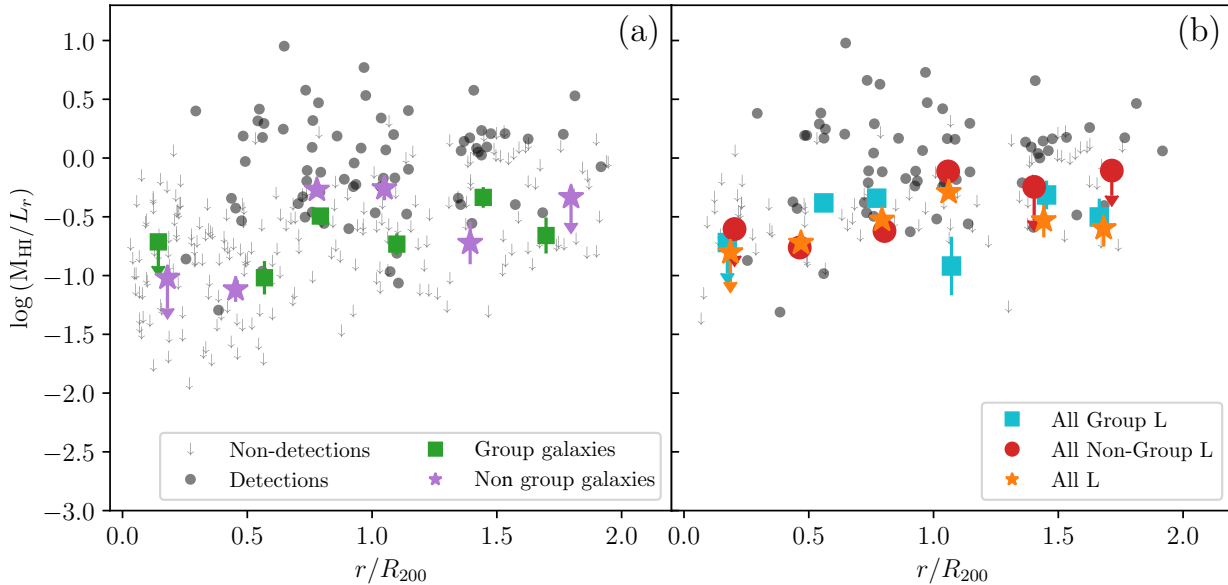


Figure 5.19: Both panels show the M_{HI}/L_r as a function of projected radius from the cluster centre. The grey symbols in both panels represent the measurements of the individual cluster galaxies: solid circles for the HI detections and arrows indicating the 3σ upper limit for the non-detections, in the case of panel (b), only the measurements for the late-type galaxies are shown. (a) The coloured squares represent the average M_{HI}/L_r ratio for cluster galaxies in groups, and purple stars for the cluster galaxies not in groups. The stacked profiles can be found in Figures A.10 and A.11, and the measured average M_{HI}/L_r ratios in Table B.7. (b) Average M_{HI}/L_r for all A2626 late-type galaxies (orange stars), late-type galaxies in groups (blue squares), and late-type galaxies not in groups (red circles). The stacked profiles can be found in Figures A.12, A.13 and A.14, and the measured average M_{HI}/L_r ratios in Table B.8

a well-defined red sequence, it is highly HI deficient and has a velocity dispersion similar to the cluster ($\sigma_{cl} = 660 \text{ km s}^{-1}$). This group has a collection of late-type galaxies on the red sequence that could be evidence for morphological transformation being the last transformation to occur (after HI removal and colour transformation, Oman et al. 2021).

5.5 Cluster and group impact on galaxy evolution

The previous section investigated how the entire cluster galaxy population is affected by the cluster environment. In this section, I ask the question: which cosmic environment has a greater effect on the HI content of the galaxies: The cluster or the local substructure/group environment? To address this, I compare the average M_{HI}/L_r of cluster galaxies in groups to those not in groups. The average M_{HI}/L_r values are measured from the stacked spectra created by HISS. As with the DEF_{HI} measurements, these samples are stacked in units of M_{HI}/L_r .

In Figure 5.19a, galaxies are separated by whether they are in a group (green) or not (purple). The stacks contain all galaxies in each radial bin associated with each sample and the individual detections and non-detections are plotted as filled grey circles and arrows respectively. The average M_{HI}/L_r ratios are very similar for the two samples, however it is important to remember that each radial bin has a wide range of luminosities. Thus the underlying magnitude distribution of each sub-sample should be verified to be similar in order to be compared properly.

Figure 5.20 shows the magnitude histograms for each radial bin. In order to determine whether the group and non-group galaxies are drawn from the same magnitude distribution, I ran a two

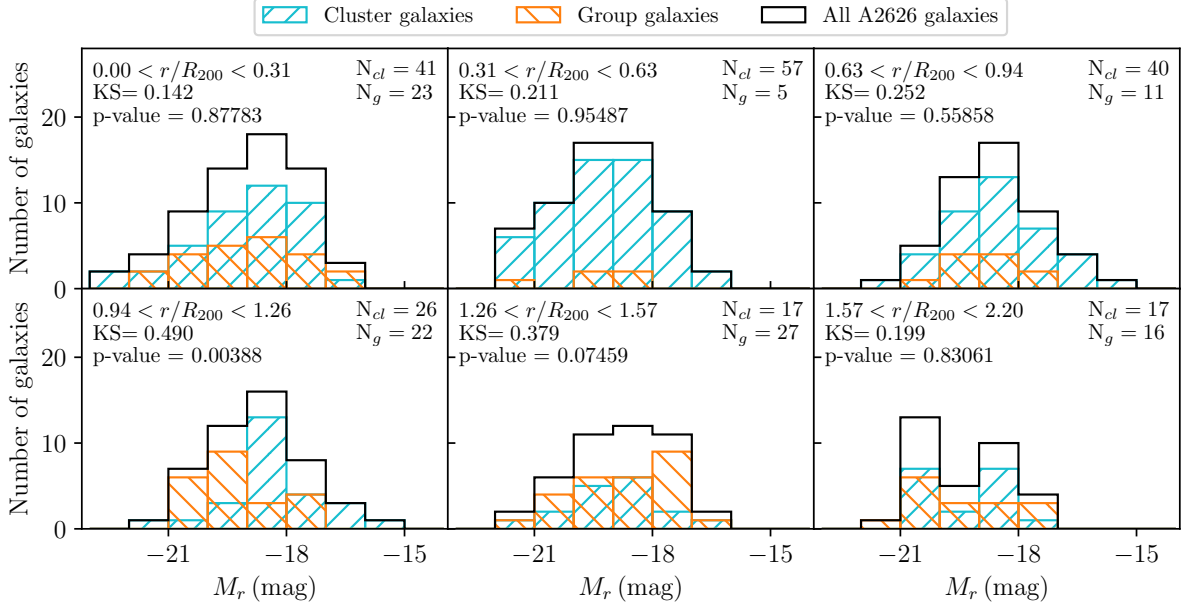


Figure 5.20: Magnitude distributions of galaxies in substructures (N_g), galaxies not in substructures (N_{cl}), and all A2626 galaxies in bins of increasing radius from the cluster centre.

Table 5.3: Results of the KS test for Figure 5.20

	N_{group}	$N_{cluster}$	KS statistic	p-value	$D(\alpha) = \sqrt{-\log(\frac{\alpha}{2}) \frac{1+\frac{m}{n}}{2m}}$
$0.00 < r/R_{200} < 0.31$	23	41	0.1421	0.87783	0.3538
$0.31 < r/R_{200} < 0.63$	5	57	0.2105	0.95487	0.6334
$0.63 < r/R_{200} < 0.94$	11	40	0.2517	0.55858	0.4624
$0.94 < r/R_{200} < 1.26$	22	26	0.4895	0.00388	0.3934
$1.26 < r/R_{200} < 1.57$	27	17	0.3791	0.07459	0.4205
$1.57 < r/R_{200} < 2.20$	16	17	0.1985	0.83061	0.4730

sample Kolmogorov–Smirnov (KS) test⁵. Assuming a null hypothesis that the two magnitude distributions (group and non-group) are the same, the null hypothesis can be rejected at the 95% confidence level ($D(\alpha = 0.05)$) if the KS statistic is greater than $D(\alpha = 0.05)$ – see Table 5.3. Based on the outcome of the KS test, the magnitude distributions for the group and non-group galaxies are the same except for the radial bin, $0.94 < r/R_{200} < 1.26$.

With the statistical confidence that the magnitude distributions for group and non-group galaxies are not responsible for the differing $\langle M_{H\text{I}}/L_r \rangle$ values, I return to the results of Figure 5.19a. Under the assumption that pre-processing is responsible for removing the H I from the group galaxies prior to cluster infall, one might expect to see the $\langle M_{H\text{I}}/L_r \rangle$ for the group galaxies to be systematically lower than the non-group galaxies. This is, however, not what is observed in Figure 5.19a: outside the cluster ($r/R_{200} > 1.3$), where both samples have a measurement (there is only an upper limit for the non-group galaxies in the outermost radial bin), group galaxies have a higher $\langle M_{H\text{I}}/L_r \rangle$ than the field galaxies, while inside the cluster (excluding the limits of the innermost bin) non-group galaxies have a higher $\langle M_{H\text{I}}/L_r \rangle$ and around $r/R_{200} \sim 0.5$ have comparable $\langle M_{H\text{I}}/L_r \rangle$. It is not clear what could be driving this. However, it should be noted that even though the KS statistics

⁵I used the SciPy KS two sample test (`scipy.stats.ks_2samp`)

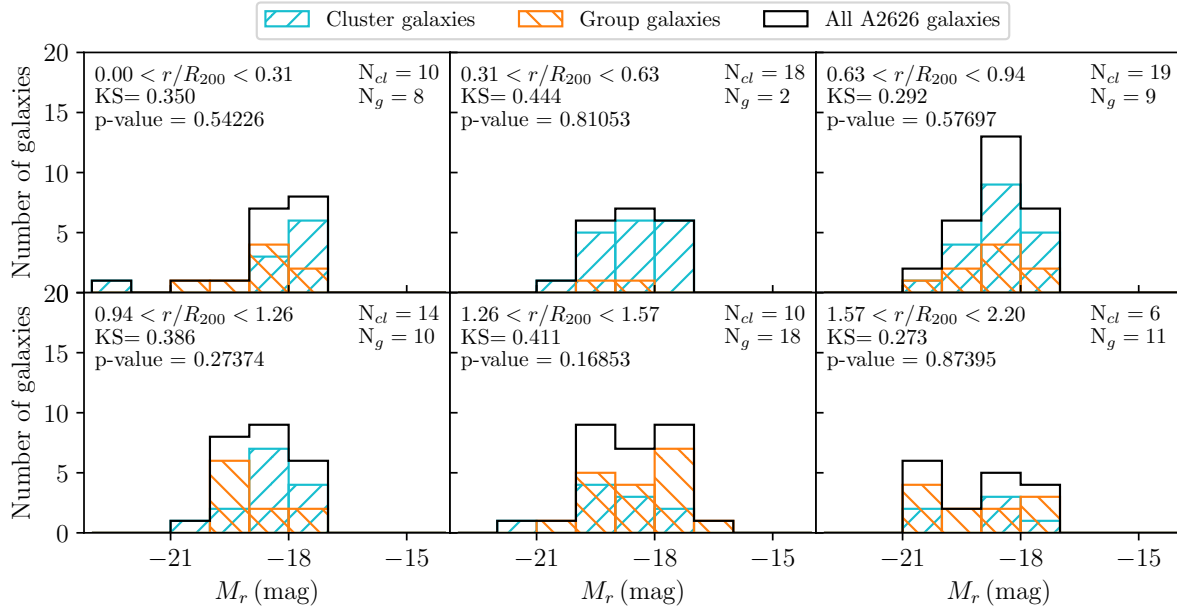


Figure 5.21: Magnitude distribution of late-type galaxies in substructure (N_g) and not in substructure (N_{cl}), and all A2626 late-type galaxies in bins of increasing radius from the cluster centre.

Table 5.4: Results of the KS test for Figure 5.21

	$N_{cluster}$	N_{group}	$D_{m,n}$	$1 - \alpha$	$D(\alpha) = \sqrt{-\log\left(\frac{\alpha}{2}\right) \frac{1+m/n}{2m}}$
$0.00 < r/R_{200} < 0.31$	10	8	0.3500	0.54226	0.6442
$0.31 < r/R_{200} < 0.63$	18	2	0.4444	0.81053	1.0123
$0.63 < r/R_{200} < 0.94$	19	9	0.2924	0.57697	0.5496
$0.94 < r/R_{200} < 1.26$	14	10	0.3857	0.27374	0.5623
$1.26 < r/R_{200} < 1.57$	10	18	0.4111	0.16853	0.5356
$1.57 < r/R_{200} < 2.20$	6	11	0.2727	0.87395	0.6893

showed the magnitude distributions between the two samples to be the same, some radial bins have very few galaxies.

An open question behind the cause of the morphology-density relation is the creation mechanism of S0 galaxies. Are S0 galaxies a result of spiral galaxies losing their gas and quenching their star formation, or is there another evolutionary pathway? Here I look at the quenching of late-type (spiral) galaxies in the group and non-group samples. Using the same method as for the full group/non-group populations to determine statistically if the magnitude distributions for each radial bin are the same (the magnitude distributions for the late-type galaxies are shown in Figure 5.21), the results from the KS test are presented in Table 5.4. The KS test results indicate that the magnitude distributions for late-type group and non-group galaxies are drawn from the same distribution at the 95% confidence level for every radial bin, but some bins, notably $0.31 < r/R_{200} < 0.62$ have very few galaxies in the group sample. It is also worth noting, that visually the $0.94 < r/R_{200} < 1.26$ and $1.26 < r/R_{200} < 1.57$ bins appear to have very different magnitude distributions, these two bins also have the lowest p-values.

Figure 5.19b presents the average M_{HI}/L_r ratios for the late-type galaxies at increasing distance

from the cluster centre. The average M_{HI}/L_r ratios for all A2626 late-type galaxies (group and non-group) are shown in orange, while the group late-type galaxies are shown in blue and non-group galaxies in red. There is no detection of the non-group galaxies in the two most distant radial bins. The average for all late-type galaxies (the orange stars) have a lower average M_{HI}/L_r ratios than the group late-type galaxies, this implies that the true average M_{HI}/L_r for the non-group galaxies is lower than the limits suggest, lower than the average M_{HI}/L_r for the group late-type galaxies.

The $\langle M_{\text{HI}}/L_r \rangle$ values for the group late-type and non-group late-type galaxies in Figure 5.19b, show that the group late-type galaxies, where there is a detection in the stacked spectrum, have higher $\langle M_{\text{HI}}/L_r \rangle$ values at radii $r/R_{200} < 0.94$. At larger radii, $r/R_{200} > 1.26$, the 3σ upper limits on the measurements for the non-group late-type galaxies are consistent with the measurements for the group late-type galaxies. However, the difference between the average for all the late-type galaxies and the group late-type galaxies would suggest that if the stacked spectra were sensitive enough to detect H I in the non-group late-type galaxies, then the measured average (for the non-group late-type galaxies) would be lower than the group late-type galaxies.

With the exception of the $0.94 < r/R_{200} < 1.26$ bin, where the group and non-group late-type galaxies are statistically different samples, the group late-type galaxies (blue squares) have a constant $\langle M_{\text{HI}}/L_r \rangle$ at radii greater than, $r \sim 0.5R_{200}$. There is no detection in the inner-most radius bin suggesting rapid change in H I content around $r \sim 0.5R_{200}$. The non-group galaxies (red circles) also show a constant $\langle M_{\text{HI}}/L_r \rangle$ from R_{200} towards the centre of the cluster as the group late-type galaxies, but at a lower $\langle M_{\text{HI}}/L_r \rangle$. The non-group galaxies are not detected at the two outermost radii (although this could be due to poor number statistics and increased noise in the spectra due to the primary beam attenuation).

The higher $\langle M_{\text{HI}}/L_r \rangle$ for the group late-type galaxies compared to the non-group late-type galaxies could suggest that the group environment plays a role in limiting how quickly the H I is removed from the member late-type galaxies. The upper limit on the average M_{HI}/L_r for the group galaxies at the very centre of the cluster could then be a result of the group environment no longer “protecting” the late-type member galaxies at peri-centric passage.

5.6 Summary and Conclusions

In this chapter, I have presented the DECaLS photometry matched to the cluster spectroscopy presented in Chapter 4. Using this photometry, along with the Abell (1958) criterion for rich clusters, I have determined that A2626 is a rich cluster (richness class 1), similar to the comparable-sized Virgo cluster.

Using the isophotal radii determined from the DECaLS r -band images, I was able to calculate the H I deficiency for the cluster galaxies, and use stacking to determine the average H I deficiency for the cluster. Figure 5.14 shows that A2626 has the same radial pattern of H I deficiency as seen in other clusters (e.g Solanes et al., 2001; Healy et al., 2021c).

Visually classified morphologies in combination with optical colour information and the H I observations enabled characterisation of the substructures found in Chapter 4. The six groups show a range of morphological and colour properties. A1 shows signs of recent gas removal through the high $\langle \text{DEF}_{\text{HI}} \rangle$; A4 shows a clear morphology-density relation, but is not particularly H I deficient. A6, the group thought to have merged with the cluster centre has a population of faint red late-type galaxies, a sign that the galaxies that have yet to undergo the final processing by the cluster: morphological transformation.

I also explore which environment (local or global) has a stronger impact on the removal of H I

from the galaxies. In Section 5.5, I compare the $\langle M_{\text{HI}}/L_r \rangle$ of cluster galaxies in groups to cluster galaxies not in groups. There is no clear trend on average for all the group/non-group galaxies, but it is possible that this trend/lack of trend could be due to small number statistics. Considering only the late-type galaxies, there is a delay in the change in the $\langle M_{\text{HI}}/L_r \rangle$ of the late-type galaxies in groups compared to non-group late-type galaxies. I postulate that this could be due to the group environment protecting the late-type galaxies until the group reaches the inner regions of the cluster.

This cluster, with the larger HI and optical spectroscopy coverage than the Coma cluster studied in Chapter 2, has provided the opportunity to tackle some of the questions asked of Coma but which we could not answer then due to non-detections in the stacked profiles. The conclusions drawn in this chapter also suffer from small number statistics. Upcoming optical spectroscopy surveys such as the WEAVE Wide-field Cluster Survey (Jin et al. in prep) and HI surveys of galaxy clusters with MeerKAT, ASKAP and the Medium Deep Survey with Apertif, will provide larger statistical samples out to larger radii around clusters, hopefully enabling even more in-depth analysis of cluster vs. group processes driving galaxy evolution.

A Stacked spectra

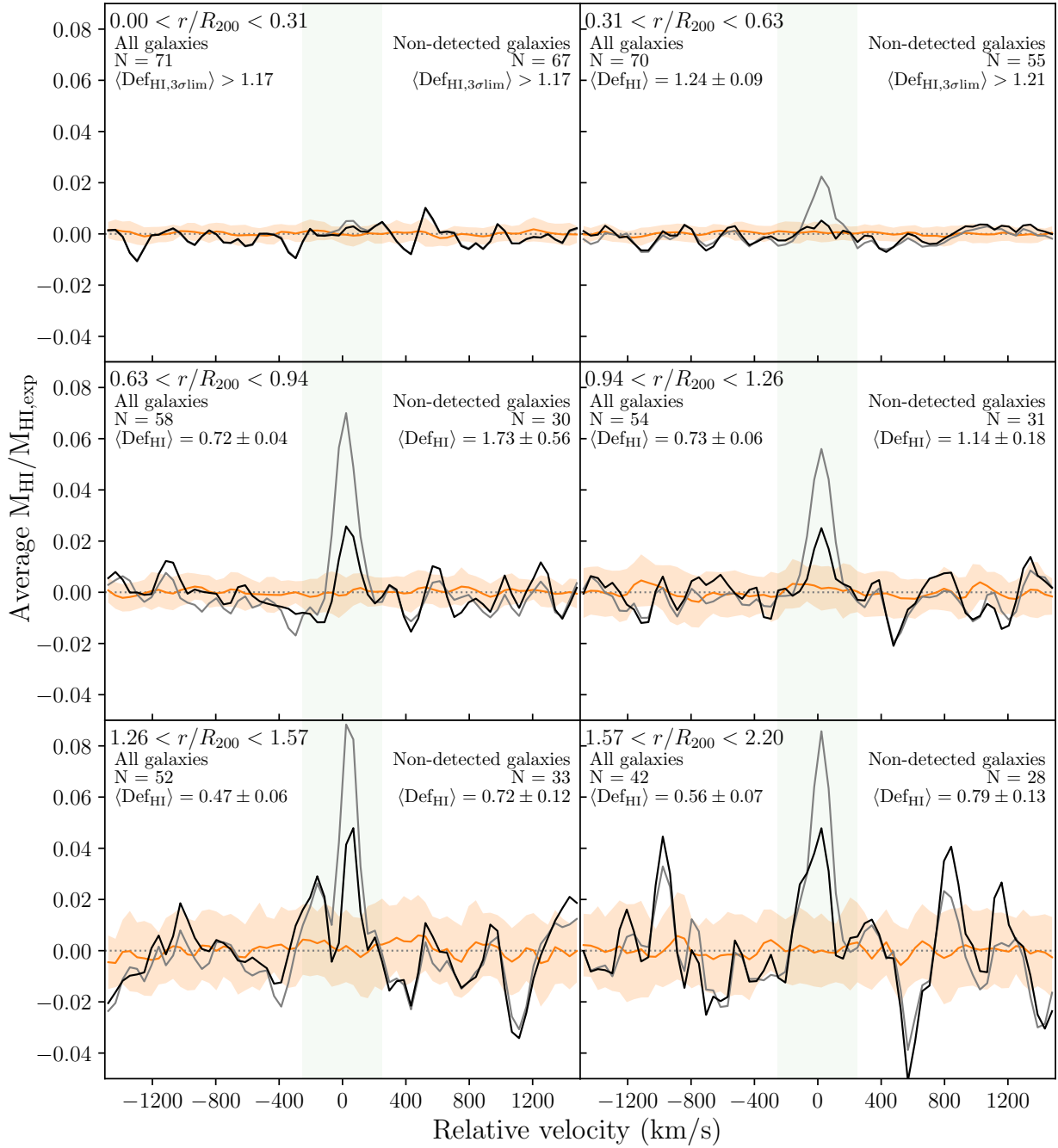


Figure A.1: Stacked spectra used to determine the $\langle \text{DEF}_{\text{HI}} \rangle$ in bins of projected radius from the cluster centre (Figure 5.14). The grey spectrum represents the stacked spectrum for all galaxies, and the black spectrum only the non-detections. The orange spectrum represents the mean of the 25 reference spectra for the non-detected sample and horizontal band indicates corresponding rms of the 25 reference spectra in each channel. The vertical green window indicates the region of the stacked spectra where the HI signal is expected.

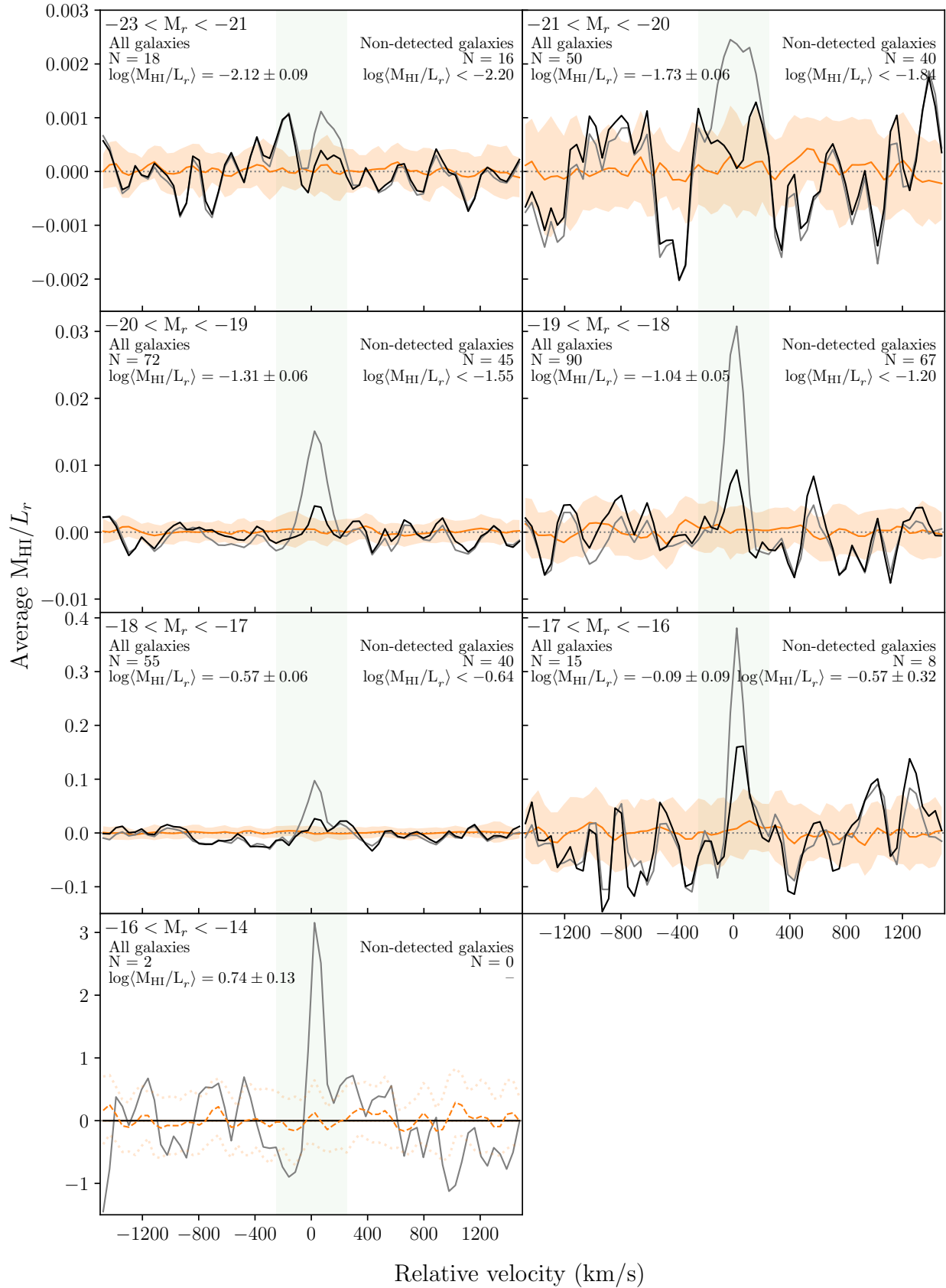


Figure A.2: Stacked spectra used to determine the $\langle M_{\text{HI}}/L_r \rangle$ in bins of absolute r -band magnitude (Figure 5.16a). The grey spectrum represents the stacked spectrum for all galaxies, and the black spectrum only the non-detections. The orange spectrum represents the mean of the 25 reference spectra for the non-detected sample and horizontal band indicates corresponding rms of the 25 reference spectra in each channel. The vertical green window indicates the region of the stacked spectra where the HI signal is expected.

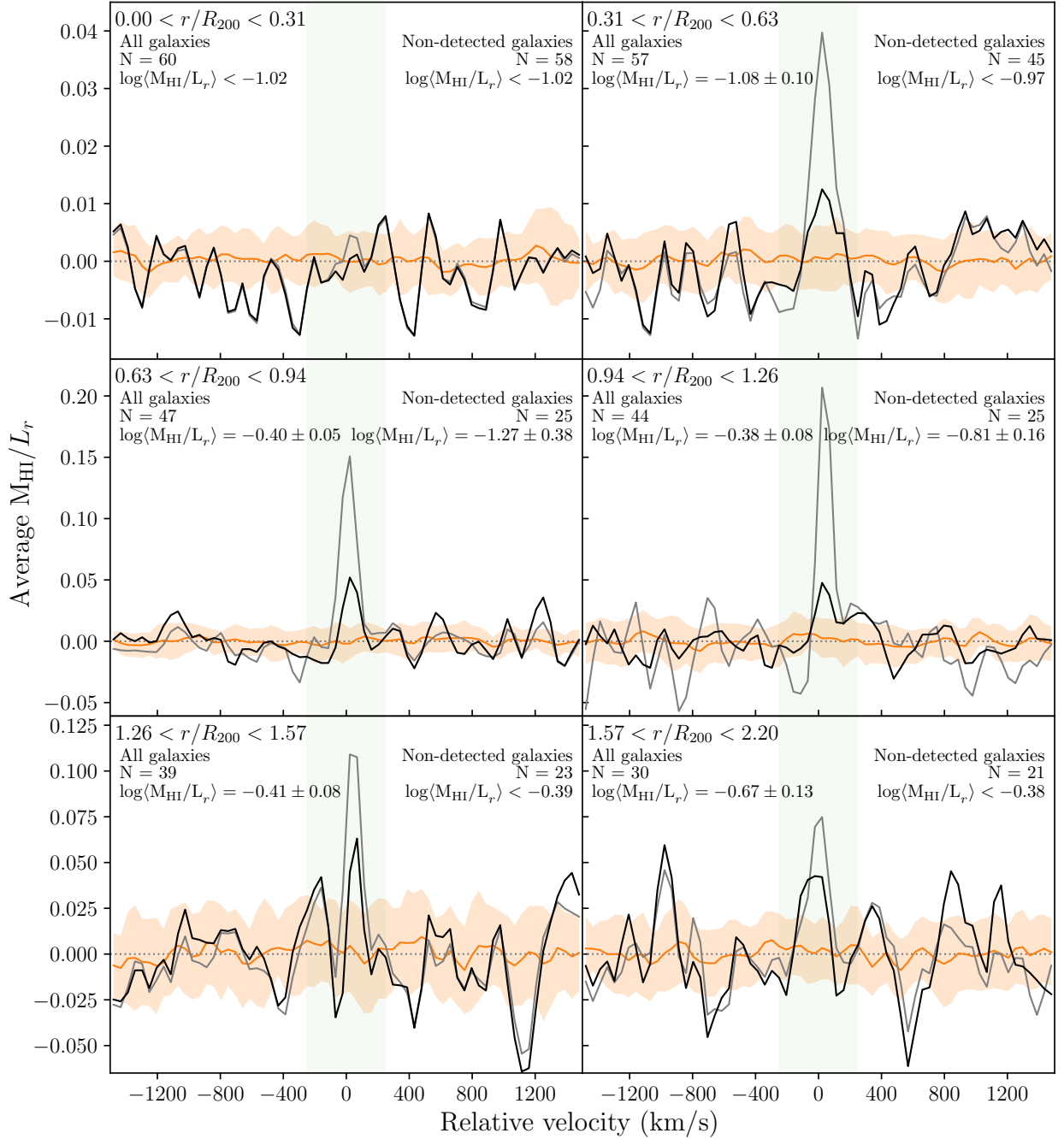


Figure A.3: Stacked spectra used to determine the $\langle M_{\text{HI}}/L_r \rangle$ in bins of projected radius from the cluster centre (Figure 5.16b). The grey spectrum represents the stacked spectrum for all galaxies, and the black spectrum only the non-detections. The orange spectrum represents the mean of the 25 reference spectra for the non-detected sample and horizontal band indicates corresponding rms of the 25 reference spectra in each channel. The vertical green window indicates the region of the stacked spectra where the H I signal is expected.

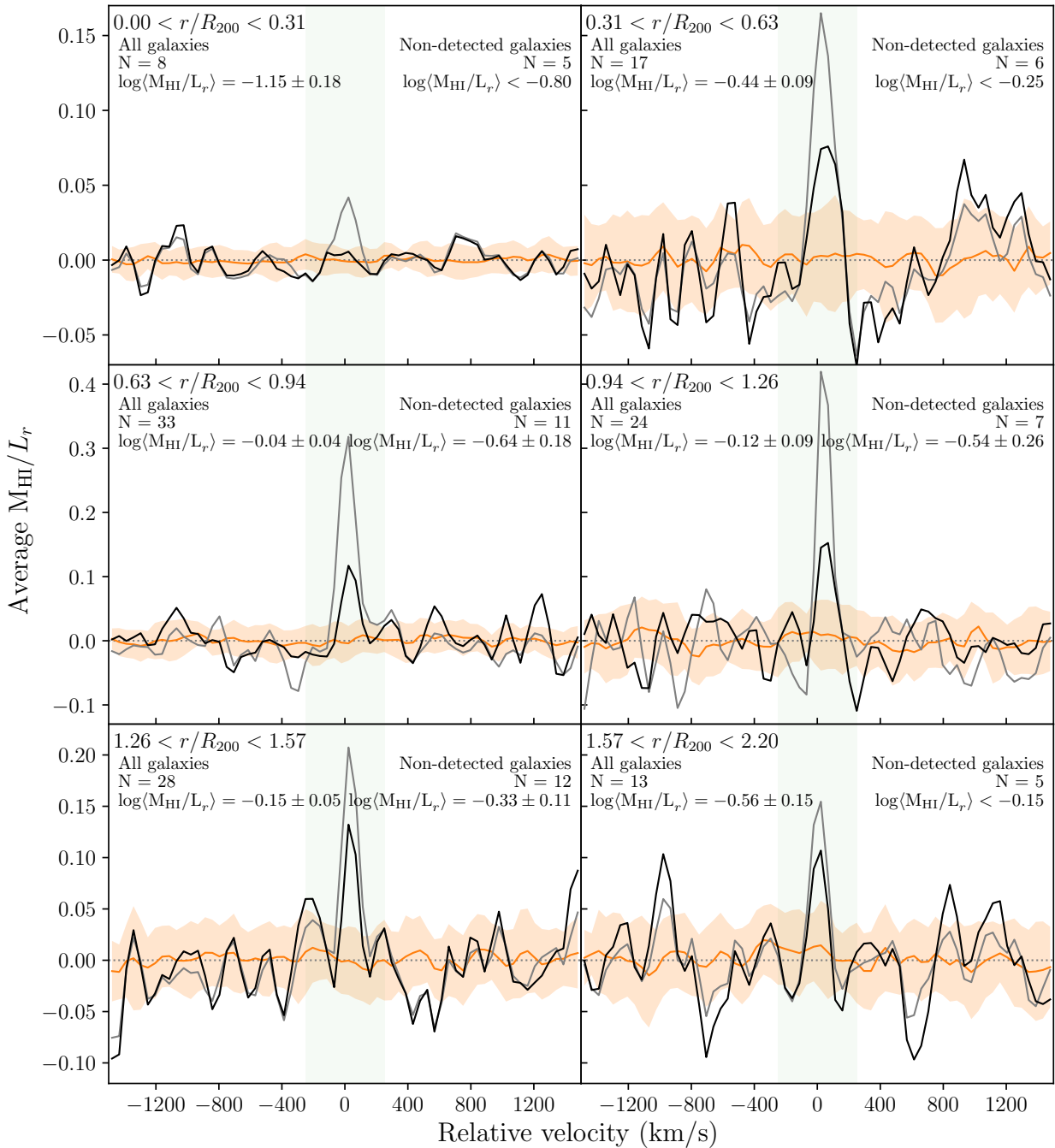


Figure A.4: Stacked spectra used to determine the $\langle M_{\text{HI}}/L_r \rangle$ in bins of projected radius from the cluster centre for blue galaxies (Figure 5.17a). The grey spectrum represents the stacked spectrum for all galaxies, and the black spectrum only the non-detections. The orange spectrum represents the mean of the 25 reference spectra for the non-detected sample and horizontal band indicates corresponding rms of the 25 reference spectra in each channel. The vertical green window indicates the region of the stacked spectra where the HI signal is expected.

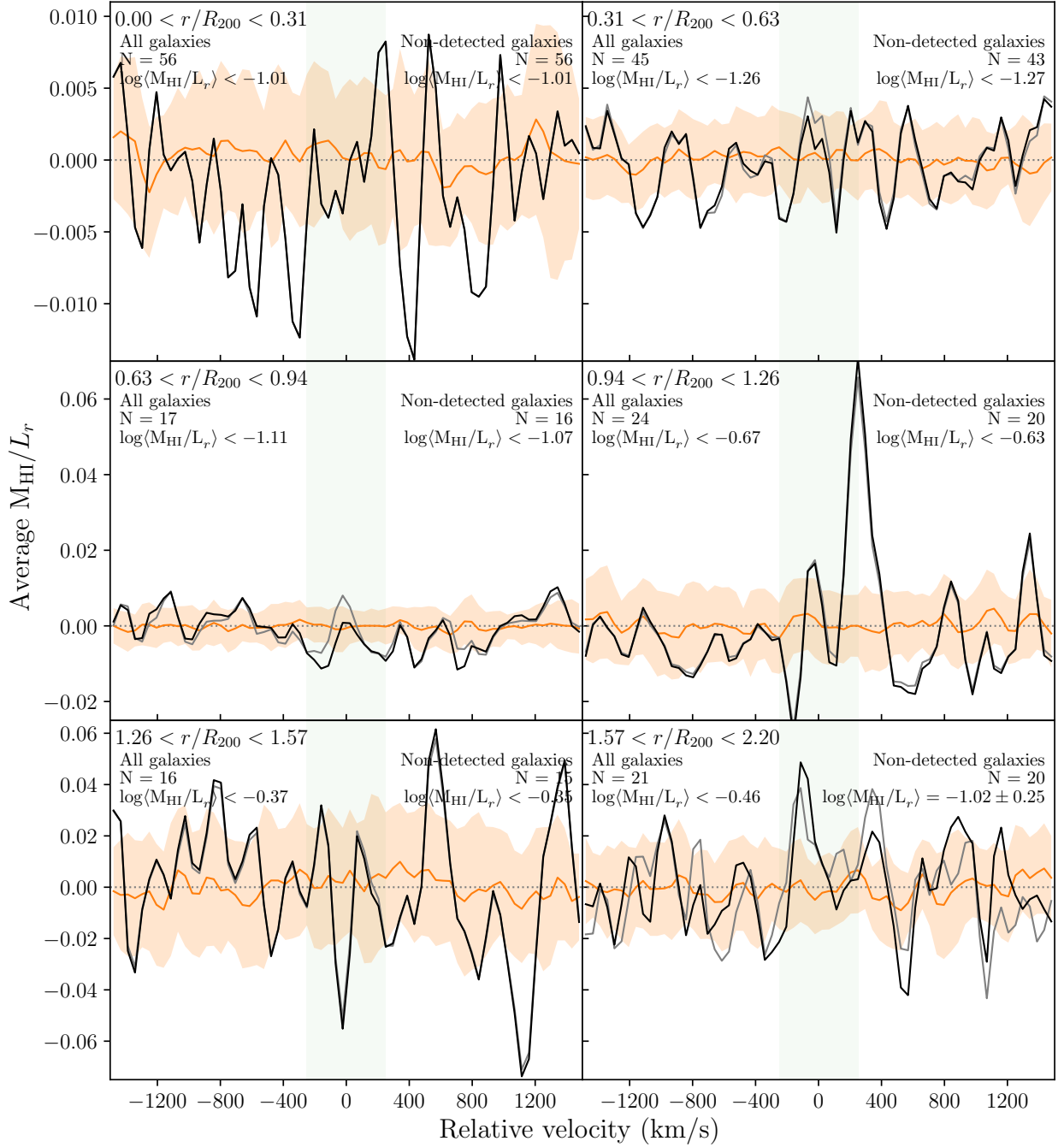


Figure A.5: Same as Figure A.4, but for the red galaxies.

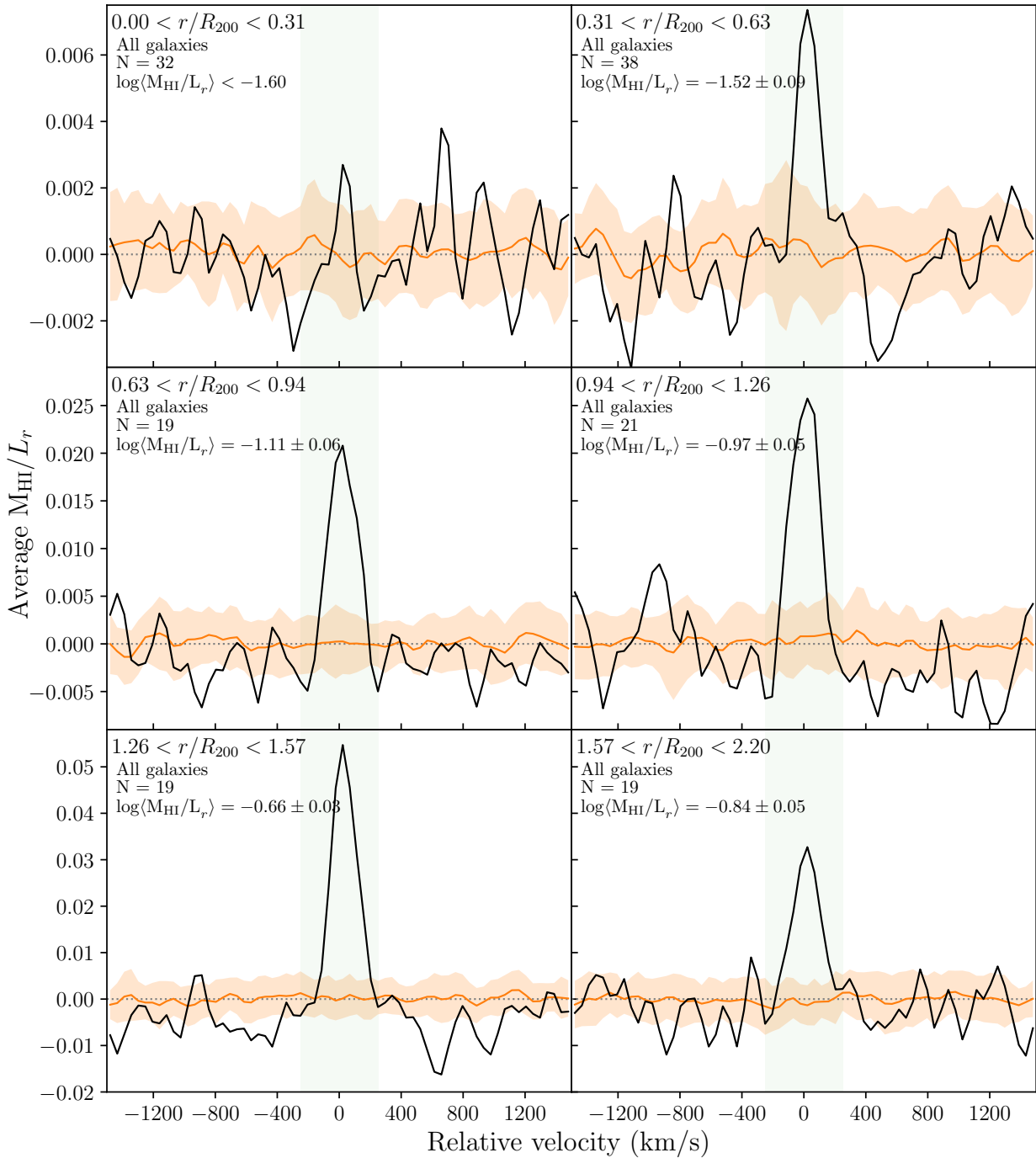


Figure A.6: Stacked spectra used to determine the $\langle M_{\text{HI}}/L_r \rangle$ in bins of projected radius from the cluster centre for bright ($M_r < -19$ mag) galaxies (Figure 5.17b). The black line represents the stacked spectrum for all galaxies. The orange spectrum represents the mean of the 25 reference spectra for the sample and horizontal band indicates corresponding rms of the 25 reference spectra in each channel. The vertical green window indicates the region of the stacked spectra where the HI signal is expected.

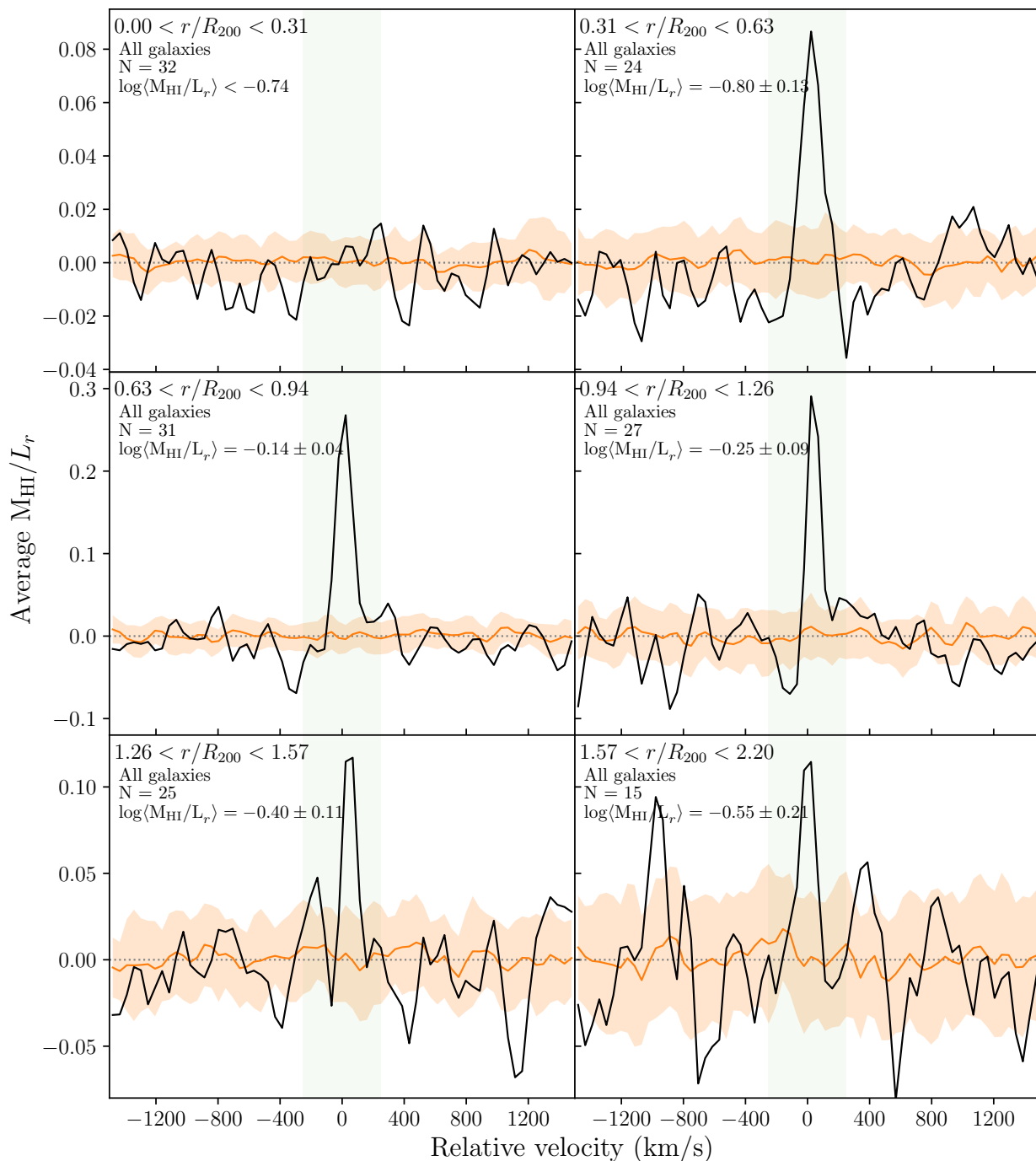


Figure A.7: Same as Figure A.6, but for the faint ($M_r > -19$ mag) galaxies.

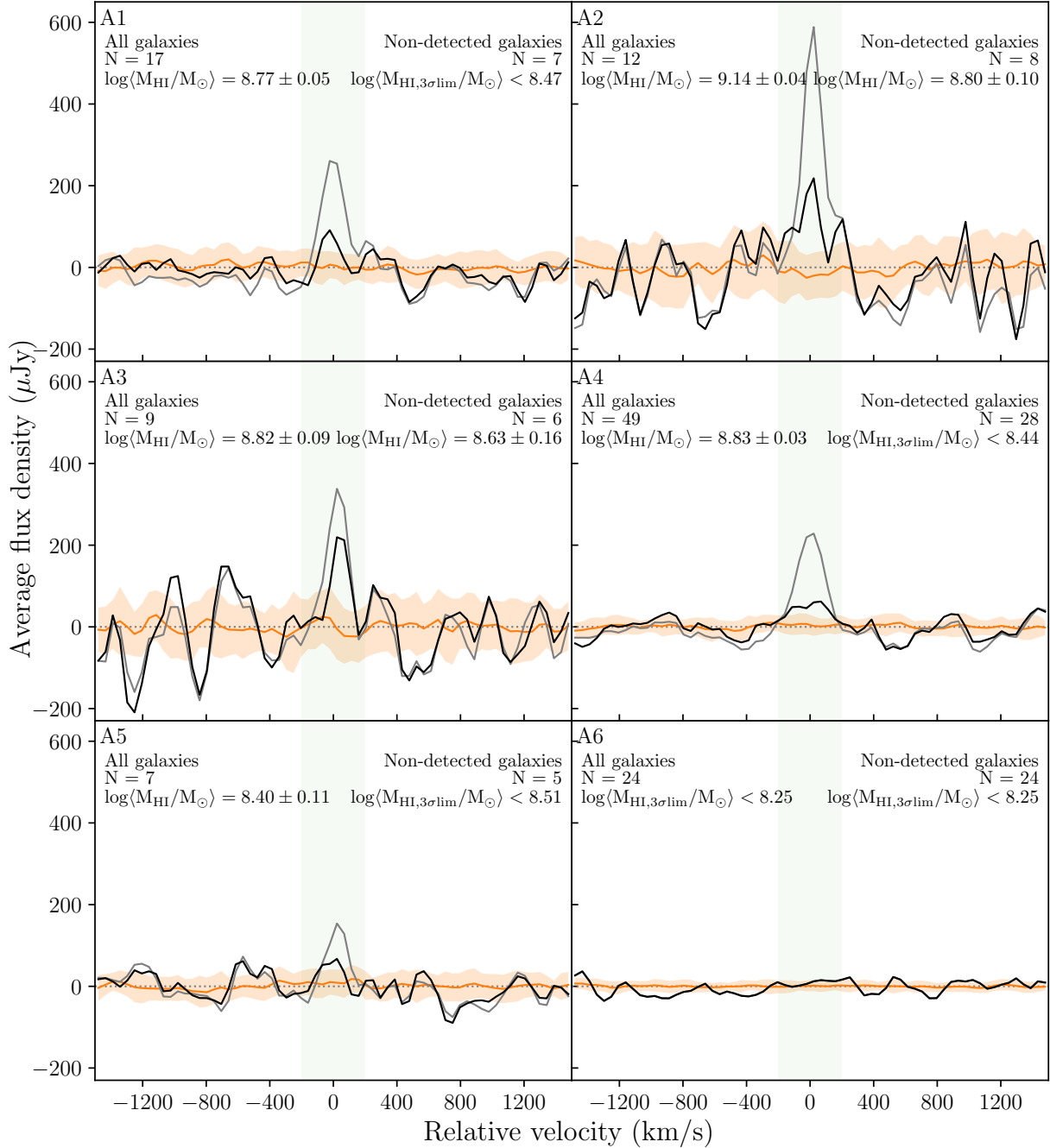


Figure A.8: Stacked spectra for the six substructures in A2626. From these spectra, I measure the average M_{HI} . The grey spectrum represents the stacked spectrum for all galaxies, and the black spectrum only the non-detections. The orange spectrum represents the mean of the 25 reference spectra for the non-detected sample and horizontal band indicates corresponding rms of the 25 reference spectra in each channel. The vertical green window indicates the region of the stacked spectra where the HI signal is expected.

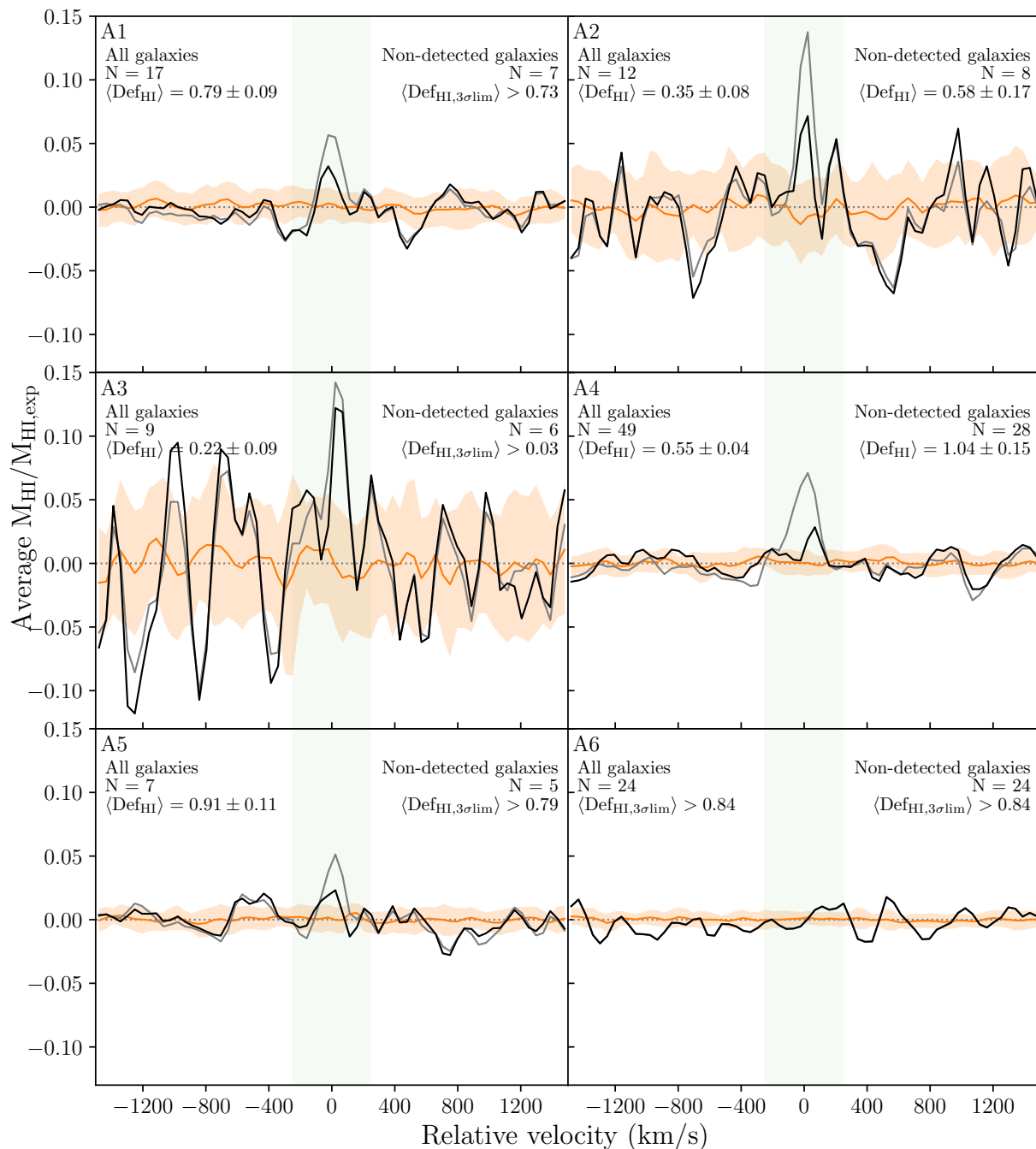


Figure A.9: Same as Figure A.8, but measure average DEF_{HI} .

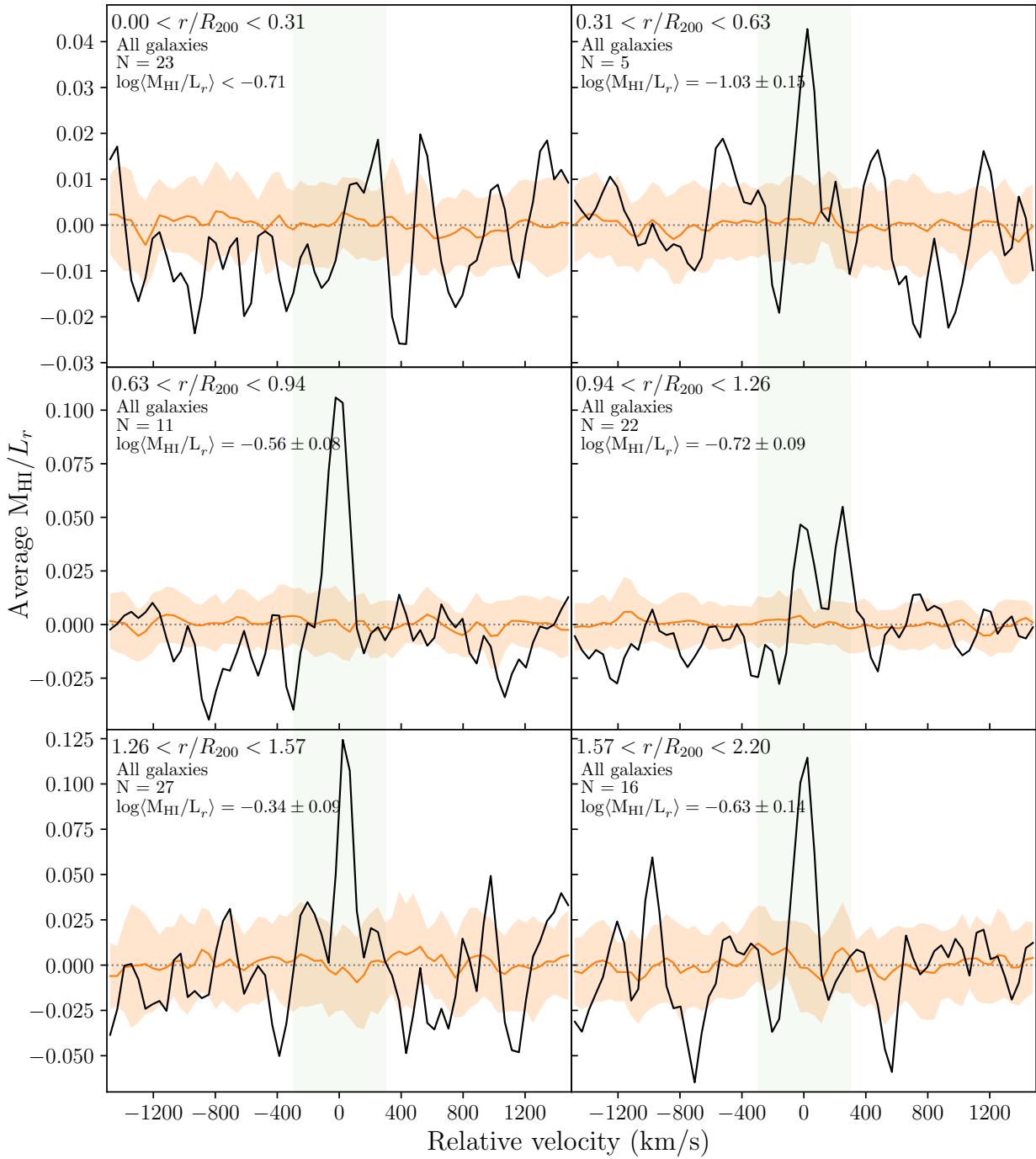


Figure A.10: Same as Figure A.6, but for the galaxies in substructure.

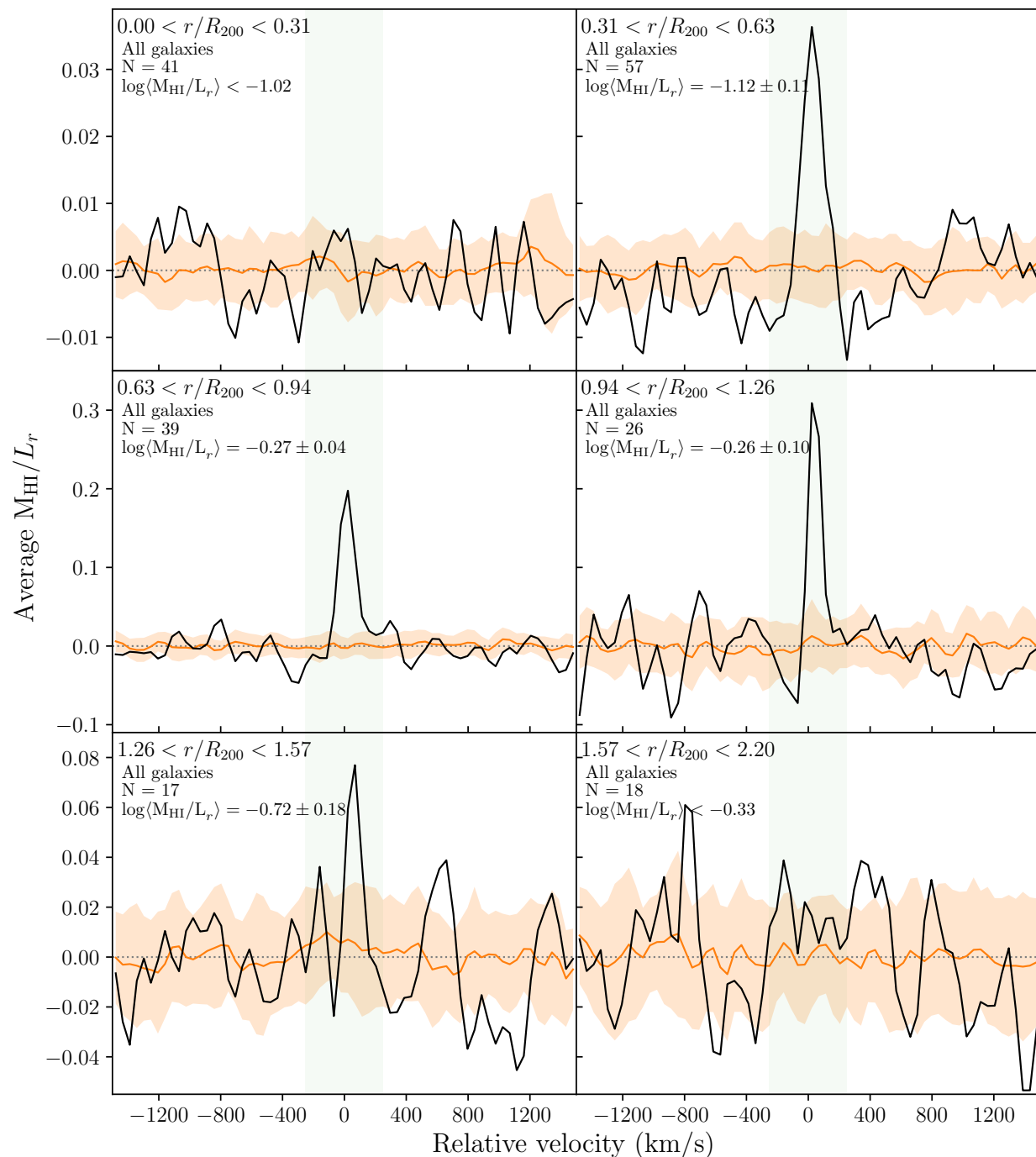


Figure A.11: Same as Figure A.6, but for the galaxies in not in substructure.

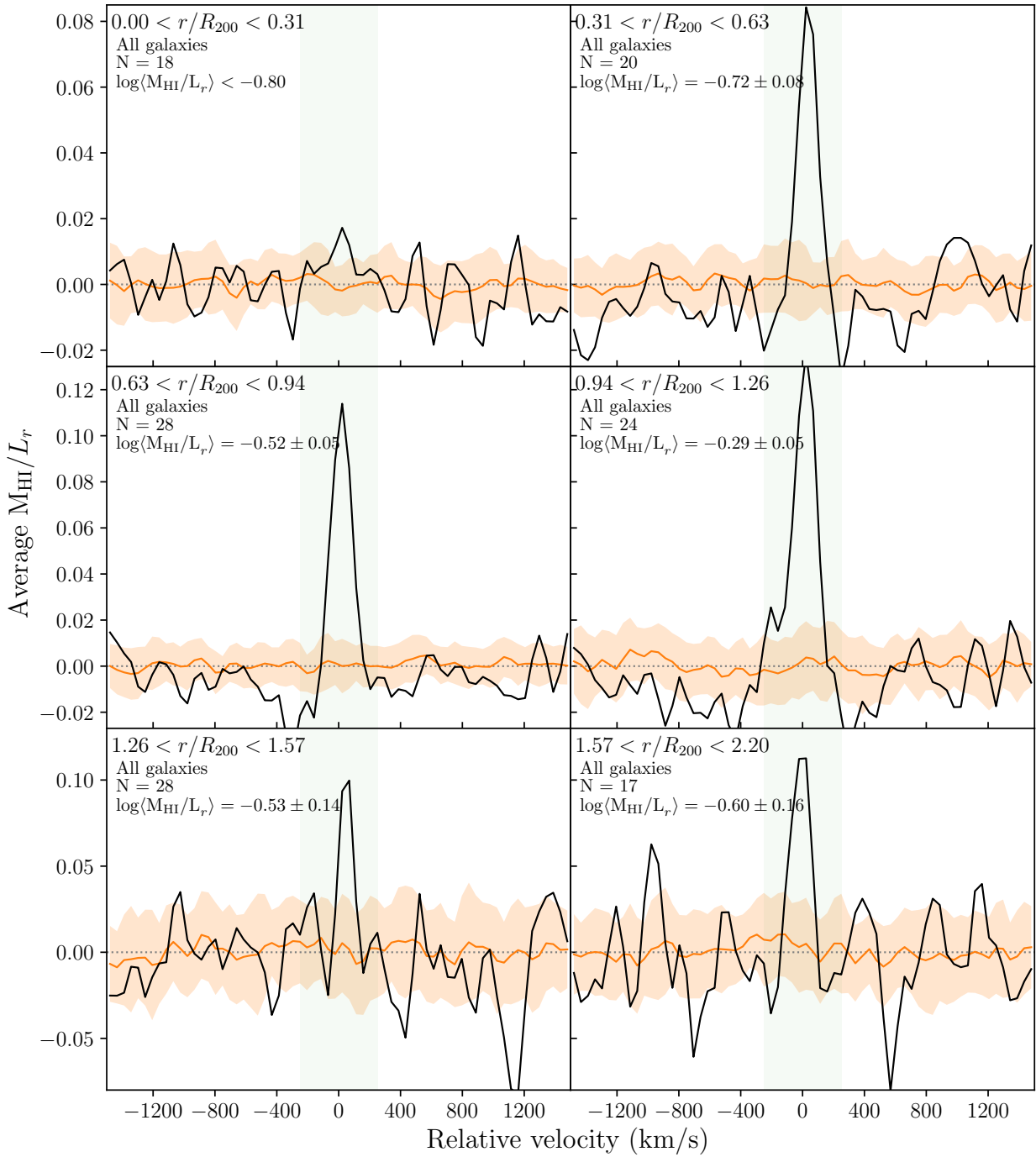


Figure A.12: Same as Figure A.6, but for all cluster late-type galaxies.

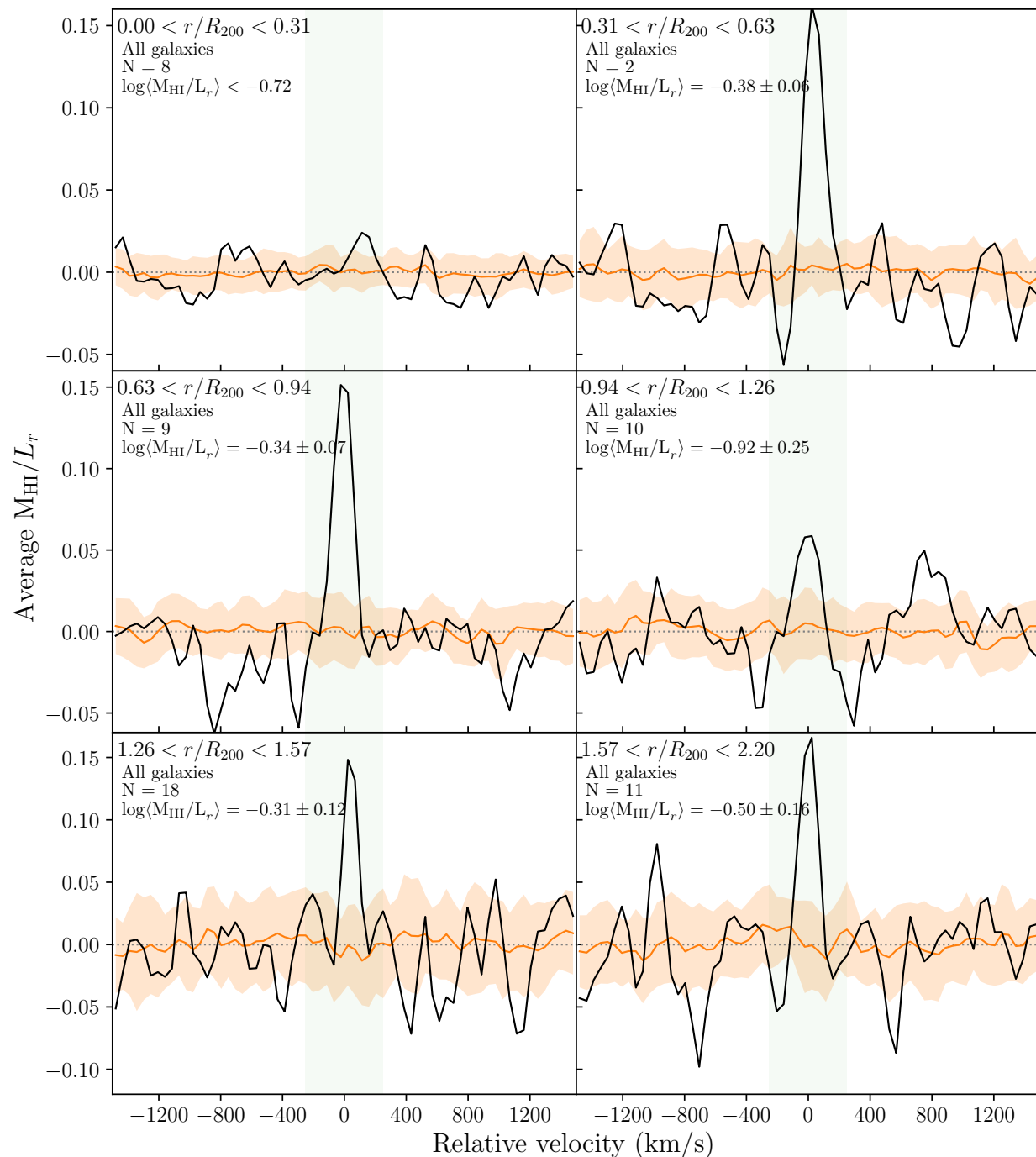


Figure A.13: Same as Figure A.6, but for late-type cluster galaxies in substructure.

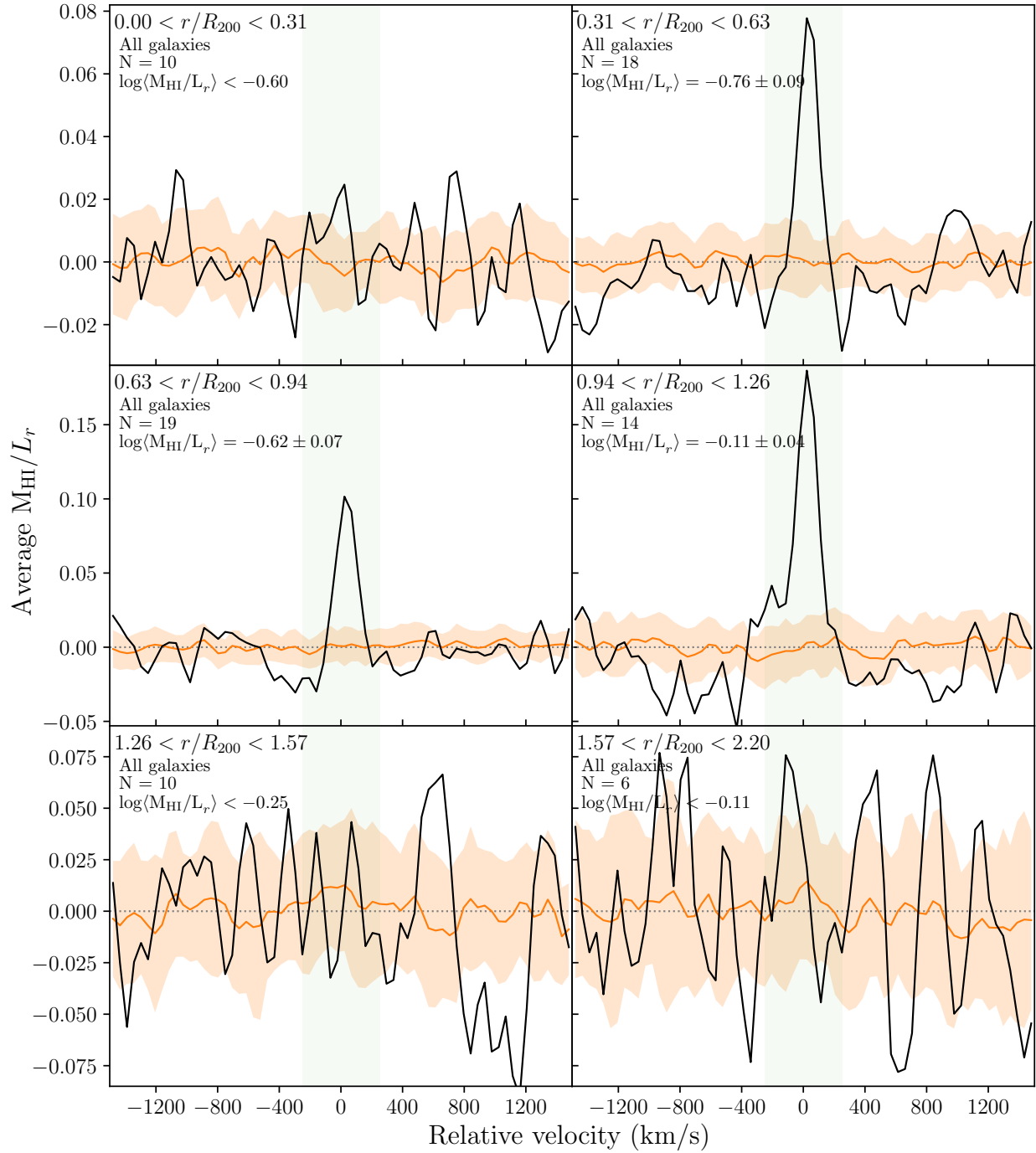


Figure A.14: Same as Figure A.6, but for late-type cluster galaxies in not in substructure.

B Data tables of measurements from stacking

Table B.1: Average DEF_{HI} measurements measured from the stacked spectra in Figure A.1. These data are presented in Figure 5.14.

	All galaxies		Only H I non-detected galaxies	
	N	$\langle \text{DEF}_{\text{HI}} \rangle$	N	$\langle \text{DEF}_{\text{HI}} \rangle$
$0.00 < r/R_{200} < 0.31$	71	< 1.17	67	< 1.17
$0.31 < r/R_{200} < 0.63$	70	1.24 ± 0.09	55	< 1.21
$0.63 < r/R_{200} < 0.94$	58	0.72 ± 0.04	30	1.73 ± 0.56
$0.94 < r/R_{200} < 1.26$	54	0.73 ± 0.06	31	1.14 ± 0.18
$1.26 < r/R_{200} < 1.57$	52	0.47 ± 0.06	33	0.72 ± 0.12
$1.57 < r/R_{200} < 2.20$	42	0.56 ± 0.07	28	0.79 ± 0.13

Table B.2: Average M_{HI}/L_r measurements measured from the stacked spectra in Figure A.2. These data are presented in Figure 5.16a.

	All galaxies		Only H I non-detected galaxies	
	N	$\log \langle M_{\text{HI}}/L_r \rangle$	N	$\log \langle M_{\text{HI}}/L_r \rangle$
$-23 < M_r < -21$	18	-2.12 ± 0.09	16	< -2.20
$-21 < M_r < -20$	50	-1.73 ± 0.06	40	< -1.84
$-20 < M_r < -19$	72	-1.31 ± 0.06	45	< -1.55
$-19 < M_r < -18$	90	-1.04 ± 0.05	67	< -1.20
$-18 < M_r < -17$	55	-0.57 ± 0.06	40	< -0.64
$-17 < M_r < -16$	15	-0.09 ± 0.09	8	-0.57 ± 0.32
$-16 < M_r < -14$	2	0.74 ± 0.13	0	–

Table B.3: Average M_{HI}/L_r measurements measured from the stacked spectra in Figure A.3. These data are presented in Figure 5.16b.

	All galaxies		Only HI non-detected galaxies	
	N	$\log\langle M_{\text{HI}}/L_r \rangle$	N	$\log\langle M_{\text{HI}}/L_r \rangle$
$0.00 < r/R_{200} < 0.31$	60	< -1.02	58	< -1.02
$0.31 < r/R_{200} < 0.63$	57	-1.08 ± 0.10	45	< -0.97
$0.63 < r/R_{200} < 0.94$	47	-0.40 ± 0.05	25	-1.27 ± 0.38
$0.94 < r/R_{200} < 1.26$	44	-0.38 ± 0.08	25	-0.81 ± 0.16
$1.26 < r/R_{200} < 1.57$	39	-0.41 ± 0.08	23	< -0.39
$1.57 < r/R_{200} < 2.20$	30	-0.67 ± 0.13	21	< -0.38

Table B.4: Average M_{HI}/L_r measurements measured from the stacked spectra in Figure A.4. These data are for the blue galaxies presented in Figure 5.17a.

	All galaxies		Only HI non-detected galaxies	
	N	$\log\langle M_{\text{HI}}/L_r \rangle$	N	$\log\langle M_{\text{HI}}/L_r \rangle$
$0.00 < r/R_{200} < 0.31$	8	-1.15 ± 0.18	5	< -0.80
$0.31 < r/R_{200} < 0.63$	17	-0.44 ± 0.09	6	< -0.25
$0.63 < r/R_{200} < 0.94$	33	-0.04 ± 0.04	11	-0.64 ± 0.18
$0.94 < r/R_{200} < 1.26$	24	-0.12 ± 0.09	7	-0.54 ± 0.26
$1.26 < r/R_{200} < 1.57$	28	-0.15 ± 0.05	12	-0.33 ± 0.11
$1.57 < r/R_{200} < 2.20$	13	-0.56 ± 0.15	5	< -0.15

Table B.5: Average M_{HI}/L_r measurements measured from the stacked spectra in Figure A.5. These data are for the red galaxies presented in Figure 5.17a.

	All galaxies		Only HI non-detected galaxies	
	N	$\log\langle M_{\text{HI}}/L_r \rangle$	N	$\log\langle M_{\text{HI}}/L_r \rangle$
$0.00 < r/R_{200} < 0.31$	56	< -1.01	56	< -1.01
$0.31 < r/R_{200} < 0.63$	45	< -1.26	43	< -1.27
$0.63 < r/R_{200} < 0.94$	17	< -1.11	16	< -1.07
$0.94 < r/R_{200} < 1.26$	24	< -0.67	20	< -0.63
$1.26 < r/R_{200} < 1.57$	16	< -0.37	15	< -0.35
$1.57 < r/R_{200} < 2.20$	21	< -0.46	20	-1.02 ± 0.25

Table B.6: Average $M_{\text{H I}}/L_r$ measurements measured from the stacked spectra in bright ($M_r < -19$ mag), Figure A.6, and the faint ($M_r > -19$ mag), Figure A.7, samples. These data are for the bright and faint galaxies presented in Figure 5.17b.

	Bright galaxies		Faint galaxies	
	N	$\log\langle M_{\text{H I}}/L_r \rangle$	N	$\log\langle M_{\text{H I}}/L_r \rangle$
$0.00 < r/R_{200} < 0.31$	32	< -1.60	32	< -0.74
$0.31 < r/R_{200} < 0.63$	38	-1.52 ± 0.09	24	-0.80 ± 0.13
$0.63 < r/R_{200} < 0.94$	19	-1.11 ± 0.06	31	-0.14 ± 0.04
$0.94 < r/R_{200} < 1.26$	21	-0.97 ± 0.05	27	-0.25 ± 0.09
$1.26 < r/R_{200} < 1.57$	19	-0.66 ± 0.03	25	-0.40 ± 0.11
$1.57 < r/R_{200} < 2.20$	19	-0.84 ± 0.05	15	-0.55 ± 0.21

Table B.7: Average $M_{\text{H I}}/L_r$ measurements measured from the stacked spectra for the cluster galaxies in groups/substructure (Figure A.10), and the non-group cluster galaxies (Figure A.11). These data are for the group and non-group galaxies presented in Figure 5.19a.

	Group galaxies		Non-group galaxies	
	N	$\log\langle M_{\text{H I}}/L_r \rangle$	N	$\log\langle M_{\text{H I}}/L_r \rangle$
$0.00 < r/R_{200} < 0.31$	23	< -0.71	41	< -1.02
$0.31 < r/R_{200} < 0.63$	5	-1.03 ± 0.15	57	-1.19 ± 0.12
$0.63 < r/R_{200} < 0.94$	11	-0.56 ± 0.08	39	-0.28 ± 0.05
$0.94 < r/R_{200} < 1.26$	22	-0.72 ± 0.09	26	-0.24 ± 0.10
$1.26 < r/R_{200} < 1.57$	27	-0.34 ± 0.09	17	-0.76 ± 0.20
$1.57 < r/R_{200} < 2.20$	16	-0.63 ± 0.14	18	< -0.33

Table B.8: Average $M_{\text{H I}}/L_r$ measurements measured from the stacked spectra for all cluster late-type galaxies (Figure A.12), the cluster late-type galaxies in groups/substructure (Figure A.13), and the non-group late-type cluster galaxies (Figure A.14). These data are for the three samples of late-type galaxies presented in Figure 5.19b.

	All late-type galaxies		Group late-type galaxies		Non-group late-type galaxies	
	N	$\log\langle M_{\text{H I}}/L_r \rangle$	N	$\log\langle M_{\text{H I}}/L_r \rangle$	N	$\log\langle M_{\text{H I}}/L_r \rangle$
$0.00 < r/R_{200} < 0.31$	18	< -0.80	8	< -0.72	10	< -0.60
$0.31 < r/R_{200} < 0.63$	20	-0.72 ± 0.08	2	-0.38 ± 0.06	18	-0.76 ± 0.09
$0.63 < r/R_{200} < 0.94$	28	-0.52 ± 0.05	9	-0.34 ± 0.07	19	-0.62 ± 0.07
$0.94 < r/R_{200} < 1.26$	24	-0.29 ± 0.05	10	-0.92 ± 0.25	14	-0.11 ± 0.04
$1.26 < r/R_{200} < 1.57$	28	-0.53 ± 0.14	18	-0.31 ± 0.12	10	< -0.25
$1.57 < r/R_{200} < 2.20$	17	-0.60 ± 0.16	11	-0.50 ± 0.16	6	< -0.11

References

- Abell G. O., 1958, *The Astrophysical Journal Supplement Series*, 3, 211
- Abell G. O., Corwin Harold G. J., Olowin R. P., 1989, *The Astrophysical Journal Supplement Series*, 70, 1
- Beijersbergen M., 2003, PhD thesis, University of Groningen, <http://adsabs.harvard.edu/abs/2003PhDT.....236B>
- Bera A., Kanekar N., Chengalur J. N., Bagla J. S., 2019, *The Astrophysical Journal*, 882, L7
- Binggeli B., Sandage A., Tammann G. A., 1985, *The Astronomical Journal*, 90, 1681
- Bird C. M., 1994, *The Astronomical Journal*, 107, 1637
- Bower R. G., Ellis R. S., Rose J. A., Sharples R. M., 1990, *The Astronomical Journal*, 99, 530
- Bower R. G., Lucey J. R., Ellis R. S., 1992, *Monthly Notices of the Royal Astronomical Society*, 254, 601
- Bravo-Alfaro H., Cayatte V., van Gorkom J. H., Balkowski C., 2000, *The Astronomical Journal*, 119, 580
- Brown T., Catinella B., Cortese L., Kilborn V., Haynes M. P., Giovanelli R., 2015, *Monthly Notices of the Royal Astronomical Society*, 452, 2479
- Cava A., et al., 2009, *Astronomy and Astrophysics*, 495, 707
- Chengalur J. N., Braun R., Wieringa M., 2001, *Astronomy and Astrophysics*, 372, 768
- Chowdhury A., Kanekar N., Chengalur J., Sethi S., Dwarakanath K. S., 2020, *Nature*, 586, 369
- Chung A., van Gorkom J. H., Kenney J. D. P., Crowl H., Vollmer B., 2009, *The Astronomical Journal*, 138, 1741
- De Blok W. J., McGaugh S. S., Van der Hulst J. M., 1996, *Monthly Notices of the Royal Astronomical Society*, 283, 18
- Deeley S., et al., 2020, *Monthly Notices of the Royal Astronomical Society*, 498, 2372
- Denes H., Kilborn V. A., Koribalski B. S., 2014, *Monthly Notices of the Royal Astronomical Society*, 444, 667
- Dey A., et al., 2019, *The Astronomical Journal*, 157, 168
- Dressler A., 1980, *The Astrophysical Journal*, 236, 351
- Dressler A., Shectman S. A., 1988, *The Astronomical Journal*, 95, 985
- Dressler A., et al., 1997, *The Astrophysical Journal*, 490, 577
- Dzudzar R., Kilborn V., Murugesan C., Meurer G., Sweet S. M., Putman M., 2019, *Monthly Notices of the Royal Astronomical Society: Letters*, 490, L6
- Gavazzi G., O'Neil K., Boselli A., van Driel W., 2006, *Astronomy and Astrophysics*, 449, 929
- Giovanelli R., Haynes M. P., Chincarini G. L., 1981, *The Astrophysical Journal*, 247, 383
- Gunn J. E., Gott J. Richard I., 1972, *The Astrophysical Journal*, 176, 1

- Haynes M. P., Giovanelli R., 1984, *The Astronomical Journal*, 89, 758
- Haynes M. P., Giovanelli R., Chincarini G. L., 1984, *Annual Review of Astronomy and Astrophysics*, 22, 445
- Healy J., Blyth S.-L., Elson E., van Driel W., Butcher Z., Schneider S., Lehnert M. D., Minchin R., 2019, *Monthly Notices of the Royal Astronomical Society*, 487, 4901
- Healy J., Willner S., Verheijen M., Blyth S.-L., 2021a, *Astronomical Journal*
- Healy J., Deb T., Verheijen M., Blyth S.-L., Serra P., Ramatsoku M., Vulcani B., 2021b, *Astronomy & Astrophysics*
- Healy J., et al., 2021c, *Astronomy & Astrophysics*, 650
- Hess K. M., Jarrett T. H., Carignan C., Passmoor S. S., Goedhart S., 2015, *Monthly Notices of the Royal Astronomical Society*, 452, 1617
- Hou A., et al., 2012, *Monthly Notices of the Royal Astronomical Society*, 421, 3594
- Hubble E., Humason M. L., 1931, *The Astrophysical Journal*, 74, 43
- Jaffé Y. L., et al., 2016, *Monthly Notices of the Royal Astronomical Society*, 461, 1202
- Kennicutt R. C. J., 1989, *The Astrophysical Journal*, 344, 685
- Kleiner D., et al., 2021
- Lah P., et al., 2009, *Monthly Notices of the Royal Astronomical Society*, 399, 1447
- Maddox N., Hess K. M., Blyth S.-L., Jarvis M. J., 2013, *Monthly Notices of the Royal Astronomical Society*, 433, 2613
- McGee S. L., Balogh M. L., Bower R. G., Font A. S., McCarthy I. G., 2009, *Monthly Notices of the Royal Astronomical Society*, 400, 937
- Mohr J. J., Geller M. J., Wegner G., 1996, *The Astronomical Journal*, 112, 1816
- Moore B., Katz N., Lake G., Dressler A., Oemler A., 1996, *Nature*, 379, 613
- Moretti A., et al., 2019, *The Astrophysical Journal*, 889, 9
- Noordermeer E., van der Hulst J. M., Sancisi R., Swaters R. A., van Albada T. S., 2005, *Astronomy & Astrophysics*, 390, 829
- Oman K. A., Hudson M. J., 2016, *Monthly Notices of the Royal Astronomical Society*, 463, 3083
- Oman K. A., Bahé Y. M., Healy J., Hess K. M., Hudson M. J., Verheijen M. A., 2021, *Monthly Notices of the Royal Astronomical Society*, 501, 5073
- Peng Y. J., et al., 2010, *Astrophysical Journal*, 721, 193
- Poggianti B. M., et al., 2016, *The Astronomical Journal*, 151, 78
- Poggianti B. M., et al., 2019, *The Astrophysical Journal*, 889
- Postman M., Geller M. J., 1984, *The Astrophysical Journal*, 281, 95
- Roediger E., Brüggén M., 2007, *Monthly Notices of the Royal Astronomical Society*, 380, 1399

- Schawinski K., et al., 2014, *Monthly Notices of the Royal Astronomical Society*, 440, 889
- Schlegel D. J. D. J., Finkbeiner D. P. D. P., Davis M., 1998, *The Astrophysical Journal*, 500, 525
- Solanes J. M., Giovanelli R., Haynes M. P., 1996, *The Astrophysical Journal*, 461, 609
- Solanes J. M., Manrique A., García-Gómez C., González-Casado G., Giovanelli R., Haynes M. P., 2001, *The Astrophysical Journal*, 548, 97
- Springel V., et al., 2005, *Nature*, 435, 629
- Swaters R. A., van Albada T. S., van der Hulst J. M., Sancisi R., 2002, *Astronomy and Astrophysics*, 390, 829
- Verheijen M., Zwaan M., 2001, in Hibbard J. E., Rupen M., van Gorkom J. H., eds, *Gas and Galaxy Evolution*, ASP Conference Proceedings. Astronomical Society of the Pacific, San Francisco, p. 867, doi:ISBN:1-58381-077-3
- Verheijen M., van Gorkom J. H., Szomoru A., Dwarakanath K. S., Poggianti B. M., Schiminovich D., 2007, *The Astrophysical Journal*, 668, L9
- Vulcani B., et al., 2018, *Monthly Notices of the Royal Astronomical Society*, 480, 3152
- Walter F., Brinks E., Blok W. J. G. D., Bigiel F., Kennicutt R. C., Thornley M. D., Leroy A., 2008, *The Astronomical Journal*, 136, 2563
- Yoon H., Chung A., Smith R., Jaffé Y. L., 2017, *The Astrophysical Journal*, 838, 81



“Space: the final frontier. These are the voyages of the starship Enterprise. Its five-year mission: to explore strange new worlds. To seek out new life and new civilizations. To boldly go where no man has gone before!” – **Captain James T. Kirk**
(Star Trek)

Chapter 6

Summary and Future Work

This thesis started with the goal of determining in which environment in galaxy clusters, the local group environment or the global cluster environment, are the processes by which galaxies are quenched, the most effective. Observed relations such as the morphology–density relation (Dressler & Shectman, 1988) describe how the fraction of galaxies of different morphological classes change with environmental density. Within clusters this is evident as the fraction of late-type galaxies increases towards the lower-density cluster outskirts, while the fraction of early-type galaxies is highest in the cluster core. Understanding what drives this relation requires identifying how galaxies are quenched. In galaxy clusters, there is a number of processes such as ram-pressure stripping (Gunn & Gott, 1972), galaxy harassment (Moore et al., 1996), and starvation (Larson et al., 1980), which are particularly effective at removing the neutral gas (H I) content from galaxies as the galaxy moves through the cluster. H I is the raw fuel from which stars are formed, thus once the H I has been depleted, the formation of molecular hydrogen from which the stars are formed slows to a stop, and star formation ceases and so starts the colour and morphological transformation of the galaxy. The gas removal processes have also been observed in group environments, and there is growing evidence that the group environments may play an important role in beginning the star formation quenching process (Vulcani et al., 2018).

In this thesis, I have investigated the H I properties of galaxies in two galaxy clusters: Abell 2626 and the Coma cluster. Galaxy clusters are well known to be H I deficient (Solanes et al., 2001), thus I use H I spectral line stacking, a statistical technique that enables me to probe the average H I content of the cluster galaxies below what can be directly detected.

6.1 Thesis highlights

6.1.1 Identifying cluster substructure

The literature provides conflicting views on the presence of substructure in both the galaxy clusters, Coma and A2626, considered in this thesis. Vital to identifying substructure is the availability of spectroscopic redshifts of the cluster member galaxies. Studies that did not find substructure tended to have insufficient redshifts. For the investigations presented in this thesis, I set out to collate comprehensive redshift catalogues for both Coma and A2626.

For Coma (see Section 2.2.1), this meant collating all the publicly available redshifts in the literature which resulted in one of the most comprehensive redshift catalogues containing ~ 1020 redshifts for galaxies in the Coma cluster within $3500 < cz \text{ (km s}^{-1}\text{)} < 10500$, and out to a radius of $\sim 1.2 R_{200}$. Despite the wealth of redshifts in the literature, there was lack of redshifts for the fainter blue galaxies in the cluster outskirts. I targeted these galaxies with spectroscopic followup during a 2-night observing campaign using the Hydra multi-object spectrograph on the WIYN telescope.

A2626 is located in a part of the sky that has not been as well studied. Existing spectroscopy for this cluster was mostly from the Wide-field Nearby Galaxy Survey (WINGS; Cava et al., 2009), but unfortunately the WINGS spectroscopy only covered the inner part of the cluster ($r < 0.7 R_{200}$). A2626 was thus targeted for follow-up spectroscopy using Hectospec on the Multi-Mirror Telescope (MMT), which was done in collaboration with Steven Willner at the Harvard Smithsonian Center for Astrophysics. The MMT observations covered $r \lesssim 1.8 R_{200}$ to match the MeerKAT HI data centred on the cluster, and included galaxies with redshifts out to $z \sim 0.46$ to facilitate future work using the low frequency portion of the MeerKAT observations not discussed in this work. The MMT redshifts more than doubled the existing redshifts in the field, and revealed structures around and behind A2626.

In order to identify the substructures within the clusters, I used the Dressler-Shectman (Dressler & Shectman, 1988) test which is sensitive to kinematic substructure. Using this method, I identified 15 groups associated with Coma, and six with A2626. In the A2626 volume, there are two other nearby spectral over-densities in which I identified substructure: six in Abell 2637, and four associated with the over-density referred to as HW1.

All of the Coma substructures were located within R_{200} due to the fact that the cluster data set did not extend beyond $\sim 1.2 R_{200}$. The substructures associated with A2626 on the other hand, were mostly located between R_{200} and $\sim 1.9 R_{200}$ (the outer limit of the A2626 catalogue). Only two of the six A2626 substructures were located within the R_{200} . Both clusters had substructures at their centres that were indicative of groups being accreted. In both cases this is also supported by the morphology of the X-ray emission at the cluster cores.

6.1.2 Quantifying the cluster HI content

The processes effecting the evolution of the cluster galaxies have been shown to occur in different parts of the cluster and affect galaxies of different masses over different timescales (e.g. Oman & Hudson, 2016). Thus investigating how the HI content of the cluster galaxies varies across the cluster, and compares to the expected HI content given the galaxy size, can provide insight into the timescales over which the gas is removed from the galaxies and where the gas removal starts to take place.

In the first part of Chapter 2, we investigated the HI gas fraction–stellar mass scaling relation. This relation is well established for field galaxies (e.g. Fabello et al., 2011; Brown et al., 2015; Healy et al., 2019). The comparison between the average HI gas fractions measured from the stacked profiles of the Coma galaxies to the average values for field galaxies was the first indication in this work that the Coma galaxies are very gas-poor. Coma has long been known to be HI deficient (Solanes et al., 2001; Gavazzi et al., 2006, e.g.), but those studies had targeted galaxies based on optical properties which indicated detectable HI. In Chapter 2, we included every galaxy in the Westerbork Coma Survey footprint that had an optical redshift, and using the HI stacking technique to probe the average HI content, we found that in galaxies that were not directly detected in HI, there was no detectable emission in the stacked spectra. From the stacked spectra we could measure upper limits on the average HI content, which implied that Coma galaxies were at least two orders of magnitude more deficient than the field counterparts. This bimodality in gas content seen between the galaxies directly detected in HI and galaxies not directly detected in HI was evident at all radii, which we suggested was due to an extremely rapid gas removal mechanism. Even galaxies outside the R_{200} showed high HI deficiency values (although many of these were lower limits), suggesting that this gas removal mechanism is effective on the cluster outskirts.

A2626 ($\sigma_{A2626} = 660 \text{ km s}^{-1}$) is a much smaller galaxy cluster than Coma ($\sigma_{Coma} = 1080 \text{ km s}^{-1}$),

with roughly a third the number of galaxies that Coma harbours. The MeerKAT HI data on A2626 presented in Chapter 3 has the same HI mass sensitivity as the HI data for the Coma cluster used in Chapter 2. In exploring the average HI deficiency of the cluster as a function of radius, A2626 has the same radial increase in HI deficiency closer to the center of the cluster as what is seen in other galaxy clusters (e.g. Solanes et al., 2001). What was interesting in the comparison between A2626 and Coma was that at the same relative radii ($0.5 < r/R_{200} < 1$) the Coma galaxies were so deficient that only the upper limits on the HI content could be measured, whereas for A2626 I was able to actually measure the average HI deficiency. The HI mass sensitivity of the two HI surveys covering Coma and A2626 are comparable ($\sim 4 \times 10^8 M_{\odot}$), which made it possible to draw some conclusion from the comparisons between the two studies, despite the many upper limits on the HI content of the Coma galaxies. In both clusters, only limits were measured on the average HI deficiencies of the galaxies within the core of the cluster ($r < 0.5R_{200}$). For radii in the range $0.5 < r/R_{200} < 1$, there were still only lower limits on the average HI deficiencies for the Coma galaxies, however for the A2626 non-detections, the measured average HI deficiencies show the A2626 galaxies to be strongly increasing in deficiency with decreasing radius to the cluster centre.

Stacking non-detections in the Coma galaxies inside R_{200} did not yield any detections in the stacked spectra, but the opposite is true for A2626 implying that the A2626 galaxies do not have the same binary distribution as Coma in the HI content. Coma is a more massive cluster than A2626, but Solanes et al. (2001) showed that there was no correlation between any of the measures of the size of a cluster and the fraction of HI deficient spirals. The galaxies in Coma that are detected in HI exhibit comparable HI deficiencies to the A2626 detections at all radii, so if the process affecting the Coma non-detections is not linked to the size of the cluster, it must occur on very rapid timescales if the same process were to affect the A2626 non-detections given that the difference in lookback-time between the two clusters is only ~ 0.5 Gyr. In both clusters, the non-detections are predominantly the red early type galaxies. Schawinski et al. (2014) showed that quenching of early-type galaxies could occur on timescales of $\tau_q < 250$ Myr, but they proposed the most likely quenching trigger process is a merger event which in the lower density region of the cluster outskirts is not very probable.

6.1.3 Local vs global environment

One of the goals of this work was to determine if there is a preference for gas removal in the local environment as defined by the substructure, or the global environment defined by the cluster as a whole. The galaxies in Coma were too HI deficient to make any definitive conclusions on this. The A2626 galaxies could be measured out to much further radii than the Coma galaxies which provides a larger volume that is not part of the virialized inner region of the cluster, in which to compare the HI content of the cluster galaxies in groups and cluster galaxies not in groups.

In Chapter 5, I use the average M_{HI}/L_r ratios to probe differences in the HI content between group galaxies and non-group galaxies inside A2626. While the average M_{HI}/L_r ratio can be affected by differences in the underlying luminosity distribution of the galaxies, I account for this using a two-sample KS test to determine statistically if the two samples are drawn from the same distribution; there are some caveats to this in that some luminosity (L_r) bins have very few sources. Initial results considering galaxies of all morphologies and luminosities show no significant differences between the samples inside and outside identified substructures. Using simulations, low mass galaxies have been shown to have a longer delay in the onset of quenching than high mass galaxies (Oman & Hudson, 2016), so I investigated how the average M_{HI}/L_r ratios are different for faint galaxies (as a proxy for low mass) in groups and not in groups as a function of clustocentric radius.

One of the big questions surrounding the morphology-density relation, is how S0 galaxies are formed. One of the common theories is that they are late-type galaxies that have been gas depleted

and subsequently quenched. Late-type galaxies, unaffected by external environmental processes have been shown to quench over very long timescales, $\tau_q > 2.5$ Gyr (Schawinski et al., 2014). However, the cluster environment in general is extremely effective at processing galaxies, such that star formation is almost always quenched by the time of peri-centric passage (Oman et al., 2013). For a cluster the size of A2626, this equates to shorter timescales than $t_{cross} \sim 2.5$ Gyr. Thus in the last part of Chapter 5, I investigated the differences in the average $M_{H\text{I}}/L_r$ ratios for late-type galaxies in groups and not in groups. Despite the low number counts in some L_r bins, an intriguing picture seems to emerge: Late-type galaxies in groups have constant average $M_{H\text{I}}/L_r$ ratios which only decrease in the innermost regions of the cluster ($r < 0.5R_{200}$); the galaxies not in groups have systematically lower average $M_{H\text{I}}/L_r$ also at a constant level. This might suggest that the group environment could possibly play a role in preventing the removal of gas from late-type galaxies until the group is very close to peri-centric passage.

6.2 Future Work

Upcoming surveys for both wide-area optical spectroscopy, and wide-area blind H I surveys of galaxy clusters will provide the data to enable future analysis of more clusters of different masses and at different redshifts.

6.2.1 Ongoing work with Abell 2626

One of the goals of the work in this thesis was to identify possible indications of pre-processing in galaxies prior to their arrival in the cluster environment. The existing MeerKAT pointing on A2626 only covered galaxies inside $2R_{200}$. In order to investigate possible pre-processing of cluster galaxies, one needs to study galaxies and substructure/group environment they may be located in, at larger radii from the cluster centre.

A further MeerKAT proposal (PI T. Deb) to observe 4 pointings on the south east side of A2626 has recently been accepted. This will enable us to observe H I out to $\sim 3R_{200}$ with the higher spectral resolution mode (32K, $\sim 7 \text{ km s}^{-1}$ velocity channels) of the telescope, which will enable us to study the galaxies that have only recently entered the cluster environment. Here, I assume that the cluster environment extends out to $r/R_{200} \sim 4.75$ (Rines & Diaferio, 2006; Jaffé et al., 2013).

However, further investigations of substructures at larger radii in the cluster environment will depend on obtaining more spectroscopic redshifts for galaxies in the cluster outskirts. The WEAVE Wide-field Cluster Survey (Jin et al., in prep), plans to spectroscopically map a selection of clusters in the nearby Universe out to $5R_{200}$, including A2626.

The combination of the WEAVE spectroscopy, and the MeerKAT H I data, will enable the identification of groups that are just starting to come into contact with the cluster. Using H I stacking, we will be able to probe the average H I content and H I deficiencies of galaxies that have only been influenced by the group environment. These results will be crucial to understanding how pre-processing affects the quenching and the morphological transformation of galaxies that underpins the morphology-density relation.

6.2.2 H I surveys of galaxy clusters

I have mentioned numerous times throughout different chapters of this thesis, the need for more wide-area blind H I surveys. The current scarcity of such data is about to become a thing of the past, with planned and ongoing surveys using the SKA Pathfinder and Precursor telescopes.

The MeerKAT Fornax Survey (PI: P. Serra), one of the large survey projects on MeerKAT will map the Fornax cluster and its infall region in H I. The survey is also supported by extensive multi-wavelength imaging (e.g. Venhola et al., 2017, 2018; Zabel et al., 2019). Early results from the MeerKAT Fornax Cluster Survey have already shown newly detected H I debris around NGC 1316, possibly after a merger event (Serra et al., 2019), as well as evidence of pre-processing in Fornax A group (Kleiner et al., 2021). As the most nearby cluster, and one that is actively accreting galaxy groups that are still forming, this body of work will provide important insights into environment-driven galaxy evolution.

Other upcoming and ongoing blind H I surveys of galaxy clusters include the MeerKAT Cluster Legacy Survey which has targeted some 100+ galaxy clusters. The Widefield ASKAP L-band Legacy Allsky Blind survey (WALLABY Koribalski et al., 2020) is expected to cover 20 galaxy clusters in the southern skies, one of which is the Hydra cluster for which commissioning data already exist.

6.2.3 H I deficiency scaling relation

The H I deficiency parameter ($\text{DEF}_{\text{H I}}$) is an effective way to identify whether galaxies contain more or less H I than expected. $\text{DEF}_{\text{H I}}$ is the logarithm of the ratio of the expected H I mass and the measured H I mass. The expected H I mass is usually calculated from a scaling relation based on an optical diameter or a photometric magnitude. Early studies (e.g. Haynes et al., 1984; Solanes et al., 2001) calibrated the scaling relations based on visually classified morphologies, which resulted in different scaling relations for the different morphological classes. This is reasonable as isolated galaxies of different morphological classes are known to contain different amounts of H I relative to their mass (e.g. Swaters et al., 2002).

There are two main issues with relying on visually identifying the morphological class of a galaxy: 1 – visual classifications can be subjective, especially in cases where a galaxy borders between two different classifications, and edge on galaxies can obscure the features used to classify the galaxy; 2 – the visual classification of galaxies varies with image resolution. Given the subjective nature of the classification, it is very difficult to understand the uncertainties built into the deficiency values, particularly when comparing to published works.

Morphological type independent scaling relations are essential with the upcoming large H I surveys expecting to provide H I measurements for thousands of galaxies. Such relations based on galaxy photometry (Denes et al., 2014) and stellar mass (Bok et al., 2020) already exist. However, the existing scaling relations based on magnitude or optical diameters have a flaw: it is unclear what types of magnitudes are used (aperture or total), and in measuring the optical diameters, very few (if any) take inclination into account. While the stellar mass relations may have less uncertainty in how the measured galaxy quantity (in this case the stellar mass) is calculated, reliable stellar mass measurements are only available for limited samples of galaxies.

Given the usefulness of the H I deficiency parameter in identifying galaxies that deviate from the expected relations, and in light of the upcoming increase in available data, it is important to develop a set of scaling relations that are based on publicly accessible data, and account for the differences in how the galaxy properties were measured.

6.2.4 Towards the future with the SKA

Considering the longer term, the SKA will enable higher sensitivity and higher resolution observations of the H I in galaxies than is currently available. Higher sensitivity observations will allow astronomers to observe the H I in cluster galaxies at higher redshifts than is currently possible without hundreds of hours of observing time. Studying the H I stripping mechanisms affecting late-type

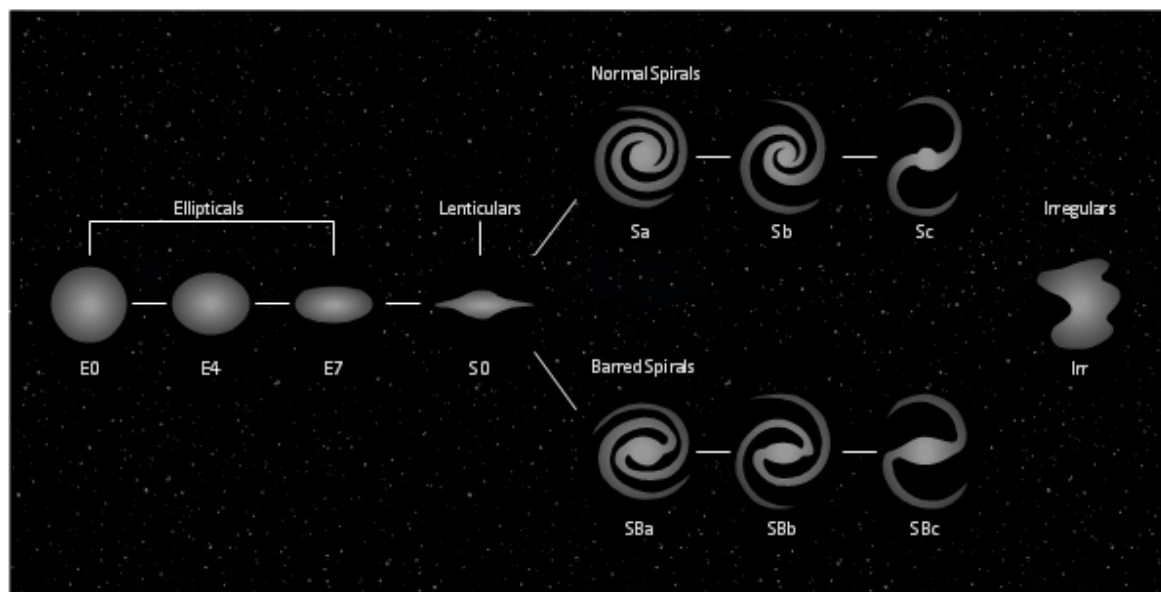
galaxies in clusters over a range of cosmic time, may help to answer open questions such as why the fraction of S0 galaxies in clusters increases from $z \gtrsim 0.5$ to $z \sim 0$. There is a tight correlation at $z = 0$ between the HI mass and HI diameter of a galaxy (Wang et al., 2016), thus the ability to resolve the HI disk of a galaxy is dependent on its mass. With the high resolution (particularly in the local Universe), it will be possible to identify and characterise the HI morphologies of much lower mass galaxies than is currently possible. The morphology of the HI disk provides important information about the external processes acting on the galaxy. Thus, it is expected that with the increased sensitivity and resolution of the SKA, astronomers studying the evolutionary effects of the cluster environment, will be able to investigate how the different gas removal mechanisms (e.g. ram-pressure stripping, harassment, starvation) affect galaxies over a large range of HI masses and deficiencies.

References

- Bok J., Skelton R. E., Cluver M. E., Jarrett T. H., Jones M. G., Verdes-Montenegro L., 2020, *Monthly Notices of the Royal Astronomical Society*, 499, 3193
- Brown T., Catinella B., Cortese L., Kilborn V., Haynes M. P., Giovanelli R., 2015, *Monthly Notices of the Royal Astronomical Society*, 452, 2479
- Cava A., et al., 2009, *Astronomy and Astrophysics*, 495, 707
- Denes H., Kilborn V. A., Koribalski B. S., 2014, *Monthly Notices of the Royal Astronomical Society*, 444, 667
- Dressler A., Shectman S. A., 1988, *The Astronomical Journal*, 95, 985
- Fabello S., Catinella B., Giovanelli R., Kauffmann G., Haynes M. P., Heckman T. M., Schiminovich D., 2011, *Monthly Notices of the Royal Astronomical Society*, 411, 993
- Gavazzi G., O’Neil K., Boselli A., van Driel W., 2006, *Astronomy and Astrophysics*, 449, 929
- Gunn J. E., Gott J. Richard I., 1972, *The Astrophysical Journal*, 176, 1
- Haynes M. P., Giovanelli R., Chincarini G. L., 1984, *Annual Review of Astronomy and Astrophysics*, 22, 445
- Healy J., Blyth S.-L., Elson E., van Driel W., Butcher Z., Schneider S., Lehnert M. D., Minchin R., 2019, *Monthly Notices of the Royal Astronomical Society*, 487, 4901
- Jaffé Y. L., Poggianti B. M., Verheijen M. A. W., Deshev B. Z., van Gorkom J. H., 2013, *Monthly Notices of the Royal Astronomical Society*, 431, 2111
- Kleiner D., et al., 2021
- Koribalski B. S., et al., 2020, *Astrophysics and Space Science*, 365, 118
- Larson R. B., Tinsley B. M., Caldwell C. N., 1980, *The Astrophysical Journal*, 237, 692
- Moore B., Katz N., Lake G., Dressler A., Oemler A., 1996, *Nature*, 379, 613
- Oman K. A., Hudson M. J., 2016, *Monthly Notices of the Royal Astronomical Society*, 463, 3083
- Oman K. A., Hudson M. J., Behroozi P. S., 2013, *Monthly Notices of the Royal Astronomical Society*, 431, 2307
- Rines K., Diaferio A., 2006, *The Astronomical Journal*, 132, 1275

- Schawinski K., et al., 2014, *Monthly Notices of the Royal Astronomical Society*, 440, 889
- Serra P., et al., 2019, *Astronomy & Astrophysics*
- Solanes J. M., Manrique A., García-Gómez C., González-Casado G., Giovanelli R., Haynes M. P., 2001, *The Astrophysical Journal*, 548, 97
- Swaters R. A., van Albada T. S., van der Hulst J. M., Sancisi R., 2002, *Astronomy and Astrophysics*, 390, 829
- Venhola A., et al., 2017, *Astronomy and Astrophysics*, 608
- Venhola A., et al., 2018, *Astronomy and Astrophysics*, 620, 165
- Vulcani B., et al., 2018, *Monthly Notices of the Royal Astronomical Society*, 480, 3152
- Wang J., Koribalski B. S., Serra P., van der Hulst T., Roychowdhury S., Kamphuis P., Chengalur J. N., 2016, *Monthly Notices of the Royal Astronomical Society*, 460, 2143
- Zabel N., et al., 2019, *Monthly Notices of the Royal Astronomical Society*, 483, 2251

Samenvatting voor niet-deskundigen



Figuur 1: De Hubble Stenvork toont de karakteristieke morfologiën van elliptische, spiraalvormige en onregelmatige sterrenstelsels. De sterrenstelsels in dit diagram bevatten ook de meer specifieke classificaties die door Gérard de Vaucouleurs zijn toegevoegd. *Figuur credits:* <https://conceptdraw.com/a2353c3/preview>

Al voordat sterrenstelsels werden geïdentificeerd als extragalactische objecten, hebben astronomen zich ingespannen om sterrenstelsels te classificeren op basis van hun vorm en kleur. De eerste classificatieschema's verdeelden de sterrenstelsels (of nevels zoals ze vóór de jaren twintig bekend waren) in drie hoofdgroepen: elliptisch, spiraalvormig of onregelmatig. Het classificatieschema evolueerde naar wat nu bekend staat als de "Hubble Tuning Fork" of "Hubble Sequence" die wordt getoond in Figuur 1. Men dacht dat sterrenstelsels van links naar rechts in het classificatieschema evolueerden, maar het is nu algemeen bekend dat sterrenstelsels juist van rechts naar links evolueren. Aangezien de evolutie van sterrenstelsels miljarden jaren duurt, levert het bestuderen van sterrenstelsels van verschillende typen een momentopname van de verschillende evolutionaire stadia.

Het licht dat door een sterrenstelsel wordt uitgezonden over het hele elektromagnetische spectrum (zie Figuur 2) is het resultaat van alle processen in een sterrenstelsel. Door de verschillende soorten elektromagnetische straling te bestuderen, kunnen we inzicht krijgen in de evolutionaire toestand van een sterrenstelsel en in de evolutionaire processen die het kunnen beïnvloeden. In dit proefschrift gebruik ik radiogegevens die ons vertellen over het koude gasgehalte van sterrenstelsels, infraroodgegevens die ons vertellen over de massa van alle sterren in een sterrenstelsel, evenals de snelheid waarmee die sterren worden gevormd, en optische gegevens waaruit ik de optische kleur van een sterrenstelsel bepaal die informatie geeft over de gemiddelde leeftijd van de sterren in een sterrenstelsel, en dus een maat voor de leeftijd van een sterrenstelsel.

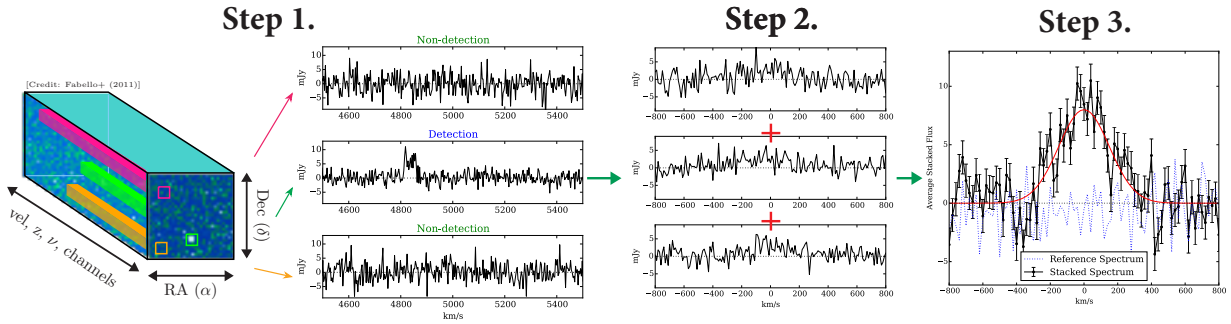


Figuur 2: Meerdere golflengten van het Whirlpoolstelsel (M51). Elk paneel toont het stelsel zoals waargenomen in een andere golflengte van het elektromagnetische spectrum. *Figuur credits:* <https://ecuip.lib.uchicago.edu/multiwavelength-astronomy/astrophysics/05.html>

Sterrenstelsels bewegen constant ten opzichte van de aarde (en de Melkweg). Het licht dat we van andere sterrenstelsels waarnemen wordt verschoven ten opzichte van de frequentie waarmee het wordt uitgezonden. Door naar het spectrum van een bewegende bron te kijken, kunnen we bepalen hoeveel bepaalde emissie- en absorptielijnkenmerken in golflengte of frequentie zijn verschoven ten opzichte van de rest-frame-waarden. De hoeveelheid waarmee de waargenomen frequentie wordt verschoven, staat bekend als de “roodverschuiving”. De roodverschuiving kan te maken hebben met hoe snel een sterrenstelsel van ons weg beweegt, en dus de afstand tot ons. In dit proefschrift worden de roodverschuivingen voornamelijk gemeten in het optische spectrum van de sterrenstelsels, maar in sommige gevallen werd de roodverschuiving gemeten in het radiospectrum.

Een manier om na te gaan hoe een sterrenstelsel verandert of evolueert, is door de stervorming te bestuderen. Terwijl sterrenstelsels sterren blijven vormen, neemt de massa van de sterrenstelsels toe. Op het moment dat de stervorming stopt worden er geen nieuwe sterren gevormd en, men denkt, dat dan de kleur en vorm van sterrenstelsels roder en elliptischer worden. Om stervorming aan de gang te houden hebben sterrenstelsels een reservoir met koud gas nodig waaruit sterren kunnen ontstaan. In dit proefschrift kijk ik naar het koude neutrale gasgehalte van sterrenstelsels en in het bijzonder naar het gehalte van het neutrale atomaire waterstofgas (H I). H I is niet alleen belangrijk voor de voortgaande stervorming, maar kan ook een belangrijke indicator zijn voor de manier waarop de gastoevoer naar een sterrenstelsel wordt afgesloten, waardoor de stervorming wordt gestopt. Het is algemeen bekend dat de H I schijf van sterrenstelsels zich buiten de stellaire schijf uitstrekt, met soms wel twee keer de straal van de stellaire schijf, waardoor deze gemakkelijk vatbaar is voor externe invloeden zoals interacties met andere sterrenstelsels of het intra-cluster- of intra-groepsmedium van clusters van sterrenstelsels of groepen.

Men heeft aangetoond dat de evolutie van een sterrenstelsel wordt beïnvloed door de omgeving waarin het zich bevindt. Geobserveerde trends zoals de relatie tussen morfologie en dichtheid, die stelt dat elliptische sterrenstelsels — sterrenstelsels met een meer geëvolueerde stellaire popu-



Figuur 3: Diagram depicting the HI stacking method

latie die meestal ook geen nieuwe sterren meer vormen — de dominante soort sterrenstelsels zijn in omgevingen met een hoge dichtheid zoals sterrenstelsels en clusters. Spiraalstelsels, die vaak nog actief bezig zijn sterren te vormen en een jongere stellaire populatie bevatten, zijn de dominante soort sterrenstelsels in omgevingen met een lagere dichtheid. In dit proefschrift bestudeer ik de sterrenstelsels in twee verschillende clusters van sterrenstelsels en identificeer ik substructuren binnen de clusters om te begrijpen hoe de lokale (substructuur) omgeving in vergelijking met de globale (cluster) omgeving de HI inhoud van de samenstellende sterrenstelsels beïnvloedt om licht te werpen op de fysieke processen die aanleiding geven tot de morfologie-dichtheidsrelatie.

HI middeling

HI middeling is een techniek die veel gebruikt wordt in dit proefschrift. Om de techniek te gebruiken heeft men een catalogus nodig met de optische ruimtelijke positie en roodverschuiving van elk sterrenstelsel. Met behulp van de optische ruimtelijke positie van een sterrenstelsel kan men het globale HI spectrum van het stelsel extraheren uit de HI datakubus (stap 1 van Figuur 3). De gehele spectra worden uitgelijnd in het referentiekader van elk sterrenstelsel met behulp van de optische roodverschuiving (stap 2 van Figuur 3). De uitgelijnde spectra worden vervolgens bij elkaar opgeteld om een gemiddeld spectrum te creëren met een hogere gevoeligheid dan de onderlinge spectra (stap 3 van Figuur 3). Uit het gemiddelde spectrum kan de gemiddelde HI-inhoud van een sterrenstelsel worden gemeten. Dit maakt het mogelijk om andere interessante parameters te berekenen zoals de HI-gasfractie en HI-deficiëntie.

Dit proefschrift

Coma en Abell 2626 (A2626), de twee clusters van sterrenstelsels die in dit proefschrift zijn bestudeerd, gaven beiden unieke mogelijkheden om de invloed van de lokale en globale omgeving op de hoeveelheid HI in de clusterstelsels te bestuderen. Het Coma-cluster, gelegen op een afstand van ~ 100 Mpc (~ 317 miljoen lichtjaar) in het sterrenbeeld Coma Berenices, is het onderwerp geweest van een reeks eerdere studies van clusters van sterrenstelsels en als gevolg bestaat er een schat aan multi-golflengtegegevens voor het cluster. A2626 daarentegen is niet zo goed bestudeerd als het Coma-cluster. A2626 is te vinden in het sterrenbeeld Pegasus op een afstand van ~ 250 Mpc (~ 740 miljoen lichtjaar). Eerdere studies van zowel Coma als A2626 hebben aangetoond dat beide clusters substructuur bevatten, als gevolg van groepen die op het cluster zijn geaccrueerd. Echter was de identificatie van substructuur onvolledig door de onvolledige observaties van populaties van sterrenstelsel clusters (met name in het geval van A2626).

In Hoofdstuk 2 heb ik een nieuwe inzicht gegeven in het Coma-cluster: met behulp van wide-area blinde metingen¹ van de HI in de clusterstelsels. Met directe HI detecties voor slechts 39 van

¹blind in deze context betekent dat we ons niet op specifieke sterrenstelsels hebben gericht

~ 850 sterrenstelsels, was het nodig om HI middeling te gebruiken om te proberen het gemiddelde HI te meten van de sterrenstelsels waarvoor dit niet direct meetbaar was. Ondanks de verbeterde gevoeligheid van de gemiddelde spectra, werd er geen signaal gedetecteerd in de gemiddelde spectra, wat leidde tot de conclusie dat de Coma-clusterstelsels zeer weinig HI bevatten en dat er een extreem snel en efficiënt proces moet zijn dat het HI gas verwijderd uit de clusterstelsels. Bewijs van een vergelijkbare trend werd niet waargenomen voor de sterrenstelsels in A2626. Met behulp van nieuwe MeerKAT HI waarnemingen van A2626 (Hoofdstuk 3) waarin zo'n 80 van ~ 350 clusterstelsels direct werden gedetecteerd in HI, voerde ik een soortgelijk middelingsexperiment uit op de A2626 sterrenstelsels als bij Coma, en was in staat om HI emissie te detecteren in de gemiddelde spectra in alle regionen behalve de binnenste regio's van het cluster (Hoofdstuk 5).

Om substructuur toe te wijden aan een cluster is er een volledige roodverschuivingscatalogus van de clusterstelsels nodig. Voor beide clusters werden roodverschuivingswaarnemingsobservaties ondernomen om de bestaande clusterroodverschuivingscatalogi aan te vullen (Hoofdstukken 2 en 4). In Coma werden vijftien substructuren geïdentificeerd en zes in A2626. De middelinganalyse van de Coma-clusterstelsels in substructuur in vergelijking met niet-substructuurstelsels was niet overtuigend. Daartegen suggereert de analyse in Hoofdstuk 5 echter dat de lokale substructuuromgeving in A2626 een rol kan spelen bij het vertragen van de gasverwijdering door de interactie met de clusteromgeving voor spiraalstelsels.

Het werk in dit proefschrift kan worden gezien als pilotstudies voor toekomstige projecten waarbij gebruik wordt gemaakt van gegevens van de nieuwe Square Kilometre Array Precursor en Pathfinder Telescopes. Ik heb de effectiviteit laten zien van technieken zoals HI middeling om de HI inhoud van sterrenstelsels die onder de detectiedrempel vallen te bestuderen. De nieuwe spectroscopie en grootschalige structuuranalyse in Hoofdstuk 4 benadrukten de behoefte aan optische breedveldspectroscopie voor de identificatie en analyse van clusters van sterrenstelsels en de grootschalige structuur waarin ze zijn ingebed. Dit soort studies zullen in de nabije toekomst mogelijk worden met de komende spectroscopie-onderzoeken met behulp van de WEAVE multi-object spectrograaf op de William Herschel Telescope.

Summary for non-experts

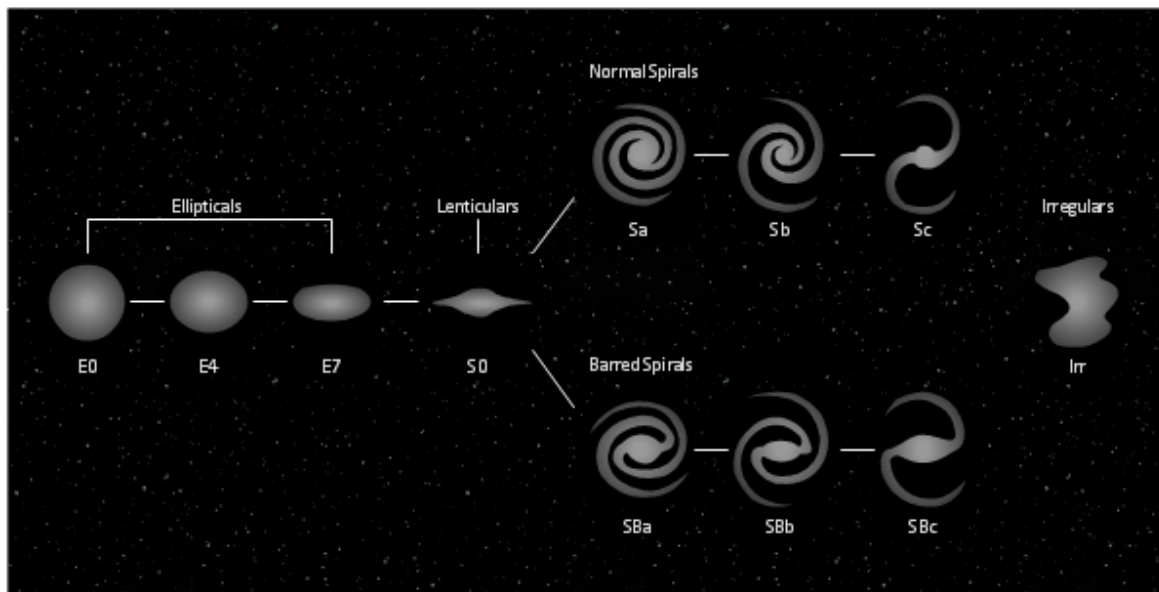


Figure 1: The Hubble Tuning Fork showing the characteristic shapes of elliptical, spiral, and irregular galaxies. The galaxies in this diagram also include the more specific classifications added by Gérard de Vaucouleurs. Image credit: <https://conceptdraw.com/a2353c3/preview>

Even before galaxies were identified as extragalactic objects, astronomers have devoted efforts to classifying galaxies by their shape and colour. The early classification schemes separated the galaxies (or nebulae as they were known prior to the 1920s) into three main groups: elliptical, spiral, or irregular. The classification scheme evolved into what is now known as the “Hubble Tuning Fork” or “Hubble Sequence” which is shown in Figure 1. It was thought that galaxies evolved from left to right along the sequence, it is now generally understood that galaxies evolve from right to left along the sequence. Since the evolution of galaxies takes billions of years, studying galaxies of different types provides a snapshot of the different evolutionary stages.

The light emitted across the electromagnetic spectrum (see Figure 2) by a galaxy is a result of all the ongoing processes within the galaxy. By studying the different types of electromagnetic radiation, we can gain an understanding of the evolutionary state of the galaxy, and what evolutionary processes may be affecting it. In this thesis, I use radio data which tells us about the cold gas content of the galaxies, infrared data which tells us about the mass of all the stars contained within the galaxy, as well as the rate at which those stars are formed, and optical data from which I determine the optical colour of the galaxy which provides information on the average age of the stars contained within the galaxy, and thus a measure of the galaxy age.

Galaxies are constantly moving relative to the Earth (and our Galaxy), thus the light we observe from other galaxies is shifted relative to the frequency at which it is emitted. By looking at the

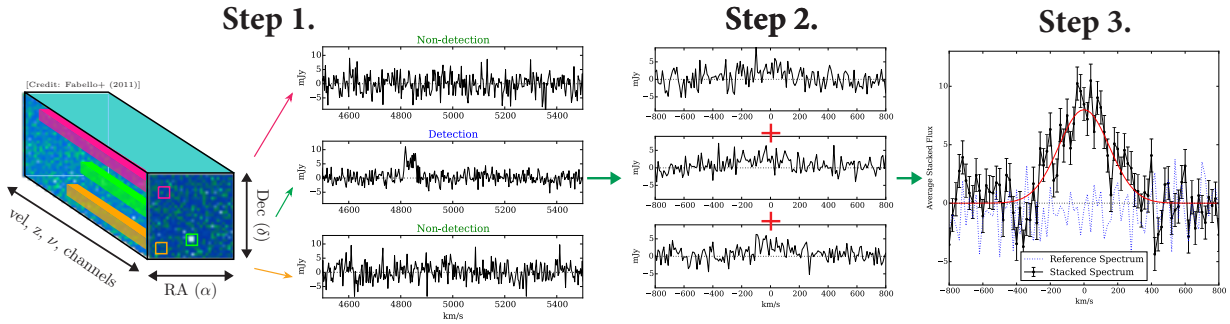


Figure 2: Multi-wavelength view of the Whirlpool galaxy (M51). Each panel shows the galaxy as observed in a different wavelength of the electromagnetic spectrum. Image credit: <https://ecuip.lib.uchicago.edu/multiwavelength-astronomy/astrophysics/05.html>

spectrum of a moving source, we can determine by how much certain emission and absorption line features are shifted in wavelength or frequency from the rest-frame values. The amount by which the observed frequency is shifted is known as the “redshift”. The redshift can be related to how fast the galaxy is moving away from us, and thus its distance from us. In this thesis, the redshifts are primarily measured from the optical spectrum of the galaxies, but in some cases, the redshift was measured from the radio spectrum.

One way to trace how a galaxy is changing or evolving, is to study the star formation. As galaxies continue to form stars the mass of the galaxies grow, when star formation ceases, no new stars form, and the colour and shape of the galaxy are thought to come redder and more elliptical. For ongoing star formation, the galaxy needs to have a reservoir of cold gas from which stars can form. In this thesis, I look at the cold neutral gas content of galaxies, in particular the neutral atomic hydrogen (H I) gas. H I is not only important for ongoing star formation, but can also be an important tracer of how the gas supply to a galaxy is shutoff, thus quenching star formation. The H I galaxy disk is known to extend beyond the stellar disk, sometimes as much as twice the stellar disk radius which makes it easily susceptible to external influences such as interactions with other galaxies or the intra-cluster or intra-group medium of galaxy clusters or groups.

The environment in which a galaxy resides has been shown to have an impact on how the galaxy evolves. Observed trends such as the Morphology-Density relation, which states elliptical galaxies, galaxies with a more evolved stellar population that are also usually no longer star forming, are the dominant galaxy type in dense environments such as galaxy groups and clusters. Spiral galaxies, which tend to be actively star-forming, and contain a younger stellar population are the dominant galaxy type in more low-density environments. In this thesis, I study the galaxies in two different galaxy clusters and identify substructures within the clusters to understand how the local (substructure) environment compared to the global (cluster) environment impacts the H I content of the constituent galaxies in order to shed light on the physical processes that give rise to the Morphology-Density relation.



Figur 3: Diagram depicting the HI stacking method

HI Stacking

HI stacking is a technique that is used frequently in this thesis. To use the technique, one needs to have catalogue containing the optical spatial position and redshift of each galaxy in the sample. Using the optical spatial position of the galaxy, one can extract the global HI spectrum of the galaxy from the HI data cube (step 1 of Figure 3). The global spectra are aligned in the reference frame of each galaxy using the optical redshift (step 2 of Figure 3). The aligned spectra are then co-added to create an average spectrum with higher sensitivity than the input spectra (step 3 of Figure 3). From the stacked spectrum, one can measure the average HI content of the galaxy population under consideration, which enables the calculation of other interesting parameters such as the HI gas fraction and HI deficiency.

This thesis

The two galaxy clusters, Coma and Abell 2626 (A2626), studied in this thesis provided unique opportunities to study how the local and global environment affected the HI content of the cluster galaxies. The Coma cluster, located at a distance of ~ 100 Mpc (~ 317 million lightyears) in the constellation of the Coma Berenices, has been the subject of many previous studies of galaxy clusters and as such a wealth of multi-wavelength data exists for the cluster. A2626, on the other hand, has not been as well studied as the Coma cluster. A2626 can be found in the Pegasus constellation at a distance of ~ 250 Mpc (~ 740 million lightyears). Previous studies of both Coma and A2626 have shown both clusters to contain some substructure, imprints of groups that have been accreted onto the cluster, however due to incomplete censuses of the cluster galaxy populations (particularly in the case of A2626), the substructure identification has been incomplete.

In Chapter 2, I presented a new view of the Coma cluster: using a wide-area blind² survey of the HI in the cluster galaxies. With direct HI detections for only 39 of ~ 850 galaxies, it was necessary to use HI stacking to attempt to measure the average HI of the galaxies not detected in HI. Despite the improved sensitivity of the stacked spectra, no signal was detected in the stacked spectra which led to the conclusion that the Coma cluster galaxies are highly HI deficient, and that there must be an extremely rapid and efficient process that is removing the HI gas from the cluster galaxies. Evidence of a similar trend was not observed for the galaxies in A2626. Using new MeerKAT HI observations of A2626 (Chapter 3) in which some 80 of ~ 350 cluster galaxies were directly detected in HI, I performed a similar stacking experiment on the A2626 galaxies as with Coma, and was able to detect HI emission in the stacked spectra at all radii except the inner-most regions of the cluster (Chapter 5).

In order to identify substructure with a cluster, one needs a complete redshift catalogue of the

²blind in this context means that we did not target specific galaxies

cluster galaxies. For both clusters, redshift observing campaigns were undertaken in order to supplement the existing the cluster redshift catalogues (Chapters 2 and 4). Fifteen substructures were identified in Coma, and six associated with A2626. The stacking analysis of Coma cluster galaxies in substructure compared to non-substructure galaxies was inconclusive. However, in A2626, the analysis in Chapter 5 suggests that the local substructure environment may play a role in slowing the gas removal by the interaction with the cluster environment for spiral galaxies.

The work in this thesis can be viewed as pilot studies for upcoming projects using data from the new Square Kilometre Array Precursor and Pathfinder Telescopes. I have shown the effectiveness of techniques such as HI stacking to study the HI content of galaxies that fall below the detection threshold. The new spectroscopy and large scale structure analysis in Chapter 4 highlighted the need for wide-field optical spectroscopy for the identification and analysis of galaxy clusters and the large scale structure in which they are embedded. These kind of studies will become possible in the near future with the upcoming spectroscopy surveys using the WEAVE multi-object spectrograph on the William Hershel Telescope.

Acknowledgements

The last 4 (and a bit) years have been quite an experience, more so than I expected when I started. Living on two different continents and uprooting my life every year or so was tough, but was made so much easier with the incredible support I have had along the way. Support from my family and friends, my incredible supervisors, as well as the members of the Department of Astronomy at the University of Cape Town and the Kapteyn Astronomical Institute at the University of Groningen.

Sarah, the last six and a bit years have been quite the journey. I am so grateful that I walked into your office in late 2014 with Ed to talk about a Masters project on HI stacking. When you suggested that I look into the possibility of doing a joint phd with Marc at the University of Groningen, I remember thinking that this would be the best of both worlds – I would be able to continue working with you and maintain my scientific connection to Cape Town, but I would also get an opportunity to live and work abroad (which seemed terrifying at the time). I am so grateful and honoured for your all your support, mentorship and teachings over the last six+ years. Thank you for reminding me to always look after myself first, and then to work, and also to include some fun while travelling for workshops/conferences.

Marc, from that first minute when you picked me up from Groningen airport, you have helped me to feel at home in Groningen. The research group and environment you have built at Kapteyn is one of almost family and it has been such an amazing experience to be part of a research group with so many women. You have taught me so much about astronomy, and academic life. I will carry with me your lessons of being critical in how I approach scientific analysis, and to keep attention on the details in all things – research related, and when giving presentations. Thank you to both you and Marti for being so welcoming and for taking us on the adventures around Groningen. These short paragraphs cannot properly convey the depth of my appreciation to both you and Sarah for your patience and guidance, especially in the last few months as things started to ramp up towards this hand-in.

Thijs, I have truly appreciated all your input over the years. Thank you for always being available to help track down some weird quirk in the the data. I have learnt so much from discussions during our group meetings, and conversations in the coffee corner. Renee, thank you for regularly checking in and for your encouragement and support. The observing trip you took us on to Sutherland in my third year was a turning point for me in cementing my interest in observational astronomy.

My journey with using stacking as a method of analysis started in my last year of my undergrad when I was given an opportunity to join the Princeton Undergraduate Summer Research Program in 2013. Those 4 weeks at Princeton gave me a peek behind the curtain of what a grad degree would entail, and what research Astronomy looked like. Thank you to Renée Hložek for your mentorship during that period, and to the rest of the Hope Network for providing such an incredible opportunity.

Behind every successful project, there are a number of people without whom, things would have been much more difficult. A big thank you to the admin team in Cape Town – Roz and Carol, as well as to the team in Groningen – Lucia, Christa, Martina, and Ramona. Thank you to the Computer Group at Kapteyn for keeping things running smoothly, especially to Leon for his quick responses

every time I needed help with my computer system or a hardware upgrade, as well as moving encke every time I appeared and disappeared from Groningen. Also to Siphelo in Cape Town, keeping things going which sometimes seemed like an uphill battle that Eskom was determined not to let you win.

When I planned my activities for 2020, the fourth and final year of my Phd, I did not in my wildest imagination think I was going to be cancelling any and all travel, and be working from my lounge as the world ground to a standstill due to COVID-19. The adjustment to having to have Skype/Zoom meetings with Marc and Sarah was not a difficult one for me as we had been doing this since the start – the side benefit of not all being in the same country. That being said, adjusting to working from home was not easy. I am grateful to my flatmate, Pranav, for his company over the last year as we became eachother's officemate as well as flatmate.

It started as an in-person weekly writing session to keep each other accountable, but quickly evolved into the now twice weekly Discord writing sessions that have become an essential part of my work week. Kelley, and with the occasional chime-in from Leon, your friendship, mentorship, willing ear and general wisdom have been a big part of what has kept me sane through this crazy year. Your vocal support over the last four years has reminded me many times that I can do this. Thank you for also being such a patient listener as I sounded through some of my ideas, and for pointing out the holes in my logic when they inevitably appeared. Your interest in and memories of your time in South Africa, have made me feel a little less homesick at times when the possibility of a visit home seemed so far off.

Miriam, Naomi, Jamie, Kerry, and Lauren. Wow, it has been such a privilege to have started and walked (most of) this post grad journey with you ladies. I have a photo of the 5 of us at Jamie's show above my desk monitor reminding me every day of your friendship and the memories of our shared offices and time together at UCT. Though we are scattered all over the world these days, I am grateful for our time in Cape Town together (and various adventures abroad), particularly those Friday lunches down at the pub.

The OG office 178 team: Helmer, Sampath, Nika – it was truly a privilege to share an office with you three. To have our camaraderie and friendship in the office extend to outside of work hours made coming to work such a pleasure. I thoroughly enjoyed all our office dinners. Hyoyin and Eduardo, thank you for letting me crash the 178 team when I came back to Groningen. Hyoyin, thank you for always being up for a game of tennis or squash (when it was allowed), such sessions kept me from going insane over this crazy year and have kept me fit. Helmer, thank you for translating my summary into Dutch! To my new officemates, Teymoor and Bayron, I am sorry we didn't get to spend more time in the office together before lockdown kicked us out, but I did enjoy the short time we were all together.

The 4.34 team in Cape Town, Khine, Narges, Hannes, Sibusiso, Lennart. I have fond memories of painting the walls, mid-afternoon exercise sessions and trying not to disturb the napping officemates as I wandered in and out of the office in the afternoons. Thank you for your friendship and welcoming me into the office during my final year in Cape Town.

Thank you to the regular Saturday coffee crew: Jonas (the ring leader), Anne, Hyoyin, and Renate. Seeing you guys every week was something I looked forward to. I am glad we were able to keep seeing eachother safely in the park while everything else was locked down. To the rest of the Kapteyn crew (both past and present), you all know who you are – thank you for your friendship and support, and thank you for making Kapteyn such a fantastic environment to work in. Simon and Olmo, thank you for trusting me to take care of your cats.

To the Astro cool kids, although not many of us are left in Groningen thank you to you all for welcoming this socially shy South African in to the fold. Kelley, Leon, Hannah, Joe, Jack, Vanessa, Glen, Sarrvesh, Aaron, Will; thanks for the all the Friday evening dinners and (actually any evening) drinks.

Thank you to my Groningen research group, past and present. Avanti, Pooja, Tirna, Anastasia, Mpati, Nadine, Jordan, Nikki, Danielle, Toli, and Kyle, I have learnt so much from all of you over the years.

Steve, Chris, Lauren, Dan, Robyn, and Kyle. Your friendship since those first days in that Maths tutorial in first year (and Physics lab in second year) have been such an important part of my life. Thank you for making sure we all stayed in touch as we moved abroad. Those early Saturday evening Jackbox sessions set us up for playing games online through the pandemic. Our now weekly game evenings are a highlight of my week. Thank you for always keeping me laughing, and making sure I am not in my head too much. Robs, our journey together and friendship started much further back in that Afrikaans class in grade 8. It has been such a privilege to have you by my side together all these years, and I look forward to celebrating with you in the near future when you submit your thesis. Liv and Klyde, I am so grateful for your friendship. Thank you for the regular pics of little Dominic – they always put a smile on my face.

I have been lucky enough to have been part of two incredible departments. UCT Astronomy has been my home for 10 years, and the people who make it the environment that it is, have had a strong role in helping me to become the astronomer and researcher I am today. Tom, your advice to me as I was finishing my masters, to apply for phd programs abroad was part of what set me on the path to Kapteyn. Thank you for all your support and encouragement, and for letting me use all the cool toys in the Viz lab :). Kapteyn welcomed me with open arms when I first arrived in Groningen, and has become my other academic home. Thank you to everyone at Kapteyn, you all contribute to make it one of the best institutes to be a part of. To everyone else at Kapteyn and UCT Astro whom I have not named, your contribution to my journey has not gone unnoticed.

My family, I don't even know where to begin, and these few paltry words are definitely insufficient to truly express my love and gratitude to you all for your support. Mom and Dad, without you two, none of this would have been possible, your unending love and support has carried me when I haven't been able to do it on my own. You two have always taught me to do my best, and not to settle for anything less. Dad, thank you for all the proof-reading you did of this manuscript! Adam and William, you two are the best brothers I could have asked for, you keep me real, and stop me taking myself too seriously. To my extended family spread across the world, thank you for all your love and support over years, I am truly blessed to call you all my family.



“Enjoying his work, the grad student solemnly ponders whether he has fallen victim to Stockholm syndrome.”

Image credit: Lego Grad Student